



Veröffentlichungen der DGK

Ausschuss Geodäsie der Bayerischen Akademie der Wissenschaften

Reihe C

Dissertationen

Heft Nr. 835

Jinwei Zhang

**Assessing the statistical relations of terrestrial water mass
change with hydrological variables and climate variability**

München 2019

Verlag der Bayerischen Akademie der Wissenschaften

ISSN 0065-5325

ISBN 978-3-7696-5247-5

Diese Arbeit ist gleichzeitig veröffentlicht in:
Wissenschaftliche Arbeiten der Fachrichtung Geodäsie der Universität Stuttgart
<http://dx.doi.org/10.18419/opus-10474>, Stuttgart 2019



Veröffentlichungen der DGK

Ausschuss Geodäsie der Bayerischen Akademie der Wissenschaften

Reihe C

Dissertationen

Heft Nr. 835

Assessing the statistical relations of terrestrial water mass change
with hydrological variables and climate variability

Von der Fakultät Luft- und Raumfahrttechnik und Geodäsie
der Universität Stuttgart
zur Erlangung des Grades eines Doktor-Ingenieurs (Dr.-Ing.)
genehmigte Dissertation

Vorgelegt von

Jinwei Zhang

Geboren am 11.08.1989 in Xi'an, China

München 2019

Verlag der Bayerischen Akademie der Wissenschaften

ISSN 0065-5325

ISBN 978-3-7696-5247-5

Diese Arbeit ist gleichzeitig veröffentlicht in:
Wissenschaftliche Arbeiten der Fachrichtung Geodäsie der Universität Stuttgart
<http://dx.doi.org/10.18419/opus-10474>, Stuttgart 2019

Adresse der DGK:



Ausschuss Geodäsie der Bayerischen Akademie der Wissenschaften (DGK)

Alfons-Goppel-Straße 11 • D – 80 539 München
Telefon +49 – 331 – 288 1685 • Telefax +49 – 331 – 288 1759
E-Mail post@dgk.badw.de • <http://www.dgk.badw.de>

Prüfungskommission:

Vorsitzender: Prof. Dr.-Ing. Thomas Hobiger

Referent: Prof. Dr.-Ing. Nico Sneeuw

Korreferenten: Prof. Dr.-Ing. Annette Eicker

Tag der mündlichen Prüfung: 30.04.2019

© 2019 Bayerische Akademie der Wissenschaften, München

Alle Rechte vorbehalten. Ohne Genehmigung der Herausgeber ist es auch nicht gestattet,
die Veröffentlichung oder Teile daraus auf photomechanischem Wege (Photokopie, Mikrokopie) zu vervielfältigen

Contents

Abstract	XV
Zusammenfassung	XVII
1 Introduction	1
1.1 Monitoring the terrestrial water cycle	2
1.2 Water mass change in ocean-land-atmosphere circulation	6
1.2.1 Teleconnection	7
1.2.2 Climate variability and climate indices	9
1.3 Motivation and Objectives	11
1.4 Outline	14
2 Signal Decomposition Techniques and Regression Approaches	15
2.1 Principal component analysis	16
2.1.1 Singular value decomposition	18
2.1.2 Eigenvalue decomposition	20
2.1.3 Links between EVD and SVD	22
2.2 Independent component analysis	24
2.2.1 Blind source separation and statistical independence	24
2.2.2 Generic algorithm of ICA	26
2.2.3 Comparison of PCA and ICA	28
2.3 Canonical correlation analysis	28
2.3.1 Principle of CCA	30
2.3.2 Comparison of PCA and CCA	32
2.4 Multivariate linear regression modelling	34
2.4.1 Least squares prediction and collocation	34
2.4.2 Principal component regression	38
2.4.3 Partial least-squares regression	40
2.4.4 Adaptive moving averaging regression	42
2.4.5 Comparison and summary	45
3 Modelling of Terrestrial Water Storage Change in the Water Cycle	47
3.1 Spaceborne observation of terrestrial water storage	48
3.1.1 From geopotential to total water mass variation	48
3.1.2 Total water storage change from GRACE product	49
3.2 Modelling terrestrial water mass change by hydrological variables	53
3.2.1 Performance metrics for model evaluation	55
3.2.2 Characterization of terrestrial water storage variation	57
3.2.3 Estimation by least squares collocation	60

3.2.4	Estimation by principal component regression	67
3.2.5	Estimation by partial least squares regression	71
3.2.6	Estimation by adaptive moving average regression	78
3.3	Spatial downscaling of water storage variation in catchment	84
3.3.1	Statistical scenario	85
3.3.2	Case study: downscaling GRACE in Amazon	87
3.4	Discussion and summary	97
4	Phase Difference and Causality Analysis	101
4.1	Phase shift detection methods	102
4.1.1	Hilbert transformation and time lag analysis	102
4.1.2	Wavelet transformation and coherency analysis	103
4.2	Characterization of water mass-water cycle relationships	110
4.3	Causality analysis between water mass variation and climate change	112
4.3.1	Time lag analysis between water storage and ENSO	112
4.3.2	Coherency analysis between ENSO and water storage in basins	114
4.4	Discussion and summary	118
5	Teleconnection Between Water Mass Variation and Climate Variability	121
5.1	Between ENSO and terrestrial water storage	122
5.1.1	Decomposition of total water storage by PCA	122
5.1.2	Identification of ENSO signature by ICA	127
5.2	Between ENSO and terrestrial water cycle	131
5.2.1	Build up links between terrestrial water cycle and ENSO	132
5.2.2	Signature of ENSO on pan-Arctic water cycle	137
5.2.3	Signature of ENSO on individual boreal catchments	146
5.3	Discussion and summary	152
6	Conclusion and Outlook	155
6.1	Conclusion	155
6.2	Outlook	158
	Bibliography	161
	Acknowledgement	XIX
A	Recipe for Computing Total Water Storage Changes from GRACE	XXI
B	Joint Approximate Diagonalization of Eigenmatrices Algorithm	XXIII

List of Figures

1.1	Illustration of mass storage components and transport between ocean, land and atmosphere.	1
1.2	GRACE twin satellites with the Earth's gravity field (courtesy: GFZ).	5
1.3	Illustration of the land-ocean-atmosphere circulation as well as the terrestrial water cycle, in which the blue arrows indicate the land-ocean-atmosphere circulation, and the black arrows indicate the terrestrial water cycle. The yellow arrows describe the relationship between climate change and sea surface temperature change. The blue dashed lines represent the impact of climate change on the terrestrial water mass change.	6
1.4	Regions which ENSO index represents in Pacific Ocean	7
1.5	ENSO indices: Nino 1+2, Nino 3, Nino 4, Nino 3.4.	9
1.6	Power spectrum of 4 ENSO indices time series. All of them show strong frequency at or close to 0.34 and 0.65, which presents 3-year and 1.5-year cycle.	10
1.7	Temporal scales of the GRACE observation, the hydrological cycle, and the climate variability.	11
2.1	Illustration of PCA principle. The first component point to the direction of maximum variance, and then the following components are projected orthogonal to the previous one.	17
2.2	Illustration of PC and EOF matrices of data X.	18
2.3	Illustration of U, Σ, V matrices of data X.	19
2.4	Illustration of SVD principle as a linear transformation process.	19
2.5	Numerical performance of PCA on a set of mixed signals. Principal components are shown in a descending order of variance.	23
2.6	Illustration of ICA principle with respect to PCA. Different from PCA, The first component of ICA does not mean the most important component, and ICA requires that each component is statistically independent from others but not necessarily orthogonal projected.	28
2.7	Numerical performance of (c) PCA and (d) ICA on a set of (b) mixed signals, which is mixed on a set of (a) source signals. Principal components are shown in a descending order of variance. Independent components are shown in a descending order of kurtosis.	29
2.8	Illustration of the CCA principle. Different from PCA, CCA seeks for the most correlated component from the covariance space, and then project onto each data set. The red arrows show the direction of components after SVD analysis on the joint data set. The blue arrows depict the projected components for each data set, which are therefore canonical correlated.	29
2.9	Illustration of U_C, Σ_C, V_C matrices of covariance matrix C_{XY}	31
2.10	Illustration of the canonical spatial mode U_C , and temporal mode V_X of X.	31

2.11	Two simulated sets of signals (b) X and (c) Y , which is mixed by a linear combination of (a) source signals.	32
2.12	Numerical performance of CCA on two mixed data sets (a) X and (b) Y . Canonical components from each field are shown in a descending order of covariance.	33
2.13	Illustration of S , L and H for training and prediction.	35
2.14	Illustration of S , L and H in PCR model for training and prediction.	39
2.15	Illustration of S , L and H in PLR model for training and prediction.	41
3.1	Map of the linear trend of global total water storage change (a) on a grid and (b) at catchment scale.	52
3.2	Map of the annual amplitude of global total water storage change (a) on a grid and (b) at catchment scale.	52
3.3	Map of 26 catchments distributed globally.	55
3.4	Relationships between TWS and P , ET , R , respectively for catchment (a) Amazon (tropical), (b) Yangtze River (temperate), (c) Mackenzie (boreal), and (d) Lena (boreal).	58
3.5	Seasonal mean of TWS and its CI index in catchment (a) Amazon, (b) Danube, (c) Yangtze River, (d) Mackenzie, (e) Ob, and (f) Lena.	59
3.6	Flowchart of predicting total water storage by river runoff using least-squares collocation with parameters.	62
3.7	Estimations of total water storage change for (a) Amazon, (b) Yangtze, (c) Mackenzie, (d) Lena, respectively, by Least-Squares Collocation on a linear-fit model of observations using precipitation, evapotranspiration and runoff.	63
3.8	Flowchart of predicting total water storage by river runoff using least-squares prediction.	64
3.9	Estimations of total water storage change for (a) Amazon, (b) Yangtze, (c) Mackenzie, (d) Lena, respectively, by Least-Squares Prediction on observation residuals using precipitation, evapotranspiration and runoff.	65
3.10	Covariance performance of prediction errors of two approaches: least-squares prediction and collocation, using (a) precipitation, (b) evapotranspiration, (c) runoff, and (d) combining all of them.	66
3.11	Spectra of the temporal PCs from first five modes by PCA decomposition on (a) precipitation, (b) evapotranspiration, and (c) runoff.	67
3.12	Flowchart of predicting total water storage by river runoff using principal component regression.	68
3.13	Sensitivity test of prediction of total water storage change in 26 catchments by (a) precipitation, (b) evapotranspiration, and (c) runoff, using principal component regression. The predictions with different selected number of modes from observations are evaluated by correlation R , NSE, CNSE and PBIAS. Each row index refers to a specific catchment.	70
3.14	Predictions of total water storage change as well as its residual for (a) Amazon, (b) Yangtze, (c) Mackenzie, (d) Lena, respectively, by principal component regression on observation anomalies, using precipitation, evapotranspiration and runoff. The observations and residuals of total water storage from GRACE are plotted as well.	71

3.15	Auto-covariance and cross-covariance of (a) full signals (i.e. P , ET , R and M) and (b) residuals (i.e. ΔP , ΔET , ΔR and ΔM) along temporal dimensions for each catchment. Each row/column index represents for a specific catchment.	72
3.16	Flowchart of predicting total water storage by river runoff using partial least-squares regression.	74
3.17	Sensitivity of prediction of total water storage change in 26 catchments by (a) precipitation, (b) evapotranspiration, and (c) runoff, using partial least squares regression. The predictions with different selected number of joint modes from observations are evaluated by R, NSE, CNSE and PBIAS. Each row index stands for a specific catchment.	75
3.18	Predictions of total water storage change as well as its residual for (a) Amazon, (b) Yangtze, (c) Mackenzie, (d) Lena, respectively, by partial least-squares regression on observation anomalies, using precipitation, evapotranspiration and runoff. The observations and residuals of total water storage from GRACE are plotted as well.	76
3.19	Spectra of the temporal PCs of the first five joint modes by CCA decomposition from (a) precipitation, (b) evapotranspiration, (c) runoff, with total water storage, respectively. The percentage of joint modes in each field is also shown in the figure.	77
3.20	Flowchart of predicting total water storage by river runoff using an adaptive moving average least squares prediction.	80
3.21	Predicting the total water storage (a) and its residuals (b) in Danube basin by adaptive moving average least-squares prediction model, using observations from precipitation (P), evapotranspiration (ET), runoff (R), respectively, and joint observations of P , ET , R . The performances of prediction are evaluated by R, NSE, and RMSE.	81
3.22	Sensitivity test of prediction of total water storage change in 26 catchments by combination of precipitation, evapotranspiration, and runoff, using least-squares prediction. The predictions with different selected order of MAR model are evaluated by correlation, NSE, CNSE and PBIAS.	81
3.23	(a) Total water storage prediction in Danube basin by least-squares prediction, principal component regression, and partial least-squares regression. (b) Total water storage prediction in Danube basin by the adaptive moving average model with least-squares prediction, principal component regression, and partial least-squares regression. (c) Prediction of residuals of total water storage in Danube basin by the adaptive moving average model with least-squares prediction, principal component regression, and partial least-squares regression. The observations and residuals of total water storage from GRACE are plotted as well. The performances of predictions are evaluated in terms of R, NSE and RMSE, shown on the right hand side of the time series.	82
3.24	Illustration of the scenario for GRACE product downscaling.	85
3.25	The downscaled TWS in Amazon from three different schemes TWS grids as well as TWS grids from GRACE, WGHM and GLDAS, at four different epochs (i.e., March 2004, September 2005, December 2006, June 2008).	88
3.26	Monthly aggregates of the TWS over the Amazon basin from GRACE, WGHM and assimilations using three different schemes.	89

3.27	(a) The linear trend, (b) the annual amplitude, (c) the RMS of full signals, and (d) the RMS of residuals of TWS grids in Amazon basin derived from GRACE, WGHM, and downscaled TWS by assimilation using three different schemes.	90
3.28	Monthly TWS of one arbitrary grid point in the Amazon basin from GRACE, WGHM and assimilations using three different schemes.	91
3.29	(a) The misclosure of the water balance in Amazon basin at epoch September 2005 as well as its (b) mean and (c) RMS, in which the water storage fluxes are obtained from GRACE, WGHM, downscaled TWS from three different schemes, respectively.	93
3.30	Downscaled total water storage in Amazon basin using adaptive moving average partial least-squares regression by different number of joint modes (i.e. 3 joint modes, 5 joint modes, 10 joint modes, 15 joint modes) (a) in September 2005 (as example), and their performances evaluated by NSE and RMSE with respect to (b) GRACE and (c) WGHM, respectively.	94
3.31	Power spectra of the temporal PC from the first 5 modes in total water storage changes in Amazon basin, which are obtained from GRACE, WGHM, and downscaled TWS, respectively.	95
3.32	The corresponding spatial EOFs corresponding to the temporal PCs (represented in spectral domain in Figure 3.31) of the total water storage changes in Amazon basin, producing from GRACE, WGHM, and downscaling, respectively.	96
4.1	Illustration of the phase difference and time lag between time series $l(t)$ and Hilbert transformed time series. The parameters b and c estimated in the Eq. (4.4) are used in amplitude and phase calculation in Eq. (4.5) and (4.6).	103
4.2	Comparison of (middle) Fourier transformation and (right) wavelet transformation with respect to the target signal (left) in time resolution at different frequencies.	104
4.3	Illustration of continuous wavelet transform (CWT).	105
4.4	Illustration of the Morlet wavelet as mother wavelet $\psi(t)$	106
4.5	Illustration of (a) simulated time series x , with its (b) power spectrum from Fourier transformation and (c) wavelet spectrum from wavelet transformation. The thick black contour in (c) indicates the 95% confidence level, and the cone of influence is shown as lighter shade.	108
4.6	Illustration of (a) time series x and y and (b) its wavelet coherency. Simulated x and y with different frequencies and amplitudes in three cases are numerated in (1), (2), (3). The thick black contour indicates the 95% confidence level, and the cone of influence is shown as lighter shade. The arrows pointing to right direction denotes in phase, and left direction stands for anti-phase. The arrows upwards indicate the phase lag of y to x by $\pi/2$, and the arrows downwards indicate the phase lead of y to x by $\pi/2$	109
4.7	Illustration of relationships between TWS and shifted P , ET , R , respectively for catchment (a) Amazon (tropical), (b) Yangtze River (temperate), (c) Mackenzie (boreal), and (d) Lena (boreal).	111
4.8	Maps of the time shifts between TWS and (a) P , (b) ET , (c) R , respectively, in 26 catchments, which are distributed globally. Positive values indicate a time lead of TWS to P , ET , R , while negative values indicate a time lag.	112

4.9	Time difference between ENSO and TWS are calculated by the linear model based on the Hilbert transformation. Positive value means that TWS leads to ENSO, while negative value denotes the lead of ENSO to TWS.	113
4.10	Time difference between ENSO and TWS in catchments, with the same description as expressed in Figure 4.9.	114
4.11	Nino 3.4 index and its wavelet spectrum.	115
4.12	(a) Terrestrial water storage change derived from GRACE in the basin (1) Ob, (2) Lena, (3) Yenisei, (4) Mackenzie and (5) Yukon, with their (b) histograms.	116
4.13	The relationship between TWS and ENSO in basins is visualized in terms of (a) cross-wavelet spectrum and (b) coherency.	117
5.1	Eigenvalues of global continental water mass change from each mode generated by PCA decomposition.	122
5.2	(a) The temporal PCs and (b) its corresponding spatial EOFs of the first modes from global continental TWS.	123
5.3	Catchments (i.e., Ob, Lena, Yenisei, Mackenzie, Yukon) in the pan-Arctic area. . .	124
5.4	The first three spatial EOFs by PCA of the TWS in the catchments: (a) Ob, (b) Lena, (c) Yenisei, (d) Mackenzie, (e) Yukon, respectively.	125
5.5	The first three principal components (PCs) by PCA of the TWS in the catchments: (a) Ob, (b) Lena, (c) Yenisei, (d) Mackenzie, (e) Yukon, respectively. The black line is from total water storage, compared with Nino 3.4 index (yellow line).	126
5.6	(a) Time series comparison between TWS PC2 of Ob basin and Nino 3.4 index, with (c) its scatter plot. (b) Wavelet coherency between TWS PC2 and Nino 3.4 index. The black line in (a) denotes total water storage, and yellow line is Nino 3.4 index. The thick black contour indicates the 95% confidence level against red noise, and the cone of influence is shown as lighter shade. Arrows pointing to right direction denote in-phase, and left direction stands for anti-phase. Arrows upwards indicate the phase lag of TWS to ENSO by $\pi/2$, and the arrows downwards indicate the phase lead of TWS to ENSO by $\pi/2$	127
5.7	The five temporal ICs (left) by ICA of the Lena basin, together with corresponding spatial patterns (right). The black line in the temporal ICs denotes total water storage, compared with Nino 3.4 index (yellow line).	129
5.8	The wavelet coherency between Nino 3.4 index and IC3 (a), IC4 (b) and IC5 (c) by ICA, respectively. Same description as Figure 5.6.	130
5.9	Procedure of data processing by CCA	132
5.10	(left) Temporal modes of each PC pair of total water storage anomalies from GRACE in the boreal region and global sea surface temperature anomalies after CCA decomposition, and (right) the scatter plot between the paired PCs from total water storage and sea surface temperature.	133
5.11	Temporal modes of sea surface temperature anomalies (blue line) compared with each variable (black line), i.e., total water storage, precipitation, evaporation, runoff, surface temperatures, water mass derivative, water fluxes, respectively, associated with Nino 3.4 index (yellow line). Nino 3.4 index are scaled by the magnitude of each variable.	135

5.12	Temporal joint mode of (a) PC1 and (b) PC4 from TWS and SST are listed in the first row. The wavelet coherency of between ENSO and joint (c) PC1, (d) PC4 from SST are listed in the second row. The wavelet coherency of between ENSO and joint (e) PC1, (f) PC4 from TWS are listed in the third row.	136
5.13	(left) (b) Temporal joint mode from total water storage and SST, with (a) the ENSO related spatial patterns from TWS and (c) SST.	138
5.14	(a) Spatial pattern of each variable in boreal region, related to ENSO effects; (b) Spatial pattern of global SST, associated with each variable. The EOFs are selected by correlation coefficients shown in Table 5.4.	140
5.15	(a) ENSO related spatial patterns of water storage fluxes EOF5 from (a) water balance equation; And ENSO related spatial patterns of water mass derivative from GRACE observations, represented in three different EOFs, i.e., (b) EOF 5, (c) EOF 6 and (d) EOF 9, respectively.	141
5.16	ENSO related spatial patterns of SST, associated with (a) water storage fluxes from water balance equation, and with water mass derivative from GRACE observations, represented in three different EOFs, i.e., (b) EOF 5, (c) EOF 6 and (d) EOF 9, respectively.	142
5.17	Wavelet coherency between Nino 3.4 index and (a) PC4 from total water storage, (b) PC3 from precipitation, (c) PC5 from runoff, (d) PC6 from evaporation and (e) PC6 from temperature, respectively. Same description as Figure 5.6.	144
5.18	ENSO related spatial patterns of SST, associated with (a) water storage fluxes from water balance equation, and with water mass derivative from GRACE observations, represented in three different EOFs, i.e., (b) EOF 5, (c) EOF 6 and (d) EOF 9, respectively.	146
5.19	ENSO related spatial patterns in the Ob basin of (a) precipitation, (b) evaporation, (c) river runoff, (d) surface temperature, (e) water storage fluxes derived from GRACE observations and (f) from water balance equation.	147
5.20	ENSO related spatial patterns in the Lena basin from (a) precipitation, (b) evaporation, (c) river runoff, (d) surface temperature, (e) water storage fluxes from water balance equation and (f) derived from GRACE observations.	148
5.21	ENSO related spatial patterns in the Yenisei basin from (a) precipitation, (b) evaporation, (c) river runoff, (d) surface temperature, (e) water storage fluxes from water balance equation and (f) derived from GRACE observations.	149
5.22	(a) Temporal modes of sea surface temperature anomalies compared with total water storage, precipitation, evaporation, runoff, surface temperatures, water mass derivative, water fluxes, respectively; (b) Temporal modes of sea surface temperature anomalies compared with Nino 3.4 index; (c) Temporal modes of each hydrologic variables compared with Nino 3.4.	150

List of Tables

1.1	Common used climate indices, including their full names, acronyms, observable and using methods.	8
2.1	Simulated source signals with certain parameters.	23
2.2	Summary of four different type of multivariate linear regression approaches. The essential required quantities for these regressions are briefly listed.	45
3.1	Data sets used in water mass variation modelling.	54
3.2	Performance of least-squares prediction and collocation using precipitation, evapotranspiration and runoff.	65
3.3	Performance of principal component and partial least-squares regression of precipitation, evapotranspiration and runoff, based on the optimal choice of modes.	78
3.4	Performance of principal component and partial least-squares regression of precipitation, evapotranspiration and runoff, based on the optimal choice of modes.	83
3.5	Settings of three different schemes used for the training and prediction in the downscaling frame.	86
5.1	Correlation ρ between Nino 3.4 index and PCs from TWS, with percentage of variance σ of PCs.	124
5.2	Correlation between Nino 3.4 index and ICs from TWS.	128
5.3	Data sets used in this study.	131
5.4	Correlation between Nino 3.4 index and 10 temporal modes of SSTs, corresponding to water mass variation, precipitation, runoff, evaporation, land surface temperature, and water fluxes derived from GRACE observations and water balance equation, respectively. The mode of largest correlation coefficient with Nino 3.4 are emphasized in the table.	136
5.5	Phase difference $\Delta\phi$ and time lag Δt_1 and Δt_2 between Nino 3.4 index and PCs from each variable. Positive values indicate the lead of ENSO, while negative values indicate the lag of ENSO to terrestrial observations. $\Delta\phi$ and Δt_1 are estimated from Hilbert transformation equation, and Δt_2 is calculated by cross-correlation.	144
5.6	Phase difference $\Delta\phi$ and time lag Δt_1 and Δt_2 between Nino 3.4 index and PCs from water storage fluxes by dM/dt and water balance $P - E - R$. Positive values indicate the lead of ENSO, while negative values indicate the lag of ENSO to water storage fluxes. $\Delta\phi$ and Δt_1 are estimated from Hilbert transformation equation, and Δt_2 is calculated by cross-correlation.	145

- 5.7 Correlation ρ between Nino 3.4 index and identified PCs from SST, which is associated with each variable (i.e., $M, P, R, E, T, dM/dt, P - E - R$), with percentage of variance of identified PCs (σ) from each variable, and the time lags (Δt) of each variable to Nino 3.4, are listed for three boreal basins (Ob, Lena, Yenisei) in the table. In this case, positive Δ means time lag to ENSO, while negative stands for time lead to ENSO. 151

List of Abbreviations

AAO	Antarctic Oscillation
ANN	Artificial Neural Network
AO	Arctic Oscillation
CAMS	Climate Anomaly Monitoring System
CCA	Canonical Correlation Analysis
CF	Earth's Center of Figure
CI	Cyclostationary Index
CLM	Common Land Model
CM	Earth's Center of Mass
CNSE	Cyclostationary Nash-Sutcliffe Efficiency
COI	Cone of Influence
CPC	Climate Prediction Center
CRU	Climate Research Unit
CSR	Center for Space Research
CWT	Continuous Wavelet Transform
DLR	Deutsches Zentrum für Luft und Raumfahrt
ECMWF	European Center for Medium-Range Weather Forecasts
ENSO	El Niño and the Southern Oscillation
EOF	Empirical Orthogonal Function
EOT	Empirical Orthogonal Teleconnection
EVD	Eigenvalue decomposition
GFZ	GeoForschungsZentrum
GHCN	Global Historical Climatology Network
GLDAS	Global Land Data Assimilation Systems
GLEAM	Global Land-surface Evaporation: the Amsterdam Methodology
GPCC	Global Precipitation Climatology Center
GPCP	Global Precipitation Climatology Project
GPM	Global Precipitation Measurement
GPS	Global Positioning System
GRACE	Gravity Recovery And Climate Experiment
GRDC	Global Runoff Data Center
GSFC	Goddard Space Flight Center
ICA	Independent Component Analysis

JADE	Joint Approximate Diagonalization of Eigenmatrices
JAXA	Japan Aerospace Exploration Agency
JPL	Jet Propulsion Laboratory
LSC	Least-Squares Collocation
LSM	Land Surface Model
LSP	Least-Squares Prediction
LST	Land Surface Temperature
LTI	Linear Time Invariant
MA	Moving Average
MEI	Multivariate ENSO Index
MSSA	Multi-channel Singular Spectrum Analysis
NAO	North Atlantic Oscillation
NASA	National Aeronautics and Space Administration
NCEP	National Centers for Environmental Prediction
NPO/WP	North Pacific Oscillation/West Pacific
NSE	Nash-Sutcliffe Efficiency
ONI	Oceanic Nino Index
PBIAS	Percent Bias
PCA	Principal Component Analysis
PCR	Principal Component Regression
PDF	Probability Density Function
PDO	Pacific Decadal Oscillation
PERSIANN	Precipitation Estimation from Remotely Sensed Information using Artificial Neural Networks
PLR	Partial Least-squares Regression
PNA	Pacific-North America
RMSC	Normalized Root Mean Squared Covariance
RMSE	Root Mean Square Error
RPCA	Rotated Principal Component Analysis
SLP	Sea Level Pressure
SLR	Satellite Laser Ranging
SOI	Southern Oscillation Index
SST	Sea Surface Temperature
SVD	Singular Value Decomposition
TRMM	Tropical Rainfall Measuring Mission
TWS	Total Water Storage
VIC	Variable Infiltration Capacity
WGHM	WaterGap Global Hydrology Model
WTC	Wavelet Transform Coherency
XWT	Cross-Wavelet Transform

Abstract

Water mass transport on the Earth is an interaction among the ocean, land and atmosphere. As a part of the circulation, the terrestrial water mass change in the water cycle and exchange in the ocean-land-atmosphere interaction are essential to assess, which motivates us to start this study. As a major spaceborne geodetic sensor, the GRACE satellite mission observes the global mass change, sensing the time-variable gravity field of the Earth. The global coverage of GRACE allows to monitor the large-scale water mass variation, despite the coarse temporal and spatial resolution and the limited lifetime. Based on the GRACE products, this thesis aims to assess the terrestrial water mass change by hydrometeorological variables and explore the teleconnection with climate variability.

Initially, the linear relationship between and the seasonality of each variable in the water balance are characterized. For estimating the terrestrial water mass change at catchment scale by multiple hydrological variables, three statistical approaches are employed in this thesis, namely, (1) least-squares prediction/collocation (LSP/LSC), (2) principal component regression (PCR), (3) partial least-squares regression (PLR). Concerning the temporal shifts among the variables in the dynamic water cycle, an adaptive moving average (MA) algorithm combined with these three approaches is developed to improve the accuracy of model estimates. The performances of the three different approaches are evaluated and compared through a validation against the observations from GRACE. The terrestrial water storage in the tropical and temperate basins is well-modeled by a combination of precipitation, evapotranspiration and runoff. However, the water storage is poorly predicted in boreal catchments, due to its weak cyclo-stationarity. In addition, some aspects regarding the model performance, e.g. the sensitivity of PCR and PLR to the selected modes, the sensitivity to the order of MA, are also investigated to find an optimal scheme.

Concerning the coarse spatial resolution of GRACE, we develop a statistical assimilation algorithm based on MA and PLR to acquire a higher resolution, by assimilating GRACE with multiple spatial highly-resolved hydrological models. In contrast with conventional assimilation approaches, e.g. Kalman filter, our algorithm is implemented without any model assumption. This spatial downscaling of GRACE is achieved with knowledge of the empirical information of high resolution water storage from a model, i.e. WGHM. The results show an obvious improvement of the spatial resolution. For a validation, we compare the downscaled water storage with GRACE and WGHM by aggregation over catchments, and through the misclosure of the water balance. As a result, it shows that our assimilation is acceptable. Additionally, the spatial and temporal patterns of separated modes of results as well as the linear trends and annual amplitudes explain the good performance of the assimilation, which retains the dominant signals from GRACE and benefits from WGHM in local details.

To explore the teleconnection between climate variability and terrestrial water mass change, the sea surface temperature (SST) anomalies are adopted as an intermedium. This thesis employs several decomposition methods, i.e. principal component analysis (PCA), independent component analysis (ICA), and canonical correlation analysis (CCA), to extract the associated variation from GRACE observed terrestrial water storage with El Niño Southern Oscillation (ENSO). Comparing with PCA and ICA, CCA demonstrates the advantage of identifying the signature of ENSO on terrestrial interannual water mass change. The spatial patterns of the identified canonical modes reveal the signature of ENSO on pan-Arctic regions, particularly on several boreal catchments, e.g. Lena, Yenisei and Ob. In addition, the disagreement of the spatial patterns of water storage fluxes from mass derivative and water balance is explained by the model errors and the inconsistency of the spatial resolution.

Furthermore, to explore the causal relationships between ENSO and terrestrial variables (i.e. water storage, precipitation, evaporation, runoff, land surface temperature) in boreal catchments, the phase and time delay with respect to ENSO is estimated by the Hilbert transformation and wavelet transformation. The different time lags of each variable allow interpretation of the dynamic process of the water mass transport. The wavelet coherency maps indirectly prove the identified joint modes by CCA. The associated temporal modes of precipitation, runoff, evaporation indicate time lags to ENSO from 0 to 2 months. Due to the inadequate temporal sampling of GRACE, the time lag of water storage cannot be distinguished within one integer month. Water storage fluxes respond to ENSO with about 1-month delay. Nevertheless, GRACE has proved its capability of sensing the interannual change of terrestrial water mass that associated with ENSO. Overall, the phase differences calculated by Hilbert transformation and represented by wavelet coherency maps help us to interpret the causal relationships between ENSO and terrestrial variables, and understanding the teleconnection in a comprehensive way.

Zusammenfassung

Der Wassertransport auf der Erde findet in der Wechselwirkung zwischen Ozean, Land und Atmosphäre statt. Als Teil der Zirkulation sind die Änderungen der terrestrischen Wassermassen im Wasserkreislauf und der Austausch in der Wechselwirkung zwischen Meer, Land und Atmosphäre von wesentlicher Bedeutung, was uns zu dieser Forschung motiviert. Als bedeutender geodätischer Sensor im Weltraum beobachtet die GRACE-Satellitenmission die globalen Massenänderungen und erfasst das zeitlich-veränderliche Schwerfeld der Erde. Die globale Abdeckung der GRACE Beobachtungen ermöglicht die Überwachung der großräumigen Wassermassenschwankung trotz der groben zeitlichen und räumlichen Auflösung und der begrenzten Lebensdauer. Basierend auf den GRACE-Beobachtungen soll diese Dissertation die terrestrische Wassermassenänderung durch hydrometeorologischer Variablen bewerten und die „Teleconnection“ mit der Klimavariabilität untersuchen.

Zunächst werden die Saisonalität jeder Variablen und die lineare Beziehung zwischen diesen im Wasserhaushalt charakterisiert. Drei statistische Ansätze, nämlich (1) „least-squares prediction/collocation“ (LSP/LSC), (2) „principal component regression“ (PCR), (3) „partial least-squares regression“ (PLR), werden in dieser Arbeit verwendet, um die Änderung der terrestrischen Wassermassen durch mehrere hydrologische Variablen je Becken abzuschätzen. Bezüglich der zeitlichen Verschiebungen zwischen den Variablen im dynamischen Wasserkreislauf wird ein adaptiver „moving average“ (MA) Algorithmus in Kombination mit diesen drei Ansätzen entwickelt, um die Genauigkeit der Modellschätzungen zu verbessern. Die Leistungen der drei verschiedenen Ansätze werden bewertet und durch eine Validierung mit den Beobachtungen von GRACE verglichen. Der terrestrische Wasserspeicher in den tropischen und gemäßigten Becken ist durch eine Kombination aus Niederschlag, Evapotranspiration und Abfluss gut modelliert. Aufgrund der schwachen Zyklus-Stationarität wird der Wasserspeicher in borealen Becken jedoch nur schlecht vorhergesagt. Außerdem werden einige Aspekte bezüglich der Modelleleistung ebenfalls untersucht, z.B. die Sensitivität von PCR und PLR für die ausgewählten Modi, und die Sensitivität für die Reihenfolge von MA, um ein optimales Schema zu finden.

Darüber hinaus entwickeln wir einen statistischen Assimilationsalgorithmus basierend auf MA und PLR, um eine höhere räumliche Auflösung des gesamten Wasserspeichers zu erhalten, indem GRACE-Lösungen mit mehreren räumlichen hochaufgelösten hydrologischen Modellen assimiliert wird. Im Gegensatz zu einem herkömmlichen Assimilationsansatz, z.B. "Kalman-Filter", wird unser Algorithmus ohne Modellannahme implementiert. Diese räumliche Herunterskalierung von GRACE wird durch Kenntnis der empirischen Informationen der Wasserspeicherung mit hoher Auflösung aus dem Modell, d.h. WGHM, erreicht. Die Ergebnisse zeigen eine offensichtliche Verbesserung der räumlichen Auflösung. Für eine Validierung vergleichen wir die rechnerische verkleinerte Wasserspeicherung aus GRACE und WGHM durch Aggregation über die Becken und durch den Abschlussfehler des Wasserhaushaltes. Das Ergebnis zeigt,

dass unsere Assimilation akzeptable Werte liefert. Die räumlichen und zeitlichen Muster der getrennten Ergebnismodi, sowie die linearen Trends und Jahresamplituden erklären die gute Leistung der Assimilation darüber hinaus, wobei die Lösungen die dominanten Signale von GRACE beibehält und in lokalen Details von WGHM profitiert.

Um die Teleconnection zwischen der Klimavariabilität und der Änderung der terrestrischen Wassermassen zu untersuchen, werden Anomalien der Meeresoberflächentemperatur (SST) als Medium angenommen. Diese Arbeit verwendet verschiedene numerisch „decomposition methods“, d.h. „principal component analysis“ (PCA), „independent component analysis“ (ICA) und „canonical correlation analysis“ (CCA), um die damit verbundene Variation aus der beobachteten terrestrischen Wasserspeicherung von GRACE mit „El Niño Southern Oscillation“ (ENSO) zu extrahieren. Im Vergleich mit PCA und ICA zeigt CCA den Vorteil der Identifizierung der Signatur von ENSO bei den zwischenjährlichen Änderungen der terrestrischen Wassermasse. Die räumlichen Muster der identifizierten kanonischen Modi zeigen die Signatur von ENSO in panarktischen Regionen, insbesondere in mehreren borealen Becken, z.B. Lena, Yenisei und Ob. Die Nichtübereinstimmung der räumlichen Muster der Wasserspeicherflüsse aus der Massenableitung und dem Wasserhaushalt wird durch die Modellfehler und die Inkonsistenz der räumlichen Auflösung erklärt.

Ferner wird die Phasen- und Zeitverzögerung in Bezug auf ENSO geschätzt, um die kausalen Beziehungen zwischen ENSO und terrestrischen Variablen (d.h. Wasserspeicherung, Niederschlag, Verdampfung, Abfluss, Landoberflächentemperatur) in borealen Becken zu untersuchen. Die Hilbert-Transformation und die Wavelet-Transformation werden eingeführt, um die Phasendifferenzen zu quantifizieren. Die unterschiedlichen Zeitverzögerungen jeder Variablen interpretieren den dynamischen Prozess des Wassermassentransports. Die Wavelet-Kohärenzkarten bestätigen indirekt die kanonischen Modi durch CCA identifizierten. Die verbundenen zeitlichen Modi von Niederschlag, Abfluss und Verdampfung weisen auf eine Zeitverschiebung bis zu 2 Monaten im Vergleich zu ENSO hin. Aufgrund der unzureichenden zeitlichen Probenahme von GRACE kann die zeitliche Verzögerung der Wasserspeicherung nur auf Monatsebene erfolgen. Wasserspeicherflüsse reagieren auf ENSO mit einer Verzögerung von etwa einem Monat. Trotzdem hat GRACE seine Fähigkeit bewiesen, die mit ENSO einhergehenden Änderungen der terrestrischen Wassermasse zu erfassen. Außerdem helfen die dargestellten Phasendifferenzen durch den Hilbert-Transformation und durch die Wavelet-Kohärenzkarten, um die kausalen Beziehungen zwischen ENSO und terrestrischen Variablen zu interpretieren, und die Teleconnection umfassend zu verstehen.

Chapter 1

Introduction

The Earth system is composed of several components: the solid Earth, hydrosphere, atmosphere, lithosphere and biosphere. Although the Earth system is mass conserving, masses are transported and redistributed in and among different parts of Earth. With the interaction among the land, ocean and atmosphere in various ways, the mass variation occurs on all temporal and spatial scales.

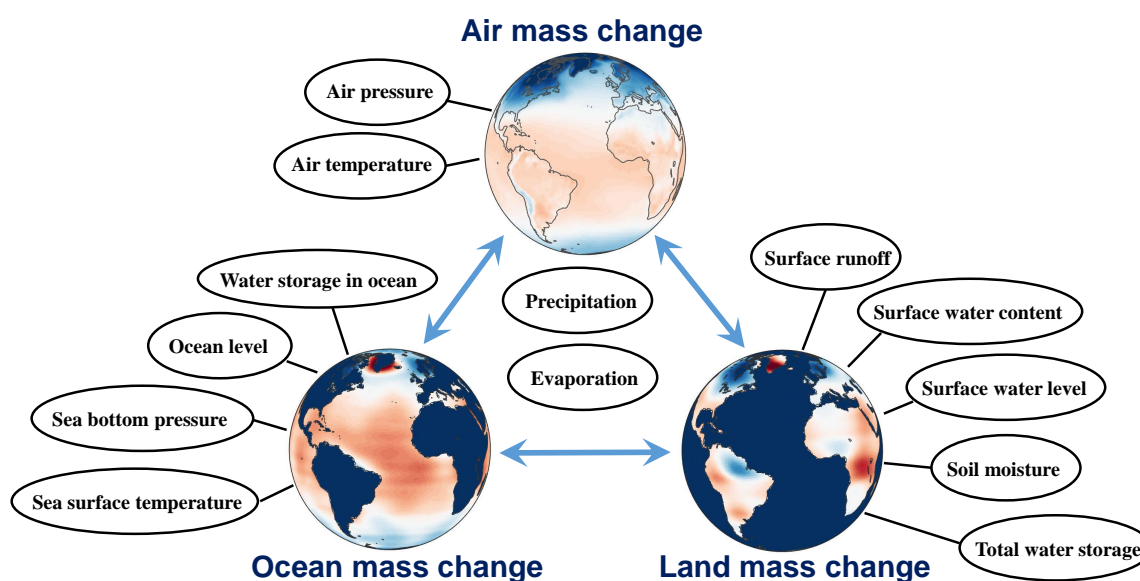


Figure 1.1: Illustration of mass storage components and transport between ocean, land and atmosphere.

A general overview of the global water mass storage and transport is illustrated in Figure 1.1. Monitoring the global water mass storage and transport is practically fulfilled through various variables. The terrestrial water mass change can be measured via the variation of surface water level, content, runoff as well as soil moisture, etc. Meanwhile, the oceanic mass change is observed by the variation of ocean level, bottom pressure and storage. Additionally, the ocean mass transport is also indicated by the surface temperature, which generally reflects the associated climate impacts. Different from ocean and land, the atmospheric mass components are mainly in form of water vapor. Hence, the air pressure and air temperature are important observed quantities, indicating the water transport in the atmosphere.

1.1 Monitoring the terrestrial water cycle

The terrestrial part of water mass variation is the main interest of this thesis, despite the oceanic and atmospheric mass changes are also significant. The hydrological cycle, particularly as the essential topic in the terrestrial water mass change, will be mainly investigated and discussed. This section introduces briefly the components of the terrestrial water balance, their measurement, and the data acquisition by various spaceborne sensors.

Theoretically, water mass is gained from rainfall into a river basin, while river runoff and evaporation cause water mass loss. As a consequence, such mass gain and loss leads to a change of the terrestrial water storage. The relationship between precipitation, evaporation and river runoff, therefore, is mathematically described in terms of the water balance equation

$$\frac{dM}{dt} = P - ET - R, \quad (1.1)$$

where P denotes precipitation, E is evaporation, and R represents river runoff. dM/dt represents the rate of water mass change, namely water storage flux. This is the fundamental principle of the terrestrial hydrological cycle.

Measurement of hydrological variables Precipitation, is generally measured using various type of rain gauges, e.g. the cylinder gauge and wedge gauge. For different purposes, a variety of recording rain gauge devices are available, e.g. hyetograph for short period, and totalizer for long-time measurement. Although surface precipitation gauges are considered as the standard in-situ measurement, some regions still lack observations.

In the recent past, satellite sensors, including both thermal infrared and microwave types, are used to measure the precipitation by remote sensing. The Tropical Rainfall Measuring Mission (TRMM), a joint mission by the National Aeronautics and Space Administration (NASA) and the Japan Aerospace Exploration Agency (JAXA) in 1997, employed microwave sensors to monitor the tropical precipitation (Huffman et al., 2007). Another joint mission by NASA and JAXA, namely Global Precipitation Measurement (GPM), building on the success of TRMM, provides frequent (every 2–3 hours) observations of precipitation (Hou et al., 2014). Unlike gauge measurements, these modern spaceborne sensors provide observations of precipitation at large-scale. Therefore, global gridded precipitation data is available. A number of agencies produce the global precipitation dataset with high spatial resolution and dense temporal sampling, e.g. Climate Research Unit (CRU), Global Precipitation Climatology Center (GPCC), Global Precipitation Climatology Project (GPCP), etc. Based on the satellite observations, various global precipitation model estimations have emerged with high spatio-temporal resolution, e.g. European Center for Medium-Range Weather Forecasts (ECMWF) produced the ERA-Interim reanalysis data, and the Center for Hydrometeorology and Remote Sensing (CHRS) at the University of California, Irvine (UCI) developed the Precipitation Estimation from Remotely Sensed Information using Artificial Neural Networks-Climate Data Record (PERSIANN-CDR) dataset. In this thesis, precipitation from model estimates are employed for terrestrial water mass change analysis.

Runoff is the overall volume of water that exits a drainage basin through either the outflow cross-section (surface or subsurface) or other means. Generally, the runoff in the field is measured at the reference gauges, e.g. weirs, notches, orifices and meter gates, in terms of water velocity. In-situ measurements of runoff are publicly available from several agencies, e.g. Global Runoff Data Center (GRDC), the Arctic Rapid Integrated Monitoring System (ArcticRIMS) project, Water Survey Canada, the U.S. Geological Survey (USGS), the U.S. Army Corps of Engineers (USACE), the Environmental Research Observatory (ORE) Geodynamical, Hydrological, and Biogeochemical Control of Erosion/Alteration and Material Transport in the Amazon Basin (HYBAM) project, etc.

Apart from the in-situ runoff measurement, runoff is also modeled on a grid by Land Surface Models (LSMs) that represent the energy and terrestrial water fluxes for climate, weather, and water resource studies, e.g. the Global Land Data Assimilation Systems (GLDAS) model produced runoff. Since the declined number of available gauge stations from those runoff databases leads to a deficiency of runoff measurement in the past decades, it has been practical to resort to sophisticated hydrological and atmospheric reanalysis models to acquire runoff estimates (Trenberth et al., 2007). Recently, spaceborne observations have demonstrated their potential and accuracy of estimating river runoff at catchment scale (Tourian et al., 2013; Sneeuw et al., 2014; Lorenz et al., 2015). This concept provides us a broad way to estimate runoff instead of in-situ measurement and validate against hydrological model estimates (Alsdorf et al., 2007).

Evapotranspiration plays a significant role in the water cycle. However, different from precipitation and runoff, evapotranspiration is difficult to directly measure and quantify in the field. One general way to measure evapotranspiration is with the aid of a weighing lysimeter. The soil humidity is measured by lysimeter and subsequently the evapotranspiration is calculated by modeling the change of water in the soil. Since the in-situ measurement of evapotranspiration is difficult, in general, it is indirectly calculated using water balance methods, water vapor transfer methods or energy balance methods (Rana and Katerji, 2000).

In recent decades, spaceborne sensors provide us a useful measure of spatial evapotranspiration. For example, remote sensing satellites provide opportunities for instantaneous snapshots of evapotranspiration over large area. Moreover, Light Detection And Ranging (LiDAR) technology has been used to monitor evapotranspiration remotely, providing detailed and frequent 3D mapping of evapotranspiration (Drexler et al., 2004). With the help of spatial observations from satellites, the global evapotranspiration datasets are consequently available, e.g. the high-resolved evapotranspiration dataset from the Global Land-surface Evaporation: the Amsterdam Methodology (GLEAM), which is calculated based on multi-satellite observations (Miralles et al., 2011). In this thesis, we acquire the gridded global evapotranspiration from these datasets.

Spaceborne geodetic sensors for monitoring water mass change In the past decades, an increasing number of satellites was designed and launched for various purposes, e.g. positioning, oceanography, cryosphere, hydrology applications, etc (Alsdorf et al., 2007). Since more spaceborne geodetic sensors provide large-scale terrestrial observations, various studies has been done on modelling the hydrological variables by the geodetic observations.

The Global Positioning System (GPS), initially a military satellite navigation and positioning system project, was developed in 1973 by the Department of Defense, USA (Evans et al., 2002).

It became fully operational in 1994 with the completion of a full constellation of 24 satellites. Not only accurate positioning information, GPS technology also provides information on several components of the terrestrial water cycle. For example, GPS has been used to determine the integrated precipitable water vapor on various temporal and spatial scales using the signal delay in the troposphere (Davis and Elgered, 1998). GPS technology is also used to investigate the hydrological loading from surface displacement time series (van Dam et al., 2001; Davis et al., 2004; Tregoning et al., 2009). Moreover, making use of the multi-path effects, the GPS reflectometry (GPS-R) is developed to measure the soil moisture (Larson et al., 2008), water level heights (Larson et al., 2013) and snow depths (Larson et al., 2009).

Radar satellite altimetry offers the possibility to measure sea surface heights globally. The sea surface height is determined by radar measurement of the distance between the satellite and the sea surface, based on the location information of the satellite during the measurement and a number of atmospheric corrections. The altimetric satellite missions (e.g. ENVISAT, TOPEX/Poseidon), originally developed for oceanographic and geophysical applications, has already demonstrated its capability on monitoring the water level of inland rivers and lakes (Berry et al., 2005; Alsdorf et al., 2007; Papa et al., 2010). Moreover, based on the spaceborne water level observations, the river discharge has been estimated by a quantile function approach (Tourian et al., 2013).

Remote sensing satellite imagery, including optical and Synthetic Aperture Radar (SAR), provides high resolution images to monitor the surface water extent. For example, utilizing the images from Moderate Resolution Imaging Spectroradiometer (MODIS), the water extent variation of lakes and rivers has been successfully captured (Gao et al., 2012; Künzer et al., 2015; Tourian et al., 2015; Elmi et al., 2016). Hence, the application of satellite imagery contributes remarkably to the terrestrial water resource monitoring.

Since the launch of the Gravity Recovery And Climate Experiment (GRACE) mission in 2002 jointly by NASA and Deutsches Zentrum für Luft und Raumfahrt (DLR), the global monitoring of the Earth's time-variable gravity field has become possible (Tapley et al., 2004). The GRACE mission, aiming at measuring the variation of Earth's gravity field, comprises two coplanar satellites in a low, near circular, near polar orbit with an inclination of 89° , at an altitude of around 500 km, separated from each other by a distance of roughly 220 km. The measurement is established by tracking the inter-satellite range and range-rate between two satellites via a K-band ranging system. Additionally, accelerometers, GPS receivers, star cameras as well as laser retro reflectors are embedded on-board on both satellites. The GRACE mission was designed initially for a 5-year period, and was terminated in 2017, well exceeding its designed life-time. In principle, the variation of gravity is sensed by the varying distance between the two satellites. By measuring the variation of distance between the two satellites, the time-variable gravity field is eventually recovered (Tapley et al., 2004).

As the variations in gravity are caused by the mass transport and redistribution within the Earth system, the GRACE-observed time-variable gravity field has provided valuable information of global mass change, which allows us to determine the large-scale water storage changes and water balance on monthly time scales (Alsdorf and Lettenmaier, 2003; Riegger and Güntner, 2004). Therefore, the GRACE product has been applied in various areas, e.g. hydrology, cryosphere, oceanography, and climate studies.

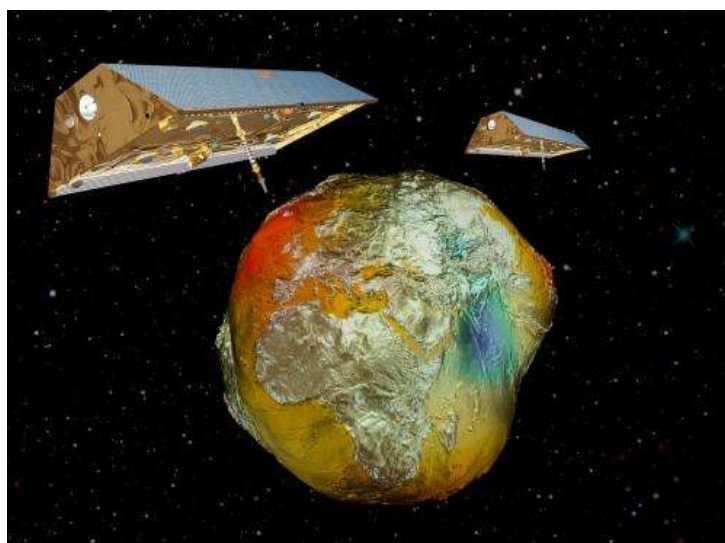


Figure 1.2: GRACE twin satellites with the Earth's gravity field (courtesy: GFZ).

Spaceborne observations from GRACE derive the terrestrial water storage and water storage fluxes, complementing the shortage of ground observations in certain area. Various studies have demonstrated the capability of GRACE in monitoring the groundwater resources (Rodell et al., 2007, 2009). GRACE has also been used to close the terrestrial water balance at catchment-scale (Pan and Wood, 2006; Sheffield et al., 2009; Frappart et al., 2011a; Sneeuw et al., 2014; Lorenz et al., 2015). In particular, GRACE has been applied to validate and refine the hydrological models (Güntner, 2008; Eicker et al., 2014).

Apart from the applications in hydrology, the capability of GRACE in assessing the continuous mass loss has been demonstrated in a number of studies, e.g. investigation on the cryospheric mass loss of ice sheets in Greenland (Baur et al., 2009; Harig and Simons, 2012) and in Antarctica (Velicogna and Wahr, 2006; Chen et al., 2009), and on the mass change of mountain glaciers in Himalaya (Matsuo and Heki, 2010) and Alaska (Chen et al., 2006). Moreover, a large amount of studies took advantage of GRACE in determining the ocean mass change as well as equivalent sea level rise (Chambers, 2006; Lombard et al., 2007; Chambers and Willis, 2008; Willis et al., 2008).

Because of the global coverage of GRACE, many researchers have proved the importance of the use of GRACE for climate studies (Rangelova et al., 2010; Forootan and Kusche, 2012; de Linage et al., 2013; Eicker et al., 2016). In practice, extreme events, e.g. floods (Seitz et al., 2008; Chen et al., 2010) and droughts (Long et al., 2013; Thomas et al., 2014), have been inferred by using GRACE observations. In addition, GRACE is also applied in monitoring the loading induced deformations (Davis et al., 2004; van Dam et al., 2007; Tregoning et al., 2009; Chen, 2015), combined with the GPS point-wise deformation time series.

The aforementioned spaceborne sensors promote a number of novel approaches in oceanography, geophysics, hydrology, hydrometeorology and climatology. Using spaceborne sensors to observe the hydrological variables is beneficial to both hydrologists and geodesists in support of global monitoring, with development of new mission concepts and potential improvement

of spatio-temporal resolution. Therefore, this contribution of spaceborne sensors helps us better understand the dynamic water balance.

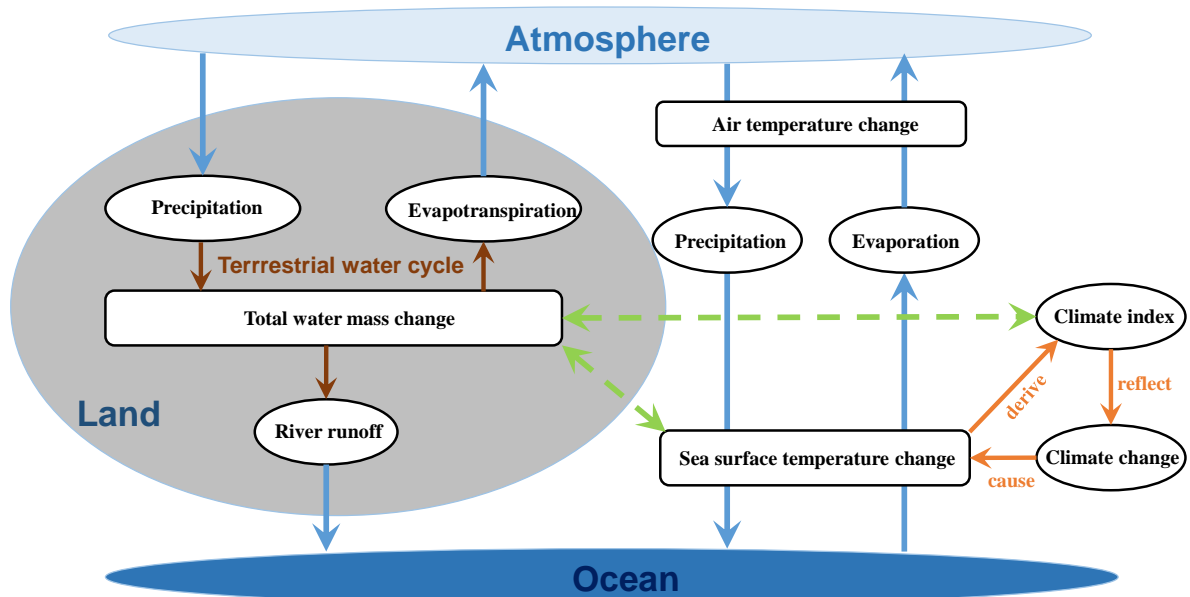


Figure 1.3: Illustration of the land-ocean-atmosphere circulation as well as the terrestrial water cycle, in which the blue arrows indicate the land-ocean-atmosphere circulation, and the black arrows indicate the terrestrial water cycle. The yellow arrows describe the relationship between climate change and sea surface temperature change. The blue dashed lines represent the impact of climate change on the terrestrial water mass change.

1.2 Water mass change in ocean-land-atmosphere circulation

Considering the ocean, land and atmosphere as components within the Earth system, the mass transport between is described as a dynamic circulation. The ocean-land-atmosphere interaction generally refers to the water mass transport, simultaneously with energy exchange (e.g. heat, moisture, momentum), which induces temperature change. As illustrated in Figure 1.3, the direct interaction mainly occurs between ocean and atmosphere, and between land and atmosphere. The river runoff from basin to ocean is the dominant part of direct ocean-land interaction.

Hence, in such a circulation, the ocean and land are coupled through the atmosphere. The water fluxes in form of precipitation and evaporation in the ocean-atmosphere interaction, and in form of precipitation and evapotranspiration in the land-atmosphere interaction. In fact, the water mass exchange in the land-atmosphere interaction is represented as the terrestrial water cycle. Since we have already discussed this in 1.1, as a consequence, the ocean-atmosphere interaction will be particularly discussed in this section. In this thesis, we limit our research and discussion only to the water mass exchange, regardless of the energy exchange.

1.2.1 Teleconnection

Because of the interaction of ocean-atmosphere and land-atmosphere, the atmospheric circulation transmits the energy and water mass over very long distances to remote regions. As a consequence, the climatologic variations are communicated through fluxes of heat, moisture, and momentum by the atmospheric circulation, and transported via large-scale continental water cycle and ocean circulation in form of precipitation and evaporation (Horel and Wallace, 1981; Wallace and Gutzler, 1981). Thus, the atmospheric circulation can be considered as a driving factor that affects land and ocean, exhibiting substantial climate variability (Alexander et al., 2002). This variability represents patterns that occur on various time scales, e.g. from diurnal, daily, weekly and monthly, to intraseasonal, seasonal, interannual and even secular scales. Therefore, teleconnections are as a concept to summarize the atmospheric interactions and describe transport process, and provide a way of quantifying the climate variability into a set of indices.

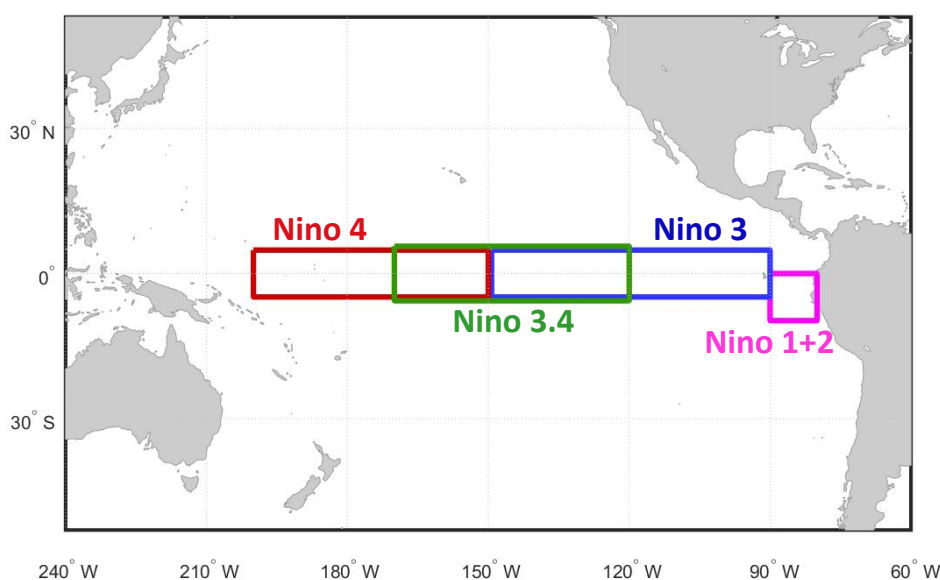


Figure 1.4: Regions which ENSO index represents in Pacific Ocean

The term *teleconnection*, coined by the British meteorologist Walker (1924) for quantifying the correlations between atmospheric pressure, temperature and rainfall, was initially used in atmospheric science to describe the climate links between geographically separated regions (Glantz et al., 1991). Atmospheric teleconnections link widely separated pressure centers, mapping the redistribution of atmospheric mass which associates with climate variability in fine anomaly patterns (Horel and Wallace, 1981; Barnston and Livezey, 1987). Now it becomes more general, that a teleconnection map describes the linkage between a region of interest and all other points in the domain that are farther than the decorrelation length scale of the variable (Nigam, 2003). In this teleconnection map, the remote region does not necessarily represent the variation of the same sign to be teleconnected. In practice, contemporaneous variations with opposite signs are often phenomena in the teleconnections. The teleconnection based on the contemporaneous correlations of variables, however, cannot discriminate between the forcing and response regions by itself. Thus, a teleconnection map in climate science provides a large

spatial scale and long time scale patterns of climate variability, reflecting the impact of regional climate anomalies on the remote regions.

Table 1.1: Common used climate indices, including their full names, acronyms, observable and using methods.

Index full name	Acronym	Observable	Method
Southern Oscillation Index	SOI	SLP anomaly	
El Niño Southern Oscillation	ENSO	SST anomaly	
Multivariate ENSO Index	MEI	SLP anomaly, SST anomaly, Surface wind zonal components, Surface wind meridional components, Sea air temperature, Total cloudiness fraction of the sky	PCA
Pacific Decadal Oscillation	PDO	SST anomaly	PCA
Oceanic Nino Index	ONI	SST anomaly	
Arctic Oscillation (or Northern Annular Mode)	AO (or NAM)	Geopotential height anomaly	PCA
North Atlantic Oscillation	NAO	SLP anomaly	PCA
Antarctic Oscillation (or Southern Annular Mode)	AAO (or SAM)	Geopotential height anomaly	PCA
Palmer Drought Severity Index	PDSI	Land surface temperature anomaly, Precipitation, Soil moisture, streamflow	Dai et al. (2004)
Pacific North America	PNA	Geopotential height anomaly	RPCA

Teleconnection patterns have widely been extracted from correlation analysis. Correlation analysis, as a measure of constructing the teleconnection maps, is intuitive and straightforward. The knowledge of the correlation between two points is represented as the teleconnection map. For example, the assessment of the North Atlantic Oscillation (NAO), the North Pacific Oscillation/West Pacific (NPO/WP), and the Pacific-North America (PNA) was pioneered via correlation analysis by (Wallace and Gutzler, 1981). Principal component analysis (PCA) is also widely applied for determining teleconnections (Giannini et al., 2000; Diaz et al., 2001). The obtained teleconnection patterns are spatially and temporally orthogonal. Moreover, an advanced PCA method, named rotated principal component analysis (RPCA), has become popular in yielding teleconnection patterns, which are no longer constrained to be orthogonal (Barnston and Livezey, 1987; McCabe et al., 2004). Alternatively, an empirical orthogonal teleconnection (EOT) analysis has been developed to identify the teleconnections, by finding a component that explains the most variance using linear regressions (Van den Dool et al., 2000). In recent studies, other statistical methods, e.g. the independent component analysis (ICA) (Forootan and Kusche, 2012; Eicker et al., 2016), and the multi-channel singular spectrum analysis (MSSA) (de Linage et al., 2013), have also successfully been applied to identify the teleconnection patterns for climate studies.

1.2.2 Climate variability and climate indices

A climate index is a simple proxy quantity that is used to characterize an aspect of a geophysical system, i.e. a circulation pattern of climate variability. Commonly, the climate indices are generated based on the selected stations, grid points or using regional average data (eg., Southern Oscillation Index (SOI), Nino 3.4 (see Figure 1.4)). As summarized in Table 1.1, some indices are based upon PCA (eg. AO, NAO) or RPCA (eg. PNA). Most indices use a single variable (eg. SLP, SST, geopotential height, precipitation, etc.), while some other indices (e.g. MEI, PDSI) use a combination of variables (e.g. air temperature, surface wind, precipitation, etc.). Particularly, some indices are known by several names, eg. the Northern Annular Mode (NAM), Southern Annular Mode (SAM) are also known as the Arctic Oscillation (AO), Antarctic Oscillation (AAO), respectively. In addition, some indices have minor controversial issues. For example, the physical distinction from NAO (Hurrell, 1995) and North Pacific (NP) (Trenberth and Hurrell, 1994) indices is not completely agreed upon by researchers that might result in user confusion. Further, use of different source data sets, different base periods, and different normalization yield different index values.

The El Niño Southern Oscillation (ENSO) — is a quasi-periodic fluctuation (every 2–7 years) in sea surface temperature (El Niño) and air pressure of the overlying atmosphere (Southern Oscillation) across the equatorial Pacific Ocean. ENSO is considered as the most dominant source of global inter-annual variability of climate. The presence of an El Niño, or its opposite, La Niña, sufficiently modifies the general flow of the atmosphere to affect normal weather conditions in many parts of the world.

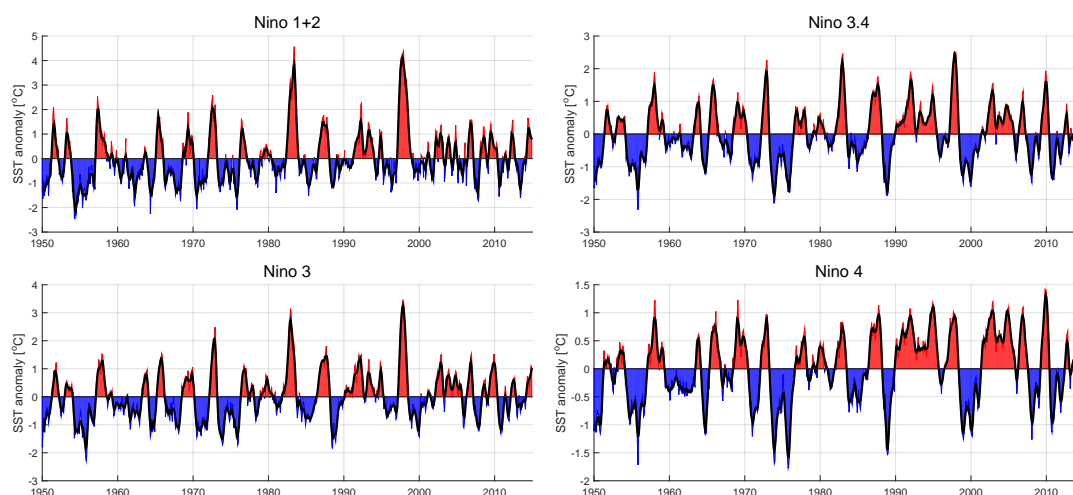


Figure 1.5: ENSO indices: Nino 1+2, Nino 3, Nino 4, Nino 3.4.

Historically, ENSO is characterized by simple indices (Nino 1+2, Nino 3, Nino 4, Nino 3.4), defined by a consecutive 5-month running mean of sea surface temperature (SST) anomalies in a certain region of the equatorial Pacific, as shown in Figure 1.4 and 1.5. The most commonly used region is the Niño 3.4 region (5°S – 5°N and 170°W – 120°W), and the most commonly used threshold is a positive SST departure from normal greater than or equal to $+0.5^{\circ}$ (Trenberth, 1997). Positive values of the index indicate El Niño conditions, corresponding to warm sea surface temperature, while negative values can be interpreted as La Niña (cold) conditions,

as illustrated in Figure 1.5. The ENSO index used in this thesis is produced by the National Oceanic and Atmospheric Administration (NOAA)'s Climate Prediction Center (CPC) (ftp.cpc.ncep.noaa.gov/wd52dg/data/indices available till 2018). According to the spectra of ENSO indices in Figure 1.6, all the indices represent the mean periods of 3 years and 1.5 years (i.e. frequencies of 1/3 and 2/3 cycle per year), which reveals the inter-annual variability of ENSO.

Apart from these four ENSO indices, other ENSO-related climate indices have also been produced, e.g. the SOI (Trenberth, 1984; Trenberth and Hoar, 1996; Trenberth and Caron, 2000), the Multivariate ENSO Index (MEI) (Wolter and Timlin, 1998), the Oceanic Nino Index (ONI) (Trenberth and Stepaniak, 2001), and the Pacific Decadal Oscillation (PDO) (Zhang et al., 1997; Mantua et al., 1997). Accordingly, ENSO indices are calculated through SST anomalies while SOI is based on SLP. The MEI is calculated as the first unrotated PC based on the six main observed variables (i.e. sea-level pressure (P), zonal (U) and meridional (V) components of the surface wind, sea surface temperature (S), surface air temperature (A), and total cloudiness fraction of the sky (C)) over the tropical Pacific. Different from ENSO indices, MEI is a bi-monthly index. Unlike Nino 3.4, ONI is calculated using a 3-month running mean instead of a 5-month running mean. PDO is characterized as the leading PC of the monthly SST anomalies in the northern Pacific Ocean.

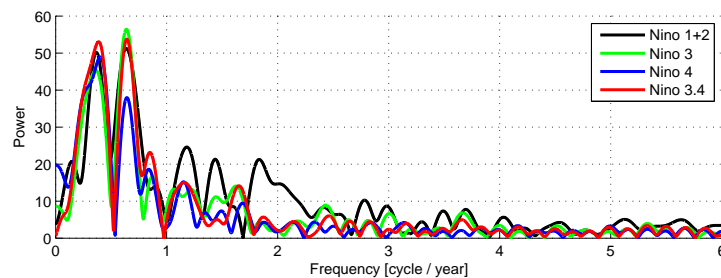


Figure 1.6: Power spectrum of 4 ENSO indices time series. All of them show strong frequency at or close to 0.34 and 0.65, which presents 3-year and 1.5-year cycle.

Climate change brings more frequent extreme events and causes abnormal variation of the terrestrial water cycle. ENSO is one of the most important climate phenomena, reflecting ocean-atmosphere interactions over the equatorial Pacific (Trenberth and Stepaniak, 2001). However, ENSO as a phenomenon is not restricted to only in Pacific but also has a globally great impact (Glantz et al., 1991; Trenberth et al., 2002; Cai et al., 2012). ENSO dominantly influences rainfall in terms of moisture advection from ocean to land, consequently impacts on evaporation and runoff, and eventually affects the terrestrial water cycle. A possible connection between ENSO and terrestrial hydrological variables, like precipitation, evaporation, and runoff, has been investigated in many regions. Previous studies found the significant relationship of precipitation (Ropelewski and Halpert, 1987; Ronchail et al., 2002; Boulanger et al., 2005) and stream flow (Chiew and McMahon, 2002; Tootle and Piechota, 2006; Johnson et al., 2013) with ENSO at inter-annual scales in various regions. Generally, terrestrial water storage reflects the water balance and, therefore, is influenced as well by global and regional climate change. Guntner et al. (2007) indicated that the inter-annual variation of terrestrial water storage is associated with ENSO using a hydrology model. After more than a decade of observations with sufficient temporal and spatial resolutions, GRACE has shown to be capable of monitoring water

mass variation and redistribution (Volkov and Landerer, 2013). Although the terrestrial water cycle commonly behaves strongly seasonally, the inter-annual variability of water storage has been observed by GRACE at different spatial scales. Various studies have revealed the GRACE-observed interannual water storage change relates to the extreme climate conditions (Humphrey et al., 2016; Kusche et al., 2016). Moreover, recent studies have explored the correlation patterns with ENSO in GRACE observations globally (Phillips et al., 2012; Ni et al., 2017) and regionally (Chen et al., 2010; García-García et al., 2011; de Linage et al., 2013; Forootan et al., 2014; Awange et al., 2014; Luo et al., 2016).

1.3 Motivation and Objectives

The insufficient spatial and temporal resolution of GRACE limits its use in regional applications. Conversely, the hydrological variables, either from the model estimates or from the spaceborne observations, can also be employed for GRACE to monitoring the global water mass variation. Moreover, regarding the important role of ocean-atmosphere interaction in the climate change and the indirect linkage of water mass exchange between ocean and land, the anomalous variation of the global terrestrial water mass is potentially relevant to the climate variability in a certain region. Despite the limited monthly solutions of GRACE, as illustrated in Figure 1.7, the temporal scale of both hydrological water cycle (from intraseasonal to interannual) and climate variability (from seasonal to interannual, even to decadal) is visible in GRACE observations (Sneeuw et al., 2005).

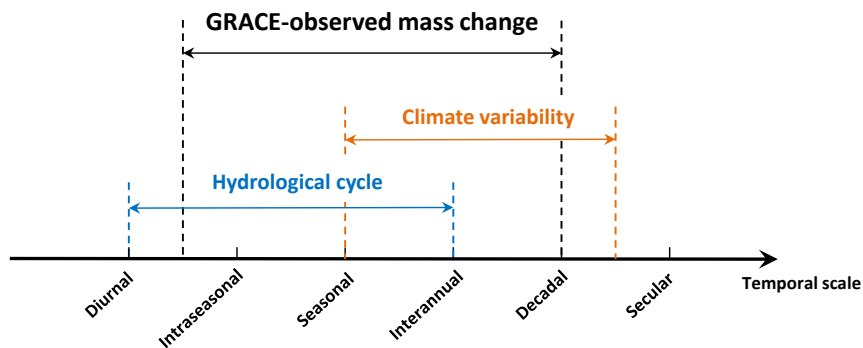


Figure 1.7: Temporal scales of the GRACE observation, the hydrological cycle, and the climate variability.

Therefore, this thesis is motivated by the following four questions:

- Can the terrestrial water storage be estimated via other hydrological variables?
- Can the spatial resolution of GRACE be downscaled through fine resolved hydrological observations?
- Can the signature of climate variability on terrestrial water storage be identified?
- How can we interpret the teleconnection between climate variability and terrestrial water cycle via ocean-land-atmosphere interaction?

In order to answer these questions, the objectives of this thesis are divided in two individual topics:

- Assessing the water mass change in the terrestrial water cycle;
- Interpreting the water mass exchange in the ocean-land-atmosphere interaction.

Assessing the water mass change in the terrestrial water cycle

To assess the terrestrial water mass change in the water cycle, we aim to estimate the continental water storage using multiple hydrological variables. Estimating the terrestrial water storage variation with the aid of hydrological observations is practically realistic and feasible. In recent studies, the water storage change in large-scale basins is predicted by a parametric spectral method given precipitation observations (Reager and Famiglietti, 2013). Apart from hydrological observations, the terrestrial water storage has been estimated by a set of climate indices as proxy that represent significant teleconnections between water storage change and SST anomalies, using an empirical statistical approach (de Linage et al., 2014). Regarding the temporal relationship between climate change and water storage, an auto-regressive model has been employed to predict regional water storage change, using multiple variables (e.g. precipitation, SST, climate indices) (Frootan et al., 2014). Hence, we propose to model the relationship between water storage and hydrological variables by statistical approaches.

Moreover, the spatio-temporal sampling of observations is important for the assessment of terrestrial water mass variation. Concerning the limited spatial and temporal resolution of GRACE and high resolution of hydrological observations, we explore to make up for the deficiency of GRACE by hydrological variables. In practice, a few studies have made efforts on downscaling of GRACE by incorporating with other hydrological variables (Seyoum and Milewski, 2017; Miro and Famiglietti, 2018). This challenge of downscaling will be attempted by a statistical assimilation in this thesis.

Interpreting the water mass exchange in the ocean-land-atmosphere interaction

We aim at the teleconnection patterns between climate variability and terrestrial variables, in order to understand the water mass exchange among ocean, land and atmosphere. As climate change is commonly reflected by the ocean-atmosphere circulation, a variety of climate indices is characterized statistically by the oceanic and atmospheric variables (e.g. SST, SLP, air pressure, etc.). Inter-annual changes in SST are found to relate to the terrestrial water cycle in river basins (Diaz et al., 1998; Gochis et al., 2007; McCabe and Wolock, 2014). Since amount of climate indices are characterized by adopting SST as the indicator, as shown in Table 1.1, consequently we use SST as an intermedium to explore the teleconnection between the continental water storage and climate variability. Apart from water storage, other terrestrial variables (e.g. precipitation, evaporation and runoff), as the major drives in the terrestrial water cycle, are expected to be connected to climate variability as well. Land surface temperature (LST) is a significant indicator of climate change and terrestrial water resource. Particularly, the relationship between evaporation and LST is characterized in dry and cold climate condition (Sun et al., 2016). Hence, the LST is also involved in our study.

Climate warming has a great impact on the Arctic, which leads to extreme events (Honda et al., 2009; Francis and Vavrus, 2012; Kug et al., 2015). Terrestrial water resources in the pan-Arctic have teleconnections to the climate warming on Arctic (Rouse et al., 1997; Morison et al., 2007;

Kim et al., 2017). Numerous studies indicate the Arctic and Eurasia are mainly under the influence of Arctic oscillation and North Atlantic oscillation (Wanner et al., 2001; Déry and Wood, 2004; Peterson et al., 2006; Peralta-Ferriz et al., 2014). However, whether ENSO has a signature as well on boreal regions is still an unanswered question. Some studies (Jevrejeva et al., 2003; Matsuo and Heki, 2012) indicate that ENSO likely has influence on high latitude region. This motivates us to focus on detecting the signature of ENSO in boreal regions. In addition, the causal relationships between terrestrial variables and ENSO is essential for interpreting the relevancy of the inter-annual change of terrestrial water storage to the climate variability. To investigate such a cause and effect, we resort to estimation of the phase/time delays in our study.

From above, to fulfill our objectives of this thesis, we propose a comprehensive study including the following four tasks:

- Estimating the continental water storage at catchment scale by multiple hydrological variables, using statistical regression models.
- Statistical downscaling the spatial resolution of GRACE by assimilating GRACE with variables from high resolution hydrological models.
- Identifying the teleconnection between ENSO and terrestrial water cycle in pan-Arctic region, and specifically in the boreal catchments, through SST anomalies.
- Investigating the causal relationship between ENSO and terrestrial variables through time leads/lags.

To estimate the terrestrial water mass change by hydrological variables and to explore the signature of climate change (e.g. ENSO) on the terrestrial water variation, it is of great importance to employ a proper approach. Several statistical analysis tools are introduced in various studies. Hilbert transformation is introduced to analyze the influence of ENSO on terrestrial water storage (TWS) (Phillips et al., 2012). The global connection between TWS change and ENSO is directly examined by using cross-correlation and coherence spectrum analysis (Ni et al., 2017). Signal decomposition techniques are commonly used to extract the dominant spatio-temporal patterns of long-term and inter-annual components from observations. PCA is powerful for finding interrelations between variables in the data, interpreting the features of data, and decreasing the number of variables to reduce the dimension of data. It is adopted by Rangelova et al. (2007) and Schmidt et al. (2008) on GRACE observations. Frappart et al. (2011b) and Forootan and Kusche (2012) improved the decomposition approach by independent component analysis (ICA). It has the advantage that it can find dominant components with statistical independence. Eicker et al. (2016) applied a complex ICA on TWS from GRACE and successfully isolated an ENSO mode from the signals. A multi-channel singular spectrum analysis (MSSA) was applied on extracting inter-annual signals from GRACE (Rangelova et al., 2010). As a multivariate method, it is capable to isolate trend and nonlinear oscillations of notable periodicity in noisy and short data sets. de Linage et al. (2013) linked sea surface temperatures with terrestrial water storage observed by GRACE using MSSA. A seasonal trend decomposition using the loess (STL) approach has been used in (Humphrey et al., 2016) to assess the temporal variability of water storage. Another multivariate method, canonical correlation analysis (CCA), has also been used in climate and water resource studies (Ouarda et al., 2001; Busuioc et al.,

2001; Barros and Silvestri, 2002). CCA is based on the joint data sets to extract the linear combination from two different fields. Different from other approaches, CCA has the advantage that it correlates linear relationship between two different variables in terms of canonical modes, regardless of units. Concerning the different units of temperature and equivalent water height, CCA is thus an appropriate approach to associate SST with terrestrial observations. Moreover, the advantage of extracting canonical modes from joint datasets can also be used in the model regressions. In order to achieve sufficient spatial resolution, a statistical downscaling of GRACE is attempted by assimilating multiple variables, i.e., precipitation, evapotranspiration, runoff, from a set of hydrological models. This assimilation is accomplished by implementation of a partial least-squares regression approach, which is based on the idea of CCA.

1.4 Outline

In line with the aforementioned two aspects as well as the given tasks, thus, this thesis is organized as follows.

Chapter 2 contains a solid theory of signal decomposition techniques and regression approaches, which are the mathematical foundations of the following chapters. The signal decomposition methods are employed mainly in Chapter 5 for teleconnection pattern analysis. The regression algorithms, some of which are based on the previous decomposition techniques, are implemented in Chapter 3 for modeling the terrestrial water mass variation.

Chapter 3 is the kernel part of the thesis. It firstly introduces the theory to derive the equivalent water height from GRACE, and characterizes the relationships between terrestrial water mass change and other hydrological variables as a statistical foundation for modeling. Later on, four different regression approaches are applied to estimate the terrestrial water storage change. In addition, a spatial downscaling of GRACE is achieved using a hydro-geodetic assimilation approach.

Chapter 4 aims to analyze the temporal delay between each variable in the water cycle to better understand the terrestrial water dynamics, and to interpret the causal relationship between terrestrial water mass variation and climate change as a preliminary step for investigating the teleconnection. In order to establish this goal, two methods: Hilbert transformation and wavelet transformation, which will also be used in Chapter 5, are addressed before the numerical analysis.

Chapter 5 is as important as Chapter 3. To investigate the teleconnection patterns between terrestrial water storage in boreal catchments and ENSO, Chapter 5 represents the applications of PCA, ICA and CCA on terrestrial variables as well as climate variables in a comprehensive way.

Chapter 6 briefly summarizes the achievement of the thesis, draws the conclusions and provides an outlook.

Chapter 2

Signal Decomposition Techniques and Regression Approaches

Generally, complicated physical mechanisms are behind the global and regional changes, like terrestrial water mass change, glaciers and ocean mass change. As a consequence, the observations in geoscience contain various types of variability, i.e., linear trend, annual, semi-annual or interannual variations, which cannot be simply recognized. Therefore, an appropriate statistical method is required to extract these significant variabilities from observed signals.

Several non-parametric statistical analysis tools have been employed in geodetic and hydrological studies. Principal component analysis (PCA) is adopted by Rangelova et al. (2007) and Schmidt et al. (2008) on GRACE observations. PCA is a powerful technique for finding relations between variables in the data, interpreting the features of data, and decreasing the number of variables to reduce the dimension of data. Frappart et al. (2011b) and Forootan and Kusche (2012) improved the decomposition approach by independent component analysis (ICA), which has the advantage of finding dominant components with statistical independence. Eicker et al. (2016) applied a complex ICA on TWS from GRACE and successfully isolated the ENSO mode from the signals. Another multivariate method, canonical correlation analysis (CCA), has also been used in climate and water resource studies (Ouarda et al., 2001; Busuico et al., 2001; Barros and Silvestri, 2002). CCA is able to identify joint modes in two different variables. Different from other approaches, CCA has the advantage of linearly correlating two different variables, regardless of units. CCA may even be improved to recognize the nonlinear relationship of signals (Hsieh, 2001).

It is necessary to establish a proper framework to model the relationship between terrestrial water mass variation with other variables in the water cycle. Several multivariate linear regression techniques, like least-squares prediction, principal component regression, and partial least-squares regression, can be used to model the spatio-temporal linear relationship in a statistical way.

In this chapter, PCA is introduced firstly from the view of both eigenvalue decomposition and singular value decomposition. We also explain the principle and generic algorithm of ICA. To explore the mutual characteristics in different variables, CCA is introduced as an important method. Additionally, the numerical performances of each method are illustrated, and the comparisons between PCA and ICA, PCA and CCA are discussed as well in the end. Multivariate linear regression approaches (i.e., least-squares prediction, principal component regression, and partial least-squares regression) which are used in this thesis, are introduced as well.

2.1 Principal component analysis

Principal component analysis (PCA) (Jolliffe, 1986) seeks structures that explain the maximum amount of variance in a two-dimensional data set. In general, the optimal directions with maximally distributed observations are formulated as orthogonal eigenvectors, which are called empirical orthogonal functions (EOFs). The decomposed observations, known as principal components (PCs), are obtained by projecting the observations along those directions. Both of the structures are orthogonal in their own dimension.

The PCs can be interpreted as a new set of variables created from the original variables. Each of the new variables is a linear combination of the original variables. EOFs and PCs are the structures that explain the most variance in a data set. The first principal component has the maximum variance among all possible choices, as illustrated in Figure 2.1.

Let us assume that we have measurements of some variable at locations $s = 1, 2, \dots, d$, taken at epochs $t = 1, 2, \dots, n$. For each epoch we can think of the measurements $x_s (s = 1, 2, \dots, d)$ as a map of field. We store these measurements in a matrix X as n maps each being d samples long

$$X = \begin{bmatrix} x_{1,1} & x_{1,2} & \dots & x_{1,d} \\ x_{2,1} & x_{2,2} & \dots & x_{2,d} \\ \vdots & \vdots & \ddots & \vdots \\ x_{n,1} & x_{n,2} & \dots & x_{n,d} \end{bmatrix} = [x_{1,s} \ x_{2,s} \ \dots \ x_{n,s}]^T = [x_{t,1} \ x_{t,2} \ \dots \ x_{t,d}] . \quad (2.1)$$

Generally, when assessing the variability of the field, one of the dimensions of X gets removed and we are left with a measure of the dispersion of the structure with itself across the spatial dimension or temporal dimension. Hence, we obtain the temporal variance-covariance matrix of data X along the spatial dimension by

$$\begin{aligned} C_{XX} = C_{\text{temporal}} &= XX^T / d \\ &= \frac{1}{d} \begin{pmatrix} \sum_{s=1}^d x_{1,s}^2 & \sum_{s=1}^d x_{1,s}x_{2,s} & \dots & \sum_{s=1}^d x_{1,s}x_{n,s} \\ \sum_{s=1}^d x_{2,s}x_{1,s} & \sum_{s=1}^d x_{2,s}^2 & \dots & \sum_{s=1}^d x_{2,s}x_{n,s} \\ \vdots & \vdots & \ddots & \vdots \\ \sum_{s=1}^d x_{n,s}x_{1,s} & \sum_{s=1}^d x_{n,s}x_{2,s} & \dots & \sum_{s=1}^d x_{n,s}^2 \end{pmatrix} , \end{aligned} \quad (2.2)$$

or spatial variance-covariance along the temporal dimension by

$$\begin{aligned} C_{XX} = C_{\text{spatial}} &= X^T X / n \\ &= \frac{1}{n} \begin{pmatrix} \sum_{t=1}^n x_{t,1}^2 & \sum_{t=1}^n x_{t,1}x_{t,2} & \dots & \sum_{t=1}^n x_{t,1}x_{t,d} \\ \sum_{t=1}^n x_{t,2}x_{t,1} & \sum_{t=1}^n x_{t,2}^2 & \dots & \sum_{t=1}^n x_{t,2}x_{t,d} \\ \vdots & \vdots & \ddots & \vdots \\ \sum_{t=1}^n x_{t,d}x_{t,1} & \sum_{t=1}^n x_{t,d}x_{t,2} & \dots & \sum_{t=1}^n x_{t,d}^2 \end{pmatrix} . \end{aligned} \quad (2.3)$$

The $n \times n$ covariance matrix C_{temporal} in (2.2) is the covariance between different time epochs, obtained by projecting on the sample of different spatial points. The dimension of space disappears and we get an $n \times n$ matrix. Similarly, C_{spatial} in (2.3) denotes the $d \times d$ covariance matrix of spatial locations with each other.

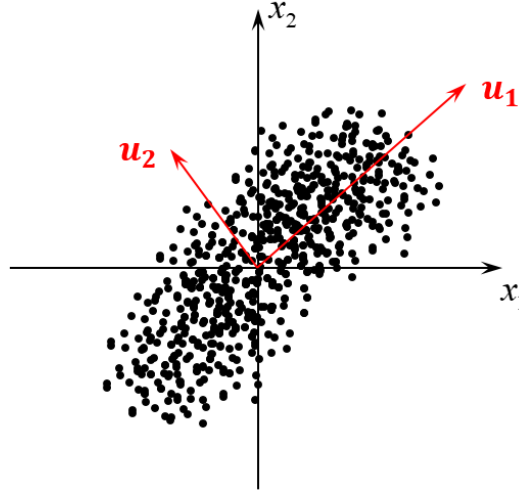


Figure 2.1: Illustration of PCA principle. The first component point to the direction of maximum variance, and then the following components are projected orthogonal to the previous one.

As illustrated in Figure 2.1, each component is statistically uncorrelated with others. Thus, the decomposed components are orthogonal with each other in their covariance matrix. In other words, PCA eventually aims to find out the optimal linear transformation matrix E that makes the covariance matrix C_{PP} of the transformed matrix P to be diagonal, for example, expressed as

$$P = X \cdot E, \quad \text{with} \quad C_{PP} = PP^T = \Lambda, \quad (2.4)$$

in which the vectors in P are orthogonal, and the vectors in E are both orthogonal and normalized, $E^T E = I$. Clearly, since X is a $n \times d$ matrix, each pair of columns from P and E represent one single mode. Thus, P contains the temporal modes, while E interprets the modes in space, as depicted in Figure 2.2. The first mode from PCA always contains the most important information from data X . Accordingly, the diagonal matrix Λ contains the variance of each mode, which writes

$$\Lambda = \begin{bmatrix} \sigma_1^2 & & & \\ & \sigma_2^2 & & \\ & & \ddots & \\ & & & \sigma_r^2 \end{bmatrix}, \quad (2.5)$$

where r is the number of the decomposed modes. Hence, in this case, the matrix X is decomposed by PCA, in terms of matrix as,

$$X = P \cdot E^T . \quad (2.6)$$

where P is named as *principal component* (PC). Generally, the eigenvectors E are called *Empirical Orthogonal Functions* (EOFs) (Jolliffe, 1986; Preisendorfer, 1988). Empirical because they are derived from data, orthogonal because they are orthogonal with each other. To accomplish the decomposition of matrix X by PCA, the task becomes to identify the transformation matrix P and E in order to diagonalize the covariance matrix from C_{XX} to Λ .

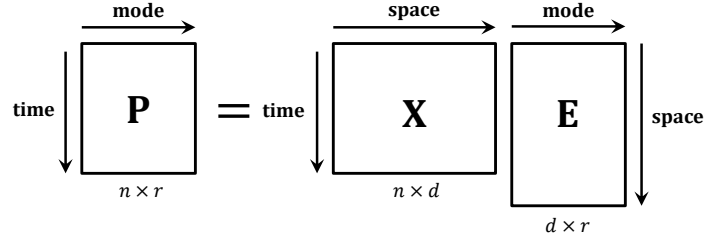


Figure 2.2: Illustration of PC and EOF matrices of data X .

For geodetic applications, in this thesis, we generally assume that we have observations of one variable with d_{lon} longitudes and d_{lat} latitude in space, taken at n time epochs. For each time epoch t , we have observations at certain location. So the $X(n \times (d_{\text{lon}} \times d_{\text{lat}}))$ is three-dimensional matrix. We rearrange X into a two-dimensional matrix by storing all the locations at one epoch in a row vector in X , so that the size of X becomes $n \times d$, where d equals $d_{\text{lon}} \times d_{\text{lat}}$. Thus, we simply interpret each of the n columns in X as a time series for a given location, whereas its row contains the entire data from all locations per time epoch. In this case, applying PCA on this geodetic observation matrix, we finally gain the principal components in terms of time series, and simultaneously the orthogonal eigenvectors in terms of maps, which represents the features in space.

2.1.1 Singular value decomposition

Singular value decomposition (SVD) is a general decomposition of a matrix, which was introduced into numerical analysis by Golub and Kahan (1965). The computational algorithms were systematically summarized by Stewart (1993). In principle, any $t \times n$ matrix X can be decomposed uniquely as

$$X = U \cdot \Sigma \cdot V^T , \quad (2.7)$$

where $U(n \times r)$, $V(d \times r)$ are both orthonormal here, we have $U^T U = I$ and $V^T V = I$. The diagonal matrix $\Sigma(r \times r)$ contains singular values of matrix X . $r = \text{rank}(X) = \text{rank}(\Sigma)$, is the rank of X . The column space of X is spanned by the first r columns of U , and the row space of X is spanned by the first r columns of V . The columns of U and V are linked by the singular values contained in the diagonalized matrix Σ . The singular values in Σ represent the amplitude, however, not the variance.

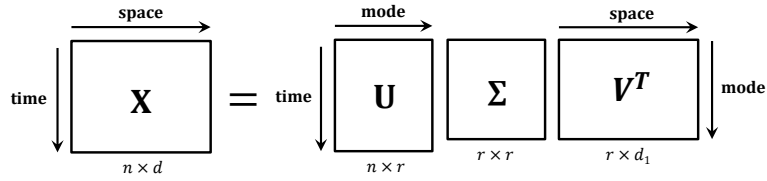


Figure 2.3: Illustration of U , Σ , V matrices of data X .

Geometrically, we can think of U and V as 2-D rotation matrices, and Σ as scaling matrix (Strang, 1993). As an example illustrated in Figure 2.4, SVD can be interpreted as a sequence of transformation of X based on the unit vectors $\mathbf{e} = [e_1 \ e_2]^T$ in the case that X has dimensions $n = d = 2$. After rotation by V^T , stretching by Σ , and rotation by U again, we get X as

$$X\mathbf{e} = U\Sigma V^T\mathbf{e}. \quad (2.8)$$

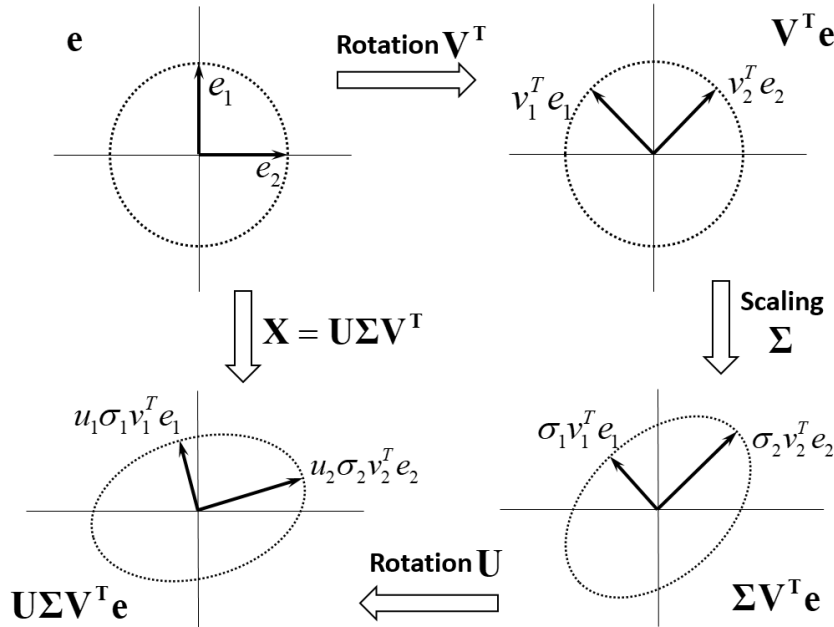


Figure 2.4: Illustration of SVD principle as a linear transformation process.

Considering the following decomposition on the covariance matrix of X , so we have

$$\begin{aligned} XX^T &= U\Sigma V^T V\Sigma U^T = U\Sigma^2 U^T, \\ X^T X &= V\Sigma U^T U\Sigma V^T = V\Sigma^2 V^T. \end{aligned} \quad (2.9)$$

Hence, we know that the columns of U are the left singular eigenvectors of XX^T , and the columns of V are the right singular eigenvectors of $X^T X$. In this case, the values in Σ^2 represents the singular values of covariance matrix of X .

If we right multiply X by V , we get

$$XV = U\Sigma V^T V = U\Sigma, \quad (2.10)$$

from which derives $(U\Sigma)^T(U\Sigma) = \Sigma^T\Sigma$. According to (2.4) and (2.6), V fulfills the condition that makes the covariance matrix of transformed XV diagonal. Thus, $P = U\Sigma$ is seen as PC of X , and V is the corresponding EOF. Similarly, if we multiply U with X^T , then we obtain

$$X^T U = V\Sigma U^T U = V\Sigma, \quad \text{and} \quad (V\Sigma)^T(V\Sigma) = \Sigma^T\Sigma. \quad (2.11)$$

In this case, $P = V\Sigma$ is seen as PC of X^T , and U is the corresponding EOF. Thus, either U or V can be chosen to represent PCs when combining with the singular value matrix Σ . In other words, both U and V represent the modes in X , and the amplitudes of each mode are reflected by Σ .

On one hand, SVD can be seen as a method for transforming correlated variables into a set of uncorrelated ones and presenting the relationships among each other. On the other hand, SVD is also a method for identifying and ordering the data based on the variance. In addition, we can also apply SVD for data reduction of X . From this view, SVD is essentially and widely used in PCA decomposition. If we take the two-dimensional data matrix of spatial dimension and temporal dimension, and do the direct SVD of this matrix, we recover the normalized EOFs, singular values, and normalized PCs in one step. It can be applied to find both the EOFs and PCs simultaneously (Preisendorfer, 1988).

2.1.2 Eigenvalue decomposition

As the data matrix X is defined in (2.2) and (2.3), we know that the variance-covariance matrix of X can be calculated either along temporal dimension or spatial dimension. In this thesis, the covariance matrix is primarily calculated by (2.3), i.e., $C_{XX} = C_{\text{spatial}} = X^T X/n$. Statistically, it contains only the information of covariance at each grid point, and reflects the dependence of any two grid points. C_{XX} is simply written to represent the C_{spatial} in the following content. Therefore, we discuss the eigenvalue decomposition of C_{XX} in the case of $C_{XX} = X^T X/n$ as an example.

The aim of PCA is to find directions \mathbf{e} in the data X , so that the projection of X on \mathbf{e} has the maximum variance, as shown in Figure 2.1. The vector e is an eigenvector of C_{XX} , which satisfies $\mathbf{e}^T \mathbf{e} = 1$. The variance of $X\mathbf{e}$ is calculated by

$$\frac{1}{t}(\mathbf{e}^T X^T)(X\mathbf{e}) = \mathbf{e}^T C_{XX} \mathbf{e}. \quad (2.12)$$

Therefore, finding a projection that maximizes the projected variance of $X\mathbf{e}$, which writes $\max(\mathbf{e}^T C_{XX} \mathbf{e})$, is equivalent to the solution of PCA, according to (2.4). To solve the equation above, C_{XX} can be decomposed in the following way through a diagonalization,

$$C_{XX} \mathbf{e} = \lambda \mathbf{e}, \quad (2.13)$$

since $\mathbf{e} = [e_1, e_2, \dots, e_i]^T$. To find the \mathbf{e} , we can use any number of standard techniques to solve the system

$$(C_{XX} - \lambda I)\mathbf{e} = 0. \quad (2.14)$$

The set of eigenvectors \mathbf{e} and associated eigenvalues λ represents a coordinate transformation into a coordinate space where the matrix C_{XX} becomes diagonal. In terms of linear algebra, we put the eigenvectors \mathbf{e} into columns of the matrix E . Accordingly, the issue turns to find a transformation E that can diagonalize the covariance matrix C_{XX} . So we have

$$C_{XX}E = E\Lambda, \quad (2.15)$$

in which the elements of the diagonal matrix Λ are the eigenvalues of C_{XX} (Jolliffe, 1986), E contains the eigenvectors with respect to Λ . (2.15) is the so called *eigenvalue decomposition* (EVD) of C_{XX} .

Because the covariance matrix C_{XX} is diagonal in this new coordinate space, the variations in these new directions are uncorrelated with each other. The eigenvectors define directions in the initial coordinate space along which the maximum possible variance can be explained. The variance explained in this direction is orthogonal to the variance explained by other directions, which is defined by the other eigenvector. Comparing with (2.4) and (2.5), we find that (2.15) fulfills the condition of PCA, which diagonalizes the covariance matrix from C_{XX} to Λ . Therefore, eigenvalue decomposition is constantly used for PCA applications.

Here, the eigenvectors E denote EOF. The first EOF e_1 thus contains the dominant pattern, as λ_1 is distinctly larger than the other eigenvalues. Accordingly, if we project the original data X on the new basis \mathbf{e} , we obtain the decomposed PCs, written as $P = XE$. The i^{th} EOF (e_i), is corresponding to the i^{th} PC $p_i = Xe_i$. Therefore, we have

$$\begin{aligned} P &= XE, \\ X &= PE^T, \end{aligned} \quad (2.16)$$

since $EE^T = E^TE = I$. Each associated pair $\{p_i, e_i\}$ is named mode of variability in X (Preisendorfer, 1988). In addition, p_i , known as PC_i , reflects the temporal amplitudes of data on basis vector e_i .

Here, P and E , in (2.16), have r number of PCs and EOFs, where r denotes the number of non-zero eigenvalues in Λ . r depends on the rank of data X . In our example, since covariance matrix C_{XX} is calculated by $C_{XX} = X^T X / t$, the eigenvectors E (i.e., EOFs) represent the modes in the spatial domain. Complementary, the PCs represent temporal modes. In other words, PCA expands X in terms of a new set of temporal PCs associated with spatial uncorrelated maps known as EOFs.

2.1.3 Links between EVD and SVD

To illustrate the relationship between SVD and EVD, we first look at the covariance matrix C_{XX} from SVD. As defined in (2.7) that $X = U\Sigma V^T$, we have

$$\begin{aligned} C_{XX} &= (U\Sigma V^T)^T(U\Sigma V^T)/n \\ &= V\Sigma^T U^T U \Sigma V^T /n \\ &= V\Sigma^T \Sigma V^T /n, \end{aligned} \quad (2.17)$$

because $U^T U = I$. From EVD in (2.15), we obtain

$$C_{XX} = E\Lambda E^T. \quad (2.18)$$

Hence, in this case, we infer that

$$V = E, \quad \text{and} \quad \Lambda = \Sigma^T \Sigma /n. \quad (2.19)$$

In (2.19), a factor n , the sample size, is between the eigenvalues Λ of the covariance matrix C , and the singular values Σ of the original data matrix.

According to (2.18), we find that SVD implementation either on covariance matrix C_{XX} or directly on data matrix X does not change the eigenvectors E , but change the amplitude of singular values. In brief, the EVD can be understood as SVD of covariance matrix C_{XX} . SVD on covariance matrix C_{XX} makes the singular values from Σ to Λ , which is explained by (2.19).

Comparing (2.7) with (2.16), PCA implemented by EVD can only normalize either EOF or PC, while both two normalized eigenvectors are obtained by SVD. The former depends on the purpose of application to normalize either EOFs or PCs. If we choose to normalize the spatial modes in order to reflect the real amplitude in time, then we obtain the unnormalized temporal modes containing the information of variance. And vice versa.

As a result, either by EVD or by SVD, a set of observations can be separated into different modes of variability, which reveal both spatial and temporal variation. In the following chapter, PCA is therefore applied on our geodetic and hydrological datasets in order to gain the individual modes for analysis. In the following content, we express the PCA decomposition as

$$X = UV^T, \quad (2.20)$$

in which U, V stand for PCs and EOFs, instead of $X = PE^T$ in (2.16) and $X = U\Sigma V^T$ in (2.7). U, V are not necessarily both normalized in this form.

Numerical illustration A simulation is introduced here to test the performance of PCA on separating significant components from a mixture of signals. The source signals in Figure 2.5(a) contain a linear trend, two sinusoidal signals with different periods, and random Gaussian noise, see Table 2.1. Each of the simulated observation y , as shown in Figure 2.5(b), are mixed by an arbitrary linear combination of the source signals x_1, x_2, x_3, x_4 ,

$$y = w_1 \cdot x_1 + w_2 \cdot x_2 + w_3 \cdot x_3 + w_4 \cdot x_4 , \quad (2.21)$$

where w_1, w_2, w_3, w_4 represent the weights of source signals.

Table 2.1: Simulated source signals with certain parameters.

Source signal	Parameters
Linear trend $x_1 = at + b$	$a = 0.05, b = 1$
Sinusoidal signal 1 $x_2 = a_1 \sin(\omega_1 t + \phi_1) + b_1 \cos(\omega_1 t + \phi_1)$	$a_1 = 1, b_1 = 0, \omega_1 = 0.1, \phi_1 = 0.5$
Sinusoidal signal 2 $x_3 = a_2 \sin(\omega_2 t + \phi_2) + b_2 \cos(\omega_2 t + \phi_2)$	$a_2 = 0, b_2 = 1, \omega_2 = 0.05, \phi_2 = 0$
Random noise $x_4 = e$	$e \sim N(0, 1)$

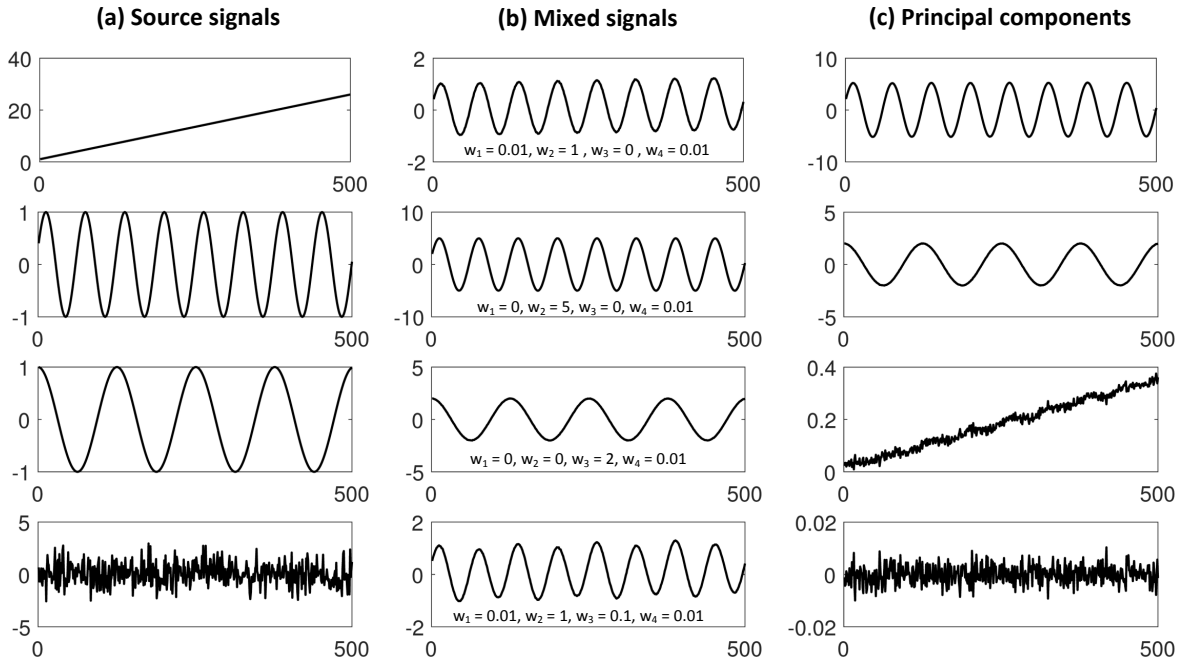


Figure 2.5: Numerical performance of PCA on a set of mixed signals. Principal components are shown in a descending order of variance.

We successfully apply PCA decomposition on these mixed signals, and then obtain the decomposed signals as principal components shown in Figure 2.5(c). The source signals are successfully separated in a descending order of variance by PCA from mixed signals. The first mode separated by PCA expresses the component with most information. If we discard the four mode of white noise, and reconstruct the rest modes into observations, then it can be regarded as a filtering process.

As a result, PCA is a powerful method to separate signals into its principal components. The first several components represent significant information in observations. According to this property, PCA is widely used in compression of data and feature recognition in geodetic and hydrological applications.

2.2 Independent component analysis

For data with non-Gaussian distribution, only using covariances or correlations will not be sufficient to distinguish the statistical dependence in the data structures. Therefore, higher than second-order statistical information needs to be explored, in which case ICA is necessarily introduced (Hyvärinen, 1999).

In contrast to PCA, which deals with the second-order statistical moments of a data distribution, independent components analysis (ICA) focuses on higher order moments in the decomposition. ICA is a computational method for separating multivariate signal into additive subcomponents that are maximally independent. All the subcomponents are assumed non-Gaussian signals and statistically independent.

2.2.1 Blind source separation and statistical independence

Blind source separation ICA is described as a signal separation technique, which is able to recover the source signals from the observations.

Let us assume that the data X is a linear mixture of some statistically independent source signals S . We often even assume that the number m of sources S is the same as the dimensionality n of the data. The data is generated by mixing the sources linearly like

$$X = a_1s_1 + a_2s_2 + \dots + a_ms_m = \begin{bmatrix} a_1 & a_2 & \dots & a_m \end{bmatrix} \begin{bmatrix} s_1 \\ s_2 \\ \vdots \\ s_m \end{bmatrix} = A S, \quad (2.22)$$

with a mixing matrix $A = [a_1, a_2, \dots, a_m]$, containing m column vectors. And unknown source signals $S = [s_1, s_2, \dots, s_m]^T$, having m row vectors.

The blind source separation is to find a de-mixing matrix or whitening matrix W that inverts this mixture, so that

$$S = w_1x_1 + w_2x_2 + \dots + w_nx_n = \begin{bmatrix} w_1 & w_2 & \dots & w_n \end{bmatrix} \begin{bmatrix} x_1 \\ x_2 \\ \vdots \\ x_n \end{bmatrix} = W X, \quad (2.23)$$

where $W = [w_1, w_2, \dots, w_n]$ denotes the de-mixing matrix, which is to be determined with n observations. W can be identified with the pseudo-inverse of A , i.e. $W = A^\dagger$.

Typically, in ICA, A or W is identified such that s_i are mutually statistically independent. In this case, the source signals S are so called *independent components* (ICs).

Statistical independence Each source signal is characterized by a probability density function (PDF) $p(s_i)$, and the joint PDF of the sources is simply the product of its individual PDFs. Therefore, the statistical independence is described based on the PDFs. For those sources, we have $p(s_1, s_2, \dots, s_m)$. It defines the joint PDF of source signals s_1, s_2, \dots, s_m with probabilities of p_1, p_2, \dots, p_m , respectively.

A fundamental assumption of ICA is that the data is a linear mixture of statistically independent sources. If we unmix the data then the resulting output components should therefore be statistically independent again. Hence, a possible criterion of independence is whether

$$p(s_1, s_2, \dots, s_m) = \prod_{i=1}^m p(s_i) . \quad (2.24)$$

Practically, the target is to minimize the difference between the joint distribution and the product of marginal distribution. This approach is optimal as a measure of statistical independence.

A mixture of an infinite number of variables could lead to a Gaussian distribution even though each source variable may have non-Gaussian distribution. To seek for components that are as different from a Gaussian distribution as possible, it could be a good strategy to search for independent output components. One measure of non-Gaussianity often used is kurtosis, see (2.25). This approach typically first extracts the most non-Gaussian signal, and eliminates the corresponding dimension from the mixed data, and then finds the second non-Gaussian signal.

Moments and cumulants can describe the statistical properties of a random variable. If one simply subtracts from the higher moments what one would expect from the lower moments already, then the corrected moments are obtained, which are called cumulants. We assume zero-mean data s , and then the cumulants of s are defined as

$$\begin{aligned} C_i &= E(s_i) = 0 , \\ C_{ij} &= E(s_i s_j) , \\ C_{ijk} &= E(s_i s_j s_k) , \\ C_{ijkl} &= E(s_i s_j s_k s_l) \\ &\quad - E(s_i s_j)E(s_k s_l) - E(s_i s_k)E(s_j s_l) - E(s_i s_l)E(s_j s_k) . \end{aligned} \quad (2.25)$$

$E(s)$ expresses the expectation of s . Notice that there are no terms subtracted from C_{ij} and C_{ijk} above because of the zero-mean constraint. In (2.25), C_i and C_{ij} are the mean and variance. C_{ijk} is named skewness of the data, and C_{ijkl} is the fourth-order cumulant which is called kurtosis. It indicates how peaky or fat the distribution is. If the data has a Gaussian distribution, the kurtosis becomes zero and all the other cumulants higher than second-order also vanish.

Cumulants are an important property of the data. If we have two (or more) statistically independent variables and add them up, the cumulants of the sum equal the sum of the cumulants. If the random variables of a higher moment can be split into two statistically independent groups, then the expectation can be written as a product of the two lower moments of the groups. For example, if two signals s_i and s_j are statistically independent of s_k , the expectation of s_i, s_j, s_k can be written as

$$E(s_i s_j s_k) = E(s_i s_j) E(s_k) . \quad (2.26)$$

As a consequence of the assumption of zero-mean of data, all the cross-cumulants vanish, e.g. $C_{ijk} = E(s_i s_j s_k) = E(s_i s_j) E(s_k) = 0$. Turning this argument around is also true. If all cross-cumulants vanish then the random variables are statistically independent. This property thus simplifies the estimation of independence criteria.

Hence, the cross-cumulants are used in the ICA algorithm to measure the statistical independence between the components. Usually, we use the fourth-order cumulants because in many cases the third-order cumulants vanish with centered data. In practice, we optimize the independent components by finding the minimal fourth-order cumulants of the output signals.

2.2.2 Generic algorithm of ICA

As explained in 2.2.1, two assumptions are made. Firstly, observations should be a linear mixture of all the source signals. Secondly, all the independent components in the mixture are non-Gaussian signals. Based on these assumptions, ICA can be optimally applied to seek for statistically independent components from observation signals.

Generally, given the multi-dimensional source data S , we find the mixing matrix A that produces the observation data

$$X = A \cdot S , \quad (2.27)$$

and conversely, with the de-mixing matrix W it becomes

$$S = W \cdot X . \quad (2.28)$$

To obtain a set of statistically independent source signals S among a set of observed mixtures X , therefore, ICA intends to estimate W or A in a proper way. A number of ways exist to solve this problem. In this thesis, we use a proper rotation of the SVD transformation, following Aires (2002) and Forootan and Kusche (2012).

As defined in (2.7), a mixture data set can be represented by SVD transformation. If we apply a proper rotation to make the output components as independent as possible, then it reads

$$X = U \Sigma R \cdot R^T V^T , \quad (2.29)$$

where R is the rotation matrix, making U and V statistically independent. $U\Sigma R$ is treated as the mixing matrix A in (2.27), and $R^T V^T$ is considered as independent components S , namely

$$\begin{aligned} S &= R^T V^T = R^T W X, \\ A &= U \Sigma R. \end{aligned} \quad (2.30)$$

Hereby the task of ICA is finding an optimal rotation matrix R that makes the output components statistically independent. To solve this problem, a statistics-based algorithm proposed by Cardoso (1993), which is known as *joint approximate diagonalization of eigenmatrices* (JADE), is employed in this thesis.

As described in 2.2.1, the fourth-order cumulant is an important property, which indicate the statistical independence of variables. Given a random vector X with size $n \times 1$ and any $n \times n$ matrix $M = (m_{ij})$, we define the associated cumulant matrix $Q(M)$ as the $n \times n$ matrix defined component-wise by (Cardoso, 1993)

$$[Q^X(M)]_{ij} = \sum_{k,l=1}^n C(X_i, X_j, X_k, X_l) M_{kl}, \quad (2.31)$$

in which $C(S_i, S_j, S_k, S_l) = C_{ijkl}$ denotes cumulants of $X = AS$. As M is a basis matrix for the linear space of $n \times n$ matrices, the cumulant tensor Q^X contains $n^2 \times n^2$ matrices. For the rotation matrix R , we define the following joint diagonality criterion

$$F = \sum_{m=1}^{n^2} R^T Q(M_m) R, \quad (2.32)$$

in which the matrix R makes $Q(M)$ simultaneously close to diagonality. Thus, the rotation matrix R is determined as the minimizer of the squared off-diagonal cumulant elements.

In general, the JADE algorithm can be briefly summarized as

- **Initialization.** Estimate a whitening matrix W and do whitening on data $Z = WX$.
- **Form statistics.** Calculate the fourth-order cumulant tensor $Q^Z(M)$.
- **Optimization.** Minimize the off-diagonal elements of F by joint diagonalization such that the cumulant matrices $Q^Z(M)$ are as diagonal as possible, and then obtain rotation matrix R .
- **Separation.** Signal separation: estimate $\tilde{W} = R^T W$ and $S = \tilde{W} X, A = X S^{-1}$.

In this thesis, the JADE algorithm is implemented using the JADE Matlab function initially developed by Cardoso (1993). The details of JADE algorithm can be found in the Appendix B.

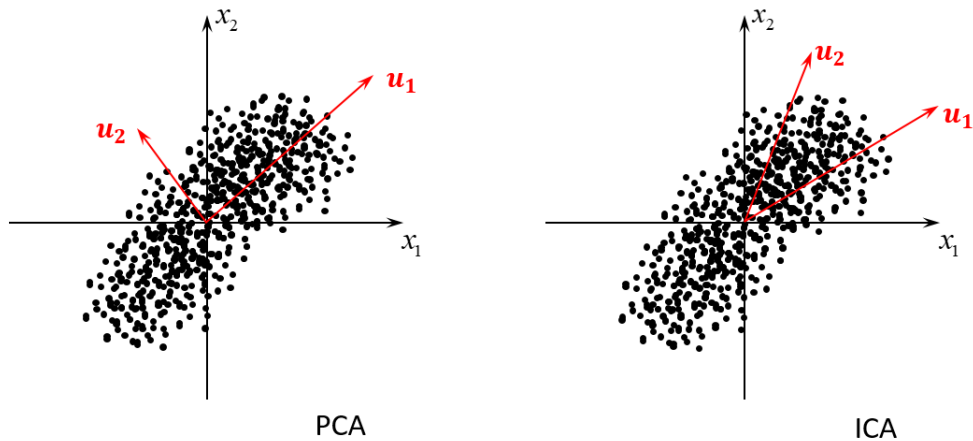


Figure 2.6: Illustration of ICA principle with respect to PCA. Different from PCA, The first component of ICA does not mean the most important component, and ICA requires that each component is statistically independent from others but not necessarily orthogonal projected.

2.2.3 Comparison of PCA and ICA

We already know that the first component from PCA indicates the most important mode of variability in data set. As explained in 2.2.1, however, the first component separated by ICA does not necessarily have the most variance. In addition, the independent components from ICA are not necessarily orthogonal to each other; they are just statistically independent. The different principles of PCA and ICA are illustrated in Figure 2.6.

A simulation is introduced here to examine the performance of ICA on finding statistically independent components from mixed signals. The source signals we used in this section are the same as listed in Table 2.1. The simulated observations are mixed according to (2.21) but with different weights from Figure 2.5, as shown in Figure 2.7(b).

PCA cannot distinguish the sinusoidal modes with different frequencies, while ICA is able to identify and separate in two independent modes, comparing Figure 2.7(c) and (d). In other words, ICA has advantages on separating signals into different modes, which are maximally statistical independent.

In summary, PCA is powerful to extract the most important information from the observations, and efficient to compress the dimension of the data, and widely used to analyze the structure of the observations and variables. However, PCA does not perform well on identifying and separating statistically independent signals from observations. This imperfection can be successfully remedied by ICA.

2.3 Canonical correlation analysis

Canonical correlation analysis (CCA) (Hotelling, 1936; Glahn, 1968) is a method of finding joint modes between two multidimensional variables. CCA aims to recognize the mutual informa-

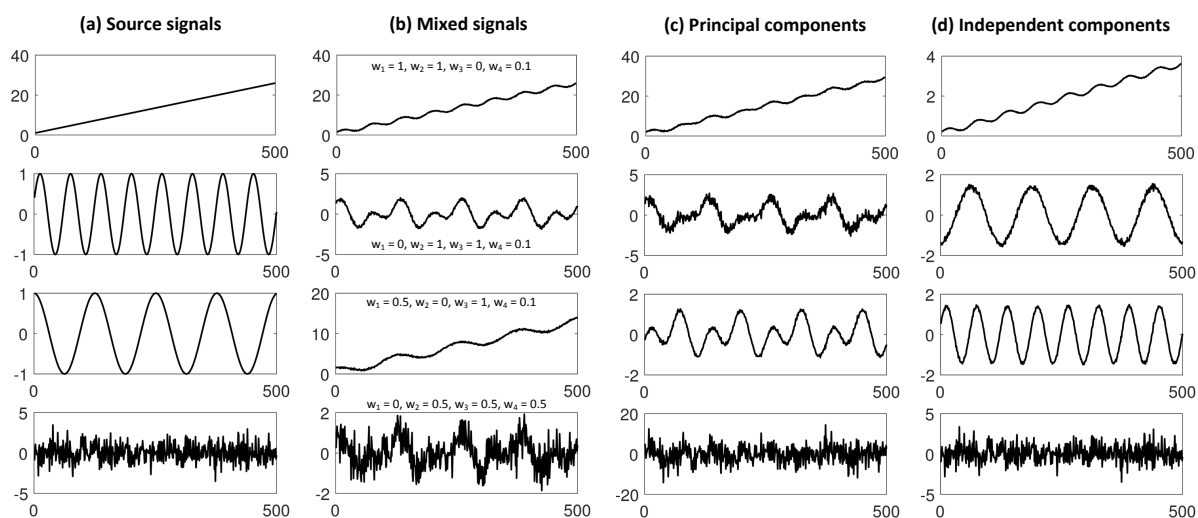


Figure 2.7: Numerical performance of (c) PCA and (d) ICA on a set of (b) mixed signals, which is mixed on a set of (a) source signals. Principal components are shown in a descending order of variance. Independent components are shown in a descending order of kurtosis.

tion from two data sets, and thus applies SVD on the covariance matrix between two data sets. Because correlation between signals is invariant to the signal magnitudes, CCA is able to find the basis vectors for two different sets of variables with different units.

Different from PCA, CCA seeks out the structures not based on maximum variance but on maximum covariance between signals. Each canonical mode from both fields represents the mutual correlated information, as illustrated in Figure 2.8.

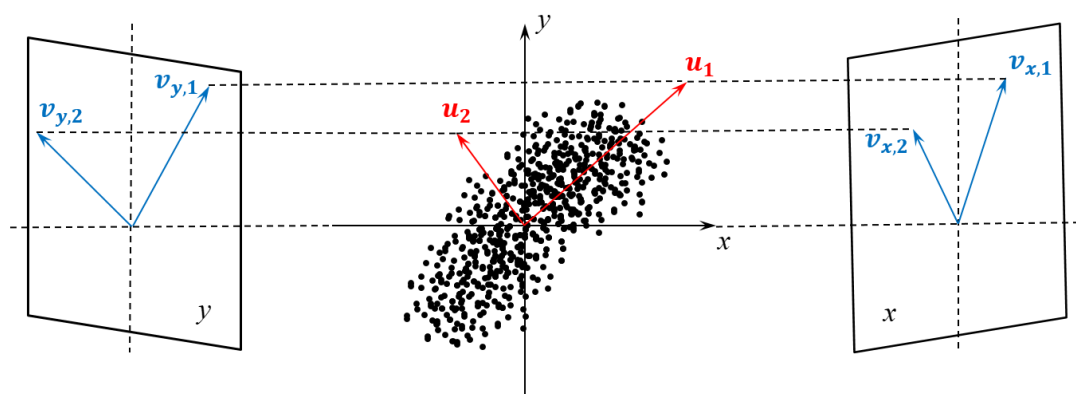


Figure 2.8: Illustration of the CCA principle. Different from PCA, CCA seeks for the most correlated component from the covariance space, and then project onto each data set. The red arrows show the direction of components after SVD analysis on the joint data set. The blue arrows depict the projected components for each data set, which are therefore canonical correlated.

There are two typical purposes of CCA. One is to reduce the dimension of data. Based on the covariance between two sets of variables, data reduction is fulfilled by using a small number

of linear combination with high correlations. The second is to find typical features (i.e., canonical modes of variability) between both fields. With the aid of features which explain most covariation between two sets of variables, we can better interpret the observed data. For teleconnection pattern analysis, in this thesis, CCA is applied mainly for feature identification of joint variables.

2.3.1 Principle of CCA

Let us define two variables X ($t_1 \times n_1$) and Y ($t_2 \times n_2$). Particularly, one of the dimensions of X and Y must have the same size. Let us assume that X and Y have the same dimension in time. Thus, t_1 and t_2 become equal. Similar to (2.2) and (2.3), the cross-covariance of X and Y is formulated as

$$C_{XY} = \frac{1}{n} X^T Y = \frac{1}{n} \begin{pmatrix} \sum_{t=1}^n x_{t,1} y_{t,1} & \sum_{t=1}^n x_{t,1} y_{t,2} & \cdots & \sum_{t=1}^n x_{t,1} y_{t,d_2} \\ \sum_{t=1}^n x_{t,2} y_{t,1} & \sum_{t=1}^n x_{t,2} y_{t,2} & \cdots & \sum_{t=1}^n x_{t,2} y_{t,d_2} \\ \vdots & \vdots & \ddots & \vdots \\ \sum_{t=1}^n x_{t,d_1} y_{t,1} & \sum_{t=1}^n x_{t,d_1} y_{t,2} & \cdots & \sum_{t=1}^n x_{t,d_1} y_{t,d_2} \end{pmatrix}. \quad (2.33)$$

Assume that two variables A and B that have the same size as X and Y , are the linear combinations of X , Y , respectively. In order to seeking the most correlated variation of A and B , we need to find out the canonical variates that maximize the cross-covariance matrix of A and B , i.e. $\max[\text{Cov}(A, B)] = \max(C_{AB})$. In other words, we need to find a linear combination $A = XU$ and $B = YV$ that maximize the C_{AB} . Thus, the U and V fulfill

$$C_{AB} = \frac{1}{n} A^T B = \frac{1}{n} U^T X^T Y V = U^T C_{XY} V. \quad (2.34)$$

According to the principle of PCA, maximizing C_{AB} is equivalent to finding a transformation U and V to diagonalize the covariance matrix of X and Y . Hence, according to (2.7), it is essential to apply SVD to the covariance matrix C_{XY} , and then it becomes

$$C_{XY} = U_C \Sigma_C V_C^T. \quad (2.35)$$

Here, the U_C and V_C are called the canonical modes or joint PC of X and Y with dimension d_1 , d_2 , respectively. Now in (2.35), the covariance matrix C_{AB} in (2.34) turns to be diagonal singular value matrix Σ_C . Meanwhile, we obtain the so-called canonical variates A and B , which reflect the maximal correlation in X and Y . Thus, the first pair of vector U_C and V_C has the maximal covariance, which indicates the canonical directions. The first pair of canonical variates A and B has the best correlation via linear combination of X and Y . Σ_C contains the singular values of covariance matrix C_{XY} . U_C , V_C are not necessarily ranked in decreasing order of variance for each field X , Y , but only in decreasing order of cross-covariance $X^T Y$.

In (2.35), column vectors in U_C , V_C are orthonormal. In other words, the canonical modes U_C , V_C satisfy $U_C U_C^T = U_C^T U_C = I$, $V_C V_C^T = V_C^T V_C = I$. Here, we need to notice that the corresponding vectors in the variates A and B are not normalized and not necessarily orthogonal, but mutually correlated between A and B .

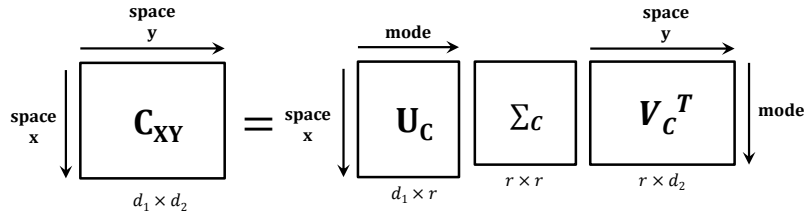


Figure 2.9: Illustration of U_C , Σ_C , V_C matrices of covariance matrix C_{XY} .

In Figure 2.9, the number of modes $r = \min(r_1, r_2)$, where r_1, r_2 denote the rank of X and Y . At this point, r_1 and r_2 are not necessarily equal. In this thesis, according to the size of data sets, the number of spatial grid cells is larger than the number of temporal samples ($n < d_1, d_2$). The cross-covariance matrix $C_{XY}(d_1 \times d_2)$ is scaled by n , i.e., divided by the length of the time series. Hence, the amount of modes $r_1 = r_2 = r$ is equal to the temporal dimension n .

Since the canonical modes U_C, V_C retain spatial information, the associated temporal modes V_X, V_Y (i.e. canonical variates A, B) are obtained by projecting the data X and Y on U_C, V_C ,

$$V_X = X \cdot U_C \quad (2.36)$$

$$V_Y = Y \cdot V_C. \quad (2.37)$$

In this case, V_X, V_Y consequently refer to the temporal information, representing the associated features from X, Y . Visually, the canonical spatial mode U_C from X and corresponding temporal mode V_X are depicted in Figure 2.10. In fact, the associated temporal PCs (V_X, V_Y) of each field are matched with respect to the canonical modes. Specifically, in this study, we use *spatial EOFs* to denote these joint canonical modes by CCA.

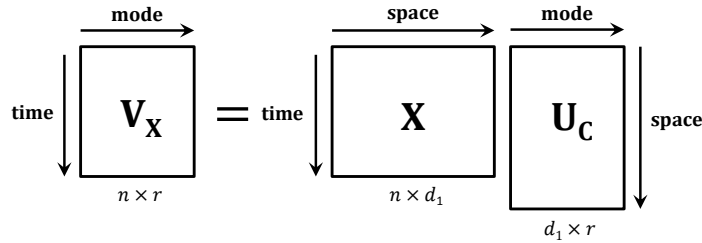


Figure 2.10: Illustration of the canonical spatial mode U_C , and temporal mode V_X of X .

In short, the canonical modes are produced by the maximum covariance between two input fields. Namely, a subset of the canonical modes of two data sets is selected, which explains the most covariance between two different datasets.

The precondition of CCA is that there is significant correlation between these two data sets, otherwise it may not make sense to search for structures in this covariance. A normalized root mean squared covariance (RMSC) is introduced here. The total squared covariance, which is sum of the squares of all the elements of the covariance matrix, is a useful measure of the strength of the simultaneous linear relationship between the fields. It can be normalized by the product of the variance of both fields. Therefore, we calculate the RMSC (Wallace et al., 1992),

which is equivalent to the square root of the temporal correlation coefficients between X and Y , averaged over all pairs of the grid points in the two fields, by

$$\text{RMSC} = \sqrt{\frac{1}{d_1 \cdot d_2} \sum_{i=1}^{d_1} \sum_{j=1}^{d_2} \frac{(x_i - \bar{x}_i)^T (y_j - \bar{y}_j)}{\sqrt{(x_i^T x_i)(y_j^T y_j)}}}. \quad (2.38)$$

In (2.38), x_i, y_j are column vectors of X and Y at grid point i, j , and \bar{x}_i, \bar{y}_j are the mean of the column vector x_i, y_j . d_1, d_2 are the number of the grid points in each field. The RMSC is typically of order 0.1 or larger for well-correlated fields, but even smaller values may indicate significant correlation if the number of independent samples is large. Hence, the correlations can be distinguished from zero. After evaluation, the RMSC between all hydrologic variables that are involved in this research and sea surface temperature are between 0.03 to 0.1. Although there is probably no strong linear relationship between those variables, it is still necessary to find out how they relate with each other, so that it can reflect implicitly the signature of climate change.

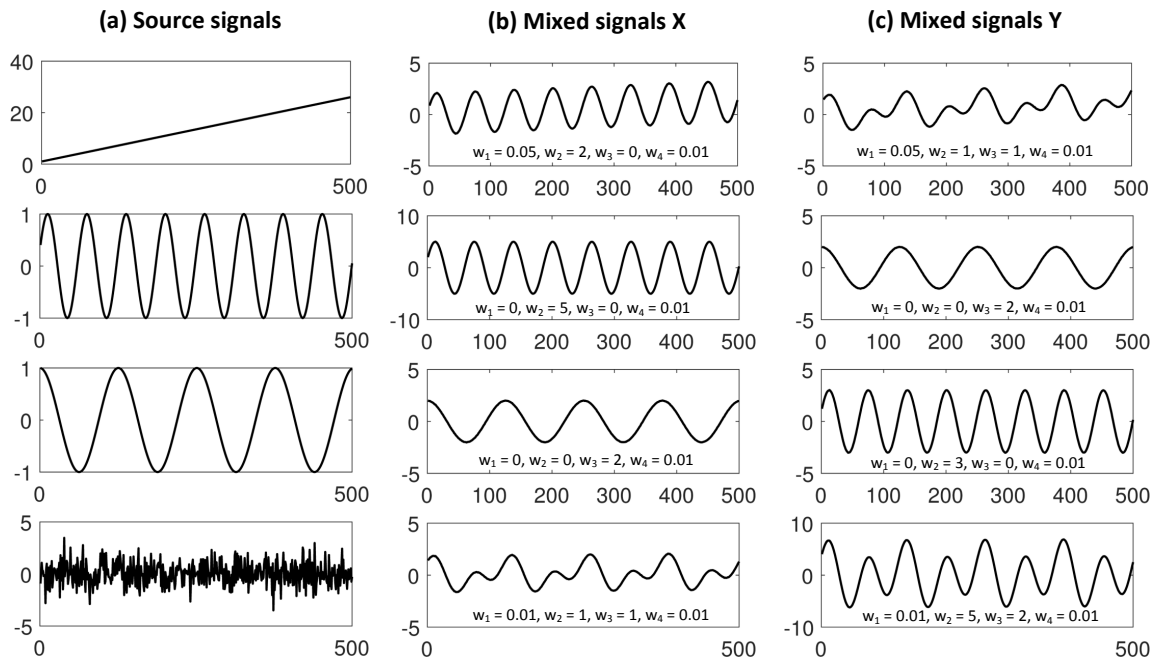


Figure 2.11: Two simulated sets of signals (b) X and (c) Y , which is mixed by a linear combination of (a) source signals.

2.3.2 Comparison of PCA and CCA

As described in 2.1 and 2.3, PCA attempts to find the modes with most variance in one set of the observations, while CCA is similar but instead attempts to search for the joint modes with most covariance between two different variables. Considering this property, a simulation is

designed here to examine the performance of CCA on finding significantly associated signals from two different sets of signals.

These two sets of signals X and Y , as shown in Figure 2.11, are mixed by an arbitrary linear combination of the same source signals in terms of weights w_1, w_2, w_3, w_4 , according to (2.21). The source signals in Figure 2.11(a) we used are the same as listed in Table 2.1.

We apply CCA, as written in (2.35) and (2.37), on these two sets of mixed signals to see whether CCA has the capability to find out the correlated signals from them. From Figure 2.12, four canonical modes are identified from each field in descending order of covariance. The first canonical mode is identified, which represents sinusoidal variability. The second mode of each field represents both sinusoidal variability as well but with larger period. Comparing with Figure 2.11(a), the third canonical mode show linear trend but with periodic component as well in the time series.

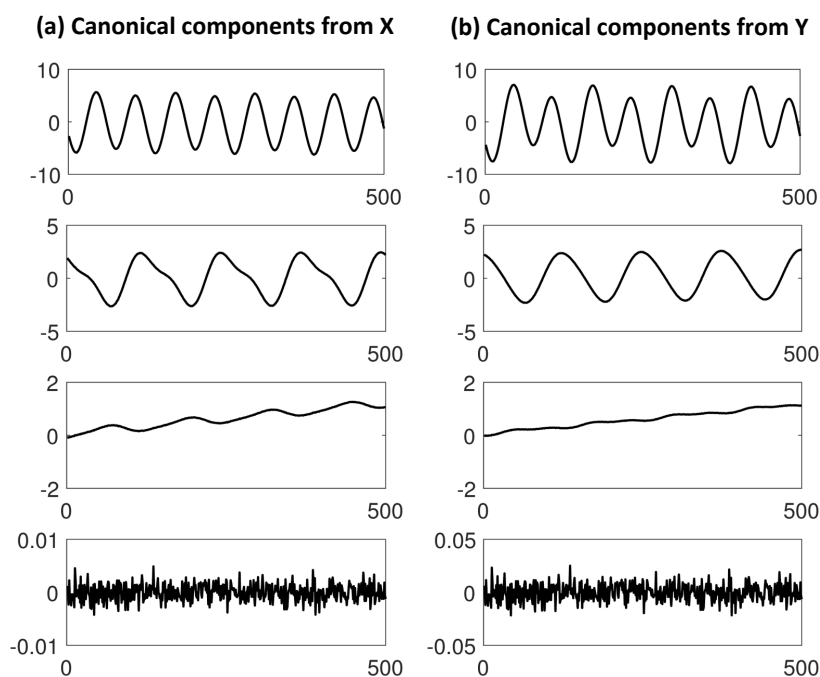


Figure 2.12: Numerical performance of CCA on two mixed data sets (a) X and (b) Y . Canonical components from each field are shown in a descending order of covariance.

Obviously, CCA is able to recognize the associated components between two mixtures. However, we also find that, CCA is not able to fully recover the source signals, according to its numerical performance in Figure 2.12. In addition, due to its insensitivity to the linear trend, in the following chapter, we therefore carefully remove the linear trends from the observations before we apply CCA.

2.4 Multivariate linear regression modelling

The generalized linear problem The linearity between hydrological variables and terrestrial water mass variation can be identified by applying the above decomposition techniques. However, it is still a challenge to model the multivariate linear relationship between them. Using one or a combination of several different hydrological quantities to estimate water mass change is one of our objectives in this thesis.

In short, concerning the linear relationship between observations and predictions, a generalized problem needs to be solved, which writes

$$s = H \cdot l . \quad (2.39)$$

In (2.39), s is the predictant, which refers to the unknown signals that need to be estimated, l is the predictor, which normally comes from measurements, H describes mathematically the relationship between predictor and predictant.

Least-squares collocation, as a mathematical tool developed by Krarup (1969) and Moritz (1980), is used for modeling the linear relationship between different terrestrial variables. By using least-squares prediction/collocation approach, the unknown quantities s can be optimally estimated from the observations l .

Generally, noise exists on the measurements. To improve the performance of prediction from observations, l needs to be filtered or corrected. Signal decomposition techniques, i.e., PCA, CCA, are therefore employed in the linear regression. Principal component regression (PCR) is useful to compress the observations and consequently eliminate the influence of random noise in the prediction. Partial least-squares regression (PLR) concerns not only the impact of noise on measurements, but also takes the mutual linear variability of measurements and unknown signals into account. An adaptive regression model is therefore established by PCR or PLR on basis of $s = Hl$.

2.4.1 Least squares prediction and collocation

The main purpose of collocation is to predict unknown signals by known measurements. Considering the presence of noise in the measurement, a second application is filtering on the observations. Besides predicting and filtering, least-squares collocation can additionally be used to determine the parameters which define a mathematical model between measurements and unknown signals (Ruffhead, 1987).

Least-squares prediction As we assume that a set of unknown signals S is approximated by a linear combination of the observations L , the model has the form

$$S = L \cdot H + e , \quad (2.40)$$

where $S(n \times d_s)$ is the target matrix to be estimated, $L(n \times d_l)$ is the observation matrix, $H(d_l \times d_s)$ is the prediction matrix, which links the linear relationship between S and L . Each column vector in S and L is a time series. Both L and S contain zero-mean column vectors. In statistical

estimation, the best linear estimate of S in terms of L is defined as the linear minimum variance unbiased estimate (Moritz, 1980). To solve this optimization problem in (2.40), we refer to the least-squares criterion that minimizes the covariance of error e ,

$$C_{ee} = E\{e^T e\} = E\{(\hat{S} - S)^T (\hat{S} - S)\} \Rightarrow \min. \quad (2.41)$$

By (2.40) and (2.41), we get the error covariance matrix as

$$\begin{aligned} e^T e &= (S - LH)^T (S - LH) \\ C_{ee} &= H^T C_{LL} H - C_{SL} H - H^T C_{LS} + C_{SS} \\ &= C_{SS} - C_{SL} C_{LL}^{-1} C_{LL} C_{LL}^{-1} C_{LS} + (H - C_{LL}^{-1} C_{LS})^T C_{LL} (H - C_{LL}^{-1} C_{LS}). \end{aligned} \quad (2.42)$$

If the latter part in (2.42) is made zero, then C_{ee} is minimum. Thus, we obtain

$$\begin{aligned} \hat{H} &= C_{LL}^{-1} C_{LS} \\ C_{ee} &= C_{SS} - C_{SL} C_{LL}^{-1} C_{LS}, \end{aligned} \quad (2.43)$$

in which $C_{LL}(d_l \times d_l)$ is auto-covariance matrix of L , and $C_{LS}(d_l \times d_s)$ is the cross-covariance matrix between S and L .

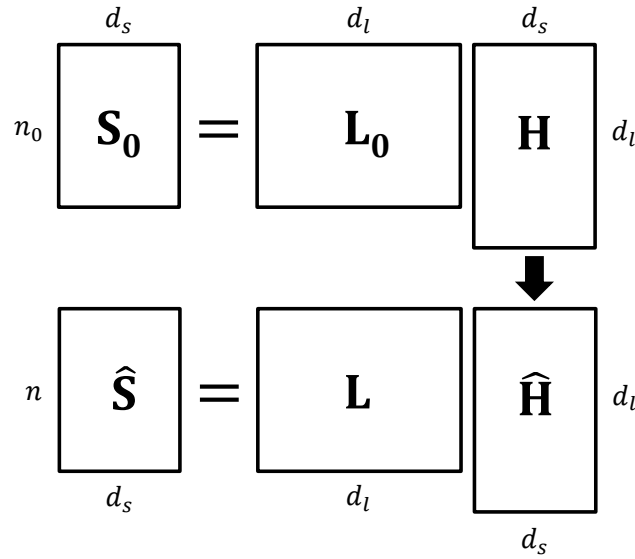


Figure 2.13: Illustration of S , L and H for training and prediction.

Substituting (2.43) into (2.40), one obtains

$$\hat{S} = L \cdot C_{LL}^{-1} C_{LS}. \quad (2.44)$$

As a result, the unknown signal S is optimally estimated in terms of a linear combination of L by its covariance C_{LL} and C_{LS} .

In brief, as illustrated in Figure 2.13, for least-squares prediction there are two steps: firstly, estimate the prediction matrix H by using prior information L_0 and S_0 to construct the covariance matrix C_{LL} and C_{LS} ; secondly, predict the unknown signal S by the observation L and the estimated prediction matrix \hat{H} . The procedure is mathematically summarized as

- Training prediction matrix: $\hat{H} = C_{LL}^{-1}C_{LS}$;
- Predicting signal by H : $\hat{S} = L \cdot \hat{H}$.

In practice, least-squares prediction does not only work with homogeneous data, but can also be applied on different quantities, i.e., water storage change, river discharge, precipitation, or water level change, in any hydro-geodetic applications.

Least-squares prediction with noise The general case of linear estimation model is initialized in (2.39). Taken random noise into consideration, the observation l can be separated into true signal part t and noise part w , written

$$l = t + w . \quad (2.45)$$

Since signal and random noise are uncorrelated, which derives $C_{WS} = 0$, consequently, we calculate the auto-covariance of observations C_{LL} and the covariance matrix C_{LS} between observations L and signals S by

$$\begin{aligned} C_{LL} &= C_{TT} + C_{WW} \\ C_{LS} &= C_{TS} + C_{WS} = C_{TS} , \end{aligned} \quad (2.46)$$

In (2.46), C_{LL} is simply the sum of the covariance matrix of signal C_{tt} and noise C_{ww} . Both s and t refer to signals, so C_{sl} becomes a pure signal covariance matrix. Substituting (2.46) into (2.43) and (2.44), we get the prediction formula

$$\begin{aligned} \hat{H} &= (C_{TT} + C_{WW})^{-1}C_{TS} \\ C_{ee} &= C_{SS} - C_{ST}(C_{TT} + C_{WW})^{-1}C_{TS} \\ \hat{S} &= L \cdot \hat{H} = L \cdot (C_{TT} + C_{WW})^{-1}C_{TS} , \end{aligned} \quad (2.47)$$

where $C_{WW}(d_l \times d_l)$ is the covariance matrix of white noise. In this case, the prediction with random noise in (2.47) is also named for *least-squares collocation* (Moritz, 1980). The only difference between (2.44) and (2.47) is the matter of the covariance of noise C_{WW} .

If we assume that $S = T$, then the collocation formula (2.47) becomes

$$\begin{aligned} \hat{T} &= L \cdot (C_{TT} + C_{WW})^{-1}C_{TT} \\ \hat{S} &= L \cdot (C_{TT} + C_{WW})^{-1}C_{TS} \\ &= \hat{T}C_{TT}^{-1}(C_{TT} + C_{WW})(C_{TT} + C_{NN})^{-1}C_{TS} \\ &= \hat{T} \cdot C_{TT}^{-1}C_{TS} , \end{aligned} \quad (2.48)$$

since $L = \hat{T}C_{TT}^{-1}(C_{TT} + C_{WW})$. The upper equation represents the filtering of the observations $L(n \times d)$ into $T(n \times d)$, in which L is mathematically replaced by \hat{T} . The lower equation expresses the prediction of signal $S(n \times d)$ based on filtered signal $T(n \times d)$, in terms of noise free case.

Therefore, when the object of the linear estimation S equals the signals T , the collocation with noise turns equivalently to data filtering. Briefly, it can be summarized as filtering on the observations and then predicting new signals based on filtered signals (Moritz, 1980).

Least-squares collocation with parameters Generally, according to (2.39) and (2.45), a physical variable l can be mathematically approximated by a linearized model $l = Ax + e$ with model parameters x . When we introduce a mathematical model in the linear collocation, a more generalized case is achieved as

$$l = Ax + t + w . \quad (2.49)$$

If we firstly simplify the case, $L = AX + e$, in which $X(m \times d_l)$ is the parameter matrix, $A(n \times m)$ is the design matrix. Then we obtain the covariance matrix of L and X in terms of $C_{LL} = AC_{XX}A^T$ and $C_{XX} = (A^TC_{LL}A)^{-1}$. Referring to (2.41), the least-squares solution of \hat{X} is given as

$$\begin{aligned} \hat{X} &= C_{XL}C_{LL}^{-1}L \\ &= (A^TC_{LL}A)^{-1}A^TC_{LL}^{-1}L . \end{aligned} \quad (2.50)$$

Next we suppose a model of observations regardless of noise, then

$$L = AX + SB + e , \quad (2.51)$$

where $S(n \times d_s)$ is linked with $L(n \times d_l)$ by the weight matrix $B(d_s \times d_l)$. Thus, S is obtained equivalently as a linear expression

$$S = (L - AX)H + e . \quad (2.52)$$

As we know, L is supposed to be modelled by AX , so that $E(L) = AX$. According to (2.52), we obtain $C_{LS} = E\{L(L - AX)H\} = E\{L(L - AX)\}H = C_{LL}H$. Hence, we get $\hat{H} = C_{LL}^{-1}C_{LS}$, which is consistent with (2.43). Eventually, it proves that S is the linear estimate of $L - AX$. As a result,

$$\begin{aligned} \hat{S} &= (L - A\hat{X})\hat{H} \\ &= (L - A\hat{X})C_{LL}^{-1}C_{LS} . \end{aligned} \quad (2.53)$$

If we consider noise in the model, then $L = AX + SB + W$, where $W(n \times d_l)$ is the white noise matrix. Similar to (2.46), the covariance of L becomes

$$C_{LL} = C_{SS} + C_{WW} . \quad (2.54)$$

(2.53) represents a model synthetically combining adjustment and prediction (Moritz, 1980). In other words, we can say that the least-squares collocation is composed of two steps: adjustment and prediction.

In fact, (2.52) describes the most general case. There are two more special cases to be discussed (Ruffhead, 1987). Firstly, if the model is known, then it can be removed directly from the observations by subtraction in the equation, i.e. $L = SB + W$. It is equivalent to the case of collocation only with noise, as defined in (2.45).

Another case is noise free collocation. If, in addition, the noise in the observation is negligible, the linear relationship between observation and estimation becomes $L = SB$, which is mathematically equivalent to least-squares prediction (LSP), $S = LH$, as expressed in (2.40). In this thesis, the least-squares collocation (LSC) approach are used for hydro-geodetic applications. Since both the observation L and the prediction S in the model are type of hydro-geodetic variables in nature, therefore, we employ the noise free prediction and collocation instead. The random noise is concerned and filtered additionally by decomposition techniques, which are involved in the following sections.

2.4.2 Principal component regression

Based upon the criterion of minimum error covariances, least-squares collocation provides an unbiased optimal linear estimate. However, the multicollinearity phenomenon exists in the linear regression models. In this sense, the ordinary least-squares prediction can not overcome this problem. Hence, principal component regression has been developed for dealing with the collinearity among multiple variables (Kendall, 1957; Massy, 1965). According to (2.20), a PCA decomposition on a measurement matrix can be expressed by

$$L = U_L \cdot V_L^T , \quad (2.55)$$

where $U_L(n \times r)$ is decomposed PCs of $L(n \times d_l)$, $V_L(d_l \times r)$ is the normalized eigenvectors with respect to U_L . r is the number of modes. Generally, r is obtained as the rank of L . For the purpose of filtering and data compression, r should be smaller than the rank. In this case, we retain r number of PCs from L and eliminate the left signals. Substituting (2.55) into (2.40), as depicted in Figure 2.14, the regression model is written in the form

$$S = L \cdot H + e = U_L \cdot V_L^T \cdot H + e = U_L \cdot K + e , \quad (2.56)$$

in which $S(n \times d_s)$ denotes prediction for unknown signals, $H(d_l \times d_s)$ is the prediction matrix, building up the linear regression model between S and L . $K(r \times d_s)$ is the reformed prediction matrix, which refers to the PC U_L of L . We find the optimal estimation of K using the least-squares approach, so K can be estimated in terms of PC U_L from L as

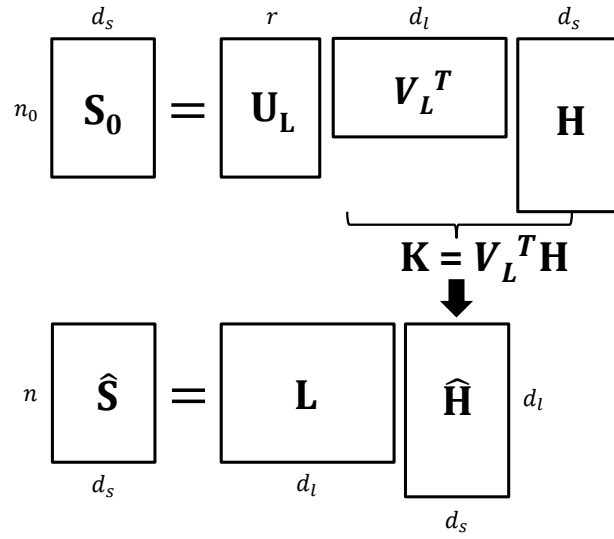


Figure 2.14: Illustration of S , L and H in PCR model for training and prediction.

$$\begin{aligned}\hat{K} &= (U_L^T U_L)^{-1} U_L^T S, \\ \hat{H} &= V_L \hat{K}.\end{aligned}\quad (2.57)$$

Since $U_L = L V_L$, substituting the U_L by $L V_L$ in (2.57), the covariance of U_L can be expressed by

$$\begin{aligned}C_{UU} &= (L V_L)^T (L V_L) = V_L^T C_{LL} V_L, \\ U_L^T S &= V_L^T L^T S = V_L^T C_{LS}.\end{aligned}\quad (2.58)$$

Combining (2.57) and (2.58), the unknown signal S is ultimately estimated by

$$\hat{S} = L \cdot \hat{H} = L V_L (V_L^T C_{LL} V_L)^{-1} V_L^T C_{LS}.\quad (2.59)$$

The regression represented in (2.59) is the so called *principal component regression (PCR)*. The procedure of training and prediction by PCR is illustrated in Figure 2.14. If we think of the eigenvectors V_L as a linear transformation matrix R of L , then (2.59) is reformed by

$$\hat{S} = L R (R^T C_{LL} R)^{-1} R^T C_{LS},\quad (2.60)$$

where $R = V_L$. In this case, according to (2.43), the error covariance from PCR is derived by

$$C_{ee} = C_{SS} - C_{SL} R (R^T C_{LL} R)^{-1} R^T C_{LS}.\quad (2.61)$$

Comparing with (2.44), R is equivalent to a constraint matrix on the least-squares prediction. If we implement the PCR on a generalized case in (2.52), then we have an updated form

$$\begin{aligned}\hat{X} &= (A^T C_{LL} A)^{-1} A^T C_{LL}^{-1} L \\ \hat{S} &= (L - A\hat{X})R (R^T C_{LL} R)^{-1} R^T C_{LS},\end{aligned}\tag{2.62}$$

since $S = (L - AX)RK + e$ represents the model of observations instead of (2.52). The regression model represented by (2.62) is, therefore, an ultimate generalized case. (2.62) is equivalent to ordinary least-squares prediction when $R = I$. In this sense, the least-squares prediction can be regarded as a special case.

From above, the procedure of PCR is briefly summarized as

- Separating observation by PCA into modes:
 $L_0 = U_L \cdot V_L^T$;
- Training prediction matrix on selected modes:
 $\hat{K} = (U_L^T U_L)^{-1} U_L^T S_0$;
- Transforming the prediction matrix from mode version K to signal version H :
 $\hat{H} = V_L \hat{K}$;
- Predicting signal by H :
 $\hat{S} = L \cdot \hat{H}$.

On one hand, PCR is one way to deal with an ill-conditioned problem. The constraint matrix R reduces the dimension of L when L is not full rank matrix. On the other hand, PCR is a linear regression model that the predicted signal S is actually regressed on the PCs of observations L . Therefore, PCR can be regarded as a synthetical approach including both filtering and prediction process. In this thesis, we employ PCR model on different hydrological variables in order to predict the water mass change.

2.4.3 Partial least-squares regression

Dimension reduction is one of the major tasks for multivariate analysis, especially critical for multivariate regressions. Besides PCR, the partial least-squares regression (PLR), which is developed by Wold et al. (1984), is another method for dealing with the collinearity problem. Although PLR is promoted and used by chemometricians (Höskuldsson, 1988), it is also applicable in hydrological and geodetic researches.

Different from PCR, PLR aims to regress on those PCs of measurements, that highly correlate with target signals. Similar to CCA, as depicted in Figure 2.15, PLR is fulfilled via SVD on the covariance matrix between predictors and predictants, expressed by

$$C_{LS} = L^T S = U_C \Sigma_C V_C^T, \tag{2.63}$$

where $U_C(d_l \times r)$, $V_C(d_s \times r)$ are the joint normalized eigenvectors from SVD for $L(n \times d_l)$ and $S(n \times d_s)$, which are also called canonical modes, respectively. Σ_C is a diagonal matrix containing covariance of L and S . U_C , V_C are associated spatial EOFs in each space. r is the number of canonical modes from SVD. Similar to (2.55), r is obtained as the rank of covariance matrix $C_{LS}(d_l \times d_s)$. In practice, r is decided by the purpose of application. In our case, we

retain r modes, which are strongly associated between L and S , and eliminate the remaining signals as redundancy.

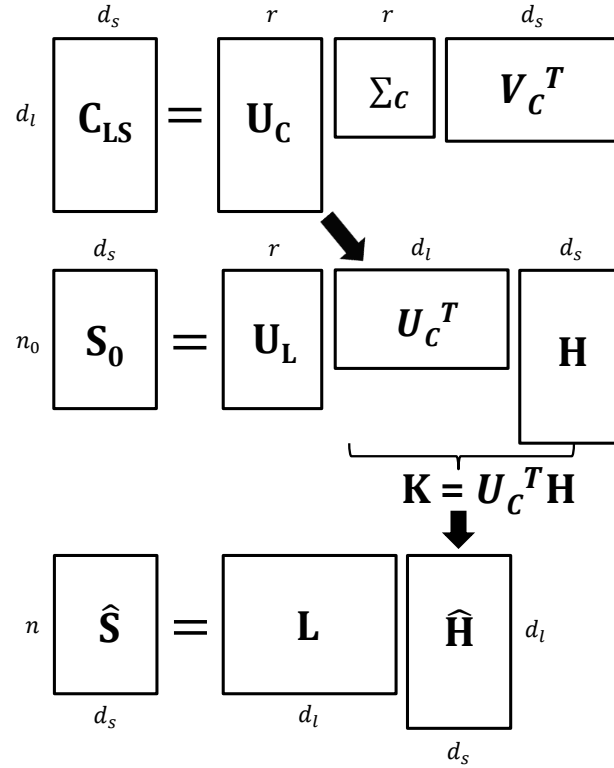


Figure 2.15: Illustration of S , L and H in PLR model for training and prediction.

We gain the PCs of L , which is significantly correlated with S , by projection of U_C on L . In the next step, substituting (2.63) into (2.40), the regression model is thus written in the form

$$\begin{aligned}
 U_L &= L U_C, \\
 S &= L H + e \\
 &= U_L U_C^T H + e \\
 &= U_L K + e.
 \end{aligned} \tag{2.64}$$

As illustrated in Figure 2.15, $U_L (n \times r)$ is the associated PCs from L . $K (r \times d_s)$ is the reformed regression matrix that is combined with U_C . The optimal estimation of K is estimated in terms of U_L , using the least-squares approach, then

$$\begin{aligned}
 \hat{K} &= (U_L^T U_L)^{-1} U_L^T S, \\
 \hat{H} &= U_C \hat{K}.
 \end{aligned} \tag{2.65}$$

In accordance with PCR, we substitute the U_L by LU_C in (2.65), so we calculate the covariance of U_L by

$$\begin{aligned} C_{UU} &= (LU_C)^T(LU_C) = U_C^T C_{LL} U_C, \\ U_L^T S &= U_C^T L^T S = U_L^T C_{LS}. \end{aligned} \quad (2.66)$$

Combining (2.65) and (2.66), the unknown signal S with its error covariance C_{ee} is consequently predicted by

$$\begin{aligned} \hat{S} &= L \cdot \hat{H} \\ &= L U_C (U_C^T C_{LL} U_C)^{-1} U_C^T C_{LS}, \\ C_{ee} &= C_{SS} - C_{SL} U_C (U_C^T C_{LL} U_C)^{-1} U_C^T C_{LS}. \end{aligned} \quad (2.67)$$

Comparing with (2.62), the transformation matrix becomes $R = U_C$. The regression represented in (2.67) is called *partial least-squares regression (PLR)*. The major difference between PCR and PLR is that PCR uses only the dominant signals of L to predict S , while PLS uses the most associated signals of L , gained on basis of both S and L to estimate the new unknown signals for S .

In summary, the procedure of PLR is implemented by four steps:

- Separating observation into modes that are associated with predictant by CCA:
 $C_{LS} = L_0^T S_0 = U_C \Sigma_C V_C^T, \quad U_L = L_0 U_C;$
- Training prediction matrix on the selected canonical modes:
 $\hat{K} = (U_L^T U_L)^{-1} U_L^T S_0;$
- Transforming the prediction matrix from mode version K to signal version H :
 $\hat{H} = U_C \hat{K};$
- Predicting signal by H :
 $\hat{S} = L \cdot \hat{H}.$

2.4.4 Adaptive moving averaging regression

Water mass transport in the water cycle is a dynamic process. Hence, each variable has either leads or delays, correlating with others. When we model the linear relationship between those hydrological variables, the temporal shifting needs to be carefully considered. Therefore, we propose an adaptive regression approach, which involves a moving average model.

Generally, a moving average model (MA) is represented as

$$\begin{aligned} s(t) &= m_1 l(t) + m_2 l(t-1) + \dots + m_k l(t-k+1) \\ &= [m_1 \ m_2 \ \dots \ m_k] \cdot [l_t \ l_{t-1} \ \dots \ l_{t-k+1}]^T, \end{aligned} \quad (2.68)$$

in which $s(t)$ is the model estimation, $l(t), l(t-1), \dots, l(t-k+1)$ are the observations with $k-1$ different number of shifting. m_1, m_2, \dots, m_k are the parameters of the model. The value k defines the order of the MA model, which is abbreviated as MA(k). A MA model is conceptually a regression of current observation against current and previous observations.

As expressed in (2.68), a variable s can be modeled by a linear combination of l in terms of MA model. Hence, a $t \times 1$ vector S is regressed by an ensemble observation matrix ΔL on all the epochs t with a shift from 0 to $k - 1$, written as

$$S = \Delta L \cdot M + e, \quad (2.69)$$

where the observation matrix

$$\Delta L = \begin{bmatrix} l(t_1) & l(t_1 - 1) & \cdots & l(t_1 - k + 1) \\ l(t_2) & l(t_2 - 1) & \cdots & l(t_2 - k + 1) \\ \vdots & \vdots & \ddots & \vdots \\ l(t_n) & l(t_n - 1) & \cdots & l(t_n - k + 1) \end{bmatrix}, \quad (2.70)$$

and the parameter matrix $M = [m_1, m_2, \dots, m_k]^T$.

Considering a linear regression for multiple variables, in which both L and \hat{S} contain more than one variable, we expand the ΔL and \hat{S} in (2.69) by

$$\begin{aligned} S &= \Delta L_1 M_1 + \Delta L_2 M_2 + \dots + \Delta L_{d_l} M_{d_l} + e \\ &= [\Delta L_1 \ \Delta L_2 \ \dots \ \Delta L_{d_l}] [M_1 \ M_2 \ \dots \ M_{d_l}]^T + e \\ &= L \cdot H + e, \end{aligned} \quad (2.71)$$

where $L = [\Delta L_1 \ \Delta L_2 \ \dots \ \Delta L_{d_l}]$ is a $n \times (k \times d_l)$ matrix for d_l different variables, $S(n \times d_s)$ has d_s number of model prediction. As defined in (2.69), ΔL_n in L is a $n \times k$ matrix, so d_l matrices $M_{d_l}(k \times d_s)$ yield a prediction matrix $H((k \times d_l) \times d_s)$ matrix for this regression model.

Similarly, L in (2.71) can be rearranged in the form of

$$\begin{aligned} L &= [L_1 \ L_2 \ \dots \ L_k], \\ S &= L \cdot H + e \\ &= [L_1 \ L_2 \ \dots \ L_k][H_1 \ H_2 \ \dots \ H_k]^T + e, \end{aligned} \quad (2.72)$$

where L_k is a $n \times d_l$ matrix,

$$L_k = \begin{bmatrix} l_{1,1} & l_{1,2} & \cdots & l_{1,d_l} \\ l_{2,1} & l_{2,2} & \cdots & l_{2,d_l} \\ \vdots & \vdots & \ddots & \vdots \\ l_{n,1} & l_{n,2} & \cdots & l_{n,d_l} \end{bmatrix}, \quad (2.73)$$

containing measurements at n epochs from d_l different variables. Each L_k stands for observations with a shift in MA(k) model, and each $H_k(d_l \times d_s)$ represents the prediction matrix with respect to L_k , consisting of $H(k \times (d_l \times d_s))$. Hence, if PCR is implemented on this moving average regression, then (2.72) becomes

$$\begin{aligned}
S &= L \cdot H + e \\
&= L_1 H_1 + L_2 H_2 + \dots + L_k H_k + e \\
&= U_1 V_1^T H_1 + U_2 V_2^T H_2 + \dots + U_k V_k^T H_k + e \\
&= [U_1 \ U_2 \ \dots \ U_k] [V_1^T H_1 \ V_2^T H_2 \ \dots \ V_k^T H_k]^T + e \\
&= U \cdot K + e .
\end{aligned} \tag{2.74}$$

In (2.74), $K(k \times (r \times d_s))$ becomes the new prediction matrix substituting H , and $U(n \times (k \times r))$ expresses an ensemble of PCs from observations L . When L is allocated as in (2.72), the PCs $U_k(n \times r)$ are thus decomposed within each moving window, delivering the dominant variation of observations in each window.

Similarly, according to (2.63) and (2.64), when PLR is implemented with moving average window, the regression model is represented by

$$\begin{aligned}
S &= L \cdot H + e \\
&= L_1 H_1 + L_2 H_2 + \dots + L_k H_k + e \\
&= U_{L_1} V_{C_1}^T H_1 + U_{L_2} V_{C_2}^T H_2 + \dots + U_{L_k} V_{C_k}^T H_k + e \\
&= [U_{L_1} \ U_{L_2} \ \dots \ U_{L_k}] [V_{C_1}^T H_1 \ V_{C_2}^T H_2 \ \dots \ V_{C_k}^T H_k]^T + e \\
&= U \cdot K + e .
\end{aligned} \tag{2.75}$$

Comparing (2.75) with (2.63) and (2.64), the joint PCs $U_{L_k}(t \times r)$ are decomposed by SVD according to the cross-covariance between each L_k and S , written as $C_{L_k S} = L_k^T S = U_{C_k} \Sigma_{C_k} V_{C_k}^T$, and obtained by projection on each L_k , then $U_{L_k} = L_k U_{C_k}$. Hence, U here is grouped by U_{L_k} .

As a result, now referring to either LSP in (2.44), or PCR in (2.59), or PLR in (2.67), an adaptive moving average regression (MAR) is established, based on the formulation in (2.72), (2.74) and (2.75). In LSP, the spatial covariance matrix between prediction and observations is estimated over time. Combining with MAR, the association among epochs is revealed in the cross-covariance matrix along the moving window. The LSP approach can, therefore, reduce the effect of lagged errors from observations.

Applying PCR with MAR, we extract and retain not the dominant signals from observations, but the significant modes of observations within each moving average window. It takes the variation of modes over time into consideration. Different from PCR, PLR takes the advantages in maximizing the covariance among multiple variables. It eventually predicts the unknown signals by the most correlated part of signals from multiple observed signals, with the help of MAR over epochs.

The adaptive moving average regression integrated with LSP, PCR or PLR (i.e. MA-LSP, MA-PCR, MA-PLR) is consequently employed in the following chapter for hydro-geodetic modelling.

2.4.5 Comparison and summary

This section describes several different linear regression approaches and discusses their advantages and disadvantages. In Table 2.2, these methods are shortly summarized from four different aspects: form of model, observation, covariance matrix of observation, and cross-covariance matrix of observation and prediction.

Table 2.2: Summary of four different type of multivariate linear regression approaches. The essential required quantities for these regressions are briefly listed.

Method	Observation	Auto-covariance	Cross-covariance	Model description
LSP	L	C_{LL}	C_{LS}	$S = LH + e$
LSC	$L - AX$	C_{LL}	C_{LS}	$S = (L - AX)H + e$
PCR	LV_L	$V_L^T C_{LL} V_L$	$V_L^T C_{LS}$	$S = U_L V_L^T H + e$
PLR	LU_C	$U_C^T C_{LL} U_C$	$U_C^T C_{LS}$	$S = U_L U_C^T H + e$

As introduced before, three different cases are addressed in least-squares collocation (LSC). The general case consists of a mathematical model, the true signal, and noise. Two special cases are introduced: in the first the measurements are the sum of true signal and noise; in the second the noise free measurement only consists of signal. In this thesis, the noise in the regression is neglected to regress, and we only employ collocation with approximated model and without approximated model. LSC is an unbiased optimal estimation method, which minimizes the square errors. When the multicollinearity exists in the measurement, in which the variables are highly correlated, it probably results in imprecise predictions.

To reduce the data dimensions and the computational effort as well as to tackle ill-conditioning, we implement two more regression methods: principal component regression (PCR), and partial least-squares regression (PLR). These two methods inherit the advantages and properties of PCA and CCA, respectively. Compared with LSC, PCR optimizes the prediction by extracting the signals with maximum variance, while PLR finds the optimal estimate by searching for signals with maximum covariance.

Considering the lagged error problem, the adaptive moving average regression (MAR) is established. MAR is implemented via a moving average window on the measurements, which we combine with either LSC, PCR, or PLR. These adaptive MA-LSP, MA-PCR, MA-PLR methods benefit from the advantages of both LSC, PCR, PLR and MA model, simultaneously concerning both the spatial and temporal correlation between multiple measurements and predictions. In addition, the stability of predictions and sensitivity of anomalous observations is examined in hydro-geodetic applications and discussed in the following chapter.

Chapter 3

Modelling of Terrestrial Water Storage Change in the Water Cycle

Continental water storage is an essential part of the water cycle. Measurements of the global time-variable gravity field by GRACE allow us to determine the total water storage variation. However, the coarse spatial scales limit the application in small regions, and the limited temporal scales restrict us to investigate the water storage change within one month. Additionally, the limited lifetime of GRACE constrains the determination of large-scale water storage change out of the range of GRACE observing period. Therefore, the inadequate spatio-temporal observations by GRACE motivate us to determine terrestrial water storage in alternative ways.

Since more spaceborne geodetic sensors provide large-scale terrestrial observations, various studies have been done on modelling the hydrological variables by the geodetic observations using hydro-geodetic approach. Sneeuw et al. (2014) modeled the river runoff with the aid of the geodetic observations using hydro-geodetic approaches. Tourian et al. (2013) estimated the river discharge from spaceborne water level observations by a quantile function approach. Several studies (Pan and Wood, 2006; Lorenz et al., 2015) adopted the Kalman filter framework to estimate the catchment-scale water budget. GRACE products have also been used in hydrological modelling through assimilation (Eicker et al., 2014). Conversely, estimating the terrestrial water storage variation with the aid of hydrological observations is practically realistic and feasible.

In this chapter, we estimate the continental water storage change at catchment scale by modelling the relationship between water storage and other hydrological variables. Three different statistical approaches are implemented for water storage prediction: least-squares collocation, principal component regression, and partial least-squares regression. Considering that a time-invariant temporal shift exists between water storage and water cycle (Riegger and Tourian, 2014), an adaptive moving average model is consequently integrated with these regression algorithms.

Furthermore, a spatial downscaling of GRACE is attempted by assimilating multiple variables (i.e., precipitation, evapotranspiration, runoff) from a set of hydrological models with a highly resolved water storage change model, in order to achieve sufficient spatial resolution. This assimilation is accomplished by implementation of an adaptive moving average partial least-squares regression approach.

3.1 Spaceborne observation of terrestrial water storage

3.1.1 From geopotential to total water mass variation

The gravitational potential field V outside of the Earth's surface, due to its source-free and curl-free property, can be described in terms of spherical harmonic expansions (Heiskanen and Moritz, 1967) by

$$V(\lambda, \theta, r) = \frac{GM}{R} \sum_{l=0}^{\infty} \left(\frac{R}{r}\right)^{l+1} \sum_{m=0}^l \bar{P}_{lm}(\cos \theta) (\bar{C}_{lm} \cos m\lambda + \bar{S}_{lm} \sin m\lambda), \quad (3.1)$$

where λ, θ are the spherical coordinates, r is the spherical radius, R is the radius of the Earth, GM is the gravitational constant, $\bar{C}_{lm}, \bar{S}_{lm}$ denote the normalized dimensionless spherical harmonic coefficients of degree l and order m , expressing the gravitational potential field of the exterior Earth. \bar{P}_{lm} represents the normalized associated Legendre functions, with

$$\begin{aligned} \bar{P}_{lm}(\cos \theta) &= N_{lm} \cdot P_{lm}(\cos \theta), \\ N_{lm} &= \sqrt{(2 - \delta_{m,0})(2l + 1) \frac{(l - m)!}{(l + m)!}}, \end{aligned} \quad (3.2)$$

in which $\delta_{m,0}$ is called Kronecker delta that equals 1 if $m = 0$, and 0 otherwise.

As assumed by Wahr et al. (1998), the mass variations on the Earth's surface occur in a thin layer close to the surface. Under this assumption, the volume mass density σ is replaced by the surface mass density. Therefore, the surface mass density change, which relates to surface mass variation, can be parameterized in terms of spherical harmonics (Wahr et al., 1998) as

$$\Delta\sigma(\lambda, \theta) = R\rho_w \sum_{l=0}^{\infty} \sum_{m=0}^l \bar{P}_{lm}(\cos \theta) (\Delta\bar{C}_{lm}^{\sigma} \cos m\lambda + \Delta\bar{S}_{lm}^{\sigma} \sin m\lambda), \quad (3.3)$$

where ρ_w is the density of water, assuming that this thin layer on the surface consists of water. $\bar{C}_{lm}^{\sigma}, \bar{S}_{lm}^{\sigma}$ denote the normalized dimensionless spherical harmonic coefficients of the surface mass density. According to Farrell (1972) loading theory, the changes of the spherical harmonic coefficients of the surface density changes can be related to the spherical harmonic coefficients of the gravity potential changes. The relationship between them is thus expressed through the load Love numbers k'_l by

$$\begin{Bmatrix} \Delta\bar{C}_{lm}^{\sigma} \\ \Delta\bar{S}_{lm}^{\sigma} \end{Bmatrix} = \frac{\rho_e}{3\rho_w} \cdot \frac{2l + 1}{1 + k'_l} \begin{Bmatrix} \Delta\bar{C}_{lm} \\ \Delta\bar{S}_{lm} \end{Bmatrix}, \quad (3.4)$$

where ρ_e is the average density of the Earth. Combining (3.3) and (3.4), eventually we formulate the surface mass density change as

$$\Delta\sigma(\lambda, \theta) = \frac{R\rho_e}{3} \sum_{l=0}^{\infty} \frac{2l + 1}{1 + k'_l} \sum_{m=0}^l \sum_{m=0}^l \bar{P}_{lm}(\cos \theta) (\Delta\bar{C}_{lm} \cos m\lambda + \Delta\bar{S}_{lm} \sin m\lambda). \quad (3.5)$$

The spherical harmonic coefficients $\Delta\bar{C}_{lm}$, $\Delta\bar{S}_{lm}$ can be obtained from the monthly GRACE solutions, since GRACE is able to measure the temporal variation of the Earth's gravity field. In general, the surface density change $\Delta\sigma$ are converted into water height change

$$\Delta M = \frac{R\rho_e}{3} \sum_{l=0}^{L_{\max}} \frac{2l+1}{1+k'_l} \sum_{m=0}^l \bar{P}_{lm}(\cos\theta) (\Delta\bar{C}_{lm} \cos m\lambda + \Delta\bar{S}_{lm} \sin m\lambda), \quad (3.6)$$

where L_{\max} is the upper bound of degree l . ΔM is commonly denoted as equivalent water height (Wahr et al., 1998). Practically, the upper limit of degree l is defined by the maximum degree of the GRACE products. To avoid of confusion with residuals in the following content, we describe the water mass variation by M instead of ΔM in this thesis.

The GRACE observed time-variable gravity field of the Earth can be equivalently considered as the terrestrial water mass variation, which is calculated via equivalent water height in (3.6). In hydrology, the water mass variation is revealed by the total water storage change in the water cycle. Therefore, to keep consistency in this thesis, the term *total water storage change* (TWS) is used instead of equivalent water height change, representing for the water mass variation M .

Furthermore, the water storage fluxes dM/dt , which represents the water balance, are calculated as the first derivative of water storage change by

$$\frac{dM}{dt} = \frac{M(t + \Delta t) - M(t - \Delta t)}{2\Delta t}, \quad (3.7)$$

where Δt is the temporal intervals. In this thesis, we use the central difference as the differentiator in order to avoid the interpolation error.

3.1.2 Total water storage change from GRACE product

The GRACE level 2 products are provided by several different sources, e.g., Center for Space Research (CSR) at the University of Texas (Bettadpur, 2007), Jet Propulsion Laboratory (JPL), GeoForschungsZentrum (GFZ), ITSG 2018 from Graz University of Technology (Mayer-Gürr et al., 2018), using different data processing techniques and model corrections in order to eliminate the effects from atmosphere and ocean tides and to recover as much original signals from gravity field variation as possible. In addition, the GRACE Mass Concentration blocks (mascons) solutions based on level 1 products are available from CSR (Save et al., 2016), JPL (Watkins et al., 2015), and Goddard Space Flight Center (GSFC) (Luthcke et al., 2013). Different from the data produced by standard spherical harmonic approach, the mascons are essentially another representation of the gravity field, which is described by small blocks. In fact, it is beyond the scope of this thesis and not further discussed here. We use the GRACE products from GFZ release 05 in form of spherical harmonic coefficients for the following study.

Degree-1 term The origin of the reference frame used for GRACE solutions is defined in the Earth's center of mass (CM). The changes in degree-one terms are closely related to the relative motion of the CM to the center of the figure (CF) of the Earth's surface. In this frame, the

degree-one spherical harmonic coefficients are zero by definition. As a result, GRACE cannot sense the motion of the mass center of the Earth, only observing the time-variable gravity field. The changes in degree-one terms represent a considerable mass variation, which cannot be neglected (Chambers, 2006b). Hence, the omission of degree-one coefficients in GRACE data has to be corrected. In this thesis, the degree-one coefficients are replaced using the product from Swenson et al. (2008).

Degree-2 terms The degree-two terms are related to the large scale mass redistribution on the Earth's surface. The changes in the spherical harmonic coefficients of degree two and order zero, $\Delta C_{2,0}$, reflect the flattening of the Earth, which is known as ΔJ_2 ($\Delta J_2 = -\sqrt{5}\Delta C_{2,0}$). Considering that degree-two terms are not accurately observed by GRACE, the optimal degree-two coefficients are obtained from the analysis of satellite laser ranging (SLR) observations (Cheng et al., 2011). Moreover, the degree-two terms in the GRACE product from GFZ are already replaced (Dahle et al., 2012).

Filtering Since the GRACE measurements are evidently affected by noise, filtering is required to reduce these effects and enhance the true physical signals when processing GRACE data. Several different filtering approaches (e.g. Gaussian filter, Han filter, destriping filter, DDK filter, etc.) are consequently proposed. Generally for GRACE data, the filter is applied in the spectral domain, and the filtered ΔM^f is then formulated as

$$\Delta M^f = \frac{R\rho_e}{3} \sum_{l=0}^{L_{\max}} \frac{2l+1}{1+k_l'} \sum_{m=0}^l \bar{P}_{lm}(\cos\theta) (W_{lm}\Delta\bar{C}_{lm} \cos m\lambda + W_{lm}\Delta\bar{S}_{lm} \sin m\lambda), \quad (3.8)$$

where W expresses the kernel of the filter in the spectral domain. Various filter operators are proposed and discussed in many researches, which commonly are consisted of two classes: deterministic filters and stochastic filters. A detailed description of different filter schemes is summarized by Devaraju (2015) for GRACE data filtering.

The Gaussian smoothing function W^G , as a deterministic filter, is formulated by Jekeli (1981) in the spatial domain,

$$W^G = e^{-r(1-\cos\alpha)}, \quad r > 0, \quad (3.9)$$

where α is the spherical distance on the sphere, and r is the averaging radius. The Gaussian smoothing function was subsequently developed by Wahr et al. (1998) in the spectral domain, formulated recursively

$$\begin{aligned} W_0^G &= \frac{1}{2\pi}, \\ W_1^G &= \frac{1}{2\pi} \left[\frac{1+e^{-2b}}{1-e^{-2b}} - \frac{1}{b} \right], \\ W_{l+1}^G &= -\frac{2l+1}{b} \cdot W_l + W_{l-1}, \\ \text{with } b &= \frac{\ln(2)}{1-\cos(r/R)}. \end{aligned} \quad (3.10)$$

Obviously, the Gaussian smoothing kernel W_l^G performs isotropically only along degree l in spectrum. Due to this property, W_l^G is classified as isotropic filter for GRACE. Unlike degree-dependent W_l^G , an anisotropic Gaussian filter was developed by Han et al. (2005), in order to perform smoothing on both degree and order. The weighting structure of the smoothing kernel is directional variant, performing both degree and order dependent in the spectral domain.

In fact, the GRACE observations are strongly affected by the correlated errors, which normally show up as north-south stripes over the unsmoothed TWS spatial patterns. A destriping filter, proposed by Swenson and Wahr (2006), aims to eliminate the spatially correlated errors.

$$W_{lm}^D = \sum_{i=0}^p \sum_{j=0}^p L_{ij}^{-1} n^i l^j, \quad (3.11)$$

with $L_{ij} = \sum_{n=l-\frac{w}{2}}^{l+\frac{w}{2}} n^i n^j, \quad n : \text{even or odd},$

where n denotes the degree that includes only the same parity as degree l . This destriping leads to the smoothed coefficients C_{lm}^D as

$$C_{lm}^D = \sum_{n=l-\frac{w}{2}}^{l+\frac{w}{2}} W_{lm}^D C_{nm}, \quad n : \text{even or odd}. \quad (3.12)$$

Swenson and Wahr (2006) found that there is no apparent correlations between even and odd coefficients. However, the correlated behavior appears at approximately $m = 8$ and also at higher orders. In this case, the spherical harmonic coefficients are smoothed for a particular order m with a quadratic polynomial in a moving window centered about degree l , where p is the order of the polynomial, w is the width of the smoothing window. The implementation of the destriping algorithms is explained by Devaraju (2015) in detail.

Moreover, various stochastic filters, e.g. Wiener filter (Sasgen et al., 2006), DDK filter (Kusche, 2007; Kusche et al., 2009), regularization filter (Lorenz, 2009), an anisotropic, non-symmetric filter developed by Klees et al. (2008), are designed to filter the observed field from GRACE based on a prior information. In addition, the EOF approach is also employed as a smoothing tool at the level of GRACE monthly solutions (Rangelova et al., 2007; Schrama et al., 2007).

In this thesis, since a thorough evaluation of different filters on GRACE is not essential for the objective of our research, the performance of filters in GRACE data processing is not further discussed. To make our results comparable with the work done by others, we simply apply a destriping filter to minimize the effect of correlated errors, and an isotropic Gaussian smoothing with radius of 350 km to the GRACE data. The procedure of calculating the TWS from GRACE coefficients are explained in detail in Appendix A.

Spatial and temporal resolution Although filtering on GRACE observations reduces the effects of noise and subsequently produces more accurate signals, it simultaneously causes signal leakage and also leads to lower spatial resolution (Devaraju and Sneeuw, 2016). For example, the filter with radius of 350 km applied in this study limits the spatial resolution to the level of ca. 400 km. Comparing with the observations from other variables, like precipitation,

evapotranspiration, river runoff, usually with 0.5° resolution, this level of resolution is not adequate for hydrological applications, particularly for regional studies on small basins.

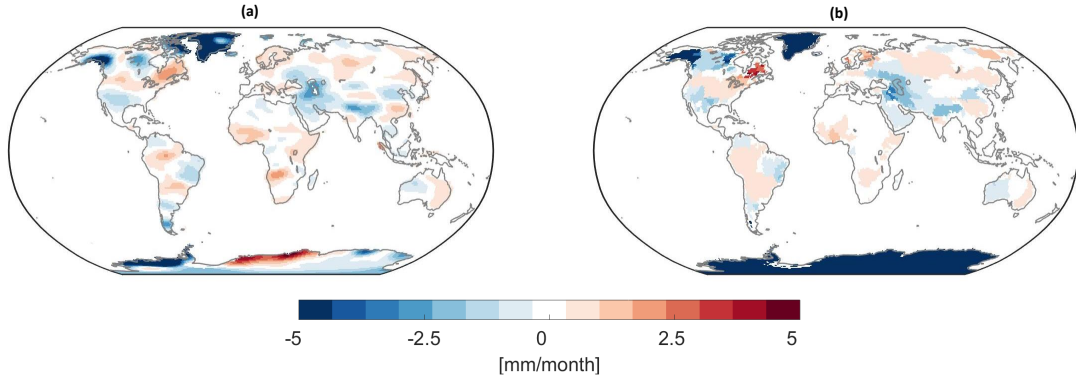


Figure 3.1: Map of the linear trend of global total water storage change (a) on a grid and (b) at catchment scale.

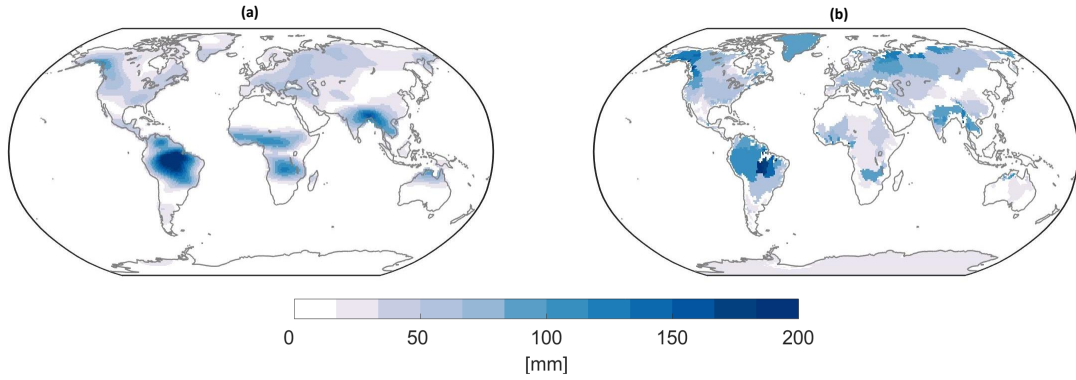


Figure 3.2: Map of the annual amplitude of global total water storage change (a) on a grid and (b) at catchment scale.

Many studies focus on the correction methods for repairing the signal damage due to filtering (Klees et al., 2007; Longuevergne et al., 2010; Landerer and Swenson, 2012; Vishwakarma et al., 2018). However, repairing the GRACE products, which is not within the scope of this thesis, is not further discussed. Downscaling GRACE is an optional solution to acquire sufficient spatial resolution, using statistical approaches.

As our current study is mainly about modelling the total water storage by multiple hydrological variables, we aggregate the observations from grid cells into catchments in order to reduce the error level. The water storage change in each grid cell is aggregated over the catchment via

$$M_{\text{basin}} = \frac{\sum_{i=1}^N M_{\text{grid}}(\lambda_i, \theta_i) \cdot A_i}{A_{\text{basin}}}, \quad (3.13)$$

where λ_i, θ_i express the longitude and latitude of the cell i , A_i is the area of the cell i within the catchment, A_{basin} is the total area of the catchment, N is the number of cells located in the catchment. Thus, we obtain the aggregate of total water storage change over the catchment

M_{basin} by doing a spatial averaging on the M_{grid} of each cell. Figure 3.1 and 3.2 show the linear trend and annual amplitude of total water storage change grids over the globe and aggregates over the catchments.

In Figure 3.1, the catchment-scale linear trends are smoothed in the catchments which are relatively stationary, and enhanced in the catchments which have evident mass gain or loss comparing with the linear trend from TWS in grids. The annual amplitude of TWS at catchment scale shown in Figure 3.2 reveals comparatively consistency with gridded products, especially for those large-scale catchments. Therefore, the spatial resolution is adequate for applications at catchment scale, especially for those catchments with an area larger than 200 000 km². For investigating the impact of climate change on continental water storage changes at large scale, the current spatial resolution (ca. 400 km) is sufficient for comprehensive analysis. Moreover, to achieve finer spatial resolution, a spatial downscaling of GRACE is attempted in this chapter, using an empirical statistical approach.

Temporal resolution of GRACE products is one month due to its monthly solutions. In hydrology, data with sub-monthly, weekly, daily sampling are commonly available. Considering that the water cycle is a dynamic process, coarse temporal sampling in GRACE products could lead to inconsistency when modeling the total water storage by hydrological observed time series.

To acquire densified temporal sampling of GRACE, some researchers estimate the daily solutions from monthly GRACE products using Kalman filter approach (Kurtenbach et al., 2009, 2012). With the aid of hydrological observations with higher sampling rates, in this thesis, we explore another way to obtain the terrestrial water storage variation with better temporal resolutions. Therefore, based on the relationships gained from statistical modelling, the water storage variation is estimated by multiple variables, for instance, precipitation, evapotranspiration, runoff. In addition, for long-term analysis, monthly observations from GRACE are sufficient and commonly used in hydrological applications.

3.2 Modelling terrestrial water mass change by hydrological variables

Datasets In this chapter, we use the monthly observation based precipitation datasets, calculated from global station data, from the Global Precipitation Climatology Center (GPCC) with 0.5° spatial resolution (Meyer-Christoffer et al., 2015), and the monthly precipitation datasets that combine observations and satellite data, from the Global Precipitation Climatology Project (GPCP) with 2.5° spatial resolution (Adler et al., 2003).

The Tropical Rainfall Measuring Mission (TRMM) by NASA and JAXA provides precipitation products based on the measurement of rainfall from multiple satellites (Huffman et al., 2007, 2010). We use the precipitation dataset from TRMM with monthly temporal resolution and 0.5° spatial resolution.

Table 3.1: Data sets used in water mass variation modelling.

Variable	Data source	Spatial resolution	Temporal resolution
P	GPCC 2.3	$0.5^\circ \times 0.5^\circ$	monthly
	GPCP V7	$2.5^\circ \times 2.5^\circ$	monthly
	ECMWF ERA-Interim	$0.5^\circ \times 0.5^\circ$	daily
	PERSIANN-CDR	$0.5^\circ \times 0.5^\circ$	monthly
	TRMM 3B43	$0.5^\circ \times 0.5^\circ$	monthly
ET	ECMWF ERA-Interim	$0.5^\circ \times 0.5^\circ$	daily
	GLEAM v3.1	$0.5^\circ \times 0.5^\circ$	monthly
R	GLDAS CLM10	$1^\circ \times 1^\circ$	monthly
	GLDAS MOS10	$1^\circ \times 1^\circ$	monthly
	GLDAS NOAH025 2.0	$0.25^\circ \times 0.25^\circ$	monthly
ΔM	GRACE RL05 GFZ	$1^\circ \times 1^\circ$	monthly

In addition, we use a 0.5° daily precipitation dataset from the Precipitation Estimation from Remotely Sensed Information using Artificial Neural Networks-Climate Data Record (PERSIANN-CDR) model (Ashouri et al., 2015), which estimates precipitation using the PERSIANN algorithm on satellite data and combining many different precipitation data sources.

The atmospheric reanalysis ERA-Interim from the European Center for Medium-Range Weather Forecasts (ECMWF) is used to derive daily fields of total precipitation and evaporation (Dee et al., 2011). These data sets are produced with 0.5° spatial resolution.

The evapotranspiration dataset, which is obtained from the Global Land-surface Evaporation: the Amsterdam Methodology (GLEAM) based on multi-satellite observations (Miralles et al., 2011; Martens et al., 2017), is used as well in the study.

The Global Land Data Assimilation Systems (GLDAS) was developed by NASA and the National Oceanic and Atmospheric Administration National Centers for Environmental Prediction (NCEP). It provides a global, high-resolution, optimal simulation of global land surface states, representing the energy and terrestrial water fluxes for climate, weather, and water resources study (Rodell et al., 2004). Currently, the GLDAS has four different land surface models (LSMs), including the Mosaic model (Koster and Suarez, 1996), the Noah model (Chen et al., 1996; Koren et al., 1999), the Common Land Model (CLM) (Dai et al., 2003), and the Variable Infiltration Capacity (VIC) model (Liang et al., 1996). These four models in GLDAS define different number of soil layers and different corresponding soil depths. In this thesis, three different runoff datasets are used from the GLDAS, namely the 1° monthly data from GLDAS CLM Model, the 1° monthly data from GLDAS Mosaic Model, and 0.25° monthly data from GLDAS NOAH LSM L4 (Rodell et al., 2004).

We choose the time period of the datasets listed above in Table 3.1 ranging from 2003 to 2016, in order to stay in accordance with the data from GRACE products.

Furthermore, to be consistent with total water storage change time series from GRACE, the temporal resolution is averaged from daily to monthly. We choose 26 catchments as case study, which are distributed globally as shown in Figure 3.3. In order to estimate the water mass

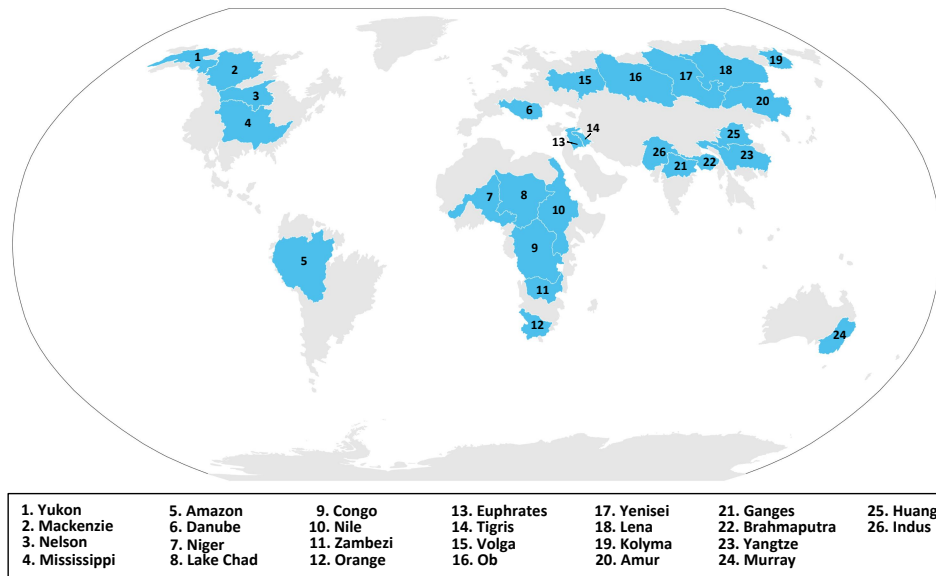


Figure 3.3: Map of 26 catchments distributed globally.

variation at catchment scale, the GRACE grids are then aggregated within each catchment using (3.13). Similarly, the other hydrological variables, such as precipitation, evapotranspiration and runoff, are also aggregated over catchment in the same way as the aggregation of water storage.

3.2.1 Performance metrics for model evaluation

To validate the estimated total water storage changes, numerous performance metrics to evaluate the time series exists (Moriasi et al., 2007). In this chapter, several important metrics, i.e., correlation coefficients, root mean square error, the Nash-Sutcliffe efficiency, and relative bias are introduced and adopted here for validating the predictions from the regression models.

Correlation coefficient (R) It describes a statistical relationship between two time series. The correlation coefficient, which ranges from -1 to 1 , indicates the similarity of them. It writes

$$R = \frac{\sum_{i=1}^n (x_i - \bar{x})(y_i - \bar{y})}{\sqrt{\sum_{i=1}^n (x_i - \bar{x})^2 \sum_{i=1}^n (y_i - \bar{y})^2}}. \quad (3.14)$$

In (3.14), x_i is observation, and y_i is prediction time series to be evaluated, \bar{x} , \bar{y} represent for the mean of observation and prediction time series, respectively. The values $R = 1$ or $R = -1$ reflect a perfect positive or negative linear relationship, while $R = 0$ indicates that no linear relationship exists. Although it is commonly used for data evaluation, the correlation coefficient is extremely sensitive to the phase shifts, but insensitive to the differences in amplitude or bias. According to this characteristic, only using the correlation coefficient is not adequate for validation of model predictions.

Relative bias (PBIAS) Since correlation coefficient is insensitive to bias, we introduce a statistical indicator that is describing the relative bias. Since it was introduced as *percent bias*, thus, we name it PBIAS in this thesis (Gupta et al., 1999):

$$\text{PBIAS} = \frac{\sum_{i=1}^n (x_i - y_i)}{\sum_{i=1}^n x_i} = 1 - \frac{\bar{y}}{\bar{x}}. \quad (3.15)$$

PBIAS is dimensionless, and calculated as a relative difference, normalized by observations. PBIAS measures the relative bias of prediction against observation. It indicates an optimal prediction when the value of PBIAS becomes 0. Positive and negative values indicate model underestimation bias and overestimation bias, respectively. The deviation from 0 reflects the relative bias, which is represented as a percentage. From PBIAS, we can simply know whether the predictand is optimally estimated by the model in view of bias.

Root mean square error (RMSE) As one of the widely used error indices, RMSE measures directly the accuracy of the estimation, which is compared with the reference time series. It is defined as

$$\text{RMSE} = \sqrt{\frac{\sum_{i=1}^n (x_i - y_i)^2}{n}}. \quad (3.16)$$

As a second-order statistic, RMSE is a non-negative value to quantify the average deviation from the observations. In general, it reflects an optimal fit when RMSE is close to 0. Different from PBIAS, RMSE is sensitive to the difference in amplitude. Hence, we use it to evaluate the level of the differences between observations and model estimates.

Nash-Sutcliffe efficiency (NSE) We introduce NSE here because of its common use to evaluate the model performance against observation (Nash and Sutcliffe, 1970) in hydrology. The NSE is a dimensionless statistic that quantifies the relative magnitude of mean square error compared to the variance, since

$$\text{NSE} = 1 - \frac{\sum_{i=1}^n (x_i - y_i)^2}{\sum_{i=1}^n (x_i - \bar{x})^2}. \quad (3.17)$$

NSE ranges from $-\infty$ to 1, where $\text{NSE} = 1$ indicates a perfect prediction. A value of NSE between 0 and 1 ($0 < \text{NSE} < 1$) reflects a prediction that is better than simply taking the average \bar{x} , which is considered generally as acceptable levels in our study. The value of NSE below 0 indicates a prediction worse than the mean observation, which is unacceptable.

Different from correlation coefficient, NSE is highly sensitive to the similarity both in phase and also in amplitude and bias. Therefore, we adopt NSE as an important statistic to evaluate our prediction results from each approach.

Cyclostationary Nash-Sutcliffe efficiency (CNSE) According to the seasonality behaviour of hydrological time series, in this study, we adopt an alternative formulation of NSE,

called cyclostationary NSE (CNSE). It compares the prediction with the cyclo-stationary mean of observation instead of the mean as

$$\text{CNSE} = 1 - \frac{\sum_{i=1}^n (x_i - y_i)^2}{\sum_{i=1}^n (x_i - \bar{x})^2}, \quad (3.18)$$

where \bar{x} is not the long-term mean of observation x , but represents the mean annual behavior, i.e. climatology. Similar to the regular NSE, CNSE reflects a perfect prediction when its value equals to 1. If the value of CNSE is between 0 and 1, it indicates a prediction better than the historic cyclostationary mean of the time series, which is acceptable. If $\text{CNSE} < 0$, it indicates that the prediction performs worse than the climatology in the observations, i.e. it does not successfully capture the significant non-seasonal variability in the observations. In geodetic-hydrological applications, therefore, CNSE is as important as NSE and even more meaningful than NSE, because $\text{NSE} > 0$ is easily achieved. Due to the strongly seasonal variability in terrestrial water storage variation, we evaluate the performance as good predictions when $\text{CNSE} > 0$ in the following content.

Cyclostationarity index (CI) To evaluate the seasonal variability in a single time series, we define a statistical indicator CI as

$$\text{CI} = 1 - \frac{\sum_{i=1}^n (x_i - \bar{x})^2}{\sum_{i=1}^n (x_i - \bar{x})^2}. \quad (3.19)$$

CI is a dimensionless measure of non-seasonal variability relative to seasonal variability. A value of $\text{CI} = 1$ indicates perfect cyclo-stationarity, whereas $\text{CI} \approx 0$ indicates that non-seasonal behaviour dominates. Hence, we use CI as an important indicator to evaluate the seasonality in the terrestrial water storage observations from GRACE.

3.2.2 Characterization of terrestrial water storage variation

Relationships of water storage-water cycle To characterize the time series of terrestrial water storage variation, we investigate the linear relationship between water storage change and hydrological variables, i.e., precipitation, evapotranspiration and runoff. A linear relationship exists between total water storage change (M or TWS) and precipitation (P), evapotranspiration (ET), river runoff (R), since the terrestrial water balance can be mathematically described by

$$\frac{dM}{dt} = P - ET - R. \quad (3.20)$$

Theoretically, estimating the total water storage changes via a linear regression model by other variables (i.e., P, ET, R) in the water cycle is therefore feasible based on (3.20).

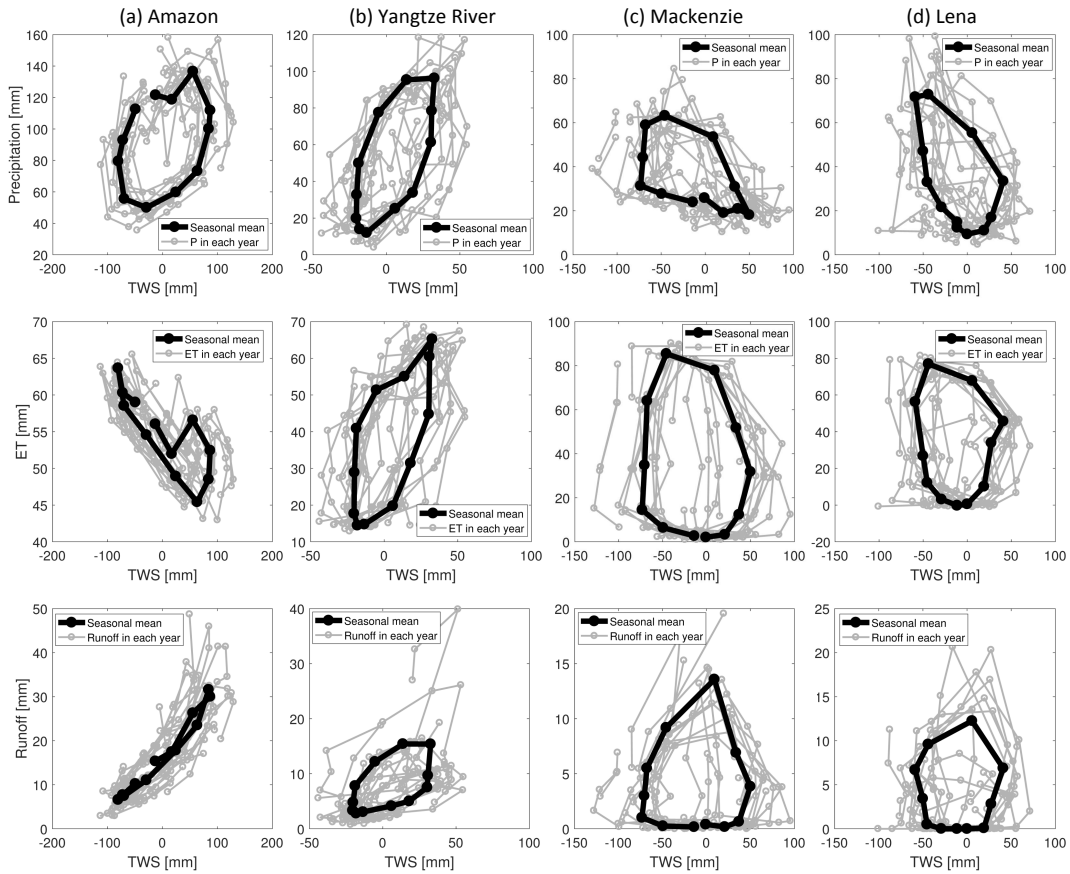


Figure 3.4: Relationships between TWS and P , ET , R , respectively for catchment (a) Amazon (tropical), (b) Yangtze River (temperate), (c) Mackenzie (boreal), and (d) Lena (boreal).

We investigate the relationships between ΔM and P , ET , R , respectively at catchment scale. These relationships are visualized in Figure 3.4. Considering the different climatic conditions, we choose four catchments as examples, in which Amazon represents basins in the tropical zone, Yangtze represents for basins in the temperate zone, while Mackenzie and Lena act on behalf of basins in the polar region influenced by arctic climate. We plot the mean annual cycle together with observations for each year as a sequence. Figure 3.4 illustrates a distinct periodic behaviour for each catchment.

In the Amazon, Figure 3.4 clearly shows linear performance except for P -TWS in the scatter plot. However, in temperate and polar regions (i.e. Yangtze, Mackenzie, Lena), ET , R and TWS are periodical, which is different from the behaviour in tropical basins (e.g. Amazon). By direct comparisons of water storage and other hydrological variables (i.e. P , ET , R), they mainly show up these periodic performance with hysteresis, indicating a non-linear relationships. Thus, the river basins are characterized as non-linear dynamic system (Kirchner, 2009; Teuling et al., 2010). However, Riegger and Tourian (2014) interpret this non-linear, periodic behaviours with a hysteresis for catchments as a linear time-invariant (LTI) system, in which a time-invariant temporal delay exists. In other words, the non-linearity between ET , R and TWS in Yangtze is thus explained by asynchronous variation in the water cycle. Thus, from Figure 3.4 (a), we

can infer that the non-linearity between P and TWS in Amazon refers to a hysteresis in this dynamical water system.

However, under dry and cold climatic conditions, the non-collinearity in boreal catchments (i.e., Mackenzie, Lena) cannot be simply explained by a time invariant or time-dependent delay between ET , R and liquid TWS change. This non-linear behavior is assigned to solid storage components like snow/ice, for which the terrestrial mass variations do not lead to changes in water balance (Riegger and Tourian, 2014). Therefore, in the boreal catchments, except for the time-invariant temporal delay, the solid/liquid components of water storage also result in the non-linear behaviour.

In a word, for tropical and boreal catchments, the time invariant time lag exists in the M - P , ET , R relationships. The liquid water mass change are P , ET , R are treated as a LTI system. In practice, this time shift has to be taken into consideration when we do regression on multiple hydrological variables.

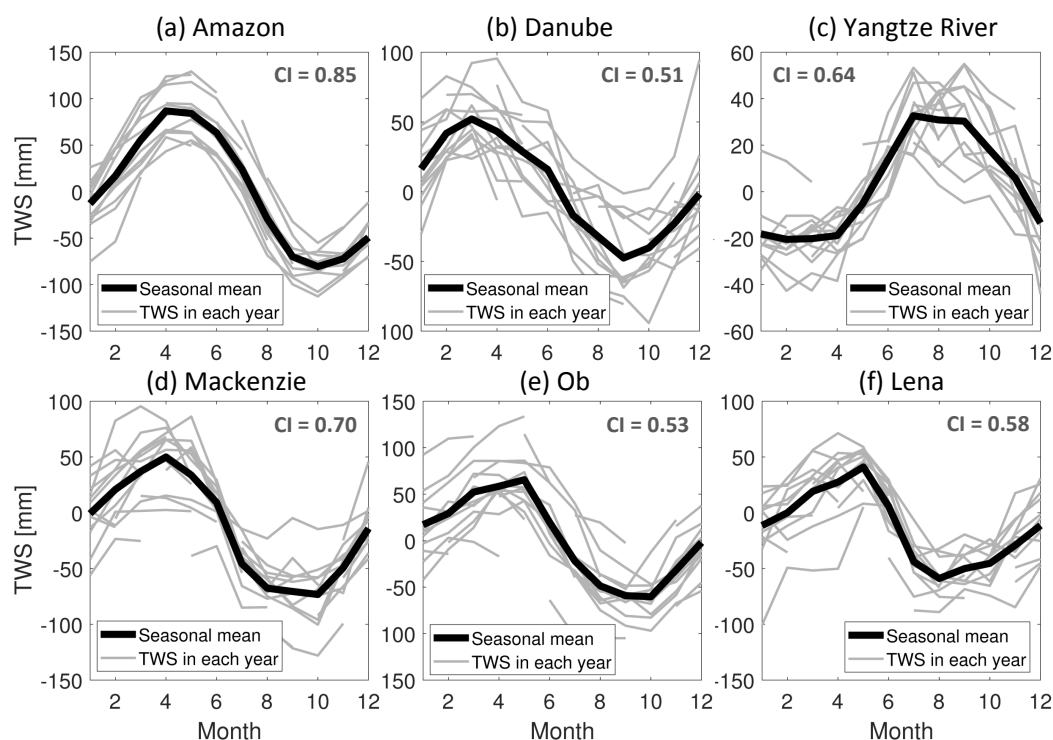


Figure 3.5: Seasonal mean of TWS and its CI index in catchment (a) Amazon, (b) Danube, (c) Yangtze River, (d) Mackenzie, (e) Ob, and (f) Lena.

Seasonality of total water storage Generally, the cyclostationarity of the observed time series is a significant characteristic in hydrology. Non-stationarity of a time series appears generally as time-dependent trend, time-variant frequency, or inconstant amplitude. Practically, the training is based on the a prior data. Non-stationarity in the training phase induces uncertainty of the model prediction. Meanwhile, the model prediction is difficult to capture the

anomalous variation if non-stationary signal exists in the prediction phase. Therefore, an observation time series that behaves as cyclo-stationary signal probably leads to poor predictions. Hence, before we implement regression on the water storage time series, the seasonal variability in the observations of water storage change is also necessary to be evaluated.

In Figure 3.5, total water storage changes in each year are plotted with their cyclo-stationary mean (i.e. seasonal mean in hydrological variables), which is calculated as the mean annual cycle of the signal. Six catchments, i.e., Amazon (tropical), Danube, Yangtze (mid-latitudes), Mackenzie, Ob, Lena (high-latitudes), are selected as examples. The cyclo-stationary mean represents the seasonal behavior in observations. The CI values indicate the cyclo-stationarity of water storage in catchments. Amazon shows a very stable seasonality with $CI > 0.8$, while TWS in Danube, Ob and Lena ($CI < 0.6$) are weakly stationary in each year.

Accordingly, for those seasonal stationary basins, the mean annual cycle retains nearly the whole of observation information, representing distinct seasonal behaviors. Therefore, the mean annual cycle can be simply adopted as the prediction. On the contrary, a low cyclo-stationarity indicates that the water cycle in these basins displays more non-seasonal behaviours. This leads to a challenge for prediction.

3.2.3 Estimation by least squares collocation

Least-squares collocation with model parameters Firstly, we assume that we have the observed time series of total water storage M , and the river runoff R , which are arranged in matrix as

$$M = \begin{bmatrix} M_{1,1} & M_{1,2} & \cdots & M_{1,s} \\ M_{2,1} & M_{2,2} & \cdots & M_{2,s} \\ \vdots & \vdots & \ddots & \vdots \\ M_{n,1} & M_{n,2} & \cdots & M_{n,s} \end{bmatrix}, \quad R = \begin{bmatrix} R_{1,1} & R_{1,2} & \cdots & R_{1,l} \\ R_{2,1} & R_{2,2} & \cdots & R_{2,l} \\ \vdots & \vdots & \ddots & \vdots \\ R_{n,1} & R_{n,2} & \cdots & R_{n,l} \end{bmatrix}. \quad (3.21)$$

In (3.21), each column of M and R is a single time series with n time epochs. M contains s number of time series, and R has l number of time series. Thus, M and R has the same length of observing period but different number of time series.

If we predict the total water storage change M for p more epochs, for example, by river runoff $R_{\text{obs}}(p \times l)$ using the least-squares collocation (LSC) approach, we have to estimate the prediction matrix, training on a prior datasets $M(n \times s)$ and $R(n \times l)$. Following (2.52) and (2.53), we have

$$\begin{cases} R = A X_R + M B, \\ \hat{X}_R = (A^T C_{RR}^{-1} A)^{-1} A^T C_{RR}^{-1} R, \\ M = (R - A X_R) H, \\ \hat{H} = C_{RR}^{-1} C_{RM}, \end{cases} \quad (3.22)$$

where $A(n \times m)$ is the design matrix for modelling the observation R , $B(s \times l)$ is the prediction matrix for predicting M , estimated based on training, $X_R(m \times l)$ contains m unknown parameters to estimate for each time series.

Applying such a least-squares collocation on R and M , we model the runoff signal itself R , and at the same time predict the target signal M . According to (3.22), the M can be seen as the predictand of $R - AX_R$, that satisfies $\hat{M} = (R - AX_R)H$. Since the model $R - AX_R$ produces the residuals, the predictand M is estimated on the residual level. Thus, we use the TWS residuals ΔM instead of M for training of the cross-covariance matrix C_{RM} . The TWS residual ΔM is calculated by subtracting the cyclo-stationary mean \tilde{M} from the full signal M ,

$$\Delta M = M - \tilde{M}. \quad (3.23)$$

Hence, by training, we gain the estimated parameter matrix $\hat{X}_R(m \times l)$, and the estimated prediction matrix $\hat{H}(l \times n)$ instead of B . As a consequence, the predicted ΔM_{pre} is calculated via

$$\Delta M_{\text{pre}} = \Delta \hat{M} = (R_{\text{obs}} - A\hat{X}_R)\hat{H} = (R_{\text{obs}} - A\hat{X}_R)C_{RR}^{-1}C_{RM}. \quad (3.24)$$

Still, we need to add the removed seasonal mean \tilde{M} back to the model prediction $\Delta \hat{M}$ as

$$M_{\text{pre}} = \Delta \hat{M} + \tilde{M}. \quad (3.25)$$

Considering the strong seasonal behaviour in runoff time series, we employ a harmonic model for R to model the annual and semi-annual components,

$$\begin{aligned} R &= a_1 \cdot \sin\omega_1 t + b_1 \cdot \cos\omega_1 t + a_2 \cdot \sin\omega_2 t + b_2 \cdot \cos\omega_2 t \\ &= [\sin\omega_1 t \quad \cos\omega_1 t \quad \sin\omega_2 t \quad \cos\omega_2 t] [a_1 \ b_1 \ a_2 \ b_2]^T \\ &= A \cdot X_R, \end{aligned} \quad (3.26)$$

where $X_R = [a_1 \ b_1 \ a_2 \ b_2]^T$ are the parameters to be estimated in (3.22), ω_1, ω_2 represent for the frequencies of annual and semi-annual components in observations. The design matrix A is constructed as $A = [\sin\omega_1 t \quad \cos\omega_1 t \quad \sin\omega_2 t \quad \cos\omega_2 t]$ and involved as input in (3.22). Similarly, the precipitation P and evapotranspiration ET are also modeled as defined in (3.26).

The procedure of this LSC on predicting total water storage M by runoff R is summarized in the flowchart shown in Figure 3.6.

The same procedure is applied also for precipitation P and evapotranspiration ET . Therefore, an integrated prediction of M by multiple variables P, ET, R can be expressed by

$$\begin{aligned} L &= A X + \Delta M B, \\ \hat{X} &= (A^T C_{LL}^{-1} A)^{-1} A^T C_{LL}^{-1} L, \\ \hat{H} &= C_{LL}^{-1} C_{LM}, \\ \Delta \hat{M} &= (L_{\text{obs}} - A\hat{X})\hat{H}, \end{aligned} \quad (3.27)$$

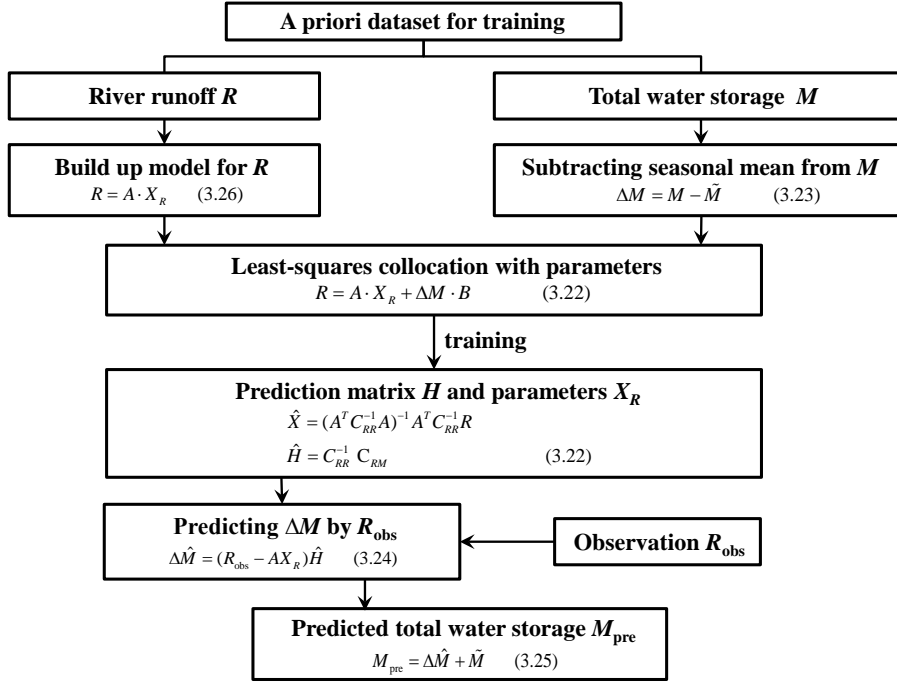


Figure 3.6: Flowchart of predicting total water storage by river runoff using least-squares collocation with parameters.

where $L = [P \ ET \ R]$ is as a prior joint dataset for training parameters X and prediction matrix H , $L_{\text{obs}} = [P_{\text{obs}} \ ET_{\text{obs}} \ R_{\text{obs}}]$ is as joint observation matrix for prediction. Accordingly, $X = [X_P \ X_{ET} \ X_R]$ contains model parameters for P, ET, R .

Briefly, in this collocation model, the model parameters of hydrological variables P, ET, R are estimated by least-squares adjustment, and simultaneously the total water storage residuals ΔM are predicted by least-squares prediction, based on the adjusted residuals from P, ET, R observations.

In our application, we implement LSC to predict ΔM in 26 catchments, which are distributed globally. The training period is from 2003 to 2010, and the prediction period is from 2011 to 2016. Results are shown in Figure 3.7 for the four catchments (Amazon, Yangtze, Mackenzie, Lena). In Figure 3.7, the combined prediction from P, ET and R is more stable than the prediction by P, ET, R individually. However, the prediction errors are still significant, especially for Lena and Mackenzie. Distinct discrepancies between predicted TWS and observed TWS from GRACE indicate insufficient prediction accuracy. The performance of least-squares collocation on TWS prediction in four catchments is quantitatively summarized in Table 3.2. Negative NSE and CNSE values reveals the unsatisfactory performance of the least-squares collocation, despite the high correlation between predictions and observation from GRACE. In short, the TWS is not well modeled by this least-squares collocation with parameters approach.

Least-squares prediction To model the observations in a non-parametric way, we refer to the seasonal mean, due to the seasonality of hydrological observations. Therefore, we derive

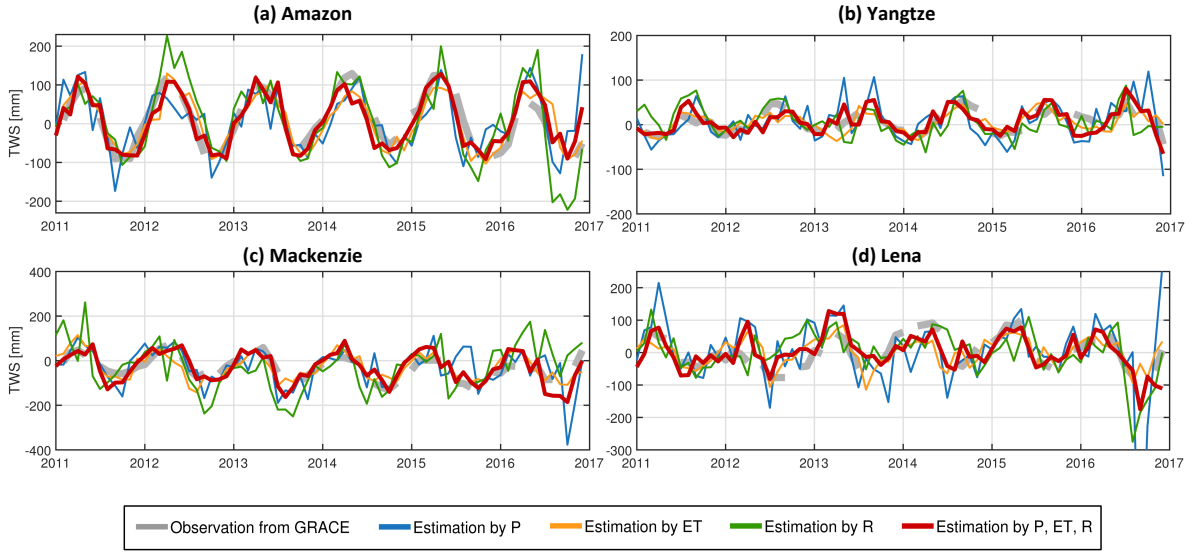


Figure 3.7: Estimations of total water storage change for (a) Amazon, (b) Yangtze, (c) Mackenzie, (d) Lena, respectively, by Least-Squares Collocation on a linear-fit model of observations using precipitation, evapotranspiration and runoff.

the residuals from observation time series by removing the cyclo-stationary mean instead of a harmonic modelling in (3.26). Thus, we have

$$\Delta R = R - \tilde{R}. \quad (3.28)$$

Different from (3.22), in the least-squares prediction (LSP), now the observation variable R is directly associated with the predictand M , getting rid of a mathematical model. Referring to (2.40), the ΔM is predicted by ΔR in form of

$$\Delta M = \Delta R \cdot H, \quad (3.29)$$

in which H the prediction matrix to estimated. As a consequence, the prediction matrix H is obtained via

$$\hat{H} = C_{RR}^{-1} C_{RM}. \quad (3.30)$$

In (3.30), both the covariance matrix C_{RR} and cross-covariance matrix C_{RM} are calculated based on the residuals ΔR and ΔM . Therefore, the predicted TWS M_{pre} is eventually obtained by

$$\begin{aligned} \Delta \hat{M} &= \Delta R_{\text{obs}} \cdot \hat{H} = \Delta R_{\text{obs}} C_{RR}^{-1} C_{RM}, \\ M_{\text{pre}} &= \Delta \hat{M} + \tilde{M}. \end{aligned} \quad (3.31)$$

We summarize the LSP on predicting total water storage M by a flowchart in Figure 3.8. Comparing with Figure 3.6, the LSP simplifies the prediction procedure in the training session.

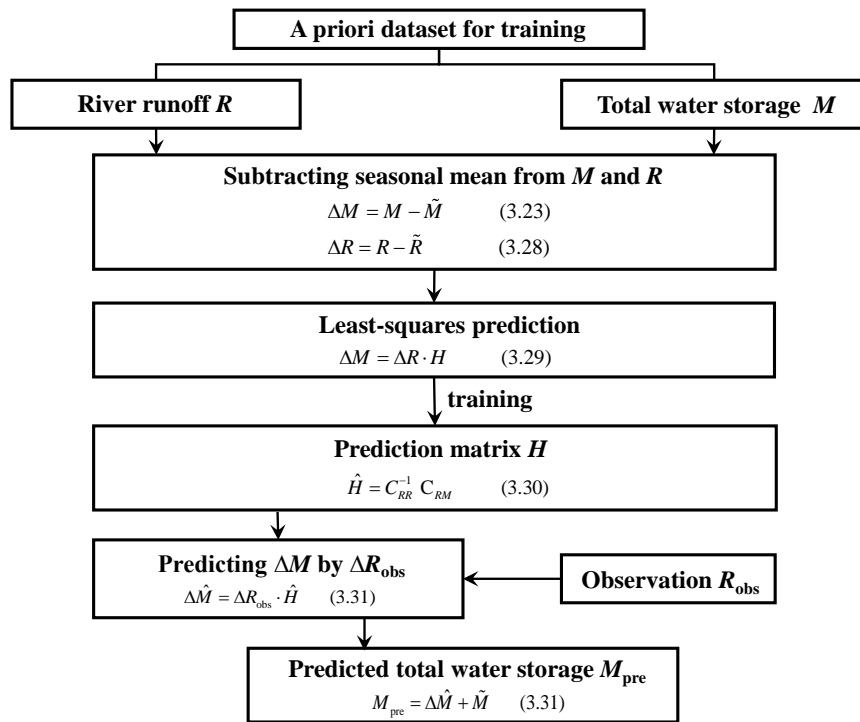


Figure 3.8: Flowchart of predicting total water storage by river runoff using least-squares prediction.

Similarly, we apply the same procedure as well for precipitation P and evapotranspiration ET . To combine all the variables in the regression model, we expand the training dataset from R to $L = [\Delta P \ \Delta ET \ \Delta R]$, and observation dataset from R_{obs} to $L_{\text{obs}} = [\Delta P_{\text{obs}} \ \Delta ET_{\text{obs}} \ \Delta R_{\text{obs}}]$, subsequently the (3.27) becomes

$$\begin{aligned} \Delta M &= L \cdot H, \\ \hat{H} &= C_{LL}^{-1} C_{LM}, \\ \Delta \hat{M} &= L_{\text{obs}} \hat{H}. \end{aligned} \quad (3.32)$$

Using the same training and predicting period as in the LSC, the predictions by LSP at residual level are depicted in Figure 3.9. Again, the estimation of TWS by assimilating of P , ET and R shows better agreement in the four catchments than prediction from individual variable, with respect to the observations from GRACE. However, the level of prediction error is still high. Comparing visually with Figure 3.7, the quality of estimation seems slightly improved, although the discrepancy between prediction and observation from GRACE is still significant.

Performance of regression by LSP and LSC To evaluate the performance of the two approaches, we refer to the statistical metrics: correlation coefficient, NSE, CNSE and PBIAS. As listed in Table 3.2, evaluation results in the four catchments are calculated. Comparing with the LSC based on a harmonic model $L = AX$, the LSP, directly implemented on the residuals, represents a better prediction for the TWS change in the four catchments, according to an overview of Table 3.2.

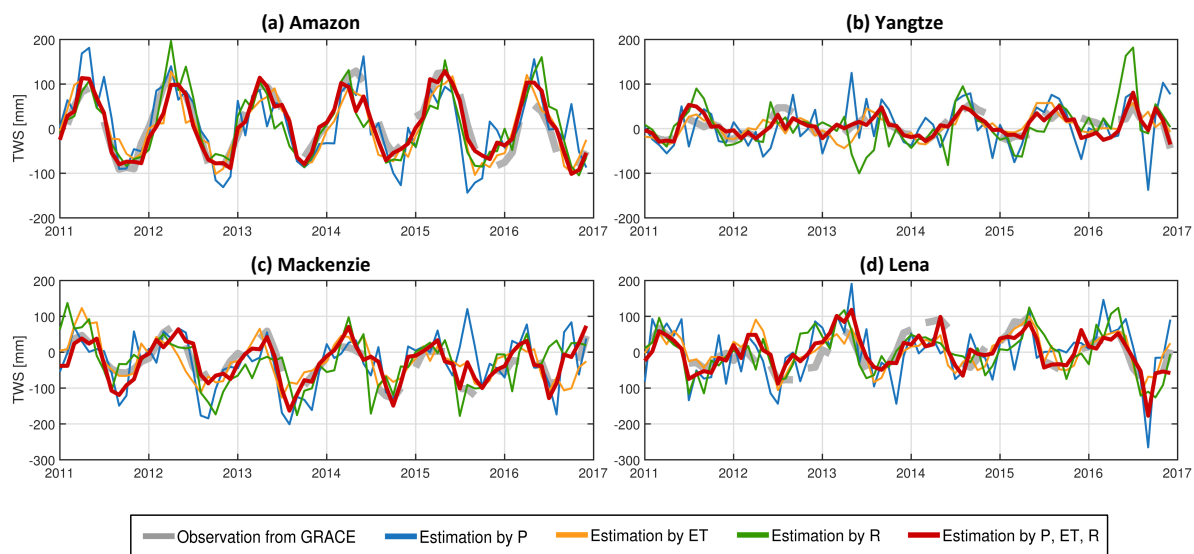


Figure 3.9: Estimations of total water storage change for (a) Amazon, (b) Yangtze, (c) Mackenzie, (d) Lena, respectively, by Least-Squares Prediction on observation residuals using precipitation, evapotranspiration and runoff.

Table 3.2: Performance of least-squares prediction and collocation using precipitation, evapotranspiration and runoff.

Basin	Observations	Least-squares prediction				Least-squares collocation			
		R	NSE	CNSE	PBIAS	R	NSE	CNSE	PBIAS
Amazon	<i>P</i>	0.77	0.59	-2.93	0.14	0.64	0.17	-4.23	-0.04
	<i>ET</i>	0.87	0.70	-0.60	0.36	0.86	0.73	-0.74	0.26
	<i>R</i>	0.80	0.63	-1.90	0.14	0.80	0.21	-4.05	-0.11
	<i>P, ET, R</i>	0.91	0.81	-0.15	0.20	0.87	0.74	-0.68	0.09
Yangtze	<i>P</i>	0.40	0.14	-8.68	-0.45	0.51	-1.15	-5.66	0.44
	<i>ET</i>	0.73	0.46	-0.77	0.33	0.76	0.55	-0.40	0.36
	<i>R</i>	0.46	0.21	-10.15	0.17	0.56	-0.54	-3.76	-0.14
	<i>P, ET, R</i>	0.74	0.49	-0.70	0.24	0.66	0.17	-1.56	0.29
Mackenzie	<i>P</i>	0.53	0.26	-4.64	-0.01	0.48	-0.88	-5.66	0.34
	<i>ET</i>	0.72	0.47	-1.16	0.20	0.73	0.33	-1.38	0.16
	<i>R</i>	0.65	0.39	-2.70	0.25	0.44	-2.34	-10.80	0.39
	<i>P, ET, R</i>	0.81	0.64	-0.53	0.04	0.77	0.32	-1.41	0.22
Lena	<i>P</i>	0.45	0.12	-4.39	-1.21	0.52	-1.16	-5.79	-4.07
	<i>ET</i>	0.70	0.32	-0.72	-0.54	0.64	0.40	-0.97	-0.45
	<i>R</i>	0.67	0.40	-1.51	0.54	0.48	-0.40	-3.42	0.21
	<i>P, ET, R</i>	0.71	0.36	-0.70	-0.45	0.63	0.23	-1.43	-0.48

The values of PBIAS reveal the bias with respect to observed time series. An extreme overestimate by P is done by LSC for Lena. By comparison, using LSP improves the accuracy of the prediction, according to the decreased bias. From Table 3.2, the better performance of LSP from combined variables is demonstrated by higher correlation, NSE, CNSE in these four catchments, despite PBIAS does not represent notable decrease of bias than other schemes. Unlike LSP, the TWS variations in Yangtze and Lena are ideally estimated by LSC using individual ET . The cyclo-stationary variability of ET in Yangtze and Lena probably leads to this better performance of LSC than other variables. This indicates that the performance of LSC depends on the accuracy of the mathematical model for variables.

In order to realize the different performance from the two approaches, we therefore look at the covariance matrix of prediction model errors. The error covariance matrix is estimated using (2.43) and (2.47). From Figure 3.10, LSP on P and the ensemble of P, ET, R anomalies evidently reduce the magnitude level of errors, comparing with the error covariance from LSC. The error covariance of ET, R are relative at the same level for LSP and LSC. This explicitly explains the different performance of LSP and LSC in Table 3.2.

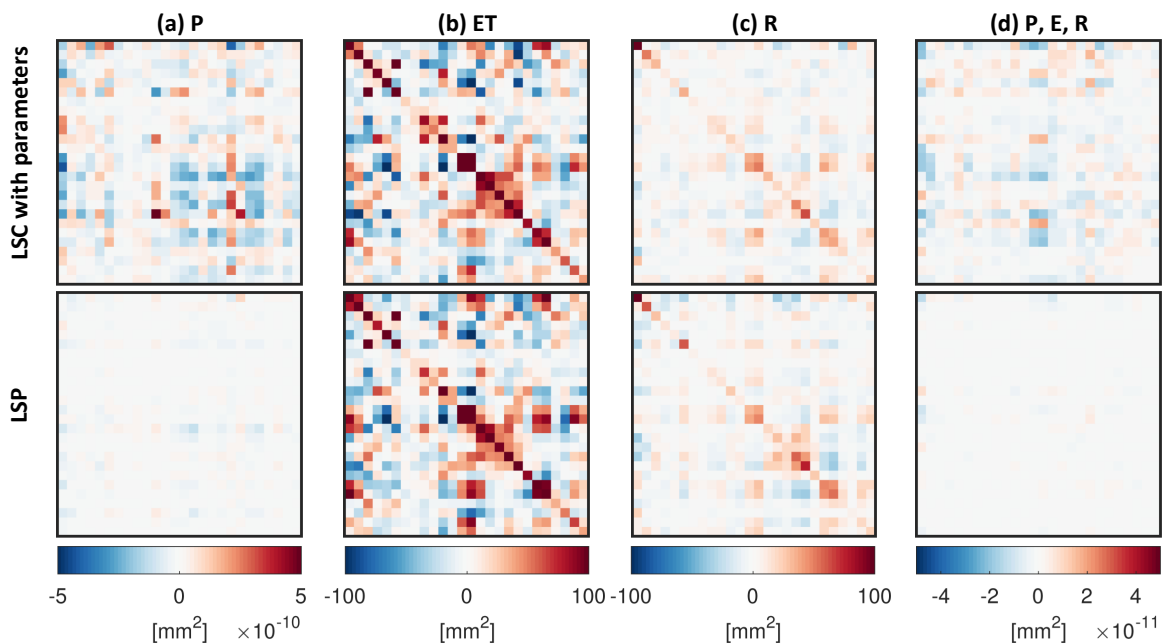


Figure 3.10: Covariance performance of prediction errors of two approaches: least-squares prediction and collocation, using (a) precipitation, (b) evapotranspiration, (c) runoff, and (d) combining all of them.

From Table 3.2, prediction from multiple variables with the preference of LSP approach provides more reliable predictions of TWS in the four catchments, which are under different climatic conditions. Figure 3.10 reveals the preference of LSP approach for TWS prediction. Therefore, it indicates that modeling the TWS change in catchments by an assimilation scheme of multiple variables is our optimal choice, using LSP approach. However, the estimations by LSP are still not good enough. Considering the time-invariant time lag between TWS and P, ET, R in most of catchment (see 3.2.2), a more adaptive approach needs to be developed.

3.2.4 Estimation by principal component regression

Variability of modes in observations In order to identify the different type of variability in hydrological observations, a PCA decomposition is performed on these observations. As expressed in (2.20), the decomposition of each variable P , ET , R by PCA is implemented by

$$P = U_P V_P^T, \quad ET = U_{ET} V_{ET}^T, \quad R = U_R V_R^T, \quad (3.33)$$

in which U_P , U_{ET} , U_R represent the temporal PCs of P , ET , R , respectively, and V_P , V_{ET} , V_R contain the corresponding spatial EOFs. To identify the variability represented by each mode, we look at the Fourier spectra of the temporal PC from each mode of the observations, cf. in Figure 3.11.

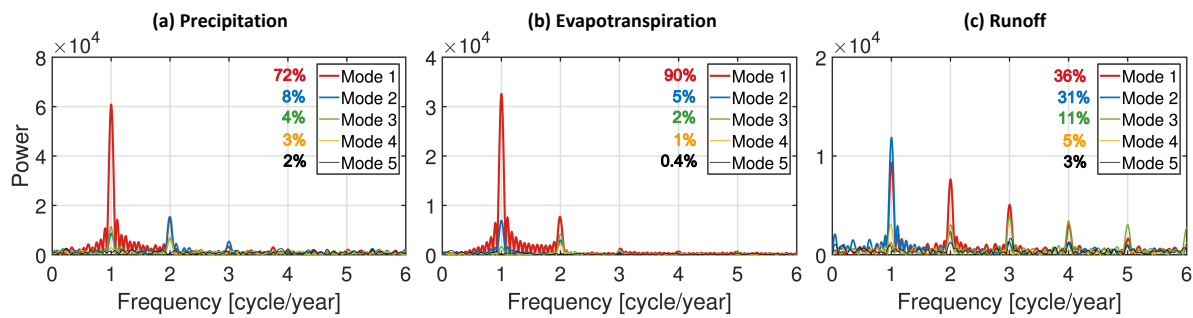


Figure 3.11: Spectra of the temporal PCs from first five modes by PCA decomposition on (a) precipitation, (b) evapotranspiration, and (c) runoff.

Mode 1 in P , ET and R represents obviously annual signals, which dominate the observations. In particular, the first modes in P and R contain 72% and 90% of total variance, respectively. We can avoid any ill-conditioning of the covariance matrix and reduce the computation if we make use of only the first five modes from observations for prediction. Alternatively, we can implement regression on the residuals with constrained number of modes in order to eliminate the noise from signals. In our study, the dominant annual cycle is removed from signals by subtracting the cyclo-stationary mean from observations. As a consequence, the residuals that we obtain contain only variation at semi-annual frequency, or even higher frequency, according to the spectra visualized in Figure 3.11. Based on the residuals without strong annual components, as demonstrated in 3.2.3, the performance of the principal component regression (PCR) model supposes to be more stable.

Prediction of TWS by PCR As introduced in 2.4.2, we employ the principal component regression (PCR) model to predict total water storage changes ΔM . Since the regression on the residuals presents us a more stable performance than using a collocation with mathematical model (as discussed in 3.2.3), we implement PCR algorithm on P , ET , R residuals in the following study.

For instance, we assume to predict the TWS residuals ΔM using runoff residuals ΔR . In this case, we subtract the cyclo-stationary mean from both M and R in order to avoid the interference from the strong seasonal signals. According to (2.56), the regression model of ΔM is built up via

$$\Delta M = \Delta R \cdot H = U_R V_R^T \cdot H = U_R \cdot K. \quad (3.34)$$

Now $K = V_R H$ is the new prediction matrix for the PC U_R instead of H . As a consequence, the K is regressed on the decomposed components U_R instead of R . Referring to (2.57), we have

$$\begin{aligned} \hat{K} &= (U_R^T U_R)^{-1} U_R^T \Delta M, \\ \hat{H} &= V_R \hat{K}. \end{aligned} \quad (3.35)$$

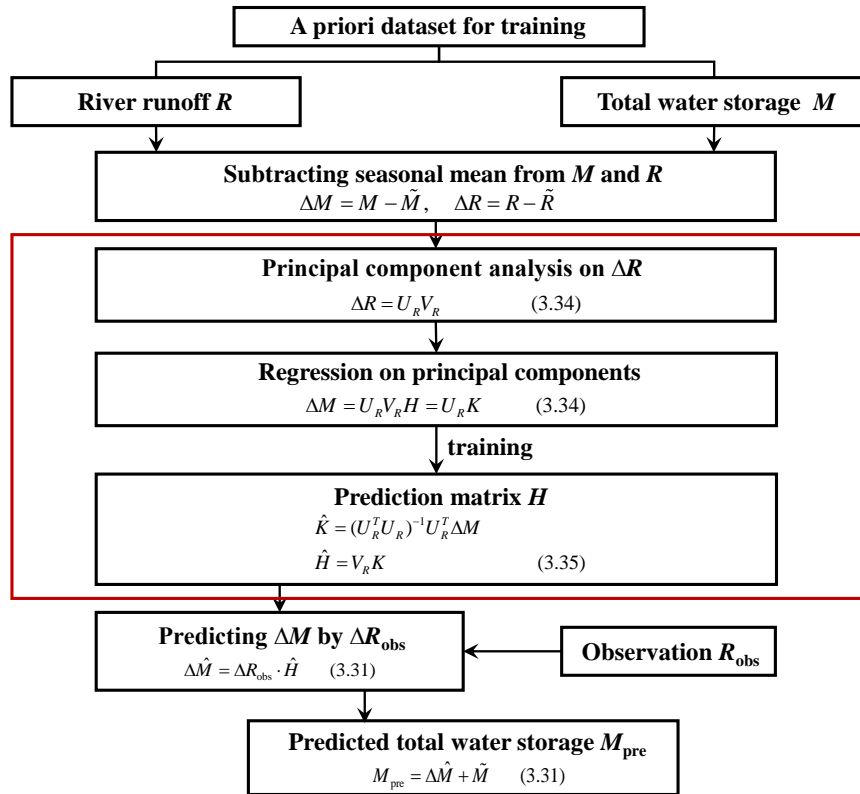


Figure 3.12: Flowchart of predicting total water storage by river runoff using principal component regression.

Once we obtain the prediction matrix \hat{K} , the rest steps for prediction is as the same as LSP. Therefore, the whole procedure of implementing the PCR algorithm is summarized in a flowchart illustrated in Figure 3.12. The decomposition of ΔR and the regression of H on the decomposed components are the crucial steps of PCR, as emphasized in a red box.

Using P and ET to predict M have the same procedure as illustrated in Figure 3.12. Combining the residuals from all the observed variables P , ET , R in a comprehensive estimation of ΔM , we have

$$\begin{aligned}
\Delta M &= \Delta P \cdot H_P + \Delta ET \cdot H_{ET} + \Delta R \cdot H_R \\
&= U_P V_P^T H_P + U_{ET} V_{ET}^T H_{ET} + U_R V_R^T H_R \\
&= U_P K_P + U_{ET} K_{ET} + U_R K_R \\
&= [U_P \ U_{ET} \ U_R] \cdot [K_P \ K_{ET} \ K_R]^T .
\end{aligned} \tag{3.36}$$

Unlike LSP, PCR separates the observation time series into different modes, and then extracts the most important modes from the observations. The regression process is implemented not directly on the observations but on those temporal PCs from the selected modes in the PCR model. We have to notice that the number of modes used in (3.36) from different variables are not uniform. In other words, U_P, U_{ET}, U_R could contain different number of PCs. As shown in Figure 3.11, P, ET, R have different spectra of modes. Consequently, we need to choose the proper number of modes for each variable, considering the different statistical characteristics. In addition, the number of modes used in the regression is not fixed. Hence, it drives us to test the performance of PCR using different number of modes.

Sensitivity of prediction to selected modes Since the PCR is implemented on the temporal modes of observations, the number of modes which we select to do regression is consequently relevant to the performance of PCR. For an optimal selection of modes, therefore, it is essential to analyze the prediction of ΔM by different number of modes from observed variables P, ET, R .

To quantify the influence of selected modes for each variable, the PCR performances in 26 catchments are evaluated by statistical metrics and visualized in Figure 3.13.

From the maps of PBIAS, the increase number of modes from ET results in a slight improvement of PBIAS in most of basins, which indicates smaller bias between prediction and observation from GRACE. Meanwhile, for P and R , no distinct improvement of PBIAS is relevant to the increasing number of modes. However, the increase number of modes does not help to improve the agreement in phase, which is revealed by correlation coefficients in Figure 3.13.

In terms of NSE, the model performance does not depend on the number of modes. It seems likely catchment-dependent. For instance, the modelling of TWS in catchments in the temperate zone (e.g. Ganges, Yangtze, Danube) relies on the number of modes, while in the tropical catchment like Amazon and in the boreal catchment like Ob and Yenisei, the prediction is invariant to the number of selected modes. As shown in Figure 3.13, regression based on 15 modes of observations has on average a good agreement with reference.

The values of CNSE reflect that in most catchments, predicting TWS by PCR is not as good as using the mean annual cycle instead for prediction, despite the high values evaluated by NSE. Combining with the results shown by PBIAS and correlation, we obtain the conclusion that varying number of modes used for PCR results in the amplitude differences in our predictions. For an optimal fit for the TWS from GRACE, 15 modes are commonly appropriate for prediction, although there are optimal selections of modes with respect to each specific catchment.

Prediction with optimal choice of modes As a case study, again the TWS in the four catchments (Amazon, Yangtze, Mackenzie, Lena) are predicted by PCR. As represented in Fig-

ure 3.13, we eventually choose the number of modes with the largest NSE values for each catchment as the optimal number of modes in the regression for prediction.

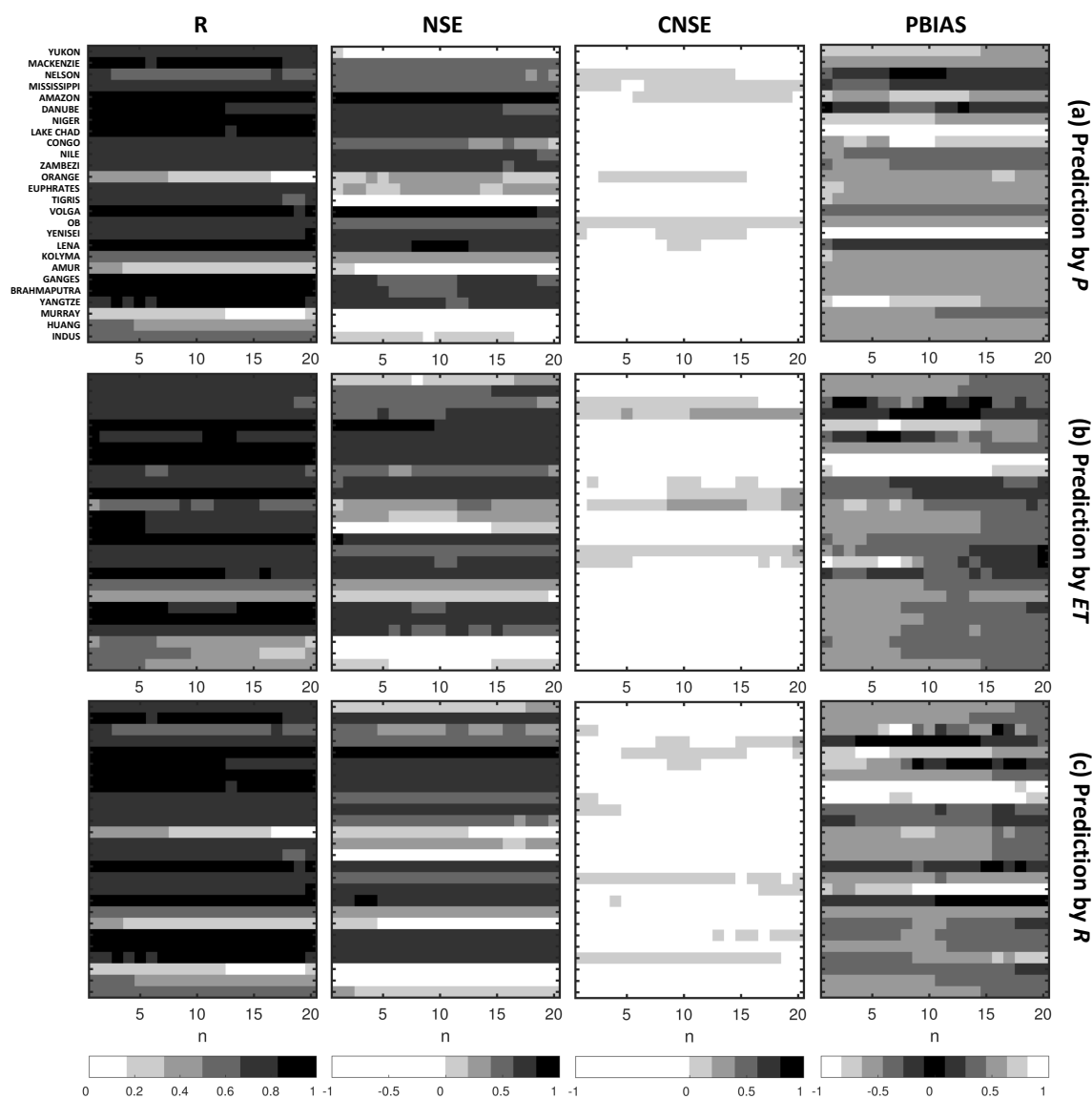


Figure 3.13: Sensitivity test of prediction of total water storage change in 26 catchments by (a) precipitation, (b) evapotranspiration, and (c) runoff, using principal component regression. The predictions with different selected number of modes from observations are evaluated by correlation R , NSE, CNSE and PBIAS. Each row index refers to a specific catchment.

The predicted monthly TWS as well as residuals by different schemes are visualized in Figure 3.14. At residual level, the prediction performs poorly in Mackenzie and Amazon. Good agreement is represented in Amazon at signal level while large disagreement is shown at residual level. The unstationary variation in the prediction period with respect to the training period might result in the underestimates of TWS, although the Amazon basin shows evident cyclostationary behaviours (see Figure 3.5). The non-stationarity in Mackenzie is revealed in the

residuals. A distinct decreasing trend of observed ΔM in Figure 3.14 (c) can hardly be captured by the PCR prediction.

Accordingly, the combination of multiple variables $\Delta P, \Delta ET, \Delta R$ has a stable performance in the four catchments, comparing with the prediction from individual variable. Therefore, predicting TWS using multiple hydrological variables will be an optimal choice. By comparison with Figure 3.7 and 3.9, the PCR improves significantly the quality of prediction. Hence, the PCR approach is the preference for predicting the TWS, comparing to LSC and LSP.

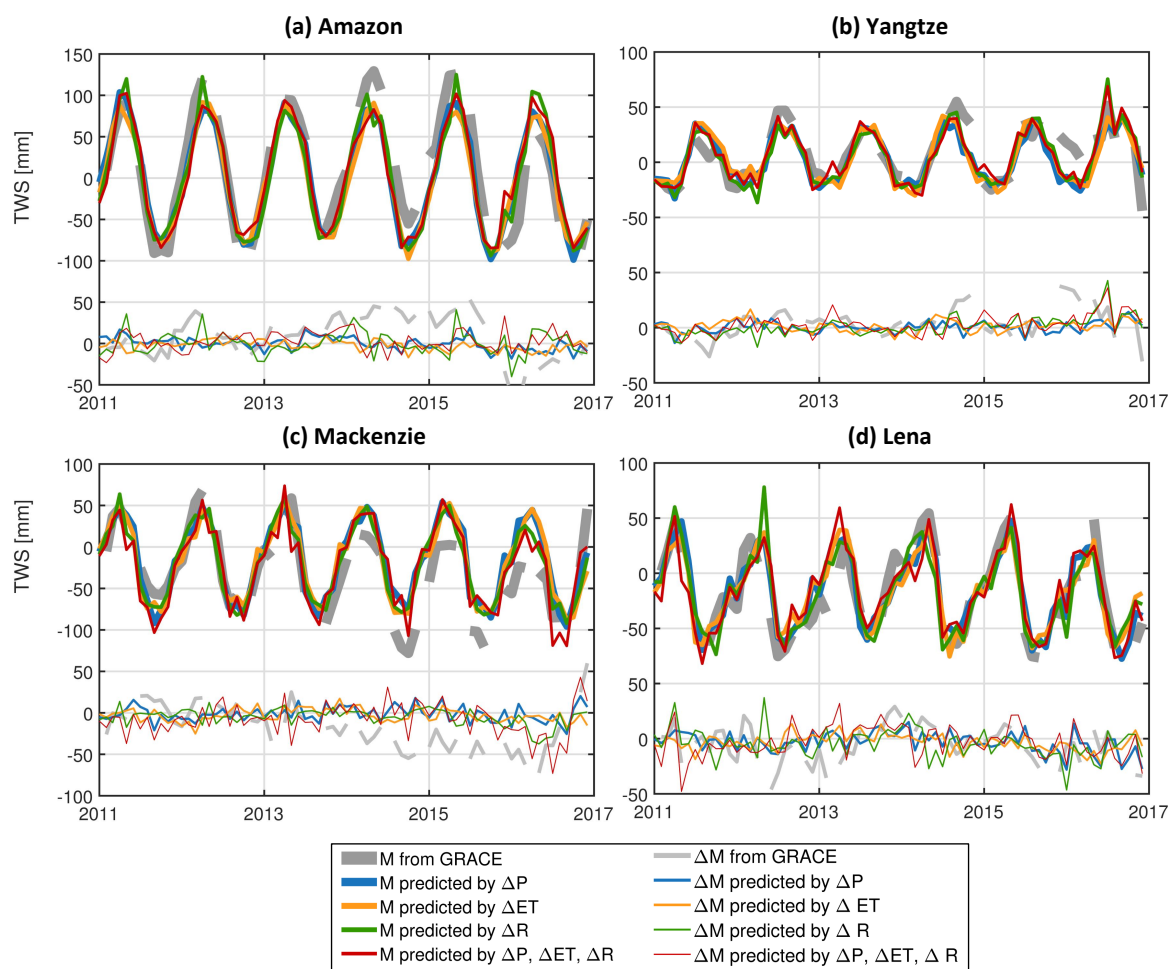


Figure 3.14: Predictions of total water storage change as well as its residual for (a) Amazon, (b) Yangtze, (c) Mackenzie, (d) Lena, respectively, by principal component regression on observation anomalies, using precipitation, evapotranspiration and runoff. The observations and residuals of total water storage from GRACE are plotted as well.

3.2.5 Estimation by partial least squares regression

Cross-covariance between TWS and P, ET, R Since the least-squares prediction is accomplished via training based on the cross-covariance, the mutual relationship between observations and predictions plays an important role. Hence, we firstly investigate the cross-

covariances between total water storage change M and precipitation P , evapotranspiration ET , runoff R .

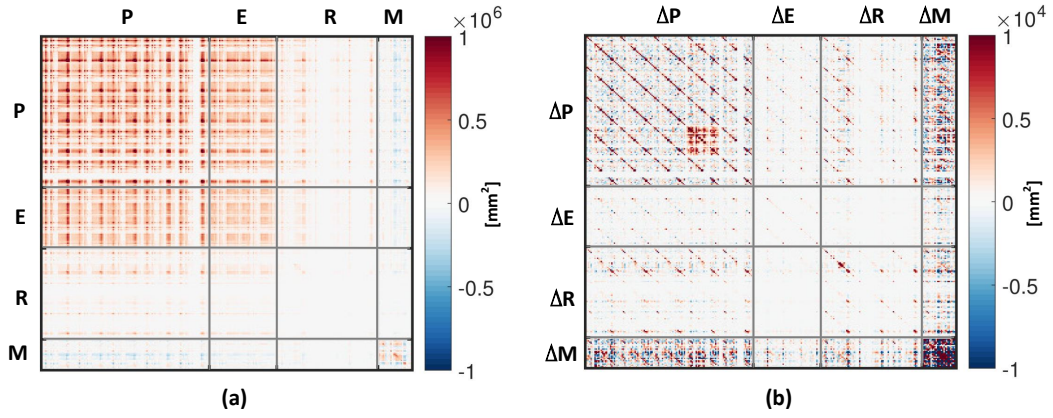


Figure 3.15: Auto-covariance and cross-covariance of (a) full signals (i.e. P , ET , R and M) and (b) residuals (i.e. ΔP , ΔET , ΔR and ΔM) along temporal dimensions for each catchment. Each row/column index represents for a specific catchment.

The cross-covariance matrix is calculated between P from five datasets, ET from two datasets, R from three datasets and M from GRACE, and visualized in Figure 3.15 (a). The large magnitude of covariance between P and M indicates the strong relevancy. However, smaller covariances between ET , R and M in the map indicates weaker relevancy than P . Despite the smaller covariance between ET , R and M displayed in the Figure (b), we cannot conclude that only weak relationships exist between ET , R and M . Moreover, the associated relationships between residuals ΔET , ΔR and ΔM are enhanced in the covariance matrix of residuals, according to Figure 3.15 (b). Besides ΔP , both ΔET and ΔR represent significant association with ΔM . Therefore, at residual level, the relevancy of all three variables P , ET , R to M needs to be taken into account in the prediction.

Prediction of TWS by PLR Considering the relevancy of P , ET , R to M , we employ the partial least-squares regression (PLR) to predict the TWS. Mathematically, predicting by PLR is similar to PCR. Different from PCR, the cross-covariance between predictor and predictand is involved in the PLR model. We use the predictors P , ET , R residuals that subtracting the cyclostationary mean from the observations to predict the TWS at residual level. As an example, we suppose to predict the total water storage changes ΔM by ΔR . According to (2.63), the cross-covariance matrix $C_{RM}(l \times s)$ between $\Delta R(n \times l)$ and $\Delta M(n \times s)$, in which the temporal dimension vanishes, can be decomposed by SVD, writes

$$\begin{aligned} C_{RM} &= \frac{1}{n} \Delta R^T \Delta M \\ &= U_{C_{RM}} \Sigma_{C_{RM}} V_{C_{RM}}^T, \end{aligned} \quad (3.37)$$

in which $U_{C_{RM}}$, $V_{C_{RM}}$ are the singular vectors of C_{RM} , which are associated with each other. Based on $U_{C_{RM}}$, the correspond PCs of ΔR , i.e. U_R , is calculated via

$$U_R = \Delta R \cdot U_{CRM}. \quad (3.38)$$

Referring to (2.64), we construct the linear model between ΔM and ΔR by

$$\Delta M = \Delta R \cdot H = U_R U_{CRM}^T H = U_R K. \quad (3.39)$$

In (3.39), K is the new prediction matrix for U_R instead of H for ΔR . Therefore, the K as well as H is regressed on the U_R as

$$\begin{aligned} \hat{K} &= (U_R^T U_R)^{-1} U_R^T \Delta M, \\ \hat{H} &= U_{CRM} \hat{K}, \end{aligned} \quad (3.40)$$

in which \hat{H} is finalized back to the scale of Δ by transformation of \hat{K} in terms of a multiplication with U_{CRM} . Comparing with (3.35), PLR regresses the prediction matrix K on the joint modes from ΔR that associating with ΔM , instead of the modes from individual ΔR .

Briefly, the procedure of implementing the PLR algorithm is illustrated by the flowchart in Figure 3.16. From the decomposition of the cross-covariance matrix to the regression of the prediction matrix H is the core part of the PLR model, which is highlighted in a red box.

In order to predict the ΔM by all the observed variables P , ET , R in a linear PLR model, we expand the observation vector from ΔR to $L = [\Delta P \ \Delta ET \ \Delta R]$. Thus, (3.39) becomes

$$\begin{aligned} \Delta M &= \Delta P \cdot H_P + \Delta ET \cdot H_{ET} + \Delta R \cdot H_R \\ &= U_P U_{CPM}^T H_P + U_{ET} U_{CETM}^T H_{ET} + U_R U_{CRM}^T H_R \\ &= U_P K_P + U_{ET} K_{ET} + U_R K_R \\ &= [U_P \ U_{ET} \ U_R] [K_P \ K_{ET} \ K_R]^T. \end{aligned} \quad (3.41)$$

Similar to PCR, PLR firstly decomposes the observations from P , ET , R but in a different way. The associated information between P , ET , R and ΔM are extracted and retained in U_P , U_{ET} , U_R . Again, as discussed in 3.2.5, the number of joint modes used in (3.41) from ΔP , ΔET , ΔR is not uniform. In other words, U_{CPM} , U_{CETM} , U_{CRM} could contain different number of joint modes. Moreover, in order to find the optimal combination of each variable with proper number of joint modes, an evaluation needs to be involved on the performance of prediction using different number of modes.

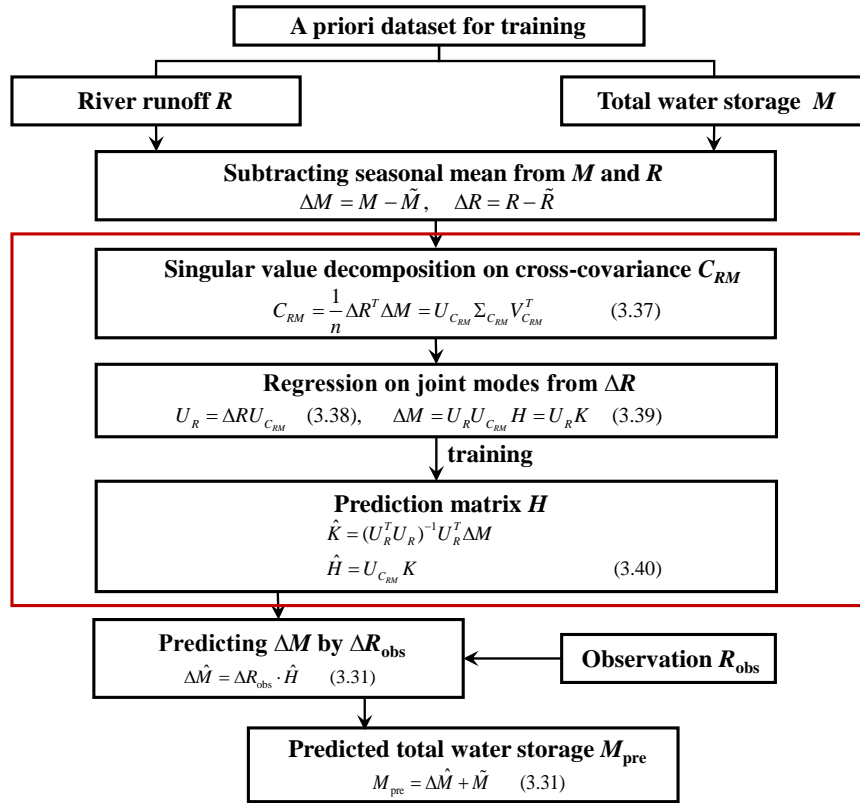


Figure 3.16: Flowchart of predicting total water storage by river runoff using partial least-squares regression.

Sensitivity of prediction to selected joint modes The associated variations in the observed time series of P , ET , R with M are assigned to the joint modes. Considering the mutual prior information represented in the cross-covariance between observation and prediction, the joint modes, which are decomposed based on these cross-covariance matrices, contain the significant associated temporal variation for each side. A different number of selected joint modes in the observations will lead to different performances of the PLR model. Therefore, we have to carefully concern on the number of selected joint modes. It is worth testing the sensitivity of prediction accuracy to the selection of the joint modes from individual observations.

For exploring statistically the performance of varying number of joint modes, we evaluate the predicted TWS for 26 catchments with respect to GRACE observed TWS, and visualize the values of metrics in Figure 3.17.

With the increase of number of modes, PBIAS is close to zero, indicating better agreement in amplitudes. On the contrary, the decrease of number of modes in some catchments (e.g. Danube, Mackenzie, Tigris) results in higher correlation in phase. It is simply to understand this correlation pattern, because the most significant correlated variation are represented in the first several modes. Using only the first several associated modes provides us good correlations but loses the information in amplitudes, while more modes involved in the regression gain more information in amplitude, but lead to more uncorrelated signals included in the predictions.

From NSE, it reveals no common optimal choice of joint modes for all catchments. In other words, we need to find the balance between amplitude agreement and phase correlation in one catchment, in order to gain the best performance. The highest values of NSE with respect to the number of modes represent such a balance in different catchments, as shown in Figure 3.17. Comparing the CNSE map in Figure 3.17 with Figure Figure 3.13, it illustrates that PLR has improved the accuracy of TWS estimation in more catchments than PCR, although it still indicates insufficient accuracy of prediction in most of basins.

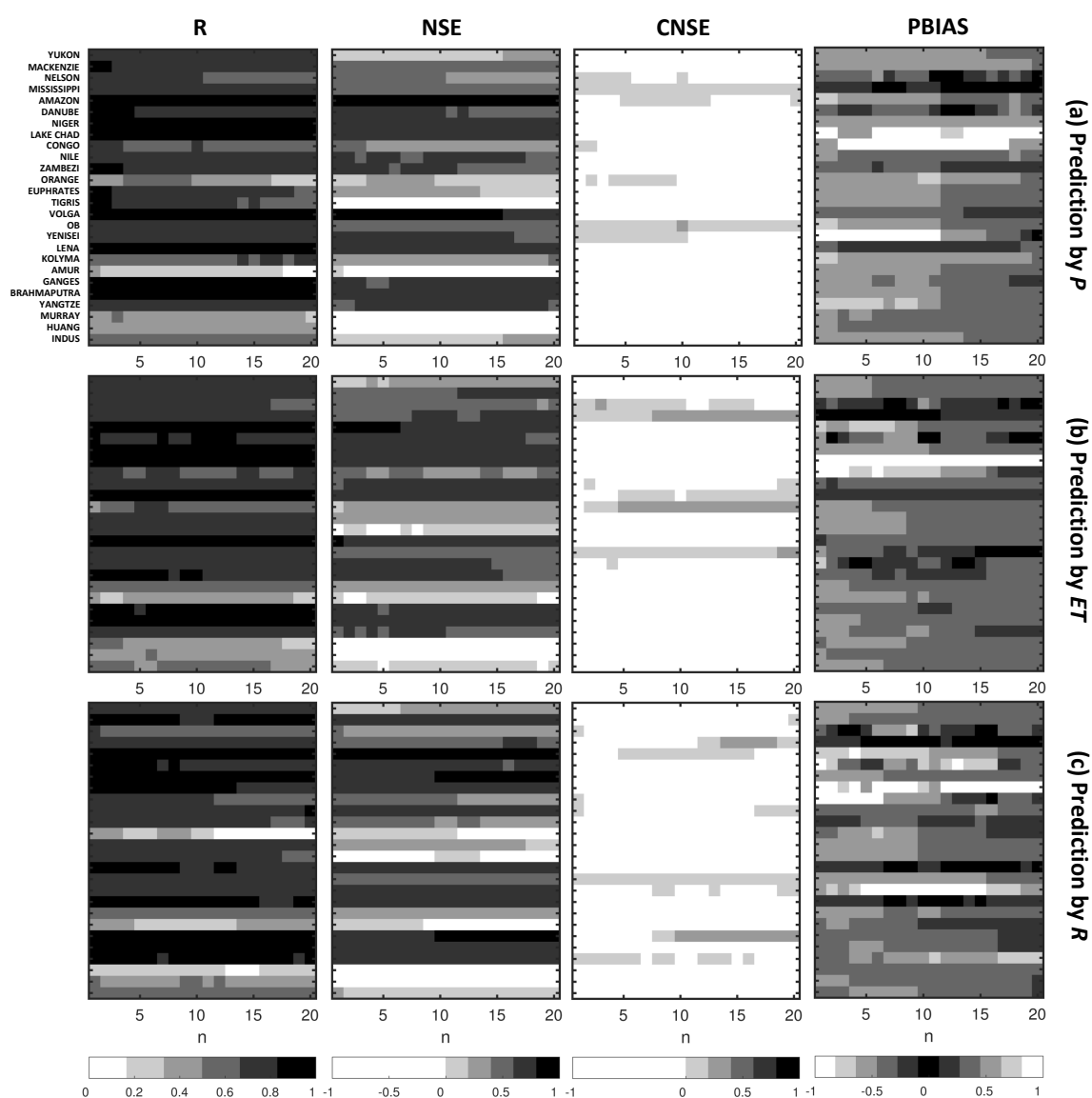


Figure 3.17: Sensitivity of prediction of total water storage change in 26 catchments by (a) precipitation, (b) evapotranspiration, and (c) runoff, using partial least squares regression. The predictions with different selected number of joint modes from observations are evaluated by R, NSE, CNSE and PBIAS. Each row index stands for a specific catchment.

Prediction with optimal choice of joint modes For a case study, we apply the PLR on prediction of TWS in four catchments with an optimal number of joint modes used in the regression, as shown in Figure 3.18. The TWS residuals are predicted by PLR using different schemes of observations. The monthly TWS prediction is obtained based on the predicted ΔM and its seasonal mean.

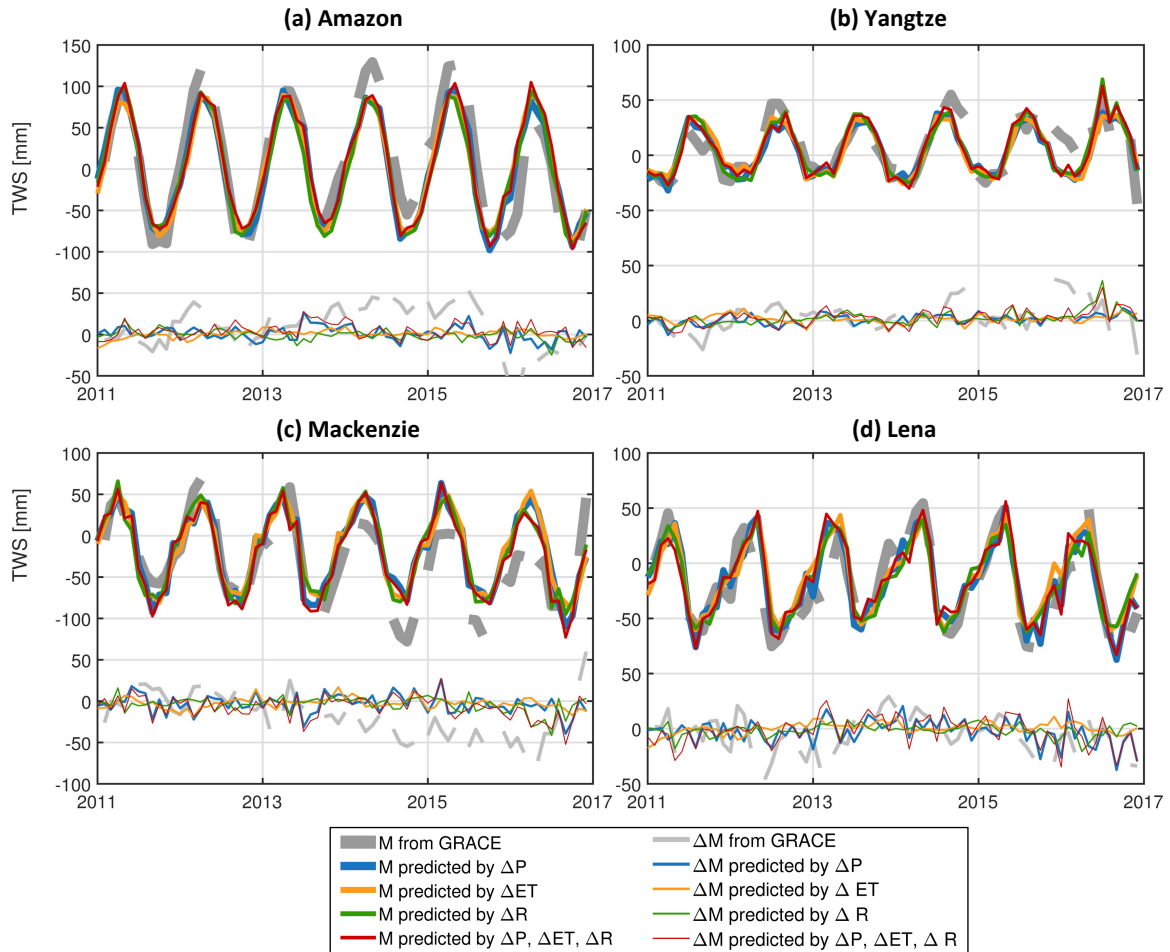


Figure 3.18: Predictions of total water storage change as well as its residual for (a) Amazon, (b) Yangtze, (c) Mackenzie, (d) Lena, respectively, by partial least-squares regression on observation anomalies, using precipitation, evapotranspiration and runoff. The observations and residuals of total water storage from GRACE are plotted as well.

From the prediction of TWS residuals, P has better performance in Amazon and Lena than ET and R . This might be explained by the strong relevancy between ΔP and ΔM that represented in the dominant joint modes. Still, the combination of $\Delta P, \Delta ET, \Delta R$ has more stable performance in predicting TWS than any other individual variables. On the contrary, ΔM predicted by ΔET and ΔR is around 0, indicating the weak dependence of ΔM on ΔET and ΔR .

Comparing with Figure 3.14, PLR shows relatively the same performance as PCR. The prediction for Lena at residual level has a slight improvement, comparing to Figure 3.14, in which the predicted ΔM in Lena is obviously overestimated. The prediction is largely improved by

PLR, compared with 3.7 and 3.9. This improvement meets our expectation, since the associated changes in TWS and precipitation, evapotranspiration and runoff are captured by the joint modes.

Performance comparison of PCR and PLR PCR and PLR share some properties. For example, both of them regress on the decomposed components of observations. This characteristic can overcome the potential ill-condition problem. Moreover, they make use of the most important information and eliminate the random noise in the observation time series.

PCR only considers the variability in observation data, whereas PLR takes the associated variability between observation and prediction data into account, which is the difference between PCR and PLR. To explain visually the difference, we analyze the spectra of each mode. The spectra of joint modes from TWS and P , ET , R are depicted in Figure 3.19, where TWS is the predictant and P , ET , R are predictors.

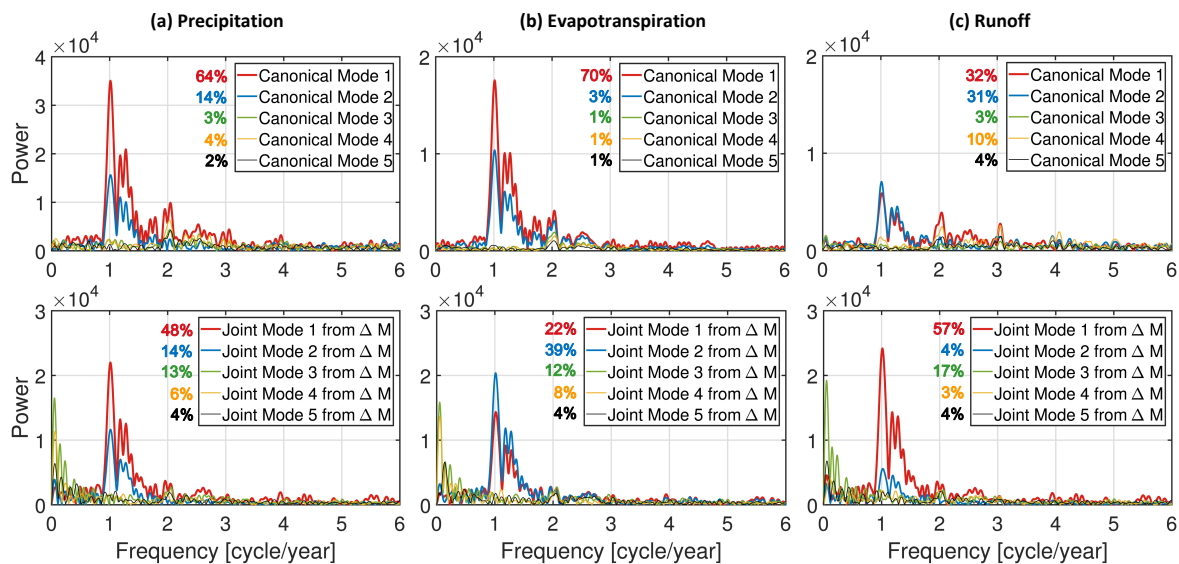


Figure 3.19: Spectra of the temporal PCs of the first five joint modes by CCA decomposition from (a) precipitation, (b) evapotranspiration, (c) runoff, with total water storage, respectively. The percentage of joint modes in each field is also shown in the figure.

The correlated variation in both fields are identified by those canonical joint modes. In Figure 3.19, the first canonical joint mode clearly represents annual variation both in TWS and other hydrological variables except for R . Notice that the first joint mode is not necessarily the dominant mode in each field, like the joint mode 1 in TWS, corresponding to evapotranspiration. Comparing with the spectra in Figure 3.11, modes with high correlation but low variance in the time series are emphasized by PLR. For instance, mode 3 of R is still identified even though it acts as a small part of signal, associating with the mode 3 in ΔM with 17% variance. In other word, unlike PCR, PLR is able to extract the correlated information and to get rid of uncorrelated noise for training.

Table 3.3 shows the performance of PCR and PLR in four catchment in terms of R, NSE, CNSE, and PBIAS. The number of modes in each catchment are decided based on the statistical results

Table 3.3: Performance of principal component and partial least-squares regression of precipitation, evapotranspiration and runoff, based on the optimal choice of modes.

Basin	Observations	Principal component regression				Partial least-squares regression			
		R	NSE	CNSE	PBIAS	R	NSE	CNSE	PBIAS
Amazon	<i>P</i>	0.93	0.85	0.05	0.56	0.93	0.84	0.06	0.41
	<i>ET</i>	0.92	0.81	0.01	0.42	0.92	0.82	0.01	0.30
	<i>R</i>	0.93	0.85	0.04	0.52	0.93	0.84	0.01	0.40
	<i>P, ET, R</i>	0.92	0.82	-0.15	0.25	0.92	0.84	-0.06	0.14
Yangtze	<i>P</i>	0.83	0.64	-0.11	0.54	0.82	0.64	-0.11	0.30
	<i>ET</i>	0.80	0.62	-0.17	0.31	0.80	0.63	-0.16	0.23
	<i>R</i>	0.85	0.68	0.01	0.34	0.85	0.68	0.02	0.35
	<i>P, ET, R</i>	0.84	0.68	0.02	0.14	0.84	0.67	0.01	0.12
Mackenzie	<i>P</i>	0.84	0.58	-0.49	0.54	0.84	0.59	-0.46	0.45
	<i>ET</i>	0.83	0.64	-0.28	0.33	0.82	0.63	-0.30	0.27
	<i>R</i>	0.85	0.65	-0.07	0.32	0.85	0.67	-0.07	0.30
	<i>P, ET, R</i>	0.84	0.70	-0.26	0.14	0.85	0.70	-0.16	0.13
Lena	<i>P</i>	0.90	0.81	-0.08	0.13	0.90	0.78	-0.24	0.12
	<i>ET</i>	0.89	0.78	-0.27	0.14	0.90	0.78	-0.25	0.17
	<i>R</i>	0.91	0.81	0.05	0.04	0.85	0.79	-0.19	0.04
	<i>P, ET, R</i>	0.89	0.79	-0.24	0.09	0.85	0.79	-0.18	0.11

that represented in Figure 3.13 and 3.17. From Table 3.3, there is no distinct difference in correlation between PCR and PLR. After compressing data into a number of modes, we obtain good consistency by both PCR and PLR. The predicted time series fit exactly with the observed one from GRACE in Amazon and Lena, indicated by high NSE. According to the values of CNSE, PCR performs relatively better performance than PLR in boreal catchments (i.e., Mackenzie and Lena). The TWS changes in Amazon and Yangtze basin are estimated with equivalent accuracy by PCR and PLR.

Assimilating *P*, *ET*, *R* in the regression models improves the prediction, which is illustrated by the evident reduction of bias in PBIAS. As represented in Table 3.3, modelling TWS by *R* gains the optimal prediction in catchments except for Mackenzie. The bad quality of prediction in Mackenzie probably owes to the time-invariant temporal shift between runoff and water storage change under cold and dry climatic condition.

3.2.6 Estimation by adaptive moving average regression

Since the terrestrial water cycle is a dynamic process, TWS does not vary simultaneously with the variation of *P*, *ET* and *R*. As a consequence, the ΔM at epoch *t* might relate to the ΔR at previous epochs, which can be expressed by a moving average model

$$\begin{aligned} \Delta M(t) &= H_1 \cdot \Delta R(t) + H_2 \cdot \Delta R(t-1) + \dots + H_k \cdot \Delta R(t-k+1) \\ &= [\Delta R_1(t) \ \Delta R_2(t) \ \dots \ \Delta R_k(t)] \cdot [H_1 \ H_2 \ \dots \ H_k]^T, \end{aligned} \quad (3.42)$$

in which $\Delta R(t-k+1)$ is expressed by ΔR_k . In this case, *k* denotes the order of the moving average (MA) model. In our applications, we define the order *k* ranging from 0 to 11, since hy-

drological observations generally have annual cycles. The monthly anomalies ΔR are obtained by removing directly the mean annual cycle from the observations.

Instead of ΔR at the same epoch with ΔM in LSP, the observations are the ensemble of ΔR_k at epochs with k temporal shift back, in the moving average regression model (MAR). Hence, as an example, a comprehensive estimation of ΔM at epoch t using ensembles of residuals ΔR with $k - 1$ temporal shifting is expressed by

$$\begin{aligned}\Delta M &= \Delta R \cdot H \\ &= [\Delta R_1 \ \Delta R_2 \ \cdots \ \Delta R_k] H ,\end{aligned}\tag{3.43}$$

where each ΔR_k in ΔR is a $n \times l$ matrix, containing l number of time series with n epochs from different sources (i.e. different hydrological models). Thus, ΔR becomes a $(n \times l) \times k$ matrix, written in form of

$$\begin{aligned}\Delta R_k &= \begin{bmatrix} \Delta R_{1,1} & \Delta R_{1,2} & \cdots & \Delta R_{1,l} \\ \Delta R_{2,1} & \Delta R_{2,2} & \cdots & \Delta R_{2,l} \\ \vdots & \vdots & \ddots & \vdots \\ \Delta R_{n,1} & \Delta R_{n,2} & \cdots & \Delta R_{n,l} \end{bmatrix} , \\ \Delta R &= [\Delta R_1 \ \Delta R_2 \ \cdots \ \Delta R_k] .\end{aligned}\tag{3.44}$$

Alternatively, the ΔR can also be arranged in form of

$$\begin{aligned}\Delta R_l &= \begin{bmatrix} \Delta R(t_1) & \Delta R(t_1 - 1) & \cdots & \Delta R(t_1 - k + 1) \\ \Delta R(t_2) & \Delta R(t_2 - 1) & \cdots & \Delta R(t_2 - k + 1) \\ \vdots & \vdots & \ddots & \vdots \\ \Delta R(t_n) & \Delta R(t_n - 1) & \cdots & \Delta R(t_n - k + 1) \end{bmatrix} , \\ \Delta R &= [\Delta R_1 \ \Delta R_2 \ \cdots \ \Delta R_l] ,\end{aligned}\tag{3.45}$$

in which ΔR_l is a $n \times k$ matrix, consisting of n epochs time series with k times shifting. Therefore, ΔR is a $(n \times k) \times l$ matrix. For regression, ΔR is prepared as an MA ensemble in LSP. The procedure of this moving average least squares prediction (MA-LSP) is briefly described in a flowchart in Figure 3.20. In fact, the only difference from LSP is the input predictor R . In MA-LSP, R is an ensemble based on the form of MA model, considering the temporal shift between ΔM and ΔR . Similarly, the MA ensembles from P and ET are also generated as represented in (3.44) or (3.45).

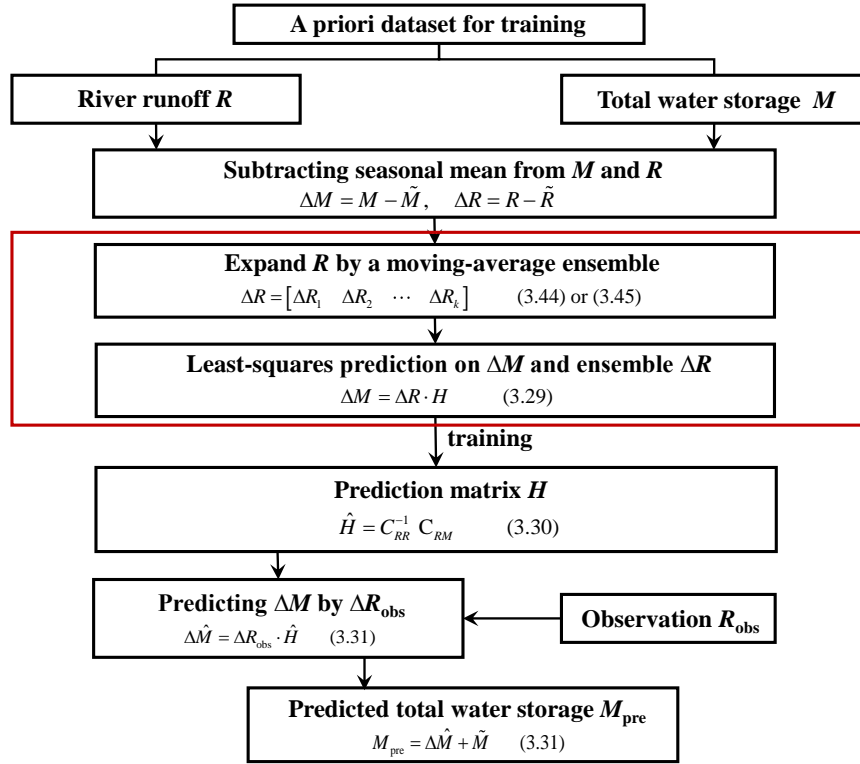


Figure 3.20: Flowchart of predicting total water storage by river runoff using an adaptive moving average least squares prediction.

Prediction by MA-LSP using multiple variables To investigate the effect of different variables on the prediction of TWS, we evaluate the performance of the prediction by the ensemble of ΔP , ΔET , ΔR , respectively. Since the Danube basin is weakly cyclo-stationary in TWS variation, prediction in such a basin is a challenge. Therefore, the Danube basin is chosen as a case study. In Figure 3.21, the predictions of M and ΔM as well as the measurements from GRACE in the Danube basin are visualized. We obtain the prediction of M by the sum of the predicted ΔM and its cyclo-stationary mean \tilde{M} . To make the predictions comparable, we consider the order $k = 12$ as a fixed parameter.

As shown in Figure 3.21 (a), the prediction by a joint dataset of P , ET and R has the largest values of R and NSE and the smallest value of $RMSE$. It indicates that a joint dataset consisting of P , ET , R performs better than any other predictions. For individual variables, ET shows a large disagreement with GRACE observed time series, represented by Figure 3.21 (a) and (b). Both P and R fit very well with observations, indicating that the TWS is successfully modeled by P and R in a MA-LSP scheme. In particular, the prediction by P is extremely close to the prediction by a combination of P , ET , R , indicating a better performance than ET and R . Additionally, after applying an adaptive moving average model on P , the performance of prediction by P has been improved remarkably, compared with Figure 3.7 and 3.9. As a result, a prediction scheme combining P , ET and R together is the basis for prediction in the following analysis.

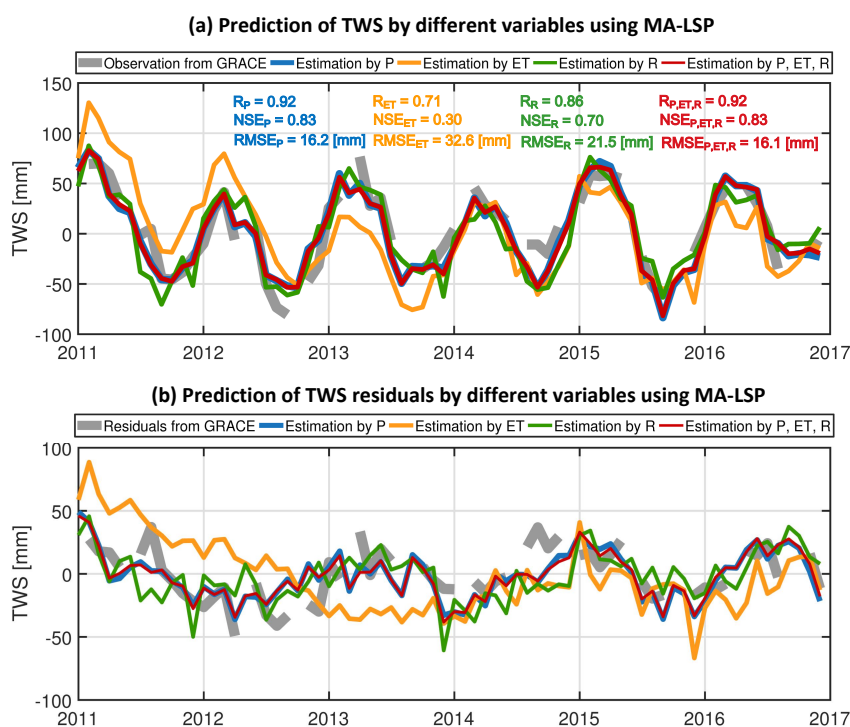


Figure 3.21: Predicting the total water storage (a) and its residuals (b) in Danube basin by adaptive moving average least-squares prediction model, using observations from precipitation (P), evapotranspiration (ET), runoff (R), respectively, and joint observations of P, ET, R. The performances of prediction are evaluated by R, NSE, and RMSE.

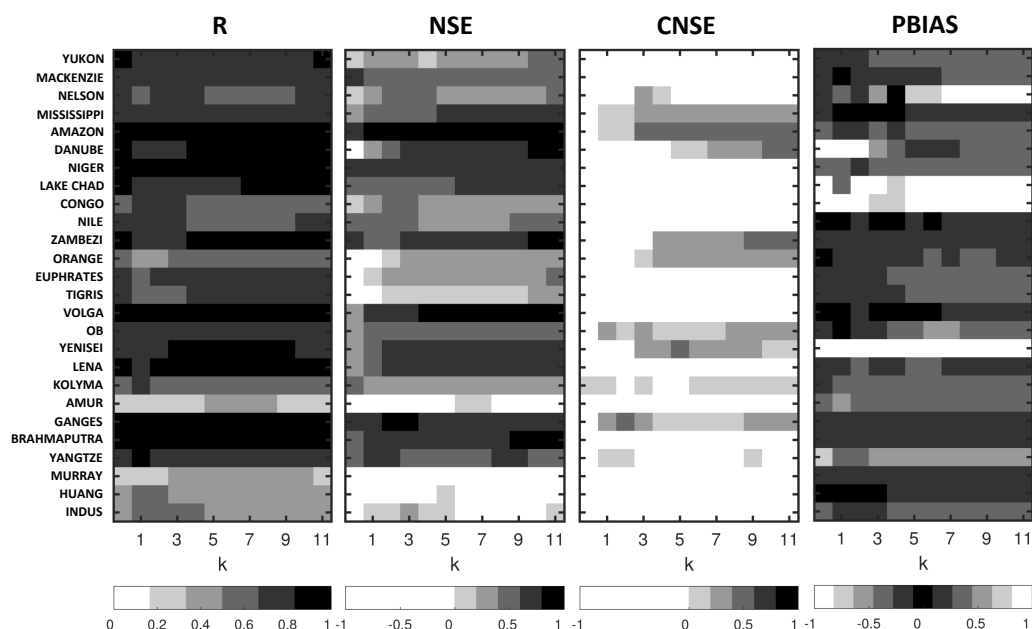


Figure 3.22: Sensitivity test of prediction of total water storage change in 26 catchments by combination of precipitation, evapotranspiration, and runoff, using least-squares prediction. The predictions with different selected order of MAR model are evaluated by correlation, NSE, CNSE and PBIAS.

Sensitivity of prediction to MAR model order The TWS in 26 catchments are now estimated by MA-LSP using time series from joint datasets of ΔP , ΔET and ΔR , with different MA order from 0 to 11.

Figure 3.22 shows that, for most of catchments, a higher MA model order leads to better correlation. The order does not affect the prediction in some big catchments like Mackenzie, Amazon, and Mississippi, represented by the constant correlations. The pattern from PBIAS indicates that smaller bias are achieved when lower order MA is applied. On the contrary, NSE shows a better performance when the order of MA increases for most of catchments. A similar conclusion is obtained from the values of CNSE in Figure 3.22. This indicates that prediction by a full cycle (i.e. $k = 11$) evidently reduces the uncertainty of observations. In other words, the influence of abnormal variation in precipitation, evapotranspiration, or runoff, which may not contribute to the changes in TWS, is likely smoothed via the MA model. Hence, considering the effect of MA order, we implement the prediction algorithm optimally with the order 11 in the following studies.

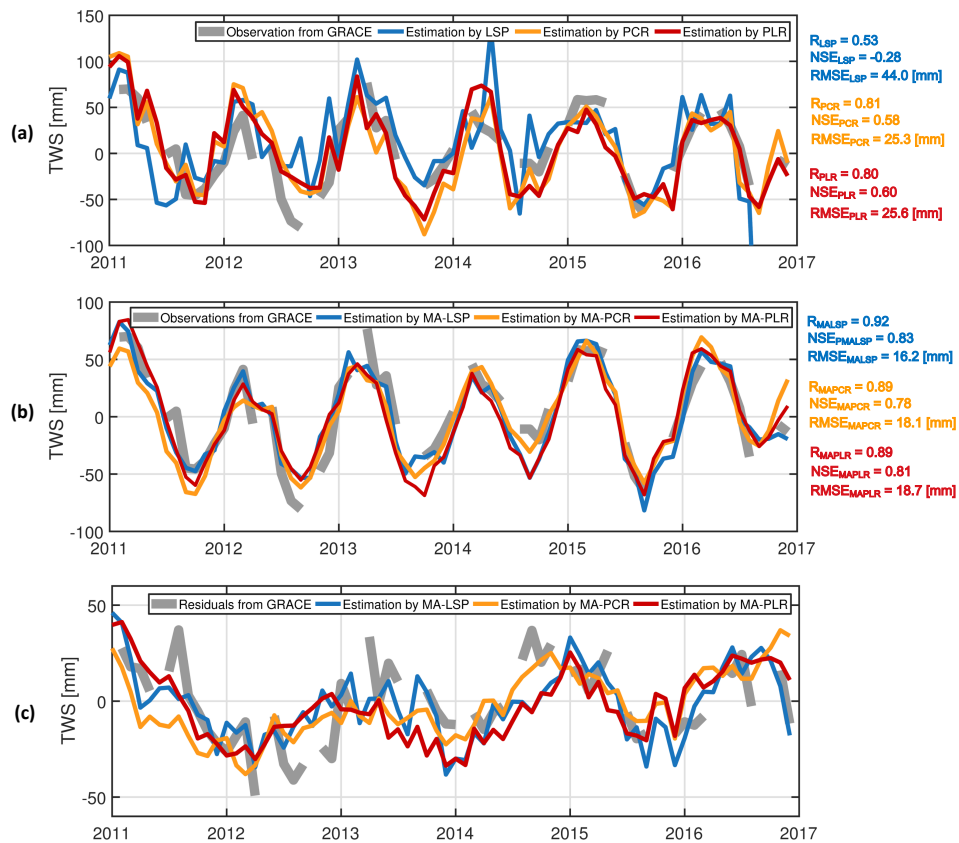


Figure 3.23: (a) Total water storage prediction in Danube basin by least-squares prediction, principal component regression, and partial least-squares regression. (b) Total water storage prediction in Danube basin by the adaptive moving average model with least-squares prediction, principal component regression, and partial least-squares regression. (c) Prediction of residuals of total water storage in Danube basin by the adaptive moving average model with least-squares prediction, principal component regression, and partial least-squares regression. The observations and residuals of total water storage from GRACE are plotted as well. The performances of predictions are evaluated in terms of R, NSE and RMSE, shown on the right hand side of the time series.

Performance comparison of MA-LSP, MA-PCR and MA-PLR From 3.2.4 and 3.2.5, we have already realized that both PCR and PLR can improve the accuracy of prediction by simple LSP. We now assess the performance of LSP, PCR, PLR in combination with MA model (MA-LSP, MA-PCR, MA-PLR, respectively), again by case study in the Danube basin.

The prediction of TWS variation in Danube basin by LSP, PCR, and PLR with and without adding MA are depicted in Figure 3.23. Figure 3.23 (a) shows that LSP performs poorly. The TWS predicted by LSP is unacceptable, considering the negative value of NSE. PCR and PLR perform more or less at the same level, with similar metrics. Both PCR and PLR performs well in estimating the TWS.

From Figure 3.23 (b), combining with MA model, it obviously improves the accuracy of prediction. The prediction by LSP is significantly improved, fitting almost perfectly with the observation time series (NSE = 0.92). The accuracy of prediction by PCR and PLR are subsequently improved as well, after integration with MA model. Compared with MA-PCR, MA-PLR has better performance overall with respect to NSE, while with larger errors revealed by RMSE. Despite the slight difference, MA-PCR and MA-PLR perform equally in the TWS prediction by multiple variables.

Figure 3.23 (c) shows the agreement between the predicted residuals and the residuals from GRACE, explaining the improvement by MA-LSP, MA-PCR and MA-PLR in Figure 3.23 (b). All the three approaches represents equivalently good performances.

Table 3.4: Performance of principal component and partial least-squares regression of precipitation, evapotranspiration and runoff, based on the optimal choice of modes.

Method	Basin	R	NSE	CNSE	PBIAS	RMSE [mm]
MALSP	Amazon	0.95	0.88	0.24	0.21	23.2
	Yangtze	0.77	0.55	-0.42	0.58	15.9
	Mackenzie	0.78	0.57	-0.35	0.32	31.9
	Lena	0.89	0.79	-0.23	-0.14	17.4
	Danube	0.92	0.83	0.26	0.42	16.2
MAPCR	Amazon	0.90	0.80	0.06	0.43	29.8
	Yangtze	0.68	0.39	-0.60	0.35	18.8
	Mackenzie	0.75	0.51	-0.73	0.25	33.9
	Lena	0.70	0.35	-0.82	-0.13	30.4
	Danube	0.89	0.78	0.08	0.65	18.1
MAPLR	Amazon	0.92	0.84	0.09	0.45	26.3
	Yangtze	0.79	0.56	-0.37	0.39	12.5
	Mackenzie	0.67	0.37	-1.25	0.19	38.6
	Lena	0.87	0.75	-0.49	-0.18	19.1
	Danube	0.89	0.81	0.14	0.61	18.7

To compare the results with those illustrated in Table 3.2 and 3.3, we also implement these three types of algorithm in Amazon, Yangtze, Mackenzie and Lena. The statistical results are represented in Table 3.4. Combining with a moving average process, we achieve extremely good correlation.

From Table 3.4, the TWS prediction by MA-LSP, MA-PCR and MA-PLR fit very well with GRACE in Amazon. For catchments with a strong cyclo-stationarity (e.g. Amazon), MA-LSP is

capable to gain sufficient accuracy and therefore is the optimal approach. However, for catchments in the temperate zone with non cyclo-stationary behaviour (e.g. Yangtze), MA-PLR acquires relatively higher prediction accuracy than MA-LSP, according to the reduction in RMSE, although both of them show negative values of CNSE. Despite MA-LSP has relatively better performance in Danube, the slight improvement indicates that MA-LSP, MA-PCR, MA-PLR have an accuracy at the same level, which is also represented in Figure 3.23.

Neither MA-LSP, MA-PCR nor MA-PLR represent sufficient accuracy in Mackenzie and Lena. By comparison, MA-LSP achieves relatively better accuracy in Mackenzie and Lena according to R, NSE and CNSE. Whereas, the smaller values of PBIAS and RMSE indicate better performance from MA-PLR. For these boreal catchments, which are under cold and dry climatic condition, we still do not find an appropriate approach to model the TWS by assimilating P , ET , R . In other words, there is no optimal regression model yet for boreal catchments.

Therefore, we need to consider the characteristics of specific catchments, when employing a proper statistical approach. As a conclusion, our analysis shows that after introducing the MA model, MA-LSP is able to predict TWS with good accuracy. Considering the slight differences between MA-LSP, MA-PCR and MA-PLR, any of them can be adopted as an appropriate assimilation approach for TWS modelling.

3.3 Spatial downscaling of water storage variation in catchment

As we have discussed in 3.1.2, due to the limited spatio-temporal resolution of GRACE, it is still difficult to involve GRACE observed total water storage (TWS) variations in the small-scale basins for hydrological studies. This consequently drives us to downscale the GRACE product for better spatial resolution. Various downscaling approaches have been employed to improve the spatial resolution of hydrological observations. Zaitchik et al. (2008) developed a model-based data assimilation method (i.e. ensemble Kalman filter) that assimilate GRACE TWS into a land surface model (LSM) to gain finer resolution of hydrological variables, but no downscaled TWS was produced from the model. Similarly, this model-based assimilation approach has been applied in some other studies (Houborg et al., 2012; Eicker et al., 2014) to improve the hydrological models. Besides the model-based assimilation, a non-parametric, empirical downscaling method has been developed based on artificial neural network (ANN) for hydro-geodetic applications in a number of studies. Sun (2013) applied an ANN-based model to predict water level change by incorporating GRACE with hydro-meteorological variables. Long et al. (2014) used an ANN to predict TWS by other variables (e.g., precipitation, soil moisture, and temperature). Seyoum and Milewski (2017) employed ANN-based downscaling to achieve high-resolution TWS, by integrating GRACE TWS with other hydrological variables.

Thus, the objective of our study is to develop and test a replicable approach to downscale the coarse TWS from GRACE. To accomplish this objective, we assimilate observed TWS from GRACE with modeled TWS from a higher spatially resolved model. Multiple hydrological variables, such as precipitation, evapotranspiration, and runoff, are integrated with TWS, since all of them are involved in the terrestrial water cycle dynamics. For the sake of assimilation, an adaptive moving average partial least-squares regression, as an empirical approach, is consequently applied on a joint dataset consisted of multiple variables.

3.3.1 Statistical scenario

Datasets According to the water balance, the linear relationship between total water storage, precipitation, evapotranspiration, and runoff can be utilized for assimilation. We use the hydrological data from models with training period 2003-2009, which are listed in Table 3.1, both for training and prediction. The WaterGap Global Hydrology Model (WGHM) (Döll et al., 2003; Döll et al., 2014a) is a global water resources and use model, providing a spatial resolution of $0.5^\circ \times 0.5^\circ$. It simulates water flows among all relevant continental water storage compartments, including canopy, snow, soil, groundwater, lakes, reservoirs, rivers and wetlands. Despite the fine resolution for small-scale change, however, the uncertainties in climate forcings limit the accuracy of WGHM in monitoring large-scale water storage variation (Döll et al., 2014a; Döll et al., 2014b). Thus, we consider to merge WGHM with GRACE in order to obtain reliable estimation of TWS both at large scale and small scale. We use the monthly $1^\circ \times 1^\circ$ TWS fields from WGHM as a priori data from January 2003 to December 2009 for training, together with monthly catchment aggregates from GRACE for training and prediction. To make it comparable with GRACE TWS grids, we average the TWS from WGHM onto a $1^\circ \times 1^\circ$ TWS field. Meanwhile, the monthly TWS grids from GLDAS NOAH model field are also involved to compare with downscaled grids, with spatial resolution of 1° , from January 2004 to December 2009 (Rodell et al., 2004; Rodell and Beaudoin, 2015).

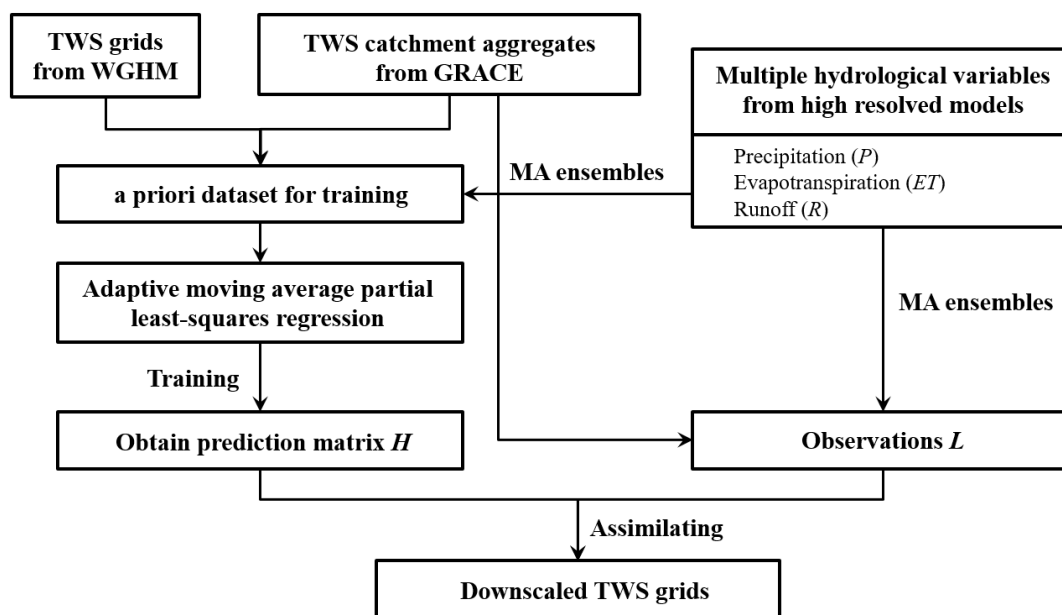


Figure 3.24: Illustration of the scenario for GRACE product downscaling.

In this downscaling framework, multiple hydrological variables (i.e. P , ET , R) as well as TWS are employed as inputs while the TWS grids are the only output of our model. Accordingly, this process can be considered as an assimilation of hydro-geodetic observations. We assimilate the observations from hydrological models and the high-resolved TWS from WGHM into our model to improve the spatial resolution of GRACE fields.

The flowchart of this statistical assimilation is shown in Figure 3.24. The associated information between TWS and multiple hydrological variables can be extracted via canonical joint modes,

using partial least-squares regression (PLR). The time-dependent temporal shifts between P , ET , R and ΔM are considered by the the moving average (MA) ensembles. Therefore, in order to assimilate the GRACE product with high resolution data from hydrological models, firstly we build up a prior training dataset, which consists of the TWS from GRACE and WGHM, and P, ET, R from a number of hydrological models. Next, we implement the MA-PLR model on this training dataset.

As discussed in 3.2, the regression on the residuals is more stable than on the full signals. Hence, before we implement the MA-PLR model, a pre-processing step is still necessary to subtract the dominant signals and retain the residuals from all the data. The cyclo-stationary mean is simply subtracted from GRACE and P, ET, R models, and subsequently we obtain the $\Delta M_{\text{GRACE}}, \Delta P, \Delta ET, \Delta R$ at residual level. In this study, for acquisition of TWS residuals from WGHM, we address two different schemes,

1. subtracting the cyclo-stationary mean of GRACE from WGHM:

$$\Delta M_{\text{WGHM}} = M_{\text{WGHM}} - \tilde{M}_{\text{GRACE}};$$

2. subtracting GRACE full signal from WGHM:

$$\Delta M_{\text{WGHM}} = M_{\text{WGHM}} - M_{\text{GRACE}}.$$

The first scheme removes the cyclo-stationary mean that is the dominant variation in TWS change, and adds it back to the output, which is estimated by the regression on the residuals. Thus, the observations from GRACE and P, ET, R are regressed on the difference between M_{WGHM} and \tilde{M}_{GRACE} . In other words, the dominant part of TWS from GRACE is maintained, and the rest part of TWS is assimilated by TWS from WGHM and other hydrological variables.

Different from the first scheme, the second scheme directly removes the full signal of GRACE from WGHM. It means that the difference between GRACE and WGHM is regressed by training on the a prior dataset. To investigate the performance of these two downscaling schemes, both of them are experimented in the following study.

In addition, there are also two different schemes when using P, ET, R from the hydrological models for assimilation,

1. using aggregates of P, ET, R over catchment:

$$\Delta P = \Delta P_{\text{basin}}, \Delta ET = \Delta ET_{\text{basin}}, \Delta R = \Delta R_{\text{basin}};$$

2. using P, ET, R grids corresponding to each grid point in ΔM_{WGHM} :

$$\Delta P = \Delta P_{\text{grid}}, \Delta ET = \Delta ET_{\text{grid}}, \Delta R = \Delta R_{\text{grid}}.$$

Table 3.5: Settings of three different schemes used for the training and prediction in the downscaling frame.

Scheme	TWS residuals from WGHM	P, ET, R residuals from models
1	$\Delta M_{\text{WGHM}} = M_{\text{WGHM}} - \tilde{M}_{\text{GRACE}}$	$\Delta P = \Delta P_{\text{basin}}, \Delta ET = \Delta ET_{\text{basin}}, \Delta R = \Delta R_{\text{basin}}$
2	$\Delta M_{\text{WGHM}} = M_{\text{WGHM}} - M_{\text{GRACE}}$	$\Delta P = \Delta P_{\text{basin}}, \Delta ET = \Delta ET_{\text{basin}}, \Delta R = \Delta R_{\text{basin}}$
3	$\Delta M_{\text{WGHM}} = M_{\text{WGHM}} - M_{\text{GRACE}}$	$\Delta P = \Delta P_{\text{grid}}, \Delta ET = \Delta ET_{\text{grid}}, \Delta R = \Delta R_{\text{grid}}$

In fact, both the first and the second scheme produce ensembles with the same size. Considering the different schemes proposed for residual calculation, three schemes are employed and compared in this thesis, as shown in Table 3.5. As a consequence, referring to (2.64), the training dataset is composed by

$$\begin{aligned}
 \Delta M_{\text{WGHM}} &= L H = U_L K \\
 &= [\Delta P \ \Delta ET \ \Delta R \ \Delta M_{\text{GRACE}}] [H_P \ H_{ET} \ H_R \ H_M]^T, \\
 \Delta P &= [\Delta P_1 \ \Delta P_2 \ \cdots \ \Delta P_m], \\
 \Delta ET &= [\Delta ET_1 \ \Delta ET_2 \ \cdots \ \Delta ET_m], \\
 \Delta R &= [\Delta R_1 \ \Delta R_2 \ \cdots \ \Delta R_m].
 \end{aligned} \tag{3.46}$$

In (3.46), H and K are the prediction matrices that need to be determined. ΔP , ΔET , ΔR are $n \times (k \times m)$ matrices, assembling m number of models and MA($k - 1$) shifting. In this case study, we gain the ensemble of ΔP , ΔET , ΔR from different number of hydrological models. We select the order of 11 for the MA model in order to take all the epochs in a year into computation. Thus, ΔP_m , ΔET_m , $\Delta R_m (n \times k)$ are composed in form of a MA(11) model with respect to (3.42), containing $k = 12$ time series. $\Delta M_{\text{WGHM}} (n \times s)$ is obtained from WGHM for training, in which s is the number of grids within the catchment. $\Delta M_{\text{GRACE}} (n \times 1)$ represents one single time series from the GRACE observed TWS after aggregation over the catchment. Therefore, the prediction matrix K as well as H is regressed by implementing MA-PLR algorithm on the training datasets ΔM_{WGHM} and L . As a result, the downscaled TWS are eventually estimated by LH or $U_L K$. The output TWS from the assimilation approach is finally calculated on a $1^\circ \times 1^\circ$ grid.

3.3.2 Case study: downscaling GRACE in Amazon

Three assimilation schemes are exemplary performed in Amazon basin for a case study. In this case, for convenience of comparisons with GRACE and WGHM, both the training and prediction step are implemented based on the same time period 2003–2009. The downscaled TWS in Amazon at different epochs is shown in Figure 3.25 as well as the TWS grids from GRACE, WGHM and GLDAS. Comparing GRACE with WGHM, they represent distinct different patterns. GRACE provides reliable measurement of large-scale terrestrial water storage change, while WGHM emphasizes the detailed water mass variation at smaller scale.

According to Figure 3.25, the assimilated TWS refines GRACE with higher spatial resolution. On one hand, comparing with the patterns from GRACE, the assimilated TWS grids have similar patterns, while it is clear that they are downscaled in terms of higher spatial resolutions. On the other hand, comparing with the patterns from WGHM, the water mass changes along the water flows are also revealed in the assimilated TWS grids, which meet our expectation. For example, in September 2005, GRACE only provides a footprint in the northeastern Amazon. The assimilated TWS keeps in accordance with GRACE, revealing similar patterns at large-scale. Meanwhile, detailed variations are emphasized spatially along the river main stream in the assimilated TWS, which is also represented by WGHM. As a result, we find that the TWS from GRACE and WGHM are successfully assimilated into our estimation with more details in spatial domain.

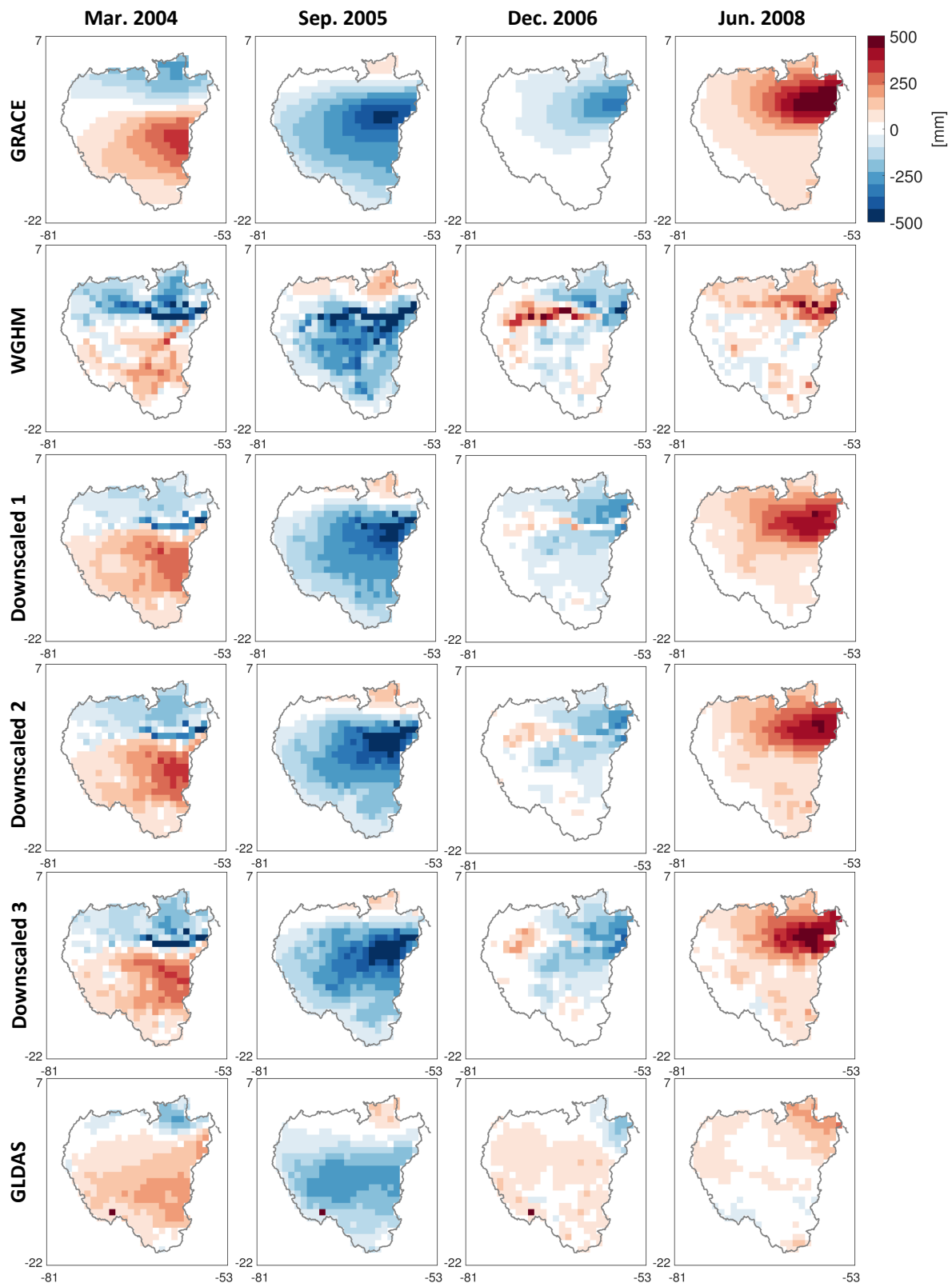


Figure 3.25: The downscaled TWS in Amazon from three different schemes TWS grids as well as TWS grids from GRACE, WGHM and GLDAS, at four different epochs (i.e., March 2004, September 2005, December 2006, June 2008).

The downscaling of spatial resolution is achieved by the three different schemes of Table 3.5, visualized in Figure 3.25. Among those patterns, scheme 3 indicates more details than the other two schemes. It indicates that using multiple hydrological variables P, ET, R at specific grid point produces higher spatial resolutions than using aggregates over catchment.

In addition, the TWS from GLDAS represents an incomparable pattern with other sources, indicating not even as good as the spatial resolution of GRACE product. Therefore, the TWS from GLDAS is not further discussed and compared with others in the following content.

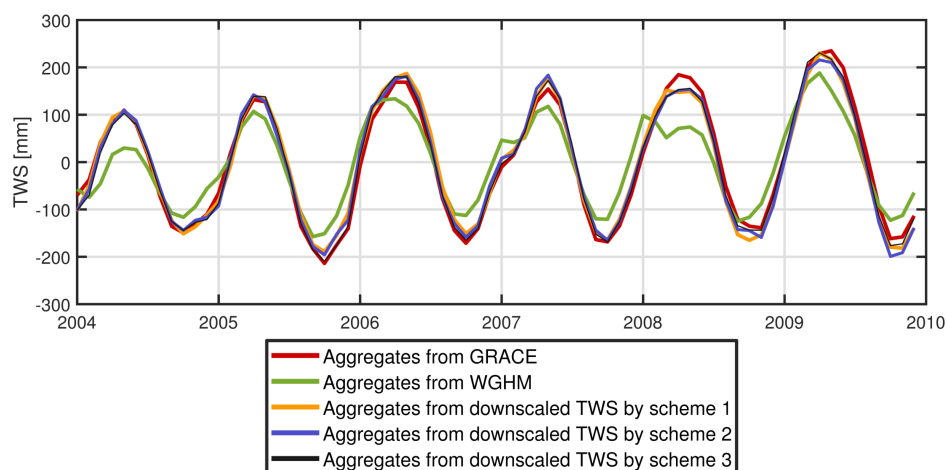


Figure 3.26: Monthly aggregates of the TWS over the Amazon basin from GRACE, WGHM and assimilations using three different schemes.

Validation by aggregation over catchment In order to validate the downscaled TWS, we aggregate the TWS grids from GRACE, WGHM, and assimilated versions over Amazon, as plotted in Figure 3.26. The aggregates of TWS from three different assimilations fit extremely well with the aggregates from GRACE. The assimilated TWS approaching to GRACE indicates that these estimated TWS grids can be considered equivalently as GRACE product. Comparing with WGHM, a distinct disagreement exists between the aggregates from assimilated versions and WGHM.

Additionally, using three different schemes for training and prediction produces equivalently reliable estimations, which are represented in Figure 3.26. In other words, either subtracting the seasonal mean of GRACE or the full signal of GRACE from WGHM does not significantly affect the assimilation results.

According to both Figure 3.25 and 3.26, the consistencies with GRACE in aggregate time series follow the mass conservation in a catchment, while the differences in spatial patterns indicate a adjusted redistribution after our assimilations. Therefore, assimilating WGHM into GRACE with multiple hydrological variables indeed downscales the spatial resolution of GRACE.

Annual amplitudes and linear trends The linear trend and the annual amplitude of assimilated TWS as well as of GRACE and WGHM in Amazon are quantified by a simple least-squares linear and harmonic regression, and visualized in Figure 3.27. Comparing with

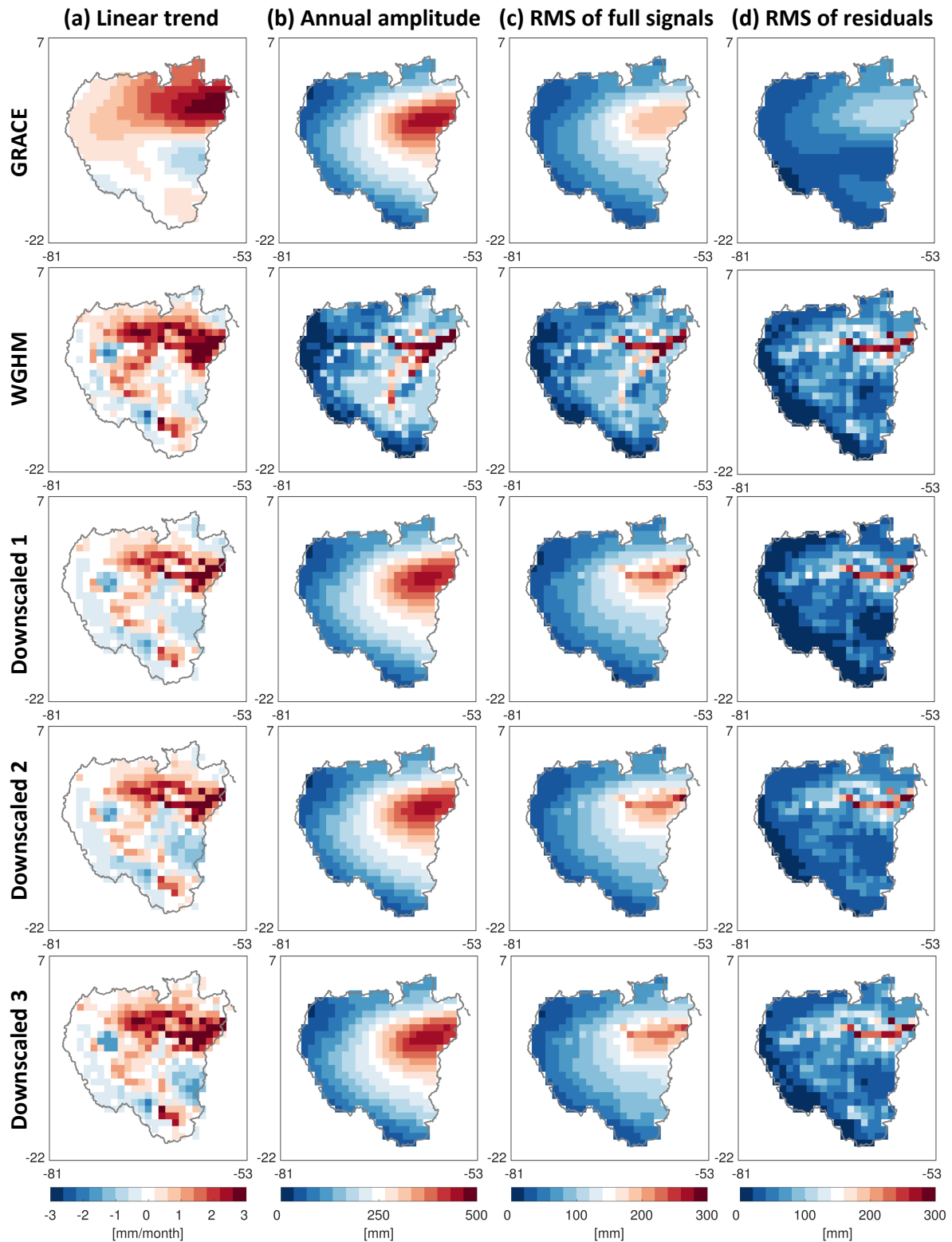


Figure 3.27: (a) The linear trend, (b) the annual amplitude, (c) the RMS of full signals, and (d) the RMS of residuals of TWS grids in Amazon basin derived from GRACE, WGHM, and downscaled TWS by assimilation using three different schemes.

GRACE, the annual variations of assimilated TWS match exactly with pattern from GRACE. From Figure 3.27 (b), it indicates that the large-scale features of GRACE-observed TWS are maintained in the downscaling process, according to the consistent annual amplitudes. However, the small-scale features revealed in WGHM are not visible in assimilations. These similar annual patterns with GRACE and differences between WGHM and assimilates illustrate that WGHM does not contribute remarkably to the annual variation in TWS through this assimilation approach. The annual signals from GRACE still play a dominant role in the assimilated TWS.

Conversely, the linear trends from GRACE and assimilates show notable difference, while the trend from assimilations represent patterns much closer to WGHM. Particularly, the pattern of assimilation by scheme 3 is more relevant to WGHM. In Figure 3.27 (a), the evident positive trend along the water flow with east-west direction in Amazon is not revealed in GRACE but identified from WGHM and our assimilation. Additionally, the strong negative trend in southeastern Amazon is enhanced by our assimilated TWS, which is also reflected in GRACE. In a word, the assimilated TWS evidently downscales the spatial resolution in aspect of linear trend, retaining the large-scale features and refining GRACE at small scale.

From Figure 3.27 (c), all the three assimilates improve the spatial resolutions distinctly, comparing with the RMS of GRACE. Both the large-scale features of GRACE and the small-scale variation from WGHM are visible in our downscaled TWS grids. Comparing Figure 3.27 (c) and (d), the notable variation in northeastern Amazon is eliminated in GRACE on residual levels, while is still retained in WGHM and assimilation. It indicates that these anomalous change along the river flows in the basin cannot be recognized from GRACE product. This deficiency in GRACE product is successfully compensated by assimilation with WGHM and multiple hydrological variables from high-resolved models.

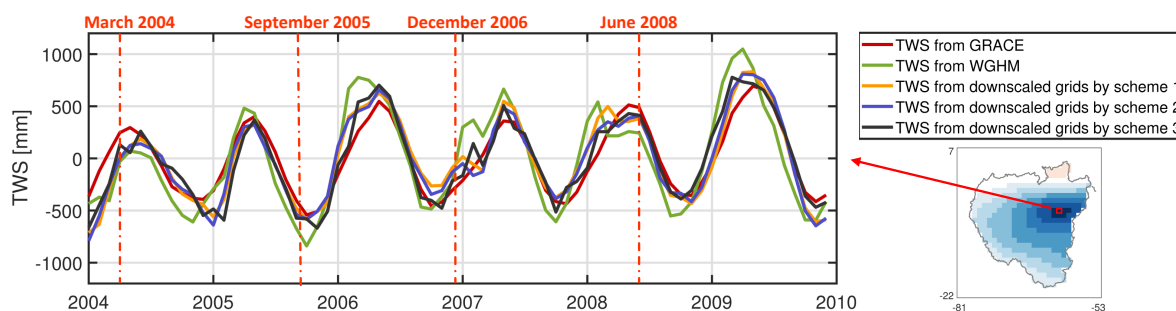


Figure 3.28: Monthly TWS of one arbitrary grid point in the Amazon basin from GRACE, WGHM and assimilations using three different schemes.

As shown in Figure 3.27 (b), it seems that downscaling is not effective due to the same spatial patterns of annual amplitude from GRACE and assimilation. In order to investigate the performance of downscaling, we choose an arbitrary gridcell in the northeastern part of Amazon to see the TWS over time. Figure 3.28 shows the time series of this selected grid point from GRACE, WGHM and assimilated products from the three different schemes. Although the aggregates of assimilated TWS over catchment shows perfect agreement with aggregates from GRACE that were illustrated in Figure 3.26, the difference is still visible in the time series at grid scale.

According to Figure 3.28, assimilated TWS is capable to capture the anomalous change at certain epochs, comparing with WGHM. Regression on the residual level in our downscaling frame explains this invisible difference in annual variation, since we acquire the residuals by subtracting the dominant annual component. In particular, evident differences are noticed at some epochs, e.g. March 2004, September 2005, December 2012, June 2008, as plotted in Figure 3.26. The corresponding spatial patterns at those epochs are visualized in Figure 3.25, respectively. In fact, the anomalous variations that is unobservable in GRACE are spatially reflected in downscaled TWS grids.

Validation by water balance The misclosure ε of the terrestrial water balance in a catchment is introduced to validate our assimilation results, which mathematically writes

$$\varepsilon = P - ET - R - \frac{dM}{dt}, \quad (3.47)$$

where the water storage fluxes dM/dt is calculated by the first derivative of TWS change M . We use the ensemble mean of all the available models listed in Table 3.1 for each variable P , ET , R , and then calculate the misclosure ε for each grid cell at each epoch as the imbalance of water budget in Amazon. Based on the misclosure, we evaluate the performance of our downscaled TWS fields in terms of ε , mean of the misclosure $\bar{\varepsilon}$, and $\text{RMS}(\varepsilon)$.

In Figure 3.29, the imbalance of the water budget is large in the northwestern part of the basin, and at the grid points along the river near the outlet. Comparing with WGHM, GRACE has better performance in terms of water balance, although the spatial resolution of GRACE is coarser. The mean of water balance in Figure 3.29 (b) represents a similar performance from each source. Large RMS values of misclosure in Figure 3.29 (c) from WGHM indicates the unprecise estimation for TWS, comparing with GRACE. Based upon the pattern of misclosures, the assimilated TWS perform stably in most regions of Amazon. Comparing the assimilated results with GRACE and WGHM, most parts of basin represent relatively the same level of closing errors, indicating the reliability of our assimilation. In northeastern Amazon, the misclosures from our assimilation match with the pattern of GRACE rather than WGHM, according to Figure 3.29 (a), (b), and (c). This consistency with GRACE in water balance suggests that the downscaled TWS grids maintain the same level of accuracy as GRACE, even though the assimilated products do not improve the accuracy of TWS estimation. The bias in the TWS from GRACE is still there in the downscaled TWS, that is not significantly eliminated by assimilating WGHM and hydrological variables. Comparing the RMS of TWS in Figure 3.27 (c) (d) with the RMS of misclosures in Figure 3.29 illustrates that our downscaled TWS enhances the small-scale variation in Amazon with aid of WGHM, and also ensures the accuracy and reliability at the same level as GRACE.

Performance of downscaling by different number of joint modes Since we already found in 3.2.5 that a different number of joint modes used in the PLR model causes differences in prediction results, it is essential to see the influence on the downscaled TWS. Therefore, to evaluate the performance of assimilation by different number of joint modes, we compare our assimilates with TWS from both GRACE and WGHM in terms of NSE and RMSE. In this case, we choose the third scheme in Table 3.5 for assimilation. 3, 5, 10, 15 joint modes between

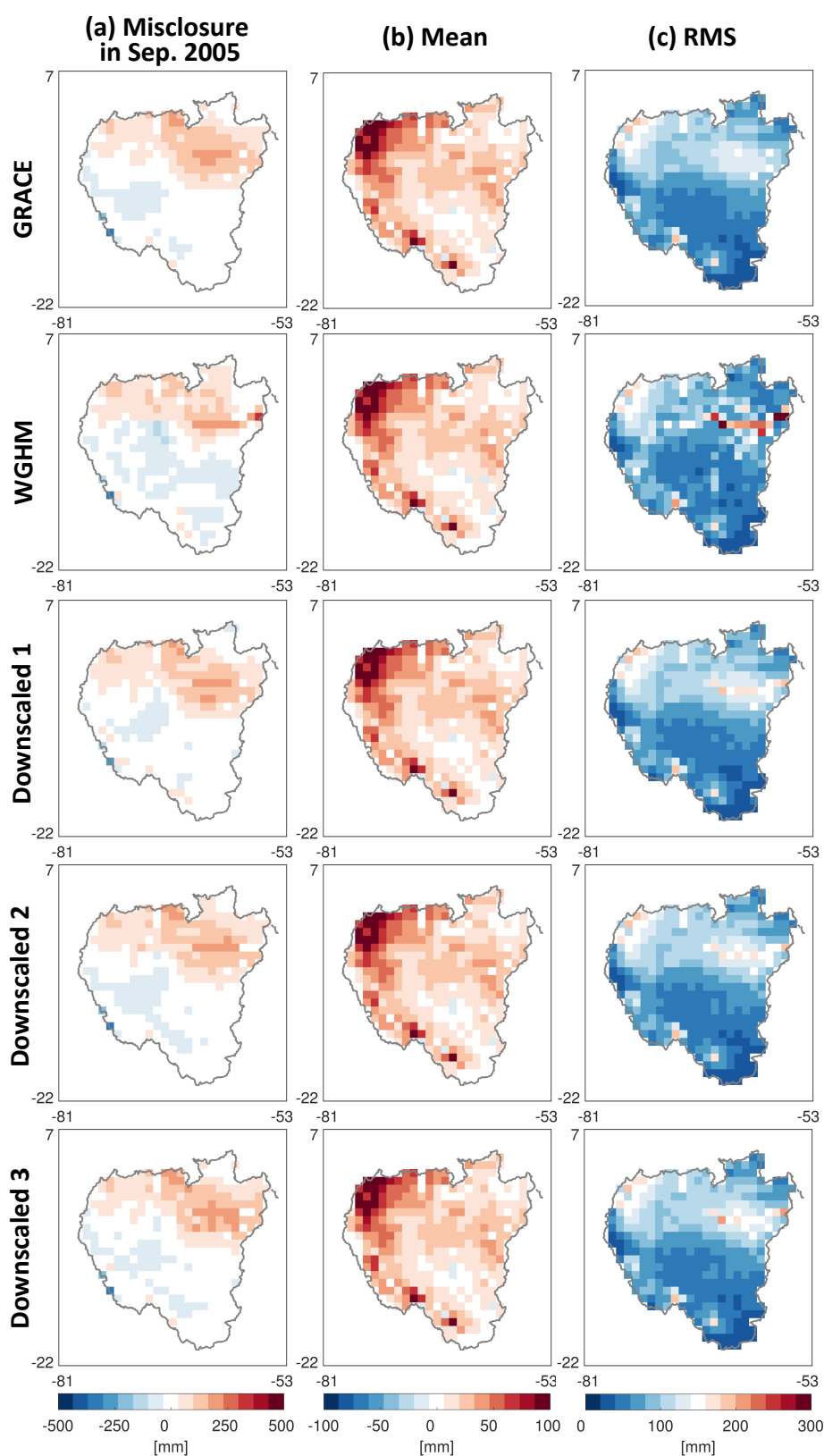


Figure 3.29: (a) The misclosure of the water balance in Amazon basin at epoch September 2005 as well as its (b) mean and (c) RMS, in which the water storage fluxes are obtained from GRACE, WGHM, downscaled TWS from three different schemes, respectively.

ΔM_{WGHM} and the ensemble of observations L are exemplarily selected in MA-PLR implementation, as shown in Figure 3.30, respectively. Additionally, an arbitrary epoch is visualized as an example.

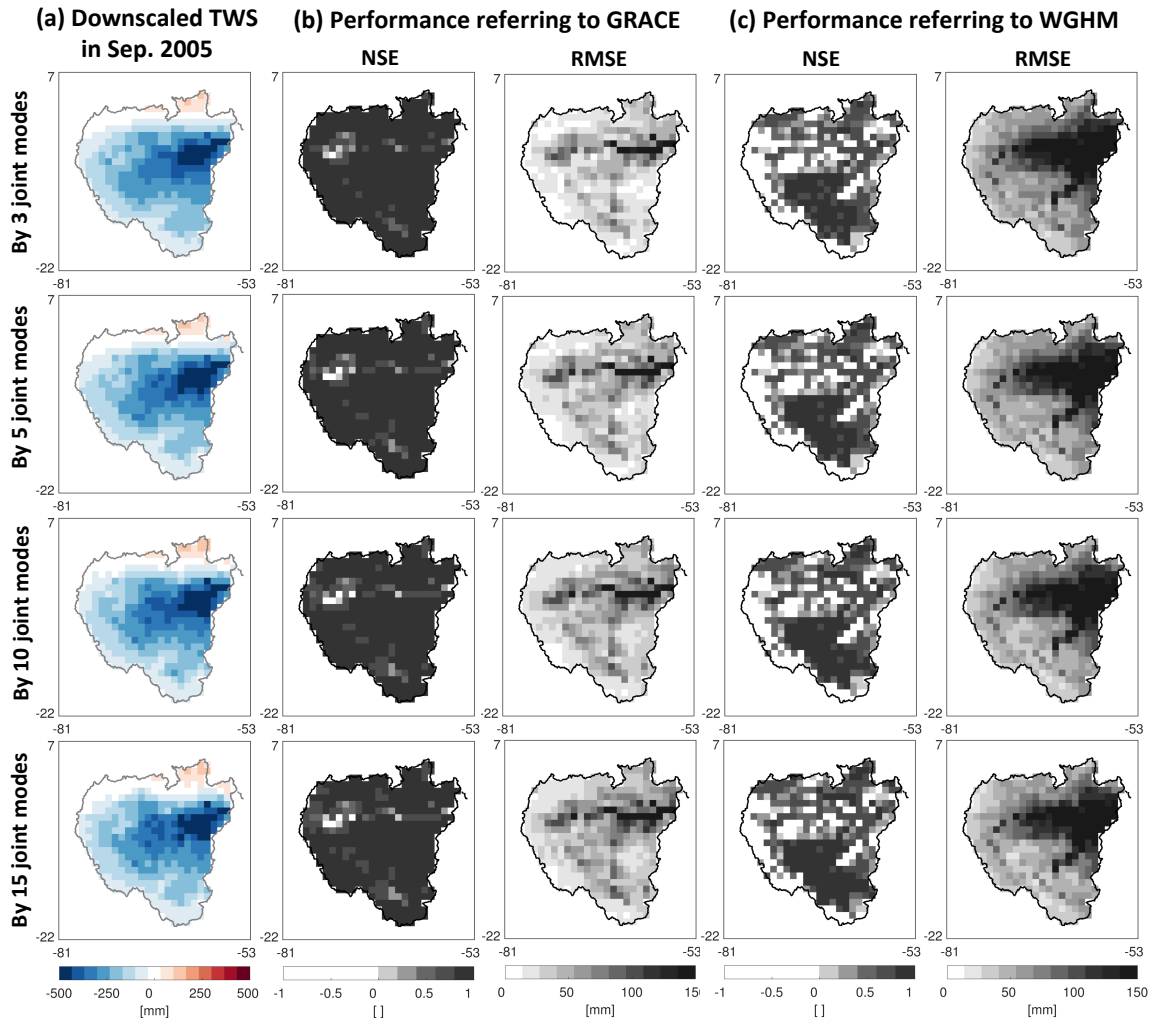


Figure 3.30: Downscaled total water storage in Amazon basin using adaptive moving average partial least-squares regression by different number of joint modes (i.e. 3 joint modes, 5 joint modes, 10 joint modes, 15 joint modes) (a) in September 2005 (as example), and their performances evaluated by NSE and RMSE with respect to (b) GRACE and (c) WGHM, respectively.

From Figure 3.30 (a), in September 2005, we find that the more joint modes we use for assimilation, the higher spatial resolution we acquire. Considering GRACE as reference, in Figure 3.30 (b), all the assimilated products fit very well with GRACE (NSE close to 1) in most part of the Amazon. The notable differences remain on the grid points along the river network in the basin, according to Figure 3.30 (b). When referring to WGHM, in Figure 3.30 (c), the down-scaled TWS shows extremely good agreement in the South and along the river flows in the basin, with NSE above 0.5. Large RMSE in northeastern Amazon represents large discrepancy between WGHM and assimilates.

Comparing the NSE with the RMSE from each level of mode selection, the increase of number of joint modes induces a smaller NSE and a larger RMSE, indicating worse agreement with GRACE. On the contrary, the increase of number of joint modes results in a larger NSE and a smaller RMSE, indicating better agreement with WGHM. In other words, the downscaled TWS approaches WGHM gradually when more number of joint modes are retained for regression, while the discrepancy becomes progressively larger between GRACE and downscaled TWS if fewer joint modes are used in the assimilation frame. It can be easily understood that the more joint modes we extract, the more information of variability in TWS we make use of. However, more joint modes may also introduce more uncertainty and noise in the regression model. Therefore, either too many or too few modes are not acceptable. According to the patterns in Figure 3.30, slight differences among the patterns by different selected number of modes indicate that the performance of PLR does not significantly rely on the number of joint modes used for GRACE downscaling. Nevertheless, we still need to find a balance to utilize a proper number of joint modes in the regression for downscaling. In this work, we eventually adopt 5 joint modes as a general choice.

Regarding the patterns shown in Figure 3.30 (b) and (c), all the three assimilated TWS grids are much closer to GRACE than to WGHM. From this aspect, it proves the reliability of our assimilation for downscaling of GRACE.

Mode analysis of downscaled TWS In order to investigate the validity of this downscaling, we refer to the most dominant modes in the downscaled TWS variation in the Amazon basin. We apply a PCA decomposition on the downscaled TWS as well as TWS from GRACE and WGHM. Thus, we obtain the temporal PCs and the spatial EOFs of each mode in TWS. The first five modes from each field are selected to analyze, since they cover already more than 90% of the total variance.

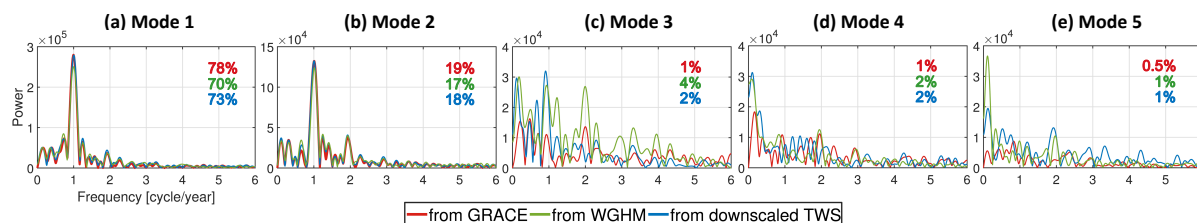


Figure 3.31: Power spectra of the temporal PC from the first 5 modes in total water storage changes in Amazon basin, which are obtained from GRACE, WGHM, and downscaled TWS, respectively.

The power spectra of each mode are visualized in Figure 3.31. Mode 1 and mode 2 of all the three different fields reveal strong responses at a frequency of 1 cycle per year, representing the annual variations. A perfect agreement is reached among GRACE, WGHM and downscaled TWS in the first two modes. This consistency indirectly proves the validity of the downscaled TWS. However, downscaled TWS behaves inconsistently with GRACE and WGHM in the mode 3, 4, 5. The notable power of semi-annual components from downscaled TWS is not revealed from either GRACE or WGHM. The limited spatio-temporal resolution of GRACE probably results in the weak spectra of signals of semi-annual and higher frequencies. This indicates that the strong semi-annual signals are probably contributed by the P, ET, R from hydrological models. By comparison, downscaled TWS represents evidently power spectra at

low frequency in mode 3, 4 and 5, in accordance with WGHM. This coherency explains the agreement of linear trend patterns, which can be considered as the long-term variation, from WGHM and assimilates in Figure 3.27 (a). From Figure 3.31, the distinct differences in mode 3, 4, 5 explain the different performances from GRACE, WGHM and our assimilated TWS in Figure 3.27 (c). Moreover, the discrepancy among the time series of GRACE, WGHM and assimilates in Figure 3.28 now can also be interpreted by the different power responses in those less important modes (i.e., mode 3, 4 and 5).

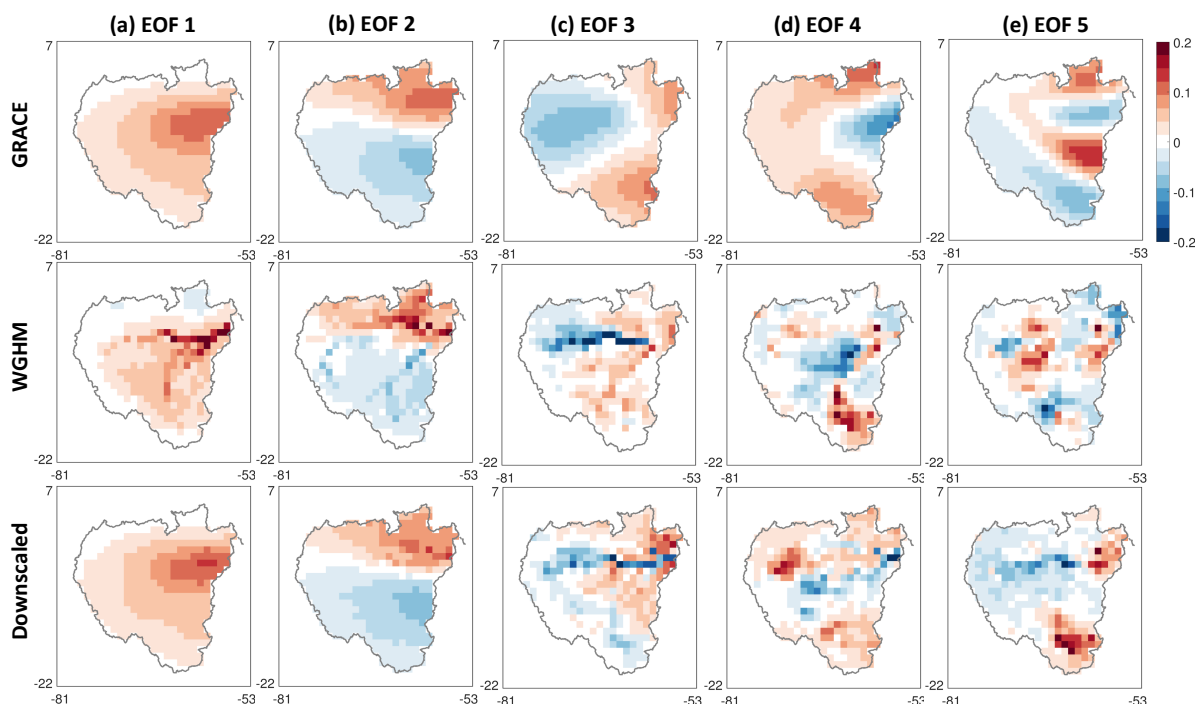


Figure 3.32: The corresponding spatial EOFs corresponding to the temporal PCs (represented in spectral domain in Figure 3.31) of the total water storage changes in Amazon basin, producing from GRACE, WGHM, and downscaling, respectively.

Additionally, from the viewpoint of spectra, the large-scale dominant changes like annual signals can be detected by GRACE, while the signals of minor variation at small-scale in Amazon cannot be gained from GRACE observations. In other words, downscaled TWS retains the dominant annual signals from GRACE, meanwhile compensates GRACE for the insufficient acquisition in linear trend and semi-annual terms. However, it is still unclear whether it is a general conclusion for any other catchments or just a special case only applied to Amazon.

The spatial associated EOFs of each mode from GRACE, WGHM and downscaled TWS are visualized in Figure 3.32. Both the EOF 1 and EOF 2 in Figure 3.32 (a) and (b) represent the dominant annual variations, corresponding to the spectra in Figure 3.31 (a) and (b). The EOF 1 represents the annual change occurring mainly in the center part of the basin, particularly along the Amazon river. The EOF2 clearly shows an annual variation in the upper part of Amazon. These two EOFs reflect the spatial pattern of the annual variation with different phases in Amazon. Regarding the power spectra of mode 3 in Figure 3.31 (c), the semi-annual change is mainly detected along the river main stem in Amazon, which is not sensed by GRACE. Ac-

cordingly, EOF 4 and 5 illustrate the spatial pattern of the long-term variation within the basin, which is invisible from GRACE. The weak semi-annual signal and the insensitivity to the long-term change of GRACE likely result in the difference between GRACE and our downscaled TWS at certain points in the northeastern part of basin, referring to Figure 3.25 and 3.27.

The spatial patterns in Figure 3.32 let us visually understand the process of our downscaling. The first and the second mode in GRACE are retained in our assimilation, accomplished by removing the cyclo-stationary mean of GRACE in training and adding it back after regression. As a consequence, the annual amplitude from downscaling TWS is nearly the same as GRACE, as shown in Figure 3.27 (b). From mode 3 to mode 5, the downscaled TWS make use of WGHM instead of GRACE, and consequently, improve the spatial resolution of GRACE. Therefore, our downscaling can be regarded as the combination of GRACE and WGHM with different modes.

3.4 Discussion and summary

This chapter accomplishes the modelling of terrestrial water storage at catchment scale by assimilating multiple hydrological variables from models, using statistical approaches. The insufficient spatial resolution and limited observing period of GRACE for hydro-geodetic applications are emphasized as a motivation for applying this modelling. The linear relationships between water storage and water cycle are as the basis of our modelling, which is characterized in this chapter as well as the seasonality characteristics.

To fulfill the terrestrial water storage modelling, three different approaches, i.e., least-squares prediction/collocation, principal component regression, partial least-squares regression, are implemented based on GRACE observed water storage changes and precipitation, evapotranspiration, runoff from hydrological models. All the three approaches are successfully applied for water storage prediction that the prediction results in most catchments generally meet our expectation. Comparing the performance of least-squares prediction on anomalies and least-squares collocation with parameters, it has been proved that predicting directly on the residuals of total water storage instead of its full signal with model parameters provides more accurate results and less biases. This improvement owes to the dominant seasonal variability in hydrological observations, of which the cyclo-mean fits much better than a parametric harmonic fit. Based on this strong seasonality in hydrological variables, subtracting the cyclo-stationary mean from the observations makes the regression procedure simple and efficient.

Considering the relevancy of total water storage change to the other hydrological variables (i.e. precipitation, evapotranspiration, runoff), partial least-squares regression has a more stable performance than the other two methods. It has advantage in making use of associated variations from both predictand and predictor, and reducing the effect of uncorrelated errors and noise. Another outstanding feature is that it reduces the computational effort by the reduction of data dimension, which is also benefited from principal component regression.

To acquire a higher quality of prediction, an adaptive moving average model is integrated with those three different regression models. Considering the existed time-invariant temporal shift among variables in the water cycle, we predict the water storage by an ensemble of observations in terms of a moving average process. This moving average process highly improves

the accuracy of prediction, especially for least-square prediction. Practically, we already obtain sufficient accuracy from least-squares prediction combined with a moving average regression in predicting the total water storage.

From the aspects of observation datasets, an assimilation scheme of combining multiple hydrological variables provides us the optimal performance, for which the predictions have much better agreement with GRACE. Runoff outperforms other variables when predicting water storage by principal component regression and partial least-squares regression. Using precipitation to predict the total water storage in a moving average way performs a notable improvement.

For evaluation of our water storage predictions, we select several catchments, i.e., Amazon, Yangtze, Danube, Mackenzie, Lena, for case study. The predictions in those catchments, which are under different climatic conditions, show up various performances. Using either of the three approaches with moving average can achieve good prediction in the tropical catchments. However, the water storage change in boreal catchments is still poorly estimated in terms of the negative CNSE. Least-squares prediction, principal component regression, and partial least-squares regression provides the prediction in boreal catchments at the same level of accuracy. In fact, not only a temporal shift exists between total water storage and other hydrological variables, but also the solid water mass variation is not involved in the dynamic water cycle. This liquid/solid water mass variation results in a non-linear relationship between water storage and the other hydrological variables. Using a moving average process can still hardly model the solid component of water mass change. The weak cyclo-stationarity in boreal catchments lead to the low accuracy of the prediction. It is still a challenge for us to model the terrestrial water storage change in high-latitude regions.

Moreover, to achieve finer spatial resolution of terrestrial water storage, a spatial downscaling of GRACE is consequently accomplished by assimilating precipitation, evapotranspiration, runoff from hydrological models as well as GRACE-observed TWS with TWS grids from WGHM. As a result, the TWS changes in Amazon basin are finally assimilated into a $1^\circ \times 1^\circ$ grid with higher resolution than GRACE product.

This assimilation produces acceptable results. The downscaled TWS grids are perfectly close to GRACE-observed TWS, comparing with catchment aggregates from both from WGHM and GRACE. The existed differences between GRACE, WGHM and downscaled TWS at specific pixels indicates the improvement of TWS estimation by our assimilation. Integrating hydrological variables (e.g., precipitation, evapotranspiration, and runoff) with GRACE and WGHM in the assimilation reproduces the TWS with fine resolution, which is capable to recognize the water storage changes at sub-catchment and even smaller scales. Although introducing multiple hydrological variables does not decrease the misclosures of water balance, the downscaled TWS represents more detailed information in certain area, for example, along the river flow of the basin. In other words, integrating GRACE with WGHM as well as other hydrological variables takes the advantage of the sensitivity of GRACE at large-scale variations and WGHM and other hydrological variables at small-scale changes. Moreover, since the Amazon basin is chosen for a case study, it is still uncertain that our downscaling framework is also applicable for any other type of catchments. Hence, more experiments and analyses need to be done in the future to prove the feasibility of our assimilation in GRACE downscaling.

Most importantly, the performance of the MA-PLR approach demonstrates its capability in data assimilation. It convinces us that the MA-PLR is an applicable approach for spatial downscaling of GRACE. Different from Kalman filter, PLR does not require any dynamic models. Despite of its good performance on downscaling, the comparisons between PLR and model-based approach (e.g. ensemble Kalman filter) and empirical approach (e.g. artificial neural network) are worth to do in order to test the reliability, which is already beyond the scope of this thesis. Additionally, a proper validation of downscaled water storage against in-situ measurements still needs to be done in the upcoming research.

The achievement in this chapter for filling the observing vacancy and densifying the spatial resolution provides us confidence in estimation of terrestrial water storage by hydro-geodetic observations in a statistical way. On one hand, the accurate estimation makes the water storage change available though the limitation exists in GRACE products. Both prediction of large-scale terrestrial water mass change in the future and reconstruction in the past become feasible. On the other hand, terrestrial water storage with fine resolution provides us more accurate information for local hydrological and climatic studies. It is particularly useful in those areas lacking of hydrological monitoring networks. Terrestrial water storage of higher spatial resolution can be potentially applied in drought and flood analysis at specific sites. In a word, assimilating spaceborne terrestrial water storage observations with hydrological variables from models helps us to better understand the water storage-water cycle relationships in a comprehensive way.

Chapter 4

Phase Difference and Causality Analysis

Many phenomena (e.g., global warming, glacier melting, ocean level change) happen not simultaneously in nature but in a causality relationship. The terrestrial water cycle is generally a dynamic process, in which water storage changes in reaction to the input (i.e., precipitation) and the output (i.e., river runoff, evapotranspiration) with relative leads or delays. It forces us to characterize the relationships between water storage and water cycle in terms of not only amplitude but also phase. Phase difference is an important indicator, which helps comprehend the cause-effect relationship between two signals in terms of leads or lags. The temporal shift is already considered in Chapter 5 for modelling water storage by the adaptive moving average approach. The improvement of estimation accuracy has proved the significant effect of phase difference in a dynamic hydrological system. However, the quantification of the phase shift between water storage and other hydrological variables (i.e., precipitation, evapotranspiration, runoff) in a catchment is not done yet.

Moreover, the ocean-land-atmosphere circulation is also dynamic. The terrestrial water mass variation is involved in such a dynamic circulation. Investigation on the causal relationship helps us understand the teleconnection between terrestrial water storage and climate change. To explain the causality of terrestrial water cycle responding to any climate changes, the phase differences are necessarily taken into consideration.

Hence, in order to further characterize the causal relationships and interpret the dynamic processes, we need to quantify the phase differences and the time lags. In this chapter, we introduce the cross-correlation coefficient, the Hilbert transformation, as well as the wavelet coherency as analysis tools to estimate the phase and time shifts.

The relative phase and time shifts between terrestrial water storage and water cycle at catchment scale are estimated using the Hilbert transformation approach. Since the climate phenomenon occurs generally with non-unique frequency, their impact on the terrestrial water cycle cannot be quantified by simple temporal shifting. In this case, we refer to the wavelet spectrum and coherency to interpret the causality of climate change and terrestrial water mass variation and circulation.

4.1 Phase shift detection methods

Correlation coefficients are widely used in time series analysis as a powerful metric, reflecting the relationship between two time series in phase. However, a correlation coefficient is only capable to identify whether these two time series are in phase or out of phase. Thus, we firstly introduce the cross-correlation to analyze the time shift instead of correlation.

Cross-correlation The time shift between two time series can also be detected by cross-correlation coefficient. The k^{th} -order cross-correlation between two time series x and y is defined as

$$\rho_k = \frac{\sum_{i=1}^{n-k} (x_i - \bar{x})(y_{i+k} - \bar{y})}{\sqrt{\sum_{i=1}^n (x_i - \bar{x})^2 \sum_{i=1}^n (y_i - \bar{y})^2}}. \quad (4.1)$$

Similar to correlation, \bar{x} , \bar{y} are the mean of x , y , respectively. k denotes the lag between two time series x and y . In practice, we use cross-correlation in this chapter to detect the time shift between x and y , at which the cross-correlation between x and y reaches the peak value. Hence, in this case, k is obtained as the estimated time shift. Notice that cross-correlation only allows to recognize the shifting on epoch level, but not on the phase level.

Furthermore, in order to quantify both the phase delay and the temporal shift between two time series, therefore, we subsequently introduce the Hilbert transformation here. Unlike correlation coefficient only in time domain, the coherency both in time and spectrum domain can be evaluated by wavelet spectrum. Thus, we introduce the wavelet transformation in the following content.

4.1.1 Hilbert transformation and time lag analysis

Hilbert transformation To measure the influence of climate phenomenon (e.g., ENSO) on the terrestrial water storage, an analysis of phase difference is involved in our study. For the purpose of estimating the phase shift between two time series, we introduce the Hilbert transform.

The Hilbert transform of a signal $x(t)$ is defined in the time domain as a convolution between the Hilbert transformer $1/(\pi t)$ and the signal $x(t)$ (Saff and Snider, 1976) as

$$\mathcal{H}[x(t)] = y(t) = \frac{1}{\pi} \int_{-\infty}^{\infty} \frac{x(\tau)}{t - \tau} d\tau, \quad (4.2)$$

where $y(t) = \mathcal{H}[x(t)]$ results in a new time series with all of the original frequency components shifted in phase by $\pi/2$. We use this phase shifting property to define a complex analytic signal $z(t)$ (Bracewell, 1986) as

$$\begin{aligned} z(t) &= x(t) + i \cdot y(t) \\ &= (1 + i\mathcal{H})x(t). \end{aligned} \quad (4.3)$$

Clearly this Hilbert transformation makes a signal in time domain transform to another time domain signal with $\pi/2$ phase shift. Making a regression of target signal with the real part and imaginary part of transformation, the phase difference can then be estimated. Therefore, following Phillips et al. (2012), we perform a Hilbert transform on reference time series $p(t)$ in a least squares regression to estimate the phase difference by

$$l(t) = a + b \cdot p(t) + c \cdot \mathcal{H}[p(t)] , \quad (4.4)$$

where $l(t)$ is the observation time series, a, b, c are the parameters to be modeled.

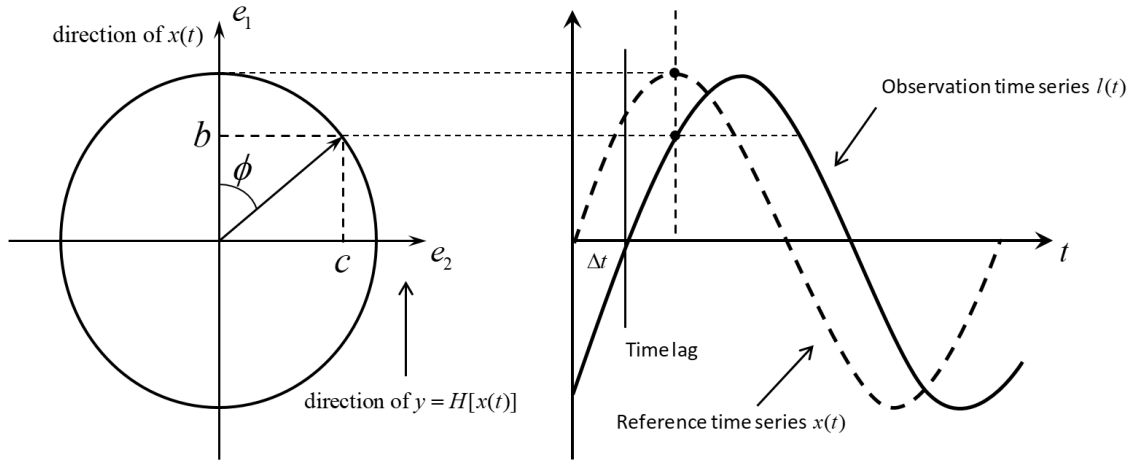


Figure 4.1: Illustration of the phase difference and time lag between time series $l(t)$ and Hilbert transformed time series. The parameters b and c estimated in the Eq. (4.4) are used in amplitude and phase calculation in Eq. (4.5) and (4.6).

As illustrated in Figure 4.1, the phase lag ϕ between $p(t)$ and $l(t)$ is obtained by

$$\phi = \arctan\left(\frac{c}{b}\right) , \quad (4.5)$$

and the influence of $p(t)$ on signal $l(t)$ is quantified by the amplification factor A

$$A = \sqrt{b^2 + c^2} . \quad (4.6)$$

According to the phase lag ϕ , we can subsequently quantify the time lag Δt in units of months between climate indices $p(t)$ and terrestrial water storage observations $l(t)$ by $\Delta t = \phi \cdot 6/\pi$.

4.1.2 Wavelet transformation and coherency analysis

The Fourier transform is a powerful tool for analyzing the components of a stationary signal, where there is no change in the signal properties. However, in nature, often the observation

signals are non-stationary. Therefore, it demands more accurate information of frequency variation in time. Unlike the Fourier transform that gives no information on time but only on frequency, the wavelet transform provides a spectrum that is localized in both time and frequency domain (Farge, 1992).

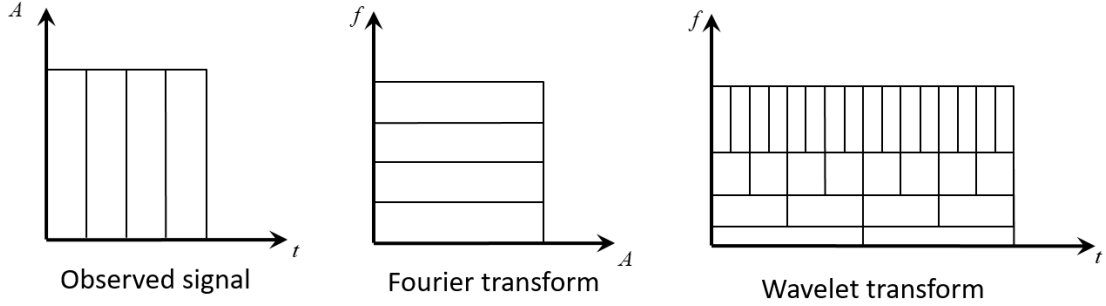


Figure 4.2: Comparison of (middle) Fourier transformation and (right) wavelet transformation with respect to the target signal (left) in time resolution at different frequencies.

Different from the Fourier transform, the spectrum from wavelet transformation is acquired in increased time resolutions at ascending frequencies. The difference between Fourier and wavelet transform is illustrated in in Figure 4.2. From the figure, we realise that the higher temporal resolution in spectrum results in lower resolution in frequency. In other words, low frequencies are better resolved in frequency domain, and signals of high frequency are better represented in time domain.

Continuous wavelet transform Wavelet transformation contains information similar to Fourier transformation, but with special properties of the wavelets. The higher the resolution in time, the lower the resolution in frequency becomes. To evaluate the relationship between climate indices and total water storage, the time-frequency spectrum provided by wavelet transform is introduced in this study.

A wavelet is a wave-like oscillation with an amplitude that begins at zero, then increases, and then decreases back to zero. A transformation basis function $\psi(t)$, named as mother wavelet, satisfies the condition (Farge, 1992; Torrence and Gilbert, 1998):

$$C_\psi = 2\pi \int_{-\infty}^{\infty} \frac{|\Psi(\omega)|^2}{|\omega|} d\omega < \infty, \quad (4.7)$$

where $\Psi(\omega)$ denotes the Fourier transform of the wavelet $\psi(t)$, C_ψ is called admissibility constant, and the integral is taken over all frequencies ω . In practice, for the mother wavelet ψ with sufficient decay, it satisfies the conditions as follows:

$$\begin{aligned} \Psi(0) &= \int_{-\infty}^{\infty} \psi(t) dt = 0, \\ \|\psi(t)\| &= \int_{-\infty}^{\infty} |\psi(t)|^2 dt = 1. \end{aligned} \quad (4.8)$$

These two conditions ensure that the wavelet function therefore oscillates around the time axis and decays out quickly in both directions of time. Therefore, given a time series $x(t)$, its continuous wavelet transform (CWT) can be defined with respect to the wavelet $\psi(t)$ (Farge, 1992; Torrence and Gilbert, 1998) by

$$W_x(\tau, s) = \int_{-\infty}^{\infty} x(t) \frac{1}{\sqrt{s}} \psi^* \left(\frac{t - \tau}{s} \right) dt, \quad (4.9)$$

in which s is a scaling factor that controls the width of the wavelet, stretching ($|s| > 1$) or compressing ($|s| < 1$) the signal, and τ is a translation parameter controlling the position of the wavelet in time (Grinsted et al., 2004). (*) stands for the complex conjugate.

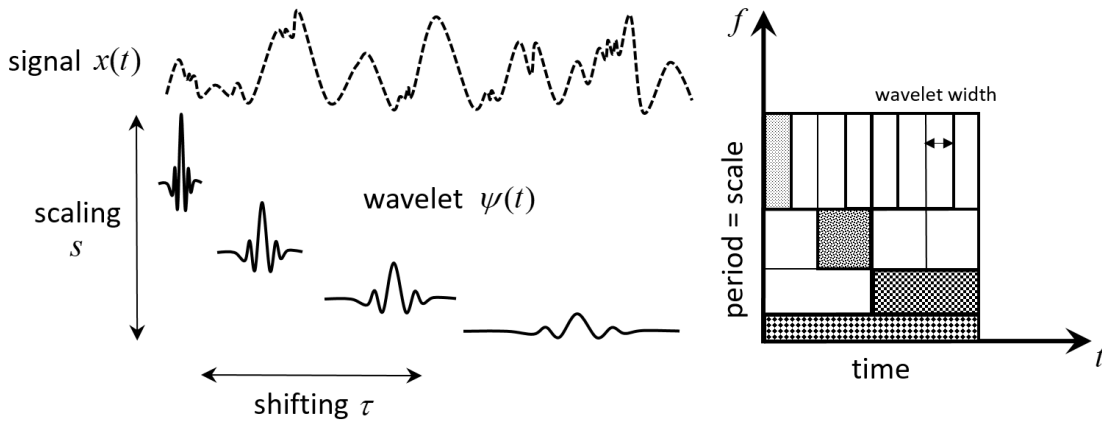


Figure 4.3: Illustration of continuous wavelet transform (CWT).

As depicted in Figure 4.3, the scaling factor s defines the size of the mother wavelet. The scales represent equivalently the frequency resolutions. The window shifting along time is expressed by the translation factor τ , and subsequently indicates the spectrum at different time period. Figure 4.3 vividly explains the wavelet transform in time and frequency aspects, which are illustrated in Figure 4.2. As a consequence, we obtain the wavelet $\psi(t)$ at different scales and locations through scaling and shifting. Therefore, with different s and τ , we eventually obtain the wavelet spectrum at different time and frequency scales. This time-frequency representation is sensitive to the non-stationary time series, whose statistics and frequencies change with time.

In fact, there are various type of mother wavelets. To satisfy the analytical requirement, it is necessary to choose an appropriate mother wavelet in CWT. Here we use the Morlet wavelet (shown in Figure 4.4) as mother wavelet in Eq. (4.7), which is defined as

$$\psi(t) = e^{i\omega_0 t} e^{-t^2/2\sigma^2}, \quad (4.10)$$

where ω_0 is the frequency, which is taken to be 6, and σ is a measure of the spread (Farge, 1992; Torrence and Gilbert, 1998). Based on its localization in time and frequency, the choice of Morlet wavelet makes it a good tool in extracting features (Grinsted et al., 2004). In addition,

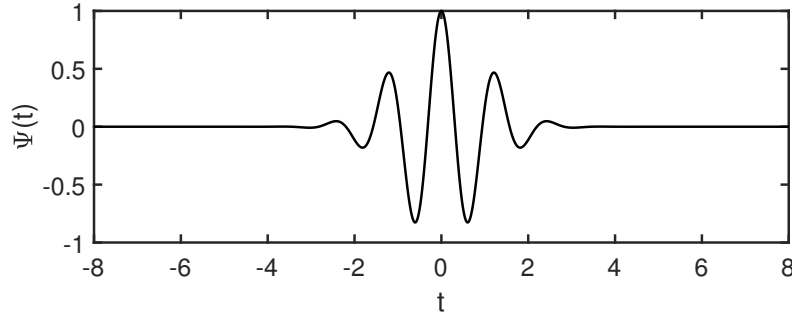


Figure 4.4: Illustration of the Morlet wavelet as mother wavelet $\psi(t)$.

the wavelet power spectrum is then $|W_x(\tau, s)|^2$, and the phase of the wavelet can be quantified (Liu, 1994) by

$$\phi_x = \arctan\left(\frac{\mathcal{I}[W_x(\tau, s)]}{\mathcal{R}[W_x(\tau, s)]}\right), \quad (4.11)$$

where \mathcal{R} and \mathcal{I} denote the real and imaginary part of $W_x(\tau, s)$.

Cross wavelet transform To analyze the mutual information of two time series, the cross-wavelet transform (XWT) of two time series $x(t)$ and $y(t)$ is introduced and simply defined (Torrence and Gilbert, 1998; Grinsted et al., 2004) as

$$W_{xy} = W_x W_y^*, \quad (4.12)$$

where W_x and W_y are the wavelet transform of x and y . The $|W_{xy}|$ is defined as cross-wavelet power (XWP), which expresses the local covariance between two time series at each time and frequency. Thus, the XWP helps us interpret the similarity of power between two time series.

Wavelet transform coherency As a correlation coefficient describes the similarity of two time series in time, coherency evaluates the correlated information in a view of frequency. Similar to the concept of coherency used in Fourier transform, the wavelet transform coherency (WTC) of two time series $x(t)$ and $y(t)$ can be defined by (Torrence and Gilbert, 1998)

$$\rho_{xy} = \frac{S(W_{xy})}{\sqrt{S(|W_x|^2)S(|W_y|^2)}}, \quad (4.13)$$

where S denotes a smoothing operator in both time and scale, written as

$$S(W_{xy}) = S_{\text{scale}}[S_{\text{time}}(W_{xy})]. \quad (4.14)$$

Smoothing, here, is necessary, otherwise the coherency would be identical at all scales and time epochs. Smoothing along the wavelet axis is given by S_{scale} , while smoothing along the time axis is given as S_{time} (Torrence and Webster, 1999). Smoothing by different filter widths and

shapes produces either smoother coherency or noisier coherency. Nevertheless, it still gives the same qualitative results. For the Morlet wavelet, a Gaussian smoothing is used for S_{time} , and a boxcar filter of width $\delta j_0 = 0.60$, which represents the scale-decorrelation length, is done for scale smoothing S_{scale} (Torrence and Webster, 1999; Grinsted et al., 2004).

The WTC is a measure of intensity of covariance between two time series. With the wavelet cross spectrum, we can therefore obtain the phase difference of two wavelets (Liu, 1994) by

$$\phi_{xy} = \arctan\left(\frac{\mathcal{I}[S(W_{xy})]}{\mathcal{R}[S(W_{xy})]}\right), \quad (4.15)$$

where \mathcal{R} and \mathcal{I} represent the real and imaginary part of spectrum. Hence, we use the phase of cross spectrum to identify the relative time lag between the two time series.

Comparing the XWT in Eq. (4.12) and WTC in Eq. (4.13), the WTC can be considered as the normalized cross-spectrum, with respect to spectrum of each signal. The cross-spectrum indicates how much linear information is transferred from one signal to the other at each frequency. While, the coherence indicates how much linear information of one signal is explained by the other one (Grinsted et al., 2004).

Above all, cross-wavelet transform and the spectrum coherency allows to estimate the relationship between two non-stationary time series, which have time-varying periodicity and amplitude. In this thesis, we use a wavelet coherence toolbox which is developed by Grinsted et al. (2004) for visualization of the wavelet spectrum and its coherency map.

Cone of influence Since the time series has finite length, when the CWT is applied on the time series, it suffers inevitably from border distortion, as with other type of transformation (e.g. Fourier transform). This edge effect is explained by the incorrect calculations occurring at the beginning and end of the wavelet spectrum. One usual method is padding the time series with sufficient zeros to limit the edge effects before implementing CWT. According to (4.9), these edge effects increase with the scale of the wavelet $\psi(t)$, which is scaled by the factor s , as visualized in Figure 4.3. Hence, the region of wavelet spectrum, in which the edge effects of transformation become important, is defined as the cone of influence (COI) (Torrence and Gilbert, 1998). The values are subject to the border distortion in this area of the time-frequency representation (see Figure 4.5). Therefore, the wavelet spectrum with COI has to be interpreted carefully.

Significance level The statistical significance of the wavelet power spectrum is assessed by a null hypothesis test. It assumes that a true feature is identified in the spectrum if the value is significantly above the mean power spectrum of time series, which is treated as the background spectrum. By the null hypothesis test, the significance of obtained wavelet spectrum is assessed against this background spectrum at the 5% level, which equivalently points to the 95% confidence level (Torrence and Gilbert, 1998). The significance level of wavelet power spectrum is estimated using Monte Carlo methods and represented as thick contour lines (Grinsted et al., 2004).

Numerical performance of wavelet transform In order to understand the advantage of wavelet coherency in estimating the relationship between two time series, we perform a simulation to test the sensitivity of signal variation in time and frequency.

In our case, we simulate a sinusoidal time series with varying frequency in this way:

$$x(t) = \begin{cases} \sin(\omega_1 t) + \epsilon, & t \in t_1 \\ \sin(\omega_2 t) + \epsilon, & t \in t_2 \\ \sin(\omega_3 t) + \epsilon, & t \in t_3 \end{cases} \quad (4.16)$$

in which $\omega_1, \omega_2, \omega_3$ denotes there different frequencies and t_1, t_2, t_3 represents the different time intervals. ϵ expresses the Gaussian random noise ($\epsilon \sim N(0, 1)$). In Figure 4.5, the time series $x(t)$ is plotted in time, with its power spectrum generated by Fourier transform, and wavelet spectrum from continuous wavelet transformation. The thick black contour in Figure 4.5 (c) indicates the 95% confidence level, and the cone of influence is shown as lighter shade.

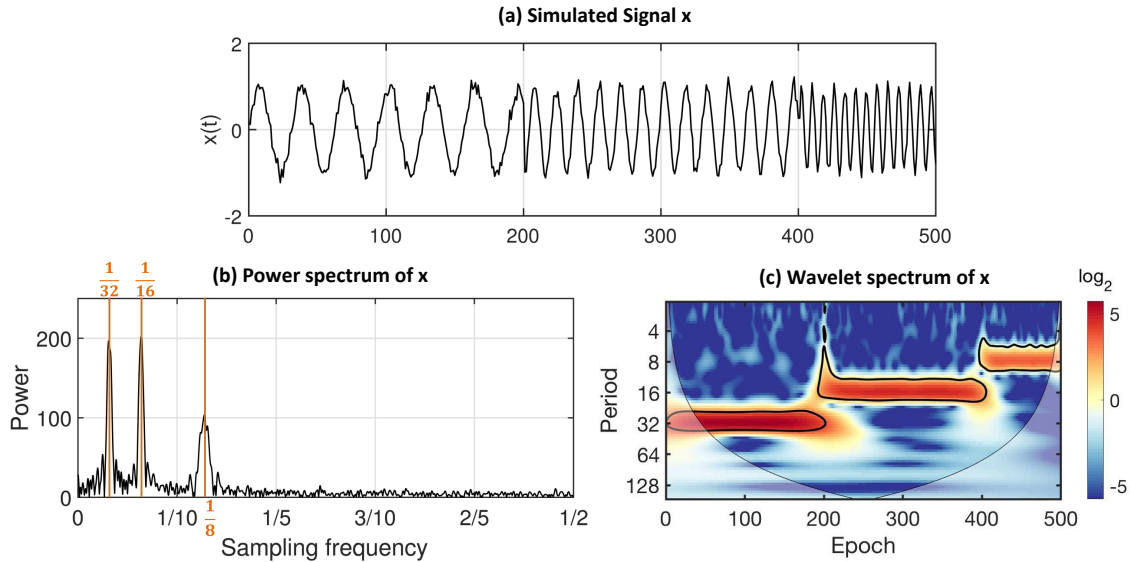


Figure 4.5: Illustration of (a) simulated time series x , with its (b) power spectrum from Fourier transformation and (c) wavelet spectrum from wavelet transformation. The thick black contour in (c) indicates the 95% confidence level, and the cone of influence is shown as lighter shade.

Figure 4.5 visually proves that the wavelet transform can reflect the variation of signal in both time and frequency. Three dominant sampling sizes 32, 16 and 8 are used to simulate signal x , and presented in their power and wavelet spectrum. Power reaches a peak at $1/32$, $1/16$ and $1/8$ in Figure 4.5 (b), which are consistent with the pattern in Figure 4.5 (c). By comparison, the wavelet spectrum expresses not only the frequencies with strong power response, but also indicates the time period, at which it has strong signals. Therefore, according to those properties, the wavelet spectrum has advantage in analyzing non-stationary time series with varying frequencies, especially for applications in climate studies.

The equivalent sampling intervals of Fourier transform make those three peaks locate densely in low-frequency area. However, the pattern of strong power at three different frequencies are presented uniformly in wavelet spectrum. Figure 4.5 (c) indicates that the wavelet spectrum

compresses the information in high frequency and amplifies in low frequency. This pattern is explained by the higher resolution in low frequency, while lower resolution in high frequency domain using wavelet transformation (as shown in Figure 4.2). For hydrological and geodetic observations, they usually contains important information in the low frequency domain, and meaningless information, e.g. random noise, exists as high-frequency components in the observations. Therefore, significant variability in hydrological and geodetic signals is emphasized in the wavelet spectrum. Due to these characteristics, in this thesis, wavelet transformation is employed as a tool for climatology-hydrology analysis.

The relationship between two time series x , y is investigated using wavelet coherence, illustrated in Figure 4.6 (1). We simulate signal y by shifting x with slight phase lag. Strong coherence in wavelet spectrum is shown at the same frequency (as in Figure 4.6 (b)). The arrows in wavelet coherence indicate the phase lag of y to x from 0 to $\pi/2$, and then after 400 epochs an anti-correlation between x and y .

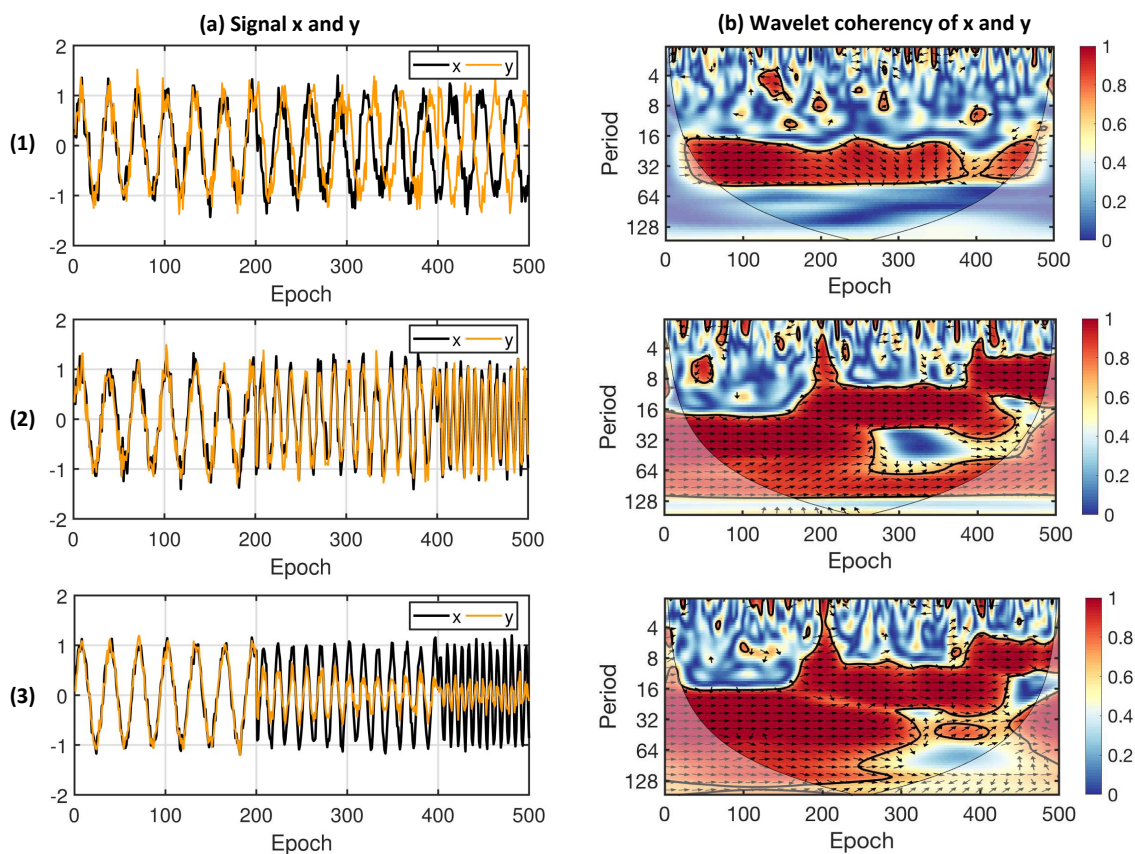


Figure 4.6: Illustration of (a) time series x and y and (b) its wavelet coherence. Simulated x and y with different frequencies and amplitudes in three cases are numerated in (1), (2), (3). The thick black contour indicates the 95% confidence level, and the cone of influence is shown as lighter shade. The arrows pointing to right direction denotes in phase, and left direction stands for anti-phase. The arrows upwards indicate the phase lag of y to x by $\pi/2$, and the arrows downwards indicate the phase lead of y to x by $\pi/2$.

From the numerical performance in Figure 4.6 (1), e.g., when $t \in [200 \ 500]$, the phase shift is clearly indicated by the change of arrow direction, which is completely consistent with the

shifting in time series. This simulation illustrates the sensitivity of wavelet spectrum to phase variation over time. It is an important property to recognize the relationship between two time series. Normally, if they are uncorrelated in phase at certain epochs, then a weak correlation would lead us to the wrong conclusion that they are not correlated. However, the relationship is not disturbed, and conversely, evidently revealed in the wavelet coherency spectrum.

The performance of wavelet coherency of x and y at varying frequencies is numerically tested and visualized in Figure 4.6 (2). Both x and y are simulated with time-varying frequencies at different epochs. From Figure 4.6 (2b), wavelet coherency is sensitive to the variation of frequency in time.

Further numerical test is made on signals with time-varying frequency and amplitude. As illustrated in Figure 4.6 (3), the wavelet coherency shows similar performance, comparing with Figure 4.6 (2). It indicates that the difference of amplitude does not influence the coherency of two time series. In other words, the amplitude difference and variation cannot be obtained from wavelet coherency. We benefit from this property when we try to detect the coherency between two time series in spite of the expansion in amplitude.

4.2 Characterization of water mass-water cycle relationships

As we discussed in 3.2.2, existing temporal shifts between terrestrial water storage change (TWS) in basins and other hydrological variables, i.e., precipitation (P), evapotranspiration (ET), runoff (R), result in non-linear relationships, which are shown in Figure 3.4. Theoretically, the relationship between TWS and P, ET, R is linear, according to the water balance equation. Therefore, in order to test whether temporal shifts induce the non-linear relationship, we correct the temporal shift to characterize the linear relationship. In this study, the Hilbert transformation approach is employed to determine the phase difference and the temporal shift.

Considering the temporal shift Δt , we obtain the adaptive P, ET, R which is synchronous to TWS (ΔM) from GRACE via

$$\begin{aligned}\hat{P}(t) &= \kappa \cdot P(t - \Delta t_1) + (1 - \kappa) \cdot P(t - \Delta t_2) , \\ \hat{ET}(t) &= \kappa \cdot ET(t - \Delta t_1) + (1 - \kappa) \cdot ET(t - \Delta t_2) , \\ \hat{R}(t) &= \kappa \cdot R(t - \Delta t_1) + (1 - \kappa) \cdot R(t - \Delta t_2) ,\end{aligned}\tag{4.17}$$

where the temporal shift $\Delta t \in [\Delta t_1 \Delta t_2]$ is calculated according to (4.5), in which $\Delta t_1, \Delta t_2$ are integer months. κ is the proportion factor, denoting the fractional part of the interval between Δt_1 and Δt_2 , written as

$$\kappa = \frac{\Delta t - \Delta t_1}{\Delta t_2 - \Delta t_1} .\tag{4.18}$$

After shifting the time series of P, ET, R by (4.17), the relationship between TWS from GRACE and the adaptive P, ET, R is supposed to be more linear than before. The relationships are visualized in Figure 4.7. Comparing with Figure 3.4, P, ET, R become linearly synchronous with TWS in Amazon and Yangtze. The non-linear behaviours are distinctly repaired by correcting

the time-invariant temporal shifts. It proves that the existing time-invariant temporal shifts have great impact on the characterization of the relationship between continental TWS and the hydrological cycle.

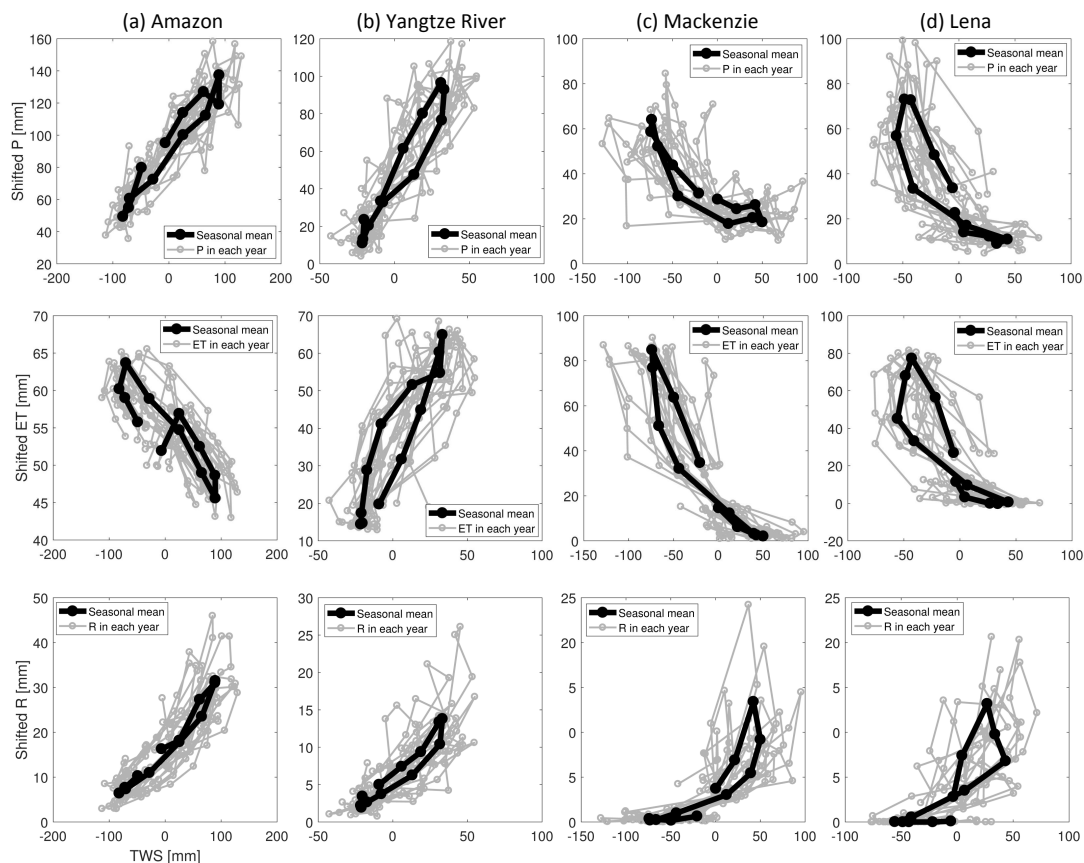


Figure 4.7: Illustration of relationships between TWS and shifted P , ET , R , respectively for catchment (a) Amazon (tropical), (b) Yangtze River (temperate), (c) Mackenzie (boreal), and (d) Lena (boreal).

However, P , ET , R in the boreal catchments (i.e., Mackenzie, Lena) do not show perfect linear relationships with TWS, although they are already much closer to linear, compared with Figure 3.4 (c) (d). The main reason might owe to the special climatic condition in the high-latitude region. The boreal catchments under cold and dry condition have not as strong seasonal variation as in other catchments under tropical and temperate conditions. As a consequence, the temporal variation of the terrestrial water storage is not linear with precipitation, evapotranspiration and runoff. The insufficient temporal resolution could also produce errors in calculating the temporal shifts by the Hilbert transformation approach. Moreover, the data from different models also result in different phase shifts. Though, the model performance in characterizing the relationships is not further discussed here.

In Figure 4.8, the time shifts between TWS and P , ET , R at catchment scale are quantified in 26 large basins. P , ET , R represent a temporal shift with TWS, ranging from -3 to 3 months. P in most of the basins shows a time lead to TWS except for the catchments in the middle of North America. All the boreal catchments represent a time lead of P to TWS. R in Amazon

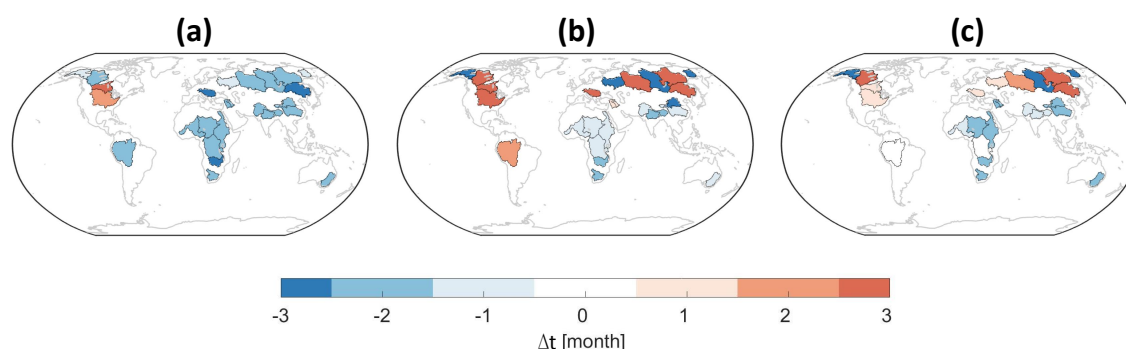


Figure 4.8: Maps of the time shifts between TWS and (a) P , (b) ET , (c) R , respectively, in 26 catchments, which are distributed globally. Positive values indicate a time lead of TWS to P , ET , R , while negative values indicate a time lag.

has zero time shift, indicating synchronous change with TWS. The synchronous variation is illustrated as well by the perfect linear relationship shown in both Figure 3.4 (a) and 4.8 (a). The ET and R in high-latitude region have consistent relationships with TWS. The terrestrial water mass variation in boreal catchments consists of the solid and fluid water mass change. Hence, the nearly zero change of ET and R (as shown in Figure 3.5) in winter and large amount of variation in summer under cold and dry condition helps to explain the consistency in Figure 4.8 (b) and (c).

In short, the relationships between terrestrial TWS and P , ET , R is characterized as linear in the tropical and temperate catchments, after considering the time-invariant temporal shifts. Non-linear relationships are revealed in the boreal catchments, in which the time shift is not the only factor.

4.3 Causality analysis between water mass variation and climate change

4.3.1 Time lag analysis between water storage and ENSO

ENSO indices In this study, we use the Nino 3.4 index which represents the Pacific region between 5°S – 5°N and 170°W – 120°W , from 2003 to 2014 produced by NOAA's Climate Prediction Center (CPC) (<ftp.cpc.ncep.noaa.gov/wd52dg/data/indices>).

To investigate the influence of ENSO on terrestrial water storage (TWS), the phase difference is supposed to be estimated. We therefore apply Hilbert transformation to explore the global connection between TWS and ENSO. The global TWS time series is gained using monthly GRACE product with time period of 2003–2014 and $1^{\circ} \times 1^{\circ}$ spatial resolution.

As introduced in 1.2, ENSO has inter-annual variability. However, the dominant signal part of GRACE shows strongly annual performance. Accordingly, before extracting ENSO influence

on the TWS, the linear trend and seasonal components are necessarily eliminated, by using a least-squares regression at each grid cell as

$$\begin{aligned} \Delta l(t) = l(t) - m_1 \cdot t - m_2 \\ - m_3 \cdot \sin(2\pi t) - m_4 \cdot \cos(2\pi t) \\ - m_5 \cdot \sin(4\pi t) - m_6 \cdot \cos(4\pi t), \end{aligned} \quad (4.19)$$

where m_i are the parameters to estimate, $l(t)$ is TWS observation time series. After detrending and deseasoning, $\Delta l(t)$ is the isolated TWS anomalies. We get the real and imaginary part of Nino 3.4 index $p(t)$ using Hilbert transformation, as defined in (4.3). We model the TWS anomalies with Nino 3.4 index by using the least-squares regression in (4.4), giving the coefficient a , b and c . Referring to (4.5), as a result, the phase lags are then estimated.

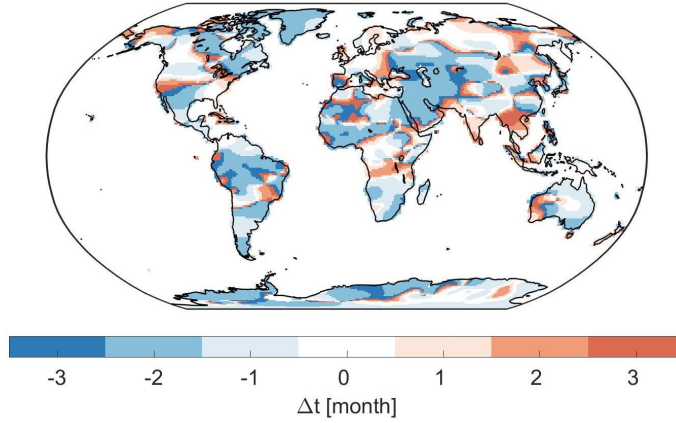


Figure 4.9: Time difference between ENSO and TWS are calculated by the linear model based on the Hilbert transformation. Positive value means that TWS leads to ENSO, while negative value denotes the lead of ENSO to TWS.

The phase difference ranges from $-\pi$ to π . Time lags between TWS and ENSO are also calculated from the phase shifts by $\Delta t = \Delta\phi \cdot 12/2\pi$, and visualized in Figure 4.9. As defined in (4.4), positive value means that TWS leads to ENSO, while negative value denotes the lead of ENSO to TWS.

In Figure 4.9, most regions indicate lags of TWS to ENSO. In particular, at high latitude like in East Russia, TWS leads 0–2 month to ENSO. On the contrary, in most regions like in North America, TWS responds to ENSO with about 2-month delay. To some extent, the temporal shifts of TWS in high-latitude region explain the impact of ENSO events from the Pacific.

Figure 4.10 shows the temporal shift between ENSO and TWS in different basins over the globe. Similar to the results shown in Figure 4.9, most of basins indicate time lags of TWS to ENSO about 1–3 month. For those basins located in high-latitude area, TWS reveals 1-month lead to ENSO in Mackenzie, while 2-month lag to ENSO in Ob. Some other basins like Yenisei, Lena and Yukon show zero temporal shift with respect to ENSO. The different temporal shifts in these boreal basins could be explained by the different distances to the tropical Pacific. The

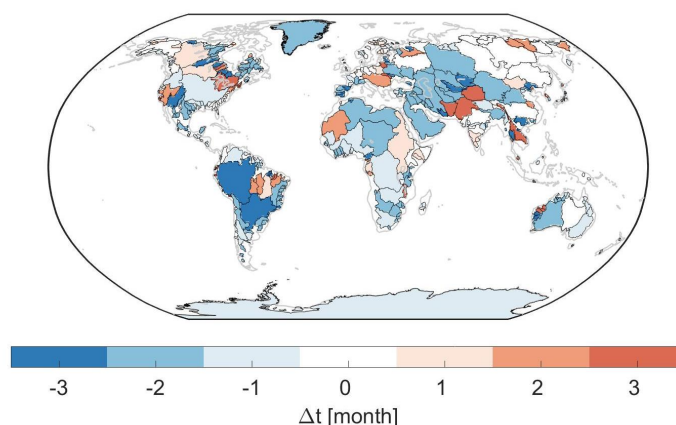


Figure 4.10: Time difference between ENSO and TWS in catchments, with the same description as expressed in Figure 4.9.

phase shifts between ENSO and TWS in the boreal basins leads to the conclusion that ENSO does not homogeneously influence the terrestrial water mass change in pan-Arctic region.

The phase shifts calculated by Hilbert-transformation approach are reliable but not stable. Many factors could influence the outputs. For instance, to avoid the interference of seasonal signals, we employ a least-squares fit to subtract the annual and semi-annual variation. Whether the modeled TWS anomalies is perfectly isolated by ENSO is still uncertain. These artificial errors might induce phase shifting. In fact, choosing different observation period might produce different phase shifts as well. These limitations of the Hilbert transformation approach in detecting phase shifts between two time series urge us to refer to other techniques for validation. Therefore, the wavelet transformation in this chapter and signal decomposition methods in next chapter are involved to validate the association between ENSO and TWS.

4.3.2 Coherency analysis between ENSO and water storage in basins

As described above, the wavelet spectrum is capable to recognize the variation of different frequencies in time series. Since most of the observations driven by climate effects are non-stationary, the wavelet transformation is an appropriate tool to evaluate the relationship between those non-stationary time series.

Figure 4.11 shows the time series of Nino 3.4 index from 1996 to 2016 with its wavelet spectrum. Figure 4.11 illustrates that annual change and inter-annual change with around 2.5 year period play a dominant role in ENSO.

We calculate the total water storage change (TWS) from GRACE observations. The GRACE data we used here cover 12 years, covering the period from January 2003 to December 2015. The TWS time series in five basins (i.e., Ob, Lena, Yenisei, Mackenzie, Yukon) are depicted in Figure 4.12. The TWS in each catchment shows non-Gaussian distribution.

With respect to ENSO, the total water storage variation clearly shows evident seasonal behaviour. If we refer to the correlation coefficients, obviously we gain low correlations between ENSO and TWS, which indicate a weak relationship. However, there is still a connection that

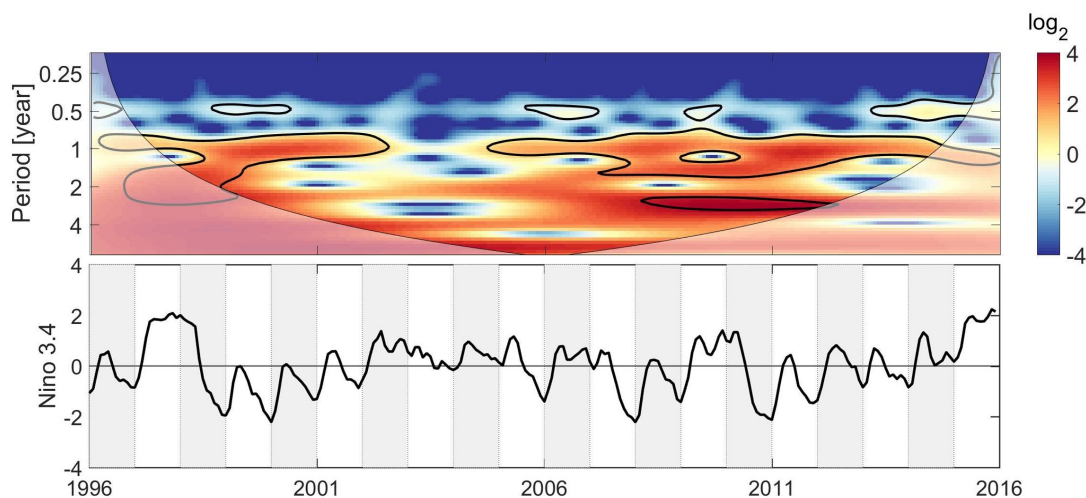


Figure 4.11: Nino 3.4 index and its wavelet spectrum.

we could not recognize only based on correlations. Therefore, a wavelet transformation is performed to detect the relationship between ENSO and TWS.

The cross-wavelet and wavelet coherency between ENSO and TWS in the five basins are visualized in Figure 4.13. From cross-wavelet spectra, TWS in every basin shows annual and biennial connection to ENSO, especially from 2003 to 2009. Accordingly, the coherency maps of Ob and Lena indicate evident association to ENSO from 2003 to 2011, whereas a weak relationship is found between ENSO and TWS in Yenisei, Mackenzie and Yukon.

The arrows in the coherency maps designate the phase difference between ENSO and TWS. Pointing to right direction denotes in-phase, and to the left direction stands for anti-phase. The arrows upwards indicate the phase lead of ENSO to TWS by $\pi/2$ (3 months), and the arrows downwards indicate the phase lead of TWS to ENSO by $\pi/2$.

Figure 4.13 reveals that ENSO lags TWS at the biennial band in Mackenzie, while it leads TWS in Ob, Lena and Yenisei. Weak association between ENSO and TWS in Yukon is indicated by a low wavelet coherency. ENSO has a lead of about 1–2 months to TWS in Ob from 2009 to 2011, indicating that ENSO events have impact on the inter-annual change of TWS. TWS in Lena has a lag of about 1–2 months to ENSO between 2007 and 2009, and roughly 3-month lag from 2009 to 2011. In the Yenisei basin, TWS has 1–2 month lag to ENSO from 2003 to 2007, while it is anti-correlated with ENSO around 2011. Different time lags in different basins indicate the dynamic process of ENSO impact on terrestrial water mass change. Particularly, from the cross-wavelet spectrum and wavelet coherency, it reveals that observing TWS in different time periods also results in different temporal shifts to ENSO.

In brief, according to the patterns revealed in Figure 4.13, the wavelet coherency is proved to successfully recognize the association between ENSO and terrestrial water storage variation. The cause and effect are revealed by the phase difference directions from the wavelet coherency maps.

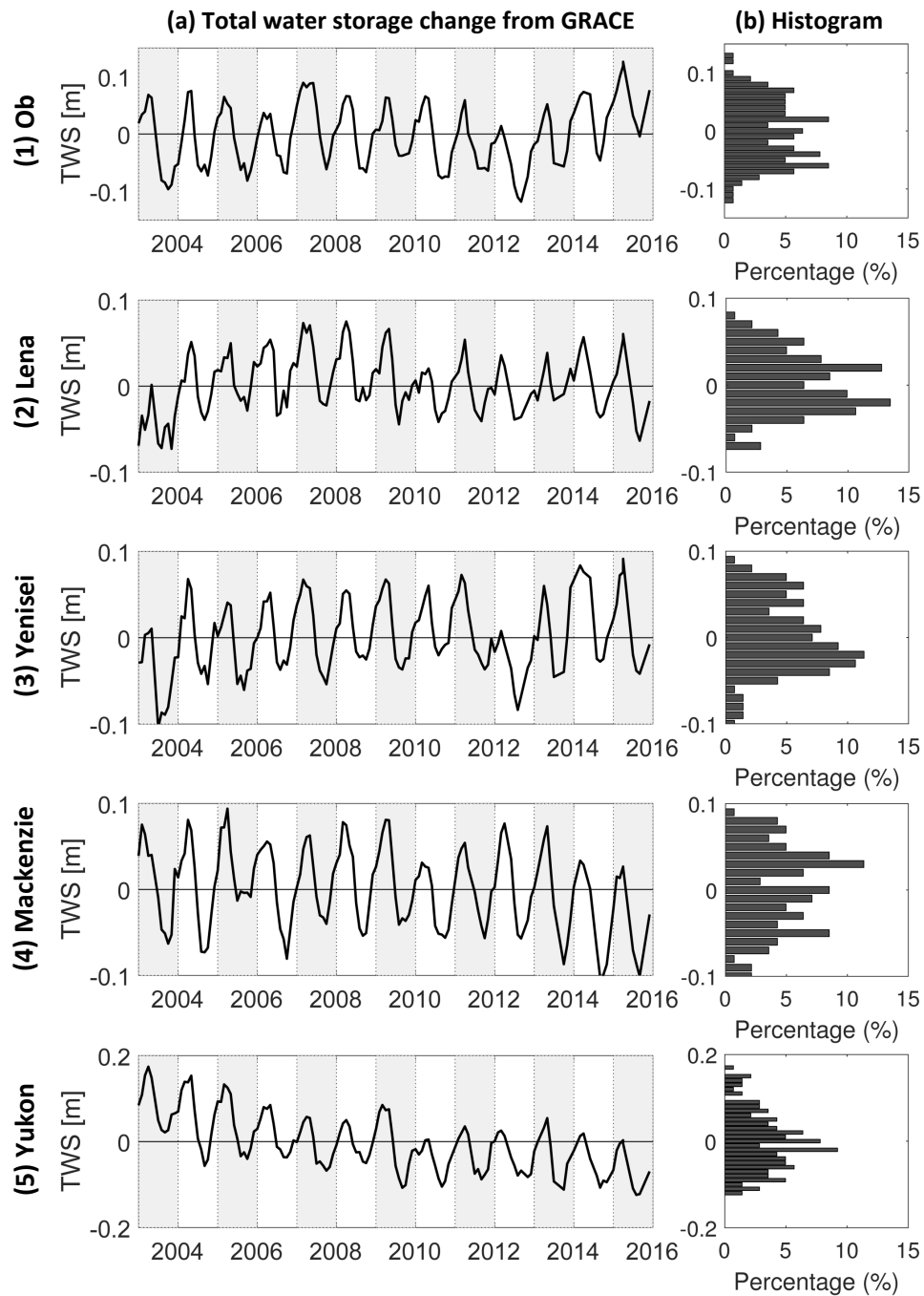


Figure 4.12: (a) Terrestrial water storage change derived from GRACE in the basin (1) Ob, (2) Lena, (3) Yenisei, (4) Mackenzie and (5) Yukon, with their (b) histograms.

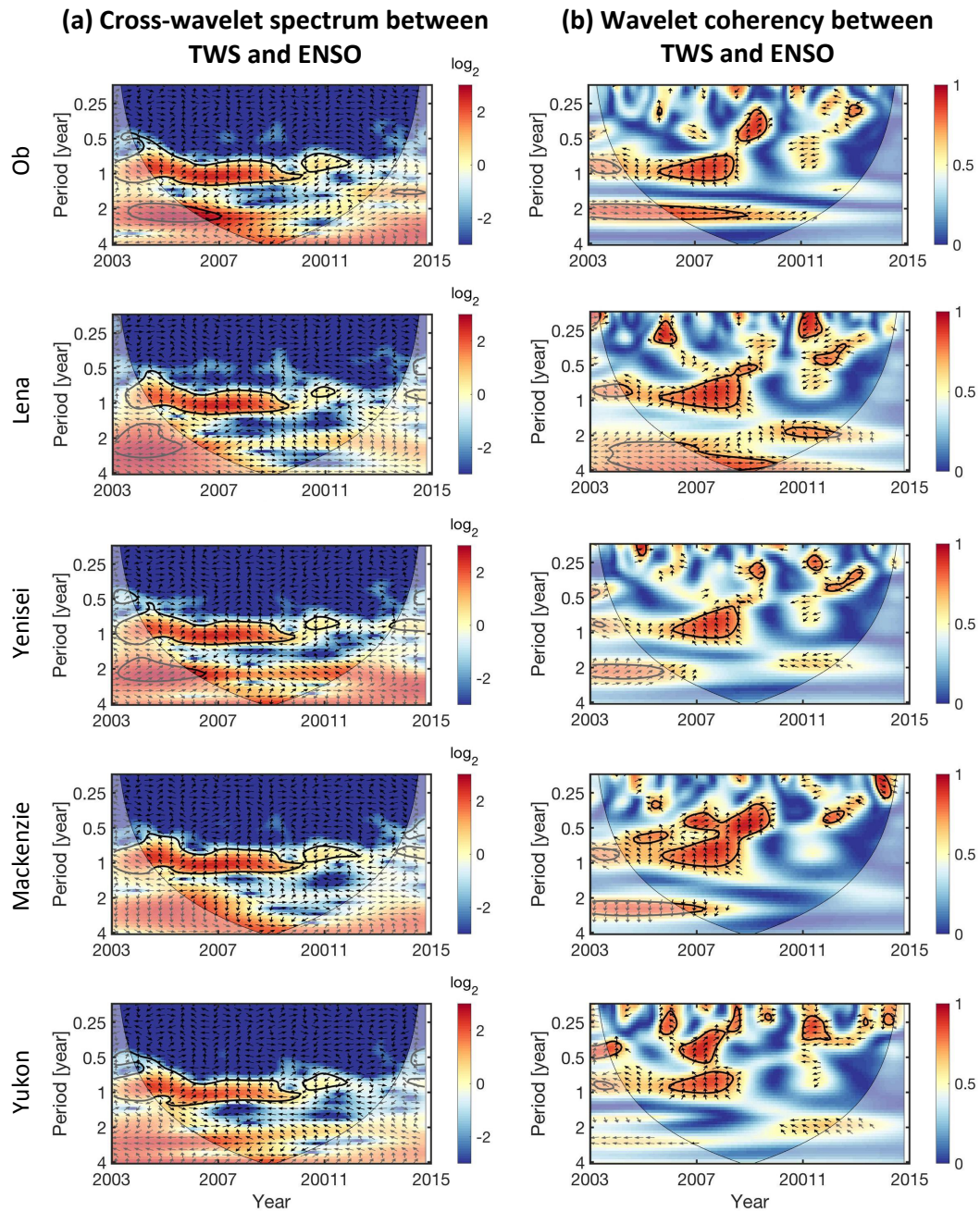


Figure 4.13: The relationship between TWS and ENSO in basins is visualized in terms of (a) cross-wavelet spectrum and (b) coherency.

4.4 Discussion and summary

This chapter successfully investigates the phase difference using the Hilbert transformation approach and the cross-wavelet transformation, and discusses the causal relationship between each hydrological variable and climate index. It is worth mentioning that the physical mechanism is not discussed in this chapter, which is beyond the scope of our statistical study.

With respect to the dynamic rainfall-runoff response of a catchment, the terrestrial water mass variation practically reflects non-linearity with other hydrological variables (Sivapalan et al., 2002; Kirchner, 2009; Teuling et al., 2010). However, the relationship among each variable in the water cycle is statistically described as linear. In this chapter, the linear relationships between water storage and precipitation, evapotranspiration and runoff in catchment are characterized in tropical and temperate basins after considering the existed temporal shifts. On the one hand, this dynamic process is mathematically interpreted in terms of quantified time leads or lags. On the other hand, the phase and time shifts estimated by the Hilbert transformation are proved reliable, by comparison of Figure 3.4 and 4.8. The relationship is still characterized as non-linear in the boreal catchments (e.g. Mackenzie and Ob), due to the solid and fluid water mass variation discussed by Riegger and Tourian (2014). As a consequence, it is essential that the temporal shifts between water storage and water cycle are taken into consideration when modelling the water storage change by other variables.

From the above, the wavelet spectrum shows the advantage on presenting time-frequency information of non-stationary time series. For those observations with non-stationary variability, the wavelet spectrum and coherency explain more details on both frequency and time than either correlation in time or phase estimated by Hilbert transformation. Comparing with the Fourier transformation, the significant information at low-frequency domain, e.g. biennial, inter-annual, and decadal variation, are enhanced in the wavelet spectrum and coherency maps.

The Hilbert transformation and wavelet coherency perform relatively comparable but still have differences in estimated phase shifts between ENSO and water storage change, comparing Figure 4.10 with 4.13. Particularly, in boreal catchments, for instance, the Mackenzie and Ob basin, the quantified phase shifts of these two different methods are not equivalent, although both of them indicate a time lead of ENSO to TWS in Mackenzie, and a time lag in Ob. The seasonal signals still likely remain in the TWS anomalies time series when we subtract the periodic terms from the TWS observations using a least-squares model, which could lead to uncertainty of phase estimation. In addition, since the ENSO index time series is not statistically stationary, the length and the localisation of the observing period also matters in the deviation of phase shifts.

Except for the inaccuracy of algorithm implementation, the climatic condition in the catchments is also a probable factor, explaining the inconsistent performance between the Hilbert transformation and the cross-wavelet coherency. In practice, since the water storage variation in the boreal catchments (e.g. Mackenzie, Lena in Figure 3.5) is not evidently stationary, subtracting the seasonal components from observations by a harmonic fit model is not appropriate. In this case, the wavelet spectrum and coherency produce more reliable patterns, representing the phase change in different observing window with varying frequencies. In other words,

the wavelet transformation is superior to the Hilbert transformation in those non-stationary basins.

Although these drawbacks of the Hilbert transformation approach potentially results in unprecise phase estimation, a quantitative evaluation of uncertainty analysis is not included in this chapter. Referring to a data-driven approach, e.g. PCA or ICA, is an option to avoid this modelling problem. This issue will be discussed in the following chapter.

In conclusion, the linear relationships in most basins are characterized by estimated temporal shifts between water storage and water cycle, which is essential for our statistical estimation of water storage by linear regression models. The cause and effect between ENSO and terrestrial water storage variation is indirectly explained by the quantified phase and time shifts. As a preliminary analysis, it supports us to investigate the teleconnection between ENSO and terrestrial water mass change in the following context, and inspires us to further explore the causality of them in the future work.

Chapter 5

Teleconnection Between Water Mass Variation and Climate Variability

Generally, water mass variation is involved in the circulation of ocean, land and atmosphere. The terrestrial water mass variation is partly relevant to climate change. In this chapter, we aim to identify the teleconnection patterns between climate change, e.g. ENSO, and terrestrial water mass change. Since the inter-annual variation of terrestrial water storage is composed with seasonal, subseasonal, and decadal variation as well as linear trend in the observations, we aim to extract the ENSO related signals from terrestrial observations from GRACE by using several decomposition techniques (i.e., PCA, ICA, CCA).

As climate change is commonly reflected by the ocean-atmosphere interaction, most climate indices (e.g., ENSO) are characterized statistically from sea surface temperature (SST) anomalies. Inter-annual changes in SST are found to relate to the terrestrial water cycle in river basins (Diaz et al., 1998; Gochis et al., 2007; McCabe and Wolock, 2014). Because of the important role of SST on climate change and terrestrial water variation, we propose a comprehensive analysis to include SST in this study.

SST is used as an intermedium to associate climate change with the major variables in the terrestrial water cycle, i.e., precipitation, evaporation and runoff are expected to connect to ENSO. We use GRACE products to calculate terrestrial water storage and water storage fluxes. In addition, surface temperature on land is involved as well. Land surface temperature (LST) is a significant variable in climate change and terrestrial water resources. Considering the inconsistent units of temperature and equivalent water height, CCA is therefore an appropriate tool applied to recognize the relationship between SST and hydrological variables, and then identify the teleconnection to ENSO by the identified temporal and spatial patterns.

In addition, to understand and interpret the dynamic processes among ocean, atmosphere and land, and the impact on the water cycle, phase leads and lags are an important indicator, that is necessarily taken into consideration. Therefore, we employ approaches, which are introduced in Chapter 4, to estimate the phase difference and time lag in a comprehensive way.

5.1 Between ENSO and terrestrial water storage

Although the phase difference between ENSO and TWS is estimated by the Hilbert transformation approach and revealed by wavelet spectrum and coherency in 4.3, it is still necessary to extract the connection patterns temporally and spatially from TWS, that associate with ENSO. Therefore, the decomposition methods (i.e., PCA and ICA) are used in this section.

5.1.1 Decomposition of total water storage by PCA

Global patterns To explore the information from GRACE that is associated with ENSO, PCA approach is now applied to the global continental gridded TWS time series. As mentioned in 2.1, the TWS changes are allocated in a 3D matrix, whose dimensions represent longitude, latitude and time, respectively. We perform PCA on a rearranged 2D matrix which contains the information of both location and time. The first 10 modes have already 85% of variance of the data. The percentage of eigenvalues for each mode is visualized in Figure 5.1.

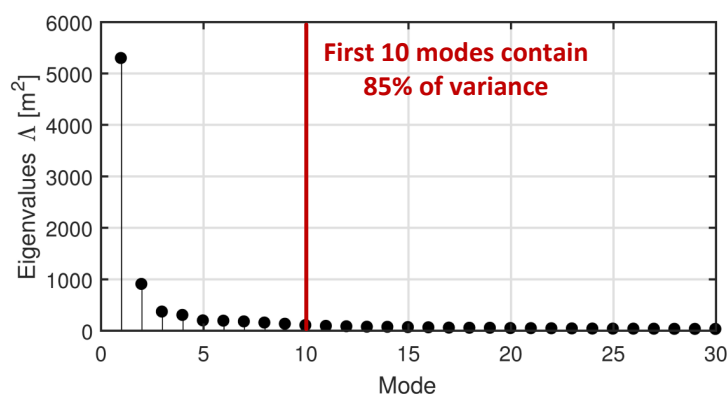


Figure 5.1: Eigenvalues of global continental water mass change from each mode generated by PCA decomposition.

The temporal and spatial patterns of the first 5 modes are shown in Figure 5.2. The first dominant mode has seasonal variability, which relates to the terrestrial water cycle. EOF 1 reflects spatially the evident seasonal signals mainly in South America, in the middle of Africa and South Asia.

From PC2 to PC5, they show variation with longer than 1-year period. However, the mode that associates with ENSO is not clearly separated by PCA. The first five decomposed components show weak relationship with ENSO.

Although PCA is powerful to compress significant variation of total water storage into the first five modes, the associated variation to ENSO cannot be separated and identified yet at global scale.

Regional study on boreal catchments The influence of ENSO on the high latitude area is still an unanswered question. Hence, to identify the signature of ENSO on high latitude area, we particularly apply PCA on this area. As discussed in 4.3, five boreal catchments in this area

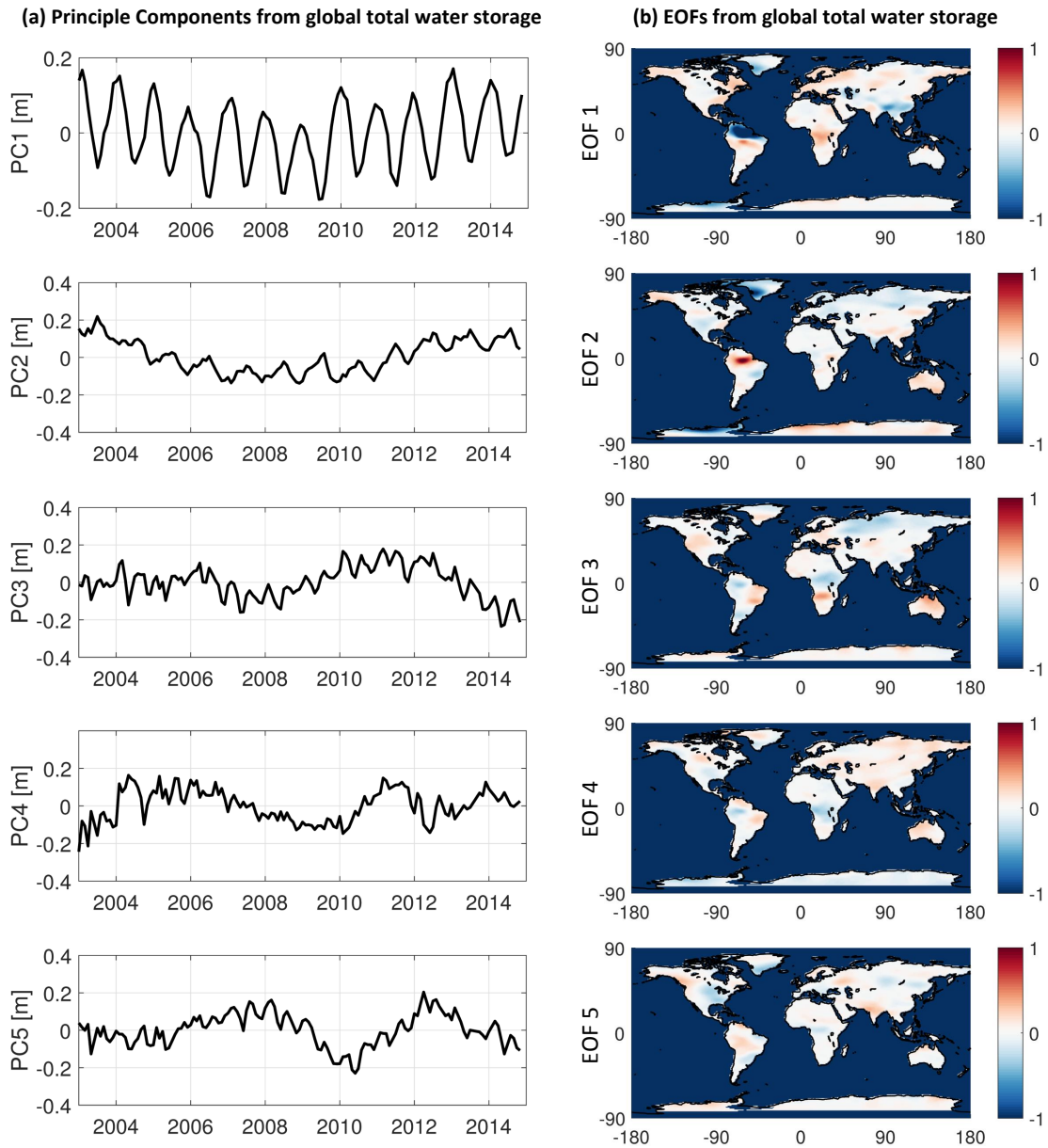


Figure 5.2: (a) The temporal PCs and (b) its corresponding spatial EOFs of the first modes from global continental TWS.

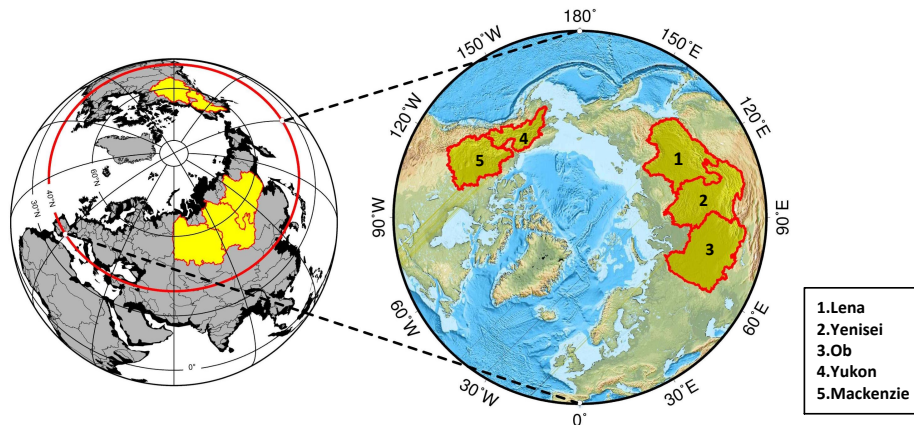


Figure 5.3: Catchments (i.e., Ob, Lena, Yenisei, Mackenzie, Yukon) in the pan-Arctic area.

are analyzed in this chapter as a case study. These five catchment are located in the pan-Arctic region, shown in Figure 5.3.

After decomposition, the temporal and spatial patterns of the first three modes in these five catchments are visualized in Figure 5.5 and 5.4, respectively.

Seasonal variation in the three catchments plays a dominant role in the water storage change. As the variance percentage of first 5 modes listed in Table 5.1, the seasonal mode is clearly notable in each catchment, particularly in the Ob and Yukon basin. The associated spatial patterns in Figure 5.4 illustrate that strong seasonal variation is allocated throughout the basins. Mode 2 and 3 represent inter-annual change in each catchment. According to the correlation with Nino 3.4 in Table 5.1, we do not find any association in temporal PCs. The low correlation indicates quite weak relationship between ENSO and water storage in catchments.

Table 5.1: Correlation ρ between Nino 3.4 index and PCs from TWS, with percentage of variance σ of PCs.

Basin	Ob		Lena		Yenisei		Mackenzie		Yukon	
	ρ	σ (%)	ρ	σ (%)	ρ	σ (%)	ρ	σ (%)	ρ	σ (%)
PC 1	-0.1	80	0.2	68	-0.2	75	0.2	79	0.1	81
PC 2	0.4	6	0.3	8	-0.3	9	-0.1	7	-0.2	7
PC 3	0.1	4	-0.1	8	-0.3	6	-0.1	4	-0.1	5
PC 4	0.1	2	0.2	6	0.1	3	0.1	3	0.1	3
PC 5	-0.1	2	-0.2	3	-0.1	2	0.2	2	-0.3	1

However, it seems that the temporal pattern of PC 2 in the Ob basin (Figure 5.5), the TWS signal has a relevant change with Nino 3.4 index. Only correlation coefficient ($\rho = 0.4$) cannot exactly reflect this relevance if phase shift exists. Considering the property of wavelet spectrum in detecting the relationship between two signals with time-varying phase, we then refer to the wavelet coherency.

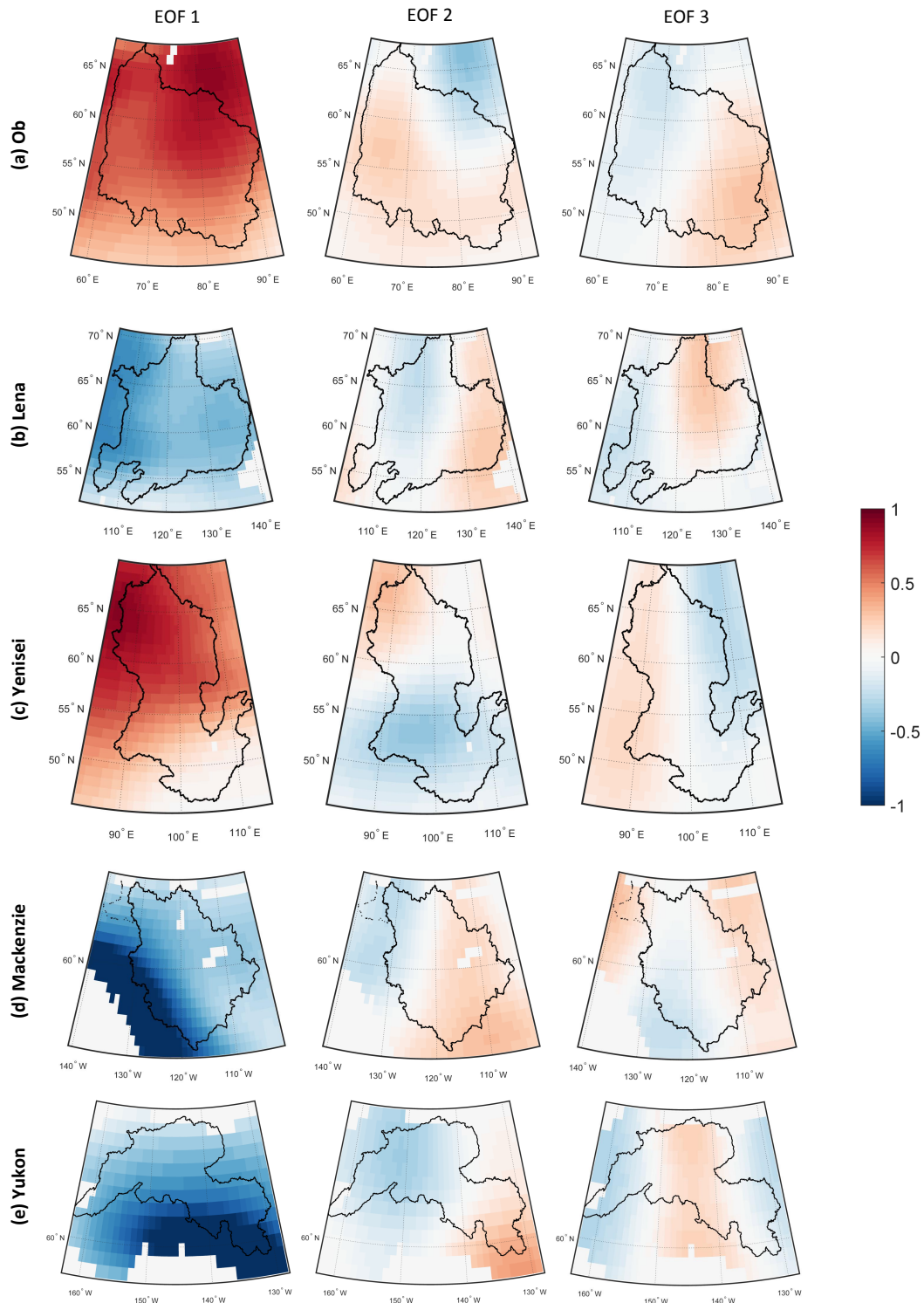


Figure 5.4: The first three spatial EOFs by PCA of the TWS in the catchments: (a) Ob, (b) Lena, (c) Yenisei, (d) Mackenzie, (e) Yukon, respectively.

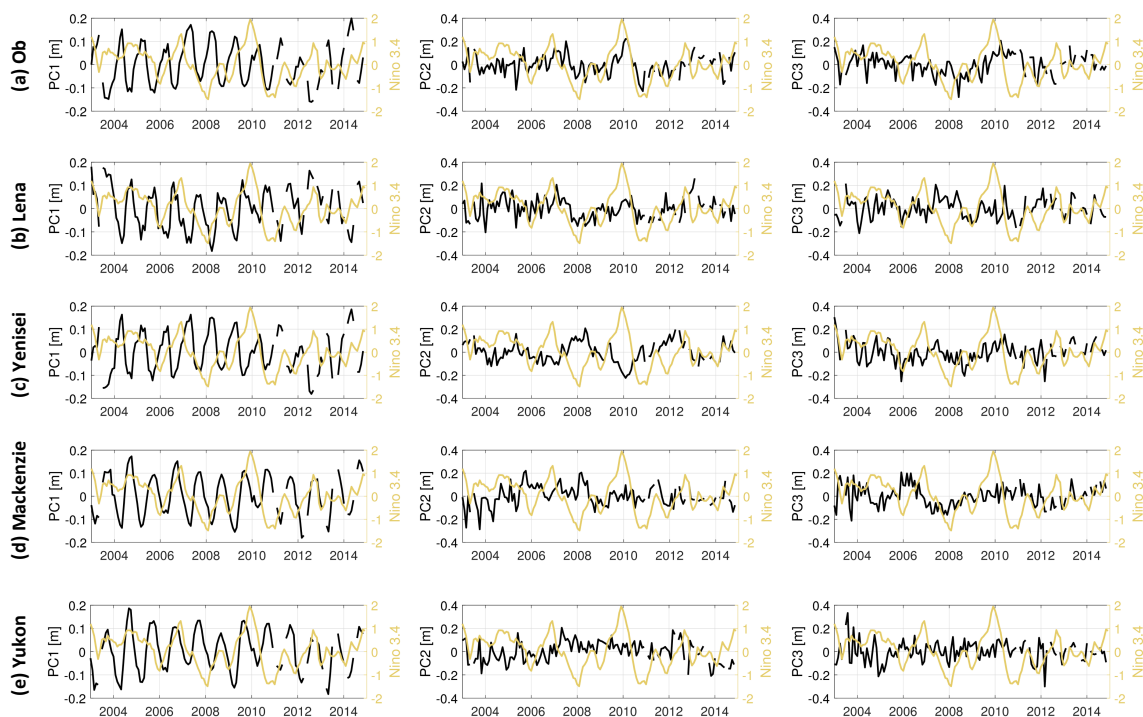


Figure 5.5: The first three principal components (PCs) by PCA of the TWS in the catchments: (a) Ob, (b) Lena, (c) Yenisei, (d) Mackenzie, (e) Yukon, respectively. The black line is from total water storage, compared with Nino 3.4 index (yellow line).

Figure 5.6 shows a clear coherency between total water storage and ENSO at the biennial band. The linear relationship is not evident from the time series and the scatter plot, but becomes clear by its wavelet coherency map. In the coherency map, arrows pointing to right direction denote in-phase, and left direction stands for anti-phase. Arrows upwards indicate a phase lag of TWS to ENSO by $\pi/2$, and downward arrows indicate a phase lead of TWS to ENSO by $\pi/2$. As illustrated in Figure 5.6, TWS leads to ENSO from 2006 to 2008 about $\pi/6$ in phase, and responds to ENSO from 2010 to 2012 with phase lag of about $\pi/6$. That is to say, TWS has 1-month lead from 2006 to 2008 and 1-month lag to ENSO from 2010 to 2012. According to Figure 5.6 (a), these time differences can be also seen from the temporal patterns. A similar situation occurs for PC 2 from Lena and Yenisei basin. Although low correlation coefficients indicate a weak connection, they are still associated with ENSO, according to the temporal patterns in Figure 5.6.

Referring to the wavelet coherency, we can recognize the association of TWS and ENSO through the modes by PCA. However, PCA is not capable to automatically identify the associated mode by itself. This limited performance proves that PCA may not be adequate to search the teleconnection between ENSO and terrestrial water storage.

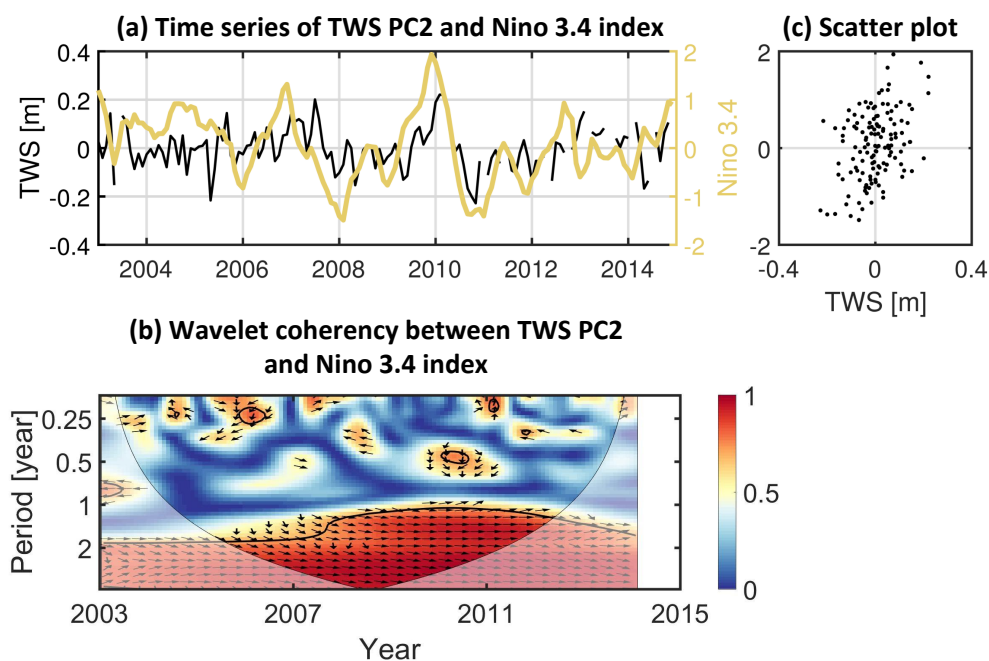


Figure 5.6: (a) Time series comparison between TWS PC2 of Ob basin and Nino 3.4 index, with (c) its scatter plot. (b) Wavelet coherency between TWS PC2 and Nino 3.4 index. The black line in (a) denotes total water storage, and yellow line is Nino 3.4 index. The thick black contour indicates the 95% confidence level against red noise, and the cone of influence is shown as lighter shade. Arrows pointing to right direction denote in-phase, and left direction stands for anti-phase. Arrows upwards indicate the phase lag of TWS to ENSO by $\pi/2$, and the arrows downwards indicate the phase lead of TWS to ENSO by $\pi/2$.

5.1.2 Identification of ENSO signature by ICA

Independent patterns The application of PCA is successfully performed on detecting relationship between ENSO and terrestrial water storage. Different from PCA, independent component analysis (ICA) has the potential to separate signals into statistically independent modes. The signals can be chosen to separate independently either in temporal information or in spatial information. This property is expected to be used to explore the patterns of unique variability in the observations.

ICA can separate observations into independent signals only if the observations are non-Gaussian. Figure 4.12 shows that all the time series in the five catchments perform have a non-Gaussian distribution. Forootan and Kusche (2012) prove that ICA is capable to extract the independent signals from global total water storage observed by GRACE. Considering that the extracted modes by PCA are not completely isolated by ENSO, instead, we apply ICA on the observations. We mainly evaluate the performance of ICA on the catchments shown in Figure 5.3. Datasets from GRACE used in this section are as the same as in 5.1.1. Particularly, we expect to see the influence of ENSO spatially on different regions. Therefore, in our case, ICA is then applied to extract the spatial independent modes from the observations.

According to the eigenvalues shown in Figure 5.1, we firstly compress the data by PCA, retaining only the first 5 modes. ICA is then performed on the reconstructed datasets. To evaluate

the relationship with ENSO, we calculate the correlation of each independent component (IC), comparing with Nino 3.4 index. The results are listed in Table 5.2. Evaluated by the correlation coefficients, all of the ICs show weak correlation with Nino 3.4. It is still necessary to look at the temporal and spatial patterns of each IC. The temporal and spatial patterns of ICs in the Lena basin, as an example, are shown in Figure 5.7. From the temporal modes, strong seasonal variation is revealed in IC 1. It looks as if IC 3 and IC 4 in Lena represent relevant variation with Nino 3.4. Each IC is independent with others in space, which is revealed by the spatial patterns in Figure 5.7. Accordingly, we cannot easily recognize the ICs which associate with ENSO only based on those temporal and spatial patterns. The weak correlations of TWS ICs indicate no clear connection to ENSO.

Table 5.2: Correlation between Nino 3.4 index and ICs from TWS.

Basins	Ob	Lena	Yenisei	Mackenzie	Yukon
IC 1	-0.1	0.2	-0.2	0.2	0.1
IC 2	-0.4	0.3	-0.3	-0.1	-0.2
IC 3	0.1	-0.1	-0.3	-0.1	-0.1
IC 4	0.1	0.2	0.1	0.1	0.1
IC 5	-0.1	-0.2	-0.1	0.2	-0.3

Coherency analysis Similar to PCA, correlation of each IC does not give us any clues of association with ENSO. Hence, we resort to wavelet coherency. The coherency maps of IC 3, IC 4 and IC 5 which contains inter-annual signals are shown in Figure 5.8. IC 3 is coherent with Nino 3.4 at the annual band with coherency of 0.5. It has no significant coherency at the biennial band after 2007. This performance reveals that IC 3 is not the mode of variability, which associates with ENSO. IC 4 has notable coherency both at the annual band from 2003 to 2008, and at the biennial band during the whole time. Similarly, IC 5 also shows coherency both at the biennial band from 2003 to 2014, and at the annual band from 2011 to 2014. The biennial variation in IC 4 is nearly synchronous with ENSO, while the IC 5 of TWS shows about $\pi/3$ phase lead to ENSO.

In other words, both IC 4 and IC 5 are identified to associate with ENSO, though with different phase shift. It is reasonable that two ICs are relevant to ENSO, because we perform the ICA on the spatial dimension and thus gain the ICs only independent in space. Compared with spatial patterns in Figure 5.7, ENSO-related IC 4 and IC 5 stands for the inter-annual change at different locations in Lena.

Different from PCA that only compresses the most significant information in the first several modes, ICA separates statistically the independent information into ICs, and each IC contains as important information as the others. Using ICA, we gain either temporal or spatial independent patterns. Like IC 4 and IC5 in Figure 5.7, temporal variations with different phase shifts are reflected in space from spatial independent patterns.

ICA successfully separates independent modes of variability at independent locations in space from TWS observations. However, like PCA, the associated modes with ENSO are not automatically identified by ICA through correlation or other metrics. Obviously, although ICA has an advantage in extracting independent patterns from observations, it is rarely helpful in detecting certain patterns like ENSO.

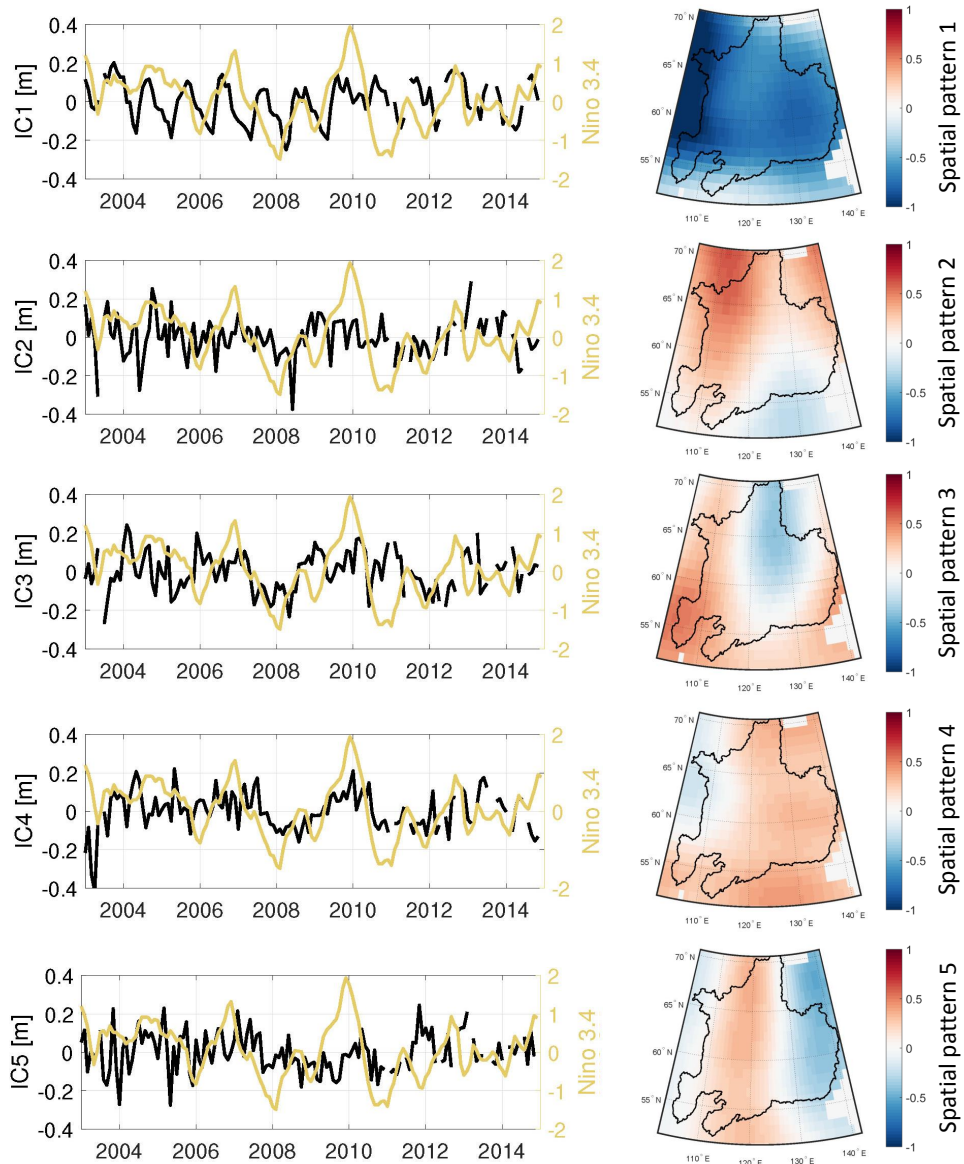


Figure 5.7: The five temporal ICs (left) by ICA of the Lena basin, together with corresponding spatial patterns (right). The black line in the temporal ICs denotes total water storage, compared with Nino 3.4 index (yellow line).

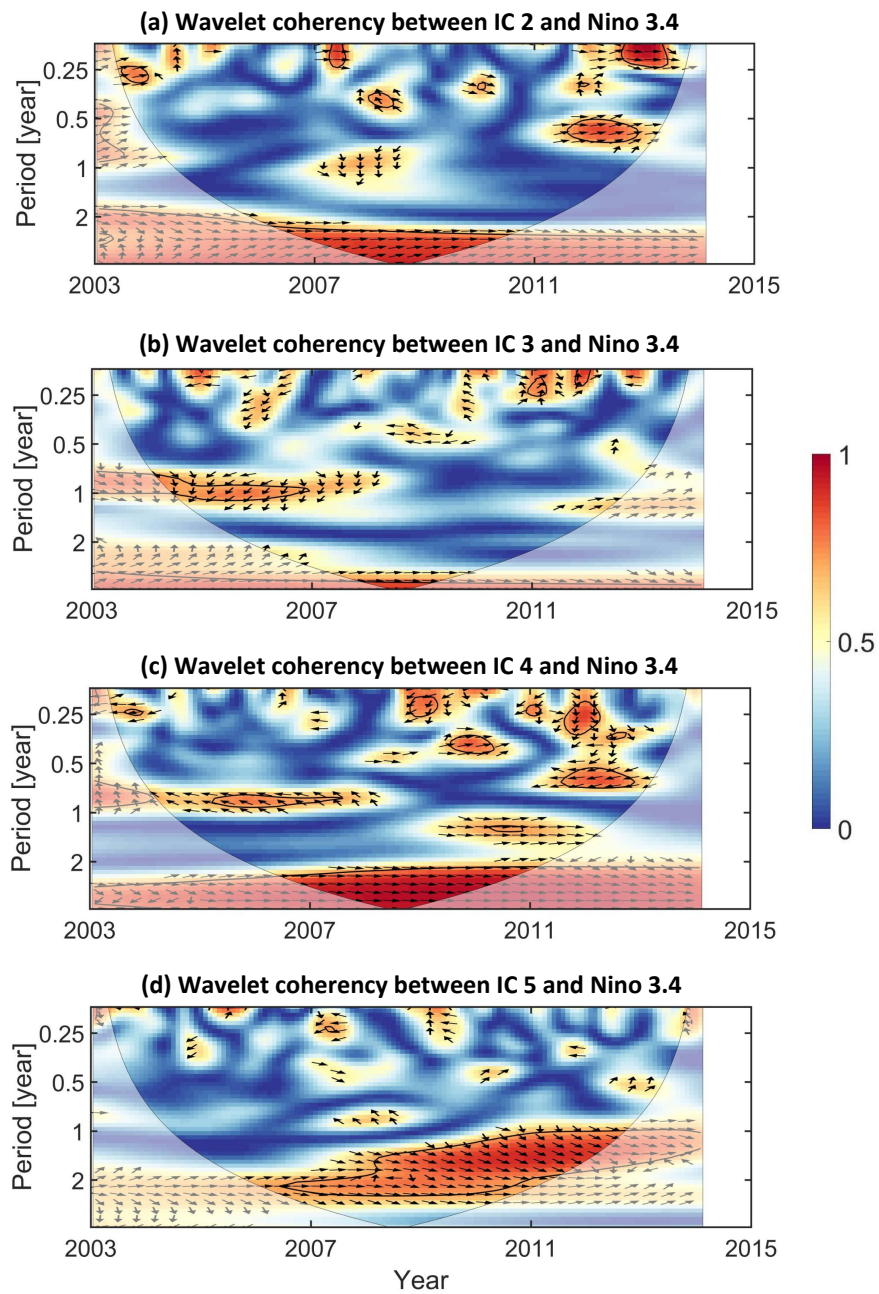


Figure 5.8: The wavelet coherence between Nino 3.4 index and IC3 (a), IC4 (b) and IC5 (c) by ICA, respectively. Same description as Figure 5.6.

5.2 Between ENSO and terrestrial water cycle

Dataset The data sets used in our study are listed in Table 5.3. Global SST anomalies are used, considering the global impact of ENSO. The hydrological and geodetic variables, such as terrestrial water storage changes M , total precipitation P , river runoff R , evapotranspiration E , and land surface temperature anomalies T , are obtained within the boreal region (latitude from 55° to 90°).

Table 5.3: Data sets used in this study.

Variable	Data Source	Temporal Resolution	Spatial Resolution
M	GRACE	monthly	$1^\circ \times 1^\circ$
P	ECMWF-Interim	daily	$0.5^\circ \times 0.5^\circ$
R	ECMWF-Interim	daily	$0.5^\circ \times 0.5^\circ$
E	ECMWF-Interim	daily	$0.5^\circ \times 0.5^\circ$
T	GHCN CAMS	monthly	$0.5^\circ \times 0.5^\circ$
SST	Kaplan Extended SST	monthly	$5^\circ \times 5^\circ$

The observation time series from GRACE is processed as the same dataset used in 5.1. The GRACE observations we used cover 12 years, from January 2003 to December 2014. The missing epochs in time series are not interpolated.

The atmospheric reanalysis ERA-Interim from the European Center for Medium-Range Weather Forecasts (ECMWF) provides daily fields of total precipitation, evaporation and runoff (Dee et al., 2011). To keep consistency with GRACE observations, we use the data sets from ECMWF only covering the period 2003–2014. These data sets are produced with 0.5° spatial resolution but are averaged here to 1° resolution. In boreal catchments, transpiration is negligible under dry and cold condition. Hence, evapotranspiration is equated with evaporation in this research. To keep consistency with time series from GRACE, the temporal resolution is averaged from daily to monthly. We then obtain monthly anomalies of precipitation, evaporation and runoff by removing the long-term mean.

Monthly land surface air temperature anomalies over the period 2003–2014, used in this study, are produced by the Climate Prediction Center (CPC), National Centers for Environmental Prediction (NCEP). This data set is station observation based, using a combination of two large individual data sets of station observations collected from the Global Historical Climatology Network version 2 (GHCN V2) and the Climate Anomaly Monitoring System (CAMS) (Fan and van den Dool, 2008). It provides global monthly mean air temperature at 2m level, with $0.5^\circ \times 0.5^\circ$ spatial resolution. The monthly anomalies of land surface temperature are obtained by removing the long term mean.

Monthly sea surface temperature (SST) anomalies are obtained from Kaplan Extended SST V2, which are gridded global SST anomalies from 1856 to present derived from UK Met Office SST data (Kaplan et al., 1998) (<http://www.esrl.noaa.gov/psd/>). The SST data are on a $5^\circ \times 5^\circ$ grid; the period we use is from 2003 to 2014. In order to investigate the global effects of ENSO, here the SST data are used at the global scale (87.5°S – 87.5°N and 2.5°E – 357.5°E).

The linear trends of all the time series in this research are removed by least-squares regression. Gaps in time series are removed from time series before decomposition analysis to prevent

interpolation errors. After removing existing gaps from the 12-year time series, we have $t = 131$ samples in the period 2003 to 2014 from all the fields. Those gaps are added back in the temporal modes afterwards.

5.2.1 Build up links between terrestrial water cycle and ENSO

Although many studies indicate the correlation between ENSO and hydrological variation, in fact, it is difficult to model the relationship between ENSO and hydrological variables. Directly projecting the individual hydrological variables, which typically have seasonal characteristics, on ENSO is not a proper strategy.

As we know, ENSO indices are derived mathematically from SST anomalies in the central Pacific, have dominantly inter-annual and long-term behaviors. So if we would isolate inter-annual and long-term variations from hydrological time series, and associate them with the comparable variation of global SST anomalies, we can consequently link associated temporal modes to ENSO. Therefore, our study is based on this strategy. To detect the linear relationship with ENSO, we apply the CCA method to combinations of SST with individual hydrological data sets, and SST anomalies are here adopted as an intermedium.

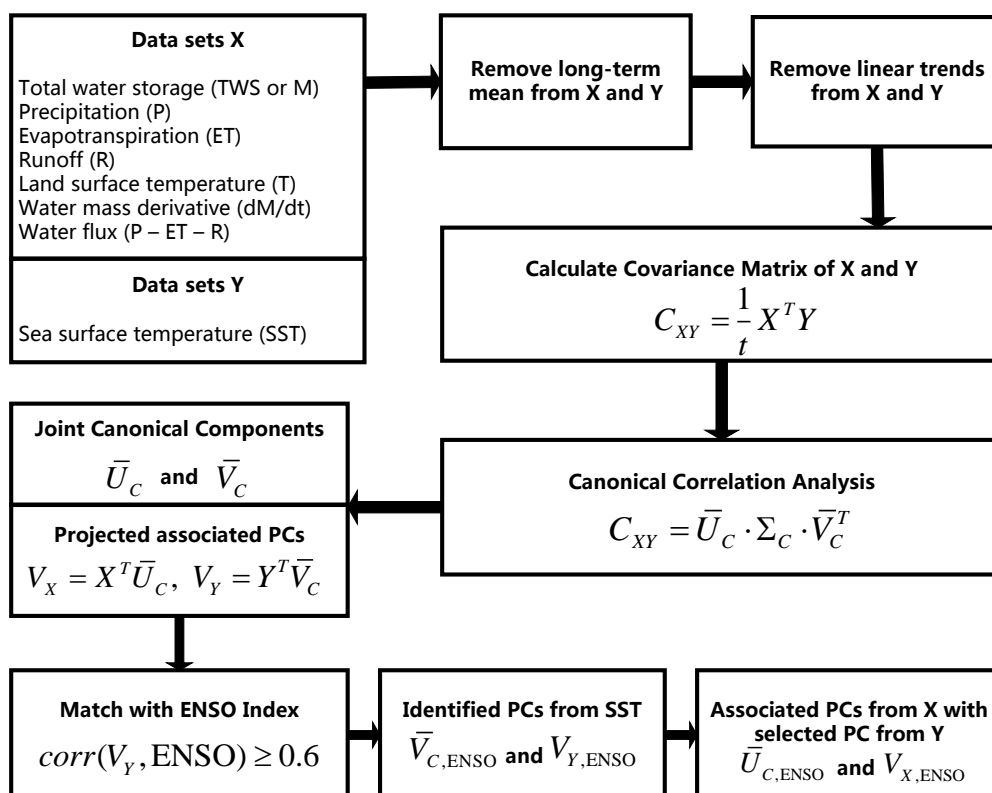


Figure 5.9: Procedure of data processing by CCA

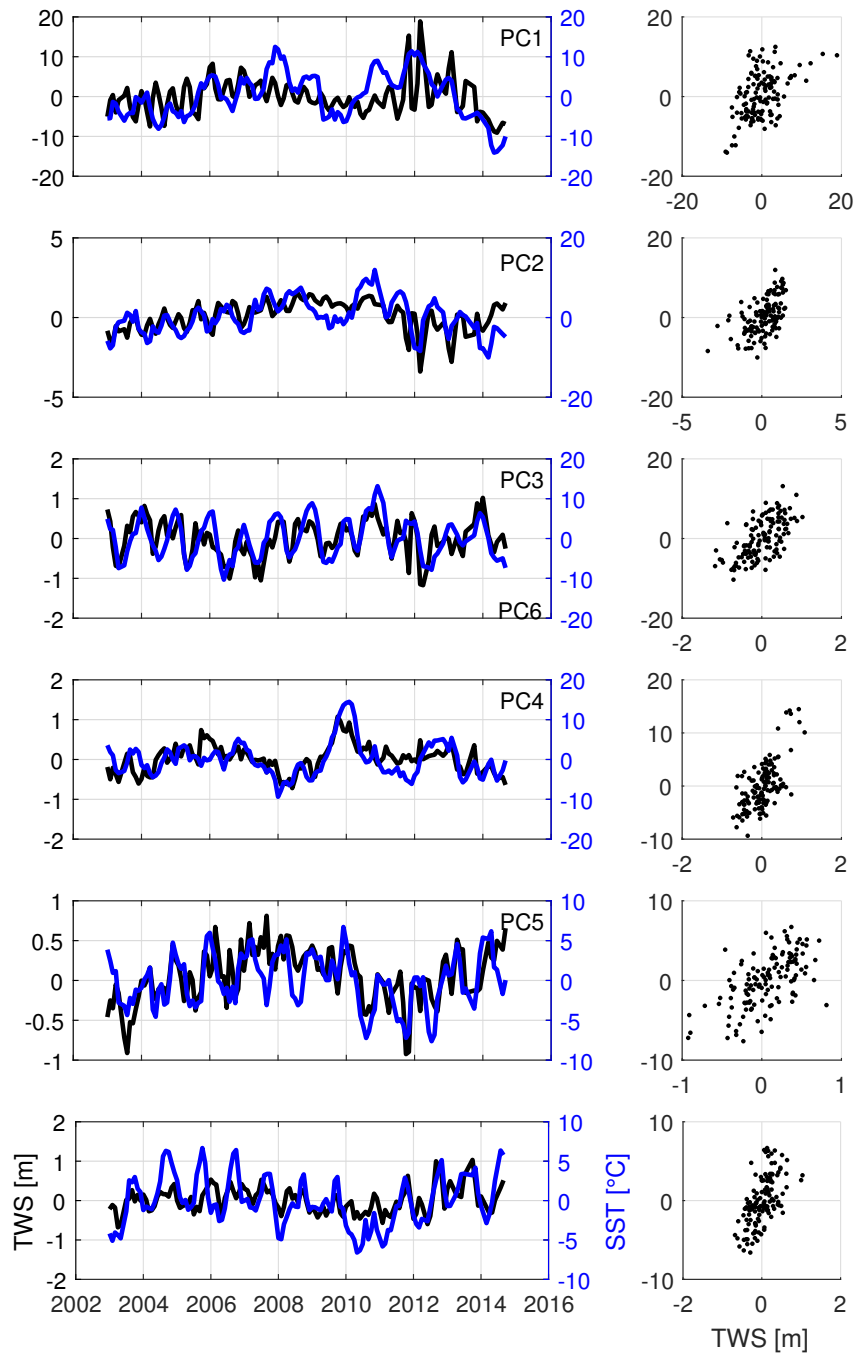


Figure 5.10: (left) Temporal modes of each PC pair of total water storage anomalies from GRACE in the boreal region and global sea surface temperature anomalies after CCA decomposition, and (right) the scatter plot between the paired PCs from total water storage and sea surface temperature.

As shown in Figure 5.9, gridded time series of total water storage, precipitation, evaporation, river runoff, surface temperature as well as water storage flux are treated as variable X , while SST is used as variable Y . Both X and Y have the same temporal sampling but different spatial resolutions. For each variable X we calculate its covariance with Y in order to obtain a time-independent covariance matrix, and then we apply CCA on these covariance matrices. As a result, \bar{U}_C, \bar{V}_C here are normalized spatial EOFs, representing spatial patterns for each variable. V_X, V_Y are then associated temporal PCs, containing temporal modes of each variable.

We match each temporal mode from SST with ENSO (Nino 3.4) time series. The target modes V_Y are identified by calculation of correlation coefficients

$$\rho = \frac{\text{Cov}(V_Y, \text{ENSO})}{\sigma_{V_Y} \sigma_{\text{ENSO}}}, \quad (5.1)$$

where V_Y is the matrix of temporal modes from SST, $\sigma_{V_Y}, \sigma_{\text{ENSO}}$ are the standard deviations of V_Y and ENSO index, $\text{Cov}(V_Y, \text{ENSO})$ is the covariance of V_Y and ENSO, and ρ denotes correlation coefficients. The modes with high correlation ($|\rho| \geq 0.6$) are retained. After we obtain the identified PCs V_Y from SST, the associated PCs V_X from other variables are consequently selected. Based on those selected modes V_X, V_Y , spatial EOFs \bar{U}_C, \bar{V}_C are then obtained by projection of V_X, V_Y on each field X, Y . Those EOFs represent the spatial response of each hydrological variable to ENSO.

Since here SST is treated as an intermedium between ENSO and hydrological variables, the spatial resolution of SST does not affect the resolution of \bar{U}_C , which refers to different hydrological variables. Hence, for reducing the computation, we use the SST data with only 5° spatial resolution instead of more dense data sets. Neglecting the long-term evolution with periods larger than 10 years, we remove the linear trend from each data set.

As described in the flowchart (Figure 5.9), first the canonical modes from SST are compared with the ENSO index, and these modes with correlation coefficients larger than 0.6 ($R > 0.6$) are selected. In this study, for each data set, we choose the first 10 canonical modes. It should be sufficient because the first 10 joint modes already contain more than 90% signal variance.

For example, in Figure 5.10, the first six joint modes of GRACE-derived TWS and SST are shown. The scatter plots of each pair represent the level of linearity between the two fields. Temporal PC 2, PC 3, and PC 5 represent strong seasonal variation of terrestrial water storage and SST, while PC 4 represents inter-annual change. Because of a similar inter-annual evolution in the ENSO index, only PC 4 is identified as a mode associated with ENSO, although PC 2, PC 3, and PC 5 have significantly high correlation between TWS and SST.

We calculate the cross-covariance matrix between SST and each variable. Applying CCA on each covariance matrix, we gain canonical PCs for each variable and SST. In Table 5.4, the correlation coefficients are shown between each of these temporal modes and the Nino 3.4 index. Each row contains the correlation coefficients between each PC and Nino 3.4 index, referring to the particular variable. Specifically, any PC_i with the same index but from different variables are different temporal modes. For instance, in Table 5.4, PC 5 from R -SST is different from PC 5 from E -SST after CCA decomposition.

SST as an intermedium is well illustrated in Figure 5.11. The PCs for each variable shown in this figure are selected based on the performance listed in Table 5.4. For each field, the joint

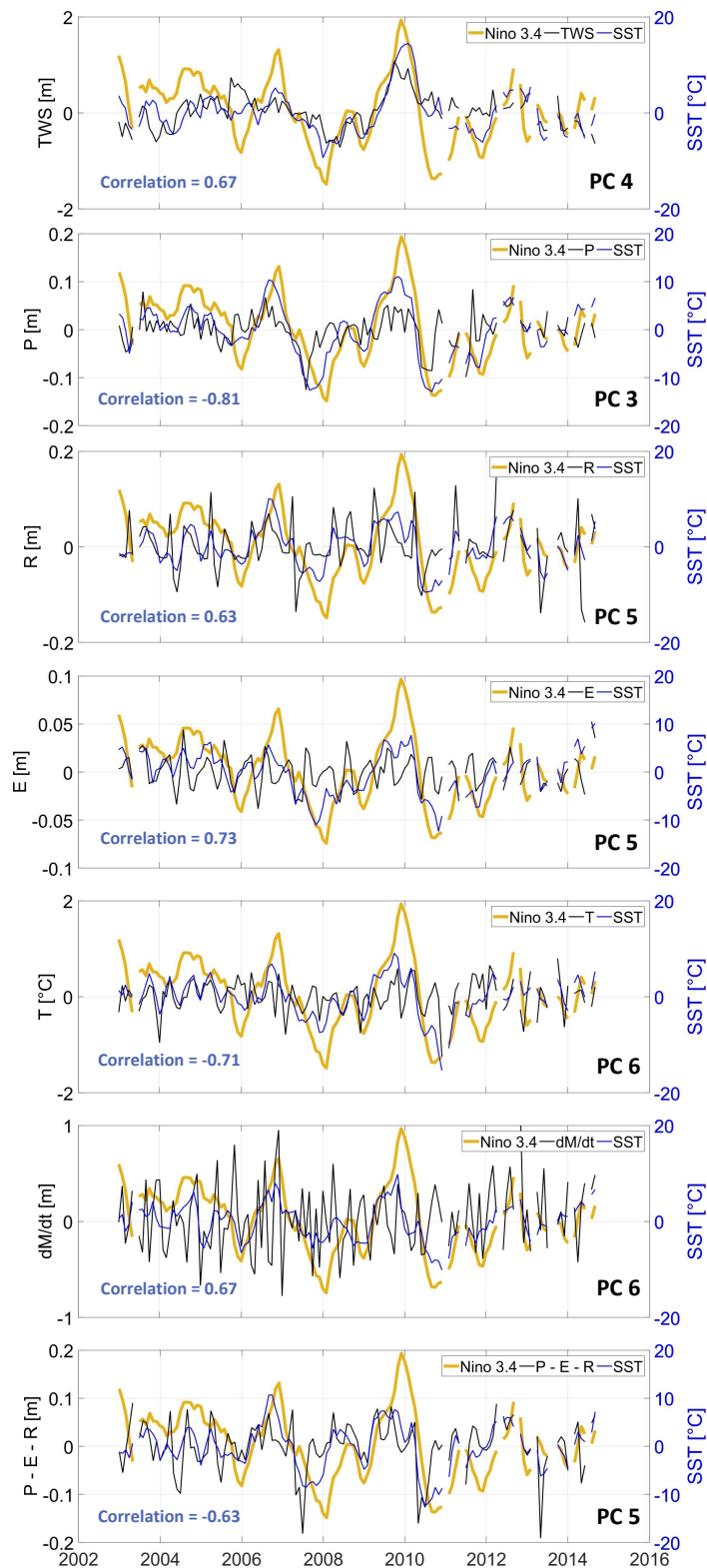


Figure 5.11: Temporal modes of sea surface temperature anomalies (blue line) compared with each variable (black line), i.e., total water storage, precipitation, evaporation, runoff, surface temperatures, water mass derivative, water fluxes, respectively, associated with Nino 3.4 index (yellow line). Nino 3.4 index are scaled by the magnitude of each variable.

Table 5.4: Correlation between Nino 3.4 index and 10 temporal modes of SSTs, corresponding to water mass variation, precipitation, runoff, evaporation, land surface temperature, and water fluxes derived from GRACE observations and water balance equation, respectively. The mode of largest correlation coefficient with Nino 3.4 are emphasized in the table.

Datasets	PC1	PC2	PC3	PC4	PC5	PC6	PC7	PC8	PC9	PC10
M	-0.65	-0.37	-0.39	0.67	0.10	0.27	0.36	-0.42	-0.12	-0.16
P	-0.31	-0.29	-0.81	0.29	0.38	0.29	-0.15	-0.47	-0.16	-0.10
R	-0.34	0.10	-0.51	0.59	0.63	0.41	0.60	0.06	0.25	-0.37
E	0.33	0.29	-0.22	0.15	0.73	-0.54	0.36	0.07	-0.42	-0.33
T	-0.29	0.62	0.41	-0.55	-0.11	-0.71	0.20	-0.47	-0.16	-0.30
dM/dt	0.40	0.43	0.24	0.36	0.62	0.67	-0.04	-0.34	0.64	-0.47
$P - E - R$	-0.32	0.28	-0.13	0.55	-0.63	0.43	0.49	0.49	-0.38	0.27

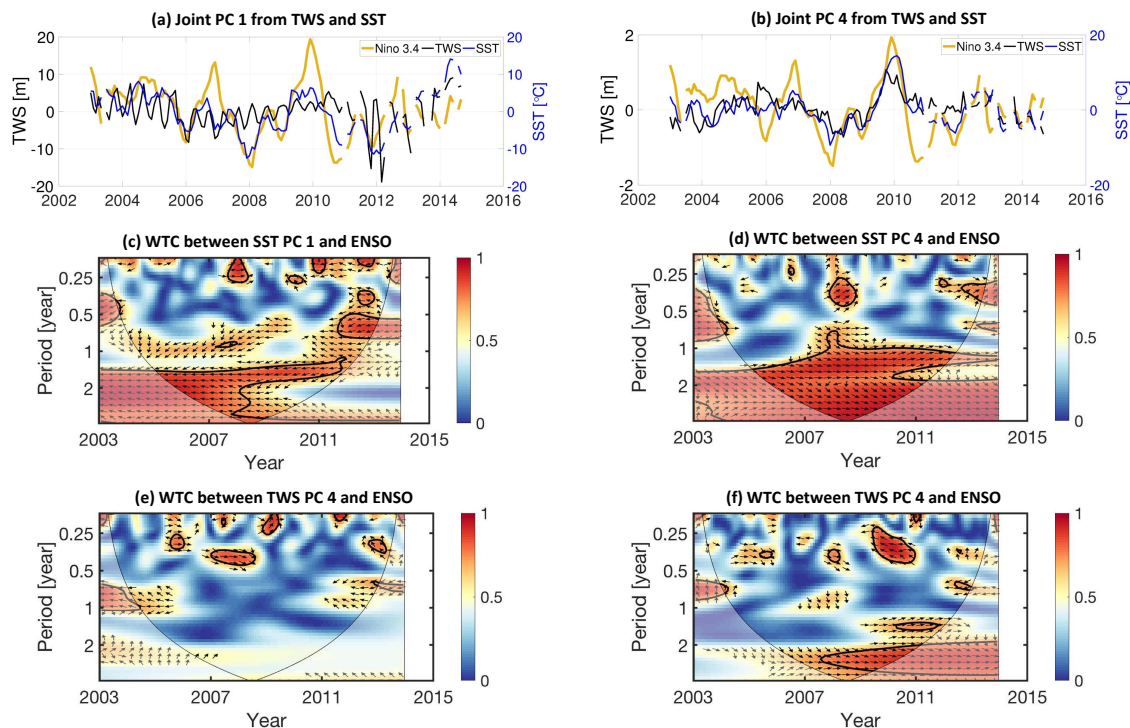


Figure 5.12: Temporal joint mode of (a) PC1 and (b) PC4 from TWS and SST are listed in the first row. The wavelet coherence of between ENSO and joint (c) PC1, (d) PC4 from SST are listed in the second row. The wavelet coherence of between ENSO and joint (e) PC1, (f) PC4 from TWS are listed in the third row.

modes in Figure 5.11 are directly calculated by CCA. Based only on these patterns, we do not know which one is associated with ENSO. In the next step, we compare the temporal modes of SST with scaled Nino 3.4 (as shown in Figure 5.11). According to the correlation coefficients between SST and Nino 3.4, the joint modes from SST, whose correlation coefficient larger than 0.6, are therefore identified. the ENSO-related mode is identified by . As a result, we gain the ENSO-related modes of terrestrial variables with the aid of the identified joint modes from SST. In this case, SST builds up a bridge between observations on land and climate variability from the ocean-atmospheric circulation. Thus, those identified PCs indicate the temporal variation on land associated with ENSO signals.

Actually, the PC identification is not unique. In Table 5.4, both PC1 and PC4 from TWS-SST are correlated to the ENSO effect. Statistically, all of the modes with high correlation reflect a link to ENSO. For M , R , T , and dM/dt , there are more than one mode with a correlation above 0.6. The non-unique identification indicates that CCA decomposition can not distinguish the different phases. Two different modes from the same variable may both represent a similar evolution. In this study, we generally selected the mode with highest correlation for further analysis. As shown in Table 5.4, we consequently identify the temporal modes related to ENSO from TWS (M), precipitation (P), runoff (R), evaporation (E), land surface temperature (T), water mass derivative (dM/dt) and water storage fluxes ($P - E - R$). All the PCs with negative correlation to ENSO are transferred to positive phase so as to support the visual comparison with others.

Regarding the non-unique solutions, we necessarily refer to the wavelet transformation. From the spectrum coherency (in Figure 5.12) of joint modes of PC 1 and PC 4 from TWS and SST, we find that both the temporal PCs from SST have strong coherency with ENSO. However, the performances of these two PCs from TWS are different. PC 1 has a low response at biennial bands in the spectrum, while PC 4 shows relatively strong coherency at 2-year and 2.5-year bands. Comparing the spectra in Figure 5.12(a) and (b), we certainly regard the joint PC 4 from TWS and SST as associated signal with ENSO.

5.2.2 Signature of ENSO on pan-Arctic water cycle

In brief, our purpose is finally to understand how the terrestrial water mass variation is involved in the circulation between ocean, land and atmosphere. Therefore, considering SST an intermedium between climate change over the ocean and terrestrial water cycle on land, signature of ENSO on pan-Arctic water cycle is investigated by applying a CCA approach. Not only water storage, several variables (i.e., precipitation, evaporation, river runoff, land surface temperature) involved in the circulation are analyzed.

With temporal PCs of canonical modes from CCA, we obtain the associated EOFs for each field by projection of each field onto PCs, as plotted in Figure 5.14 . Those corresponding EOFs represent the spatial patterns associated with ENSO effects. All the PCs with negative correlation to ENSO are transferred to positive phase to support the visual comparison with others. Associated spatial patterns are transferred conversely as well.

Signature of total water storage Firstly, as an example, Figure 5.13(b) shows the temporal pattern of PC 4 for TWS and SST, while Figure 5.13 (a) and (c) illustrate the associated spatial patterns of TWS and SST. In Figure 5.13, it shows a notable connection on 120°E, and negative

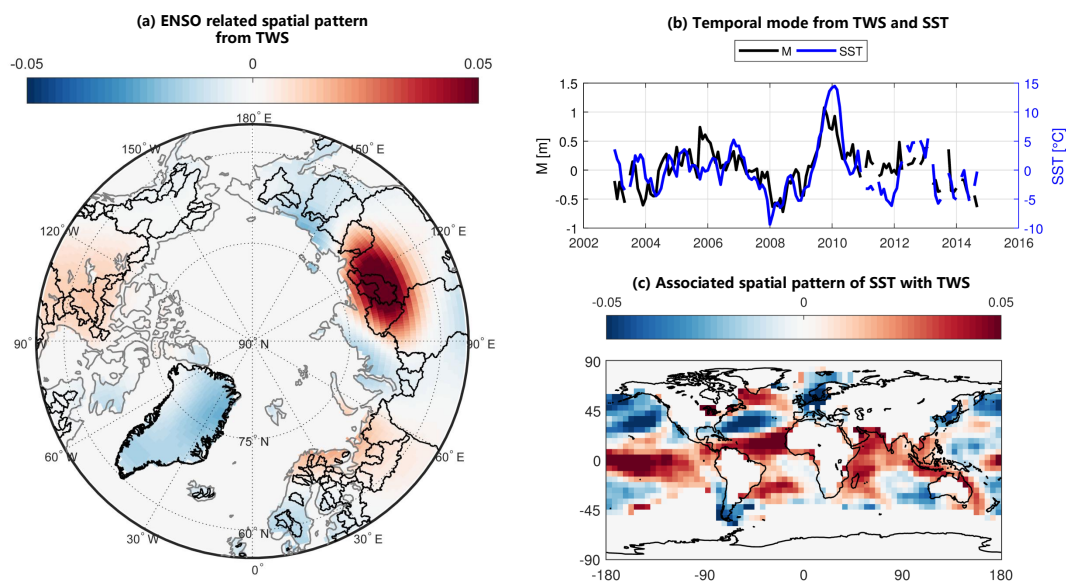


Figure 5.13: (left) (b) Temporal joint mode from total water storage and SST, with (a) the ENSO related spatial patterns from TWS and (c) SST.

response on 90°E and 150°E . Comparison with the map in Figure 5.3 reveals that TWS evidently relates to ENSO in the Lena and Yenisei basins. It illustrates an alternating patterns of terrestrial water mass in east-west direction in Siberia, which refers to ENSO. The spatial pattern in central Pacific identifies that the associated PC from TWS relates to Nino 3.4.

As we gain the spatio-temporal patterns of TWS associated with ENSO, the notable signature of ENSO is illustrated on pan-Arctic region. In other words, TWS in pan-Arctic and ENSO in the Pacific are statistically associated through the teleconnection patterns in Figure 5.13. The results have revealed notable teleconnection patterns of ENSO on boreal catchments. The patterns of TWS in Figure 5.13 only reveals the connection between terrestrial water storage and ENSO in Siberia.

In order to analyze the association between ENSO and boreal water cycle and realize how the TWS is involved in boreal water cycle, we also need to evaluate the spatio-temporal performance of precipitation, runoff, evaporation and surface temperature. Their spatial and temporal patterns are collected later in the Figure 5.14.

Signature on precipitation PC 3 of precipitation and SST is identified to associate with Nino 3.4 index (Figure 5.11). ENSO related spatial patterns of precipitation and SST are shown in Figure 5.14 (a) and (b). Those reveal the teleconnection between ENSO and rainfall in boreal region. As illustrated in the spatial patterns, the anomalies of SST in east Pacific result in temporal evolution of precipitation in Siberia and North America. The spatial response of precipitation to ENSO is positive in Ob and Lena, and negative in Yenisei. It indicates that rainfall increases in Lena and Ob, while it reduces in Yenisei, referring to ENSO. Similarly, ENSO relates to a reduction of rainfall in Yukon and Mackenzie basin.

Signature on runoff The ENSO related spatial patterns of runoff and SST are depicted in Figure 5.14. We find that runoff in the boreal region is statistically correlated to inter-annual evolution of SST in central Pacific and southeast Asia, and North Atlantic as well. In contrast to Figure 5.14 (a), ENSO has a strong positive association with runoff in the Yukon basin. Between Ob and Yenisei, there is a negative correlation to ENSO. Different from evaporation, the spatial pattern of river runoff in the Lena basin reveals a strong positive correlation with ENSO.

Signature on evaporation ENSO related spatial patterns of evaporation and SST are shown in Figure 5.14 (a) and (b), together with their identified temporal modes in Figure 5.11. For evaporation, Figure 5.14 (b) illustrates an evident association in western and eastern Siberia and in Alaska. ENSO related inter-annual change of evaporation is identified in the boreal region by the associated temporal mode in Figure 5.11. In terms of boreal basins, it reveals a positive relation to ENSO in Yenisei but negative relation in Yukon. On the contrary, a minor impact is found on Ob, Yenisei and Mackenzie basin. In fact, evaporation links indirectly to ENSO. The abnormal climate condition induces anomalous land surface temperature, which gives then rise to the evaporation. The signature of ENSO on evaporation has to be confirmed by temperature patterns. Therefore, the surface temperature change on land is investigated in order to better understand and interpret the effect of ENSO on evaporation.

Signature on land surface temperature In boreal regions, land surface temperature anomalies play an important role in the terrestrial water cycle. We apply the same procedure on LST and match them with SST. There is an evident spatial oscillation of LST from Scandinavia to Eastern Russia and in North America. The ENSO related spatial pattern of LST shows a strong positive signal in Mackenzie and Yukon. Also, a negative signal in southern part of Lena and Yenisei and northern part of Ob is obvious, while positive in northern part of Lena and Yenisei.

Generally, evaporation maintains a negative relationship with land surface temperature (Sun et al., 2016). A reduction of evaporation causes a rise of temperature. From the spatial patterns in Figure 5.14, evaporation and temperature inversely relate to ENSO. However, compared with Figure 5.14 (b), SST inter-annual changes in central Pacific, Indian ocean and in Scandinavia are consistent with the SST pattern associated with precipitation. The precipitation and temperature represent similar spatial patterns in the pan-Arctic region. Hence, we infer that on one hand, the inter-annual changes of rainfall in boreal region follows the ENSO events; on the other hand, the temperature anomalies likely reflect the impact of ENSO on precipitation. The reduction of rainfall in Mackenzie and Yukon basin possibly causes a temperature rise. Additionally, the precipitation, unusually increasing in Lena and decreasing in Yenisei, leads to significant temperature anomalies. Referring to land surface temperature in Figure 5.14 (a), it indicates that ENSO likely causes abnormal reduction of rainfall in Yenisei, and induce the decrease of water storage fluxes, as well as land surface temperature.

Signature on water storage fluxes Despite the inconsistency in most areas, evaporation probably still relates to the temperature change in some areas. For instance, they both have strongly negative response in East Siberia. Considering that most of the boreal region is covered by snow and ice, the temperature anomaly increase might directly induce ice melting, but not water evaporation. In Alaska, both temperature and runoff show a positive pattern in the

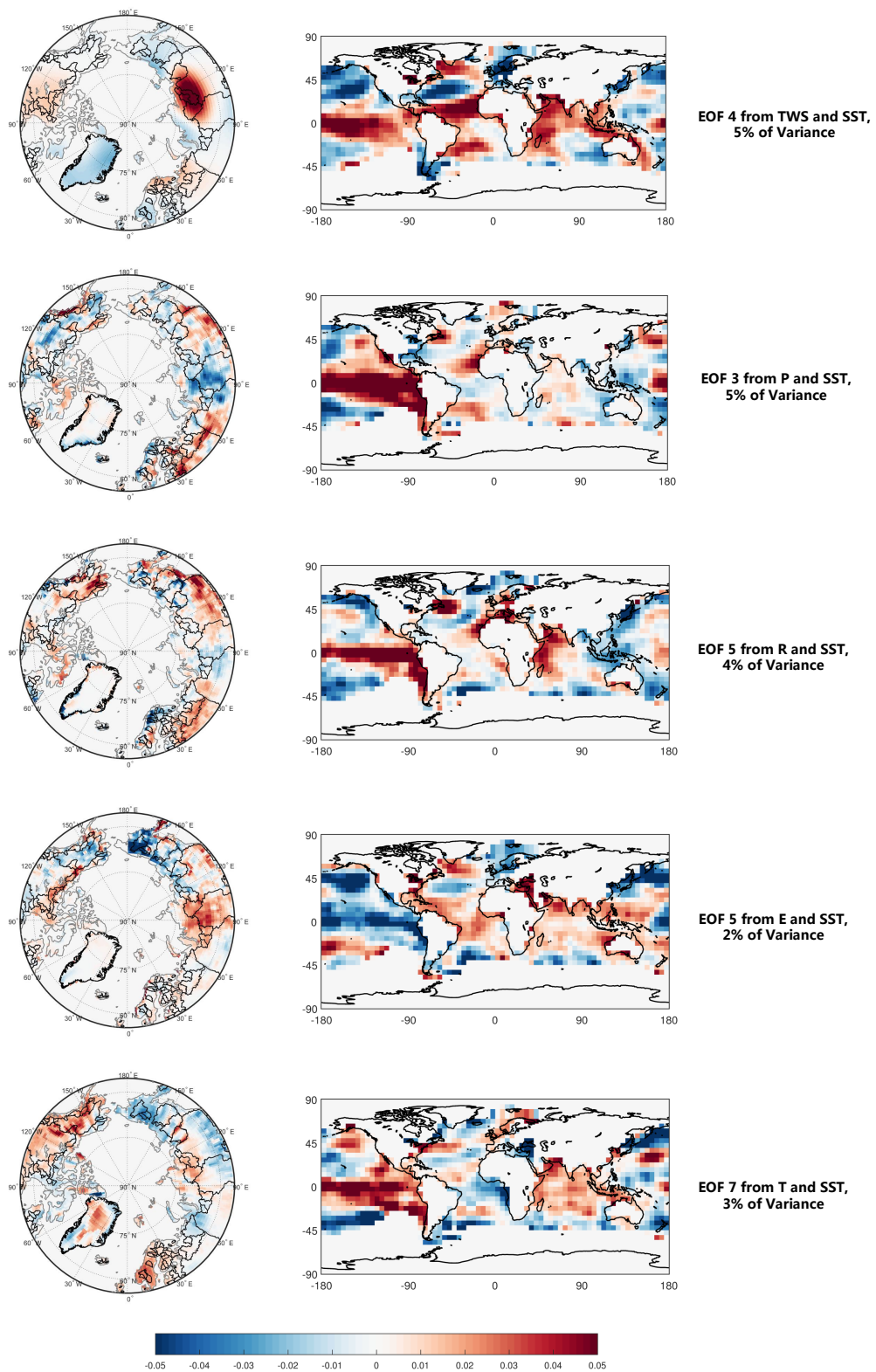


Figure 5.14: (a) Spatial pattern of each variable in boreal region, related to ENSO effects; (b) Spatial pattern of global SST, associated with each variable. The EOFs are selected by correlation coefficients shown in Table 5.4.

Yukon basin, confirming the cause and effect. The water storage flux is additionally analyzed in 5.2.3 to dig out the connection of precipitation, evaporation and runoff to ENSO.

By comparing the spatial patterns between different variables, we find that TWS behaves differently than others. It is still a question how water mass change relates to ENSO. Theoretically, as the water balance described in Eq. (1.1), not water storage itself but water mass derivative directly relates to the water balance. As shown in 5.2.2, the signature of ENSO on water storage does not visually agree with precipitation, evaporation and runoff. Therefore, we now apply CCA also on water storage fluxes to investigate the signature of ENSO on terrestrial water storage fluxes.

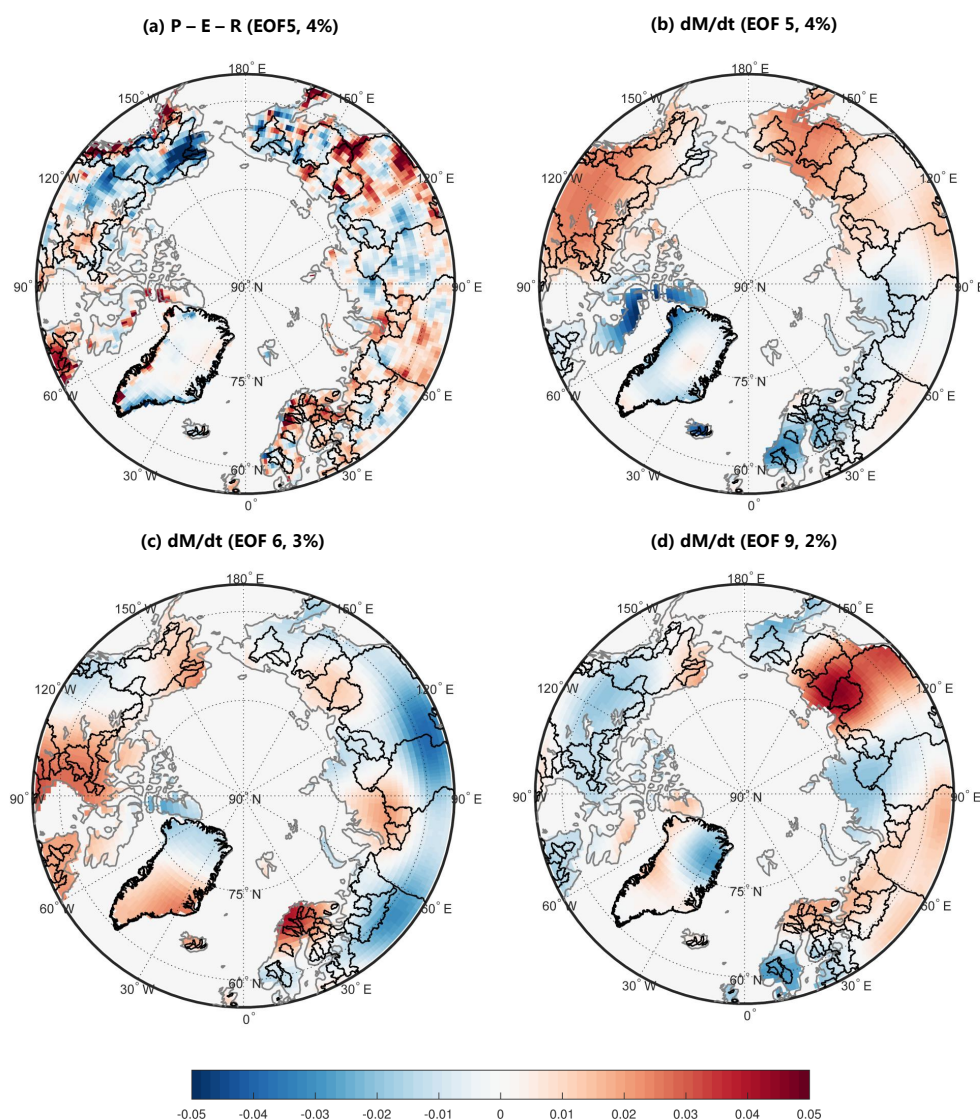


Figure 5.15: (a) ENSO related spatial patterns of water storage fluxes EOF5 from (a) water balance equation; And ENSO related spatial patterns of water mass derivative from GRACE observations, represented in three different EOFs, i.e., (b) EOF 5, (c) EOF 6 and (d) EOF 9, respectively.

The water mass derivative (dM/dt) is derived from GRACE observations, and the water storage flux ($P - E - R$) is calculated by the difference of precipitation, evaporation and runoff. Figure 5.15 and 5.16 show the ENSO related spatial patterns from water storage fluxes. PC 5 listed in Table 5.4 shows the largest correlation with Nino 3.4. Thus, the associated spatial pattern of PC 5 is depicted in Figure 5.15 (a). It indicates a surplus of water storage in the Ob basin, while a deficit of water storage occurs in Yenisei. Corresponding to ENSO, Lena has a water budget surplus in most area. On the contrary, in Yukon and Mackenzie water storage fluxes negatively relate to ENSO.

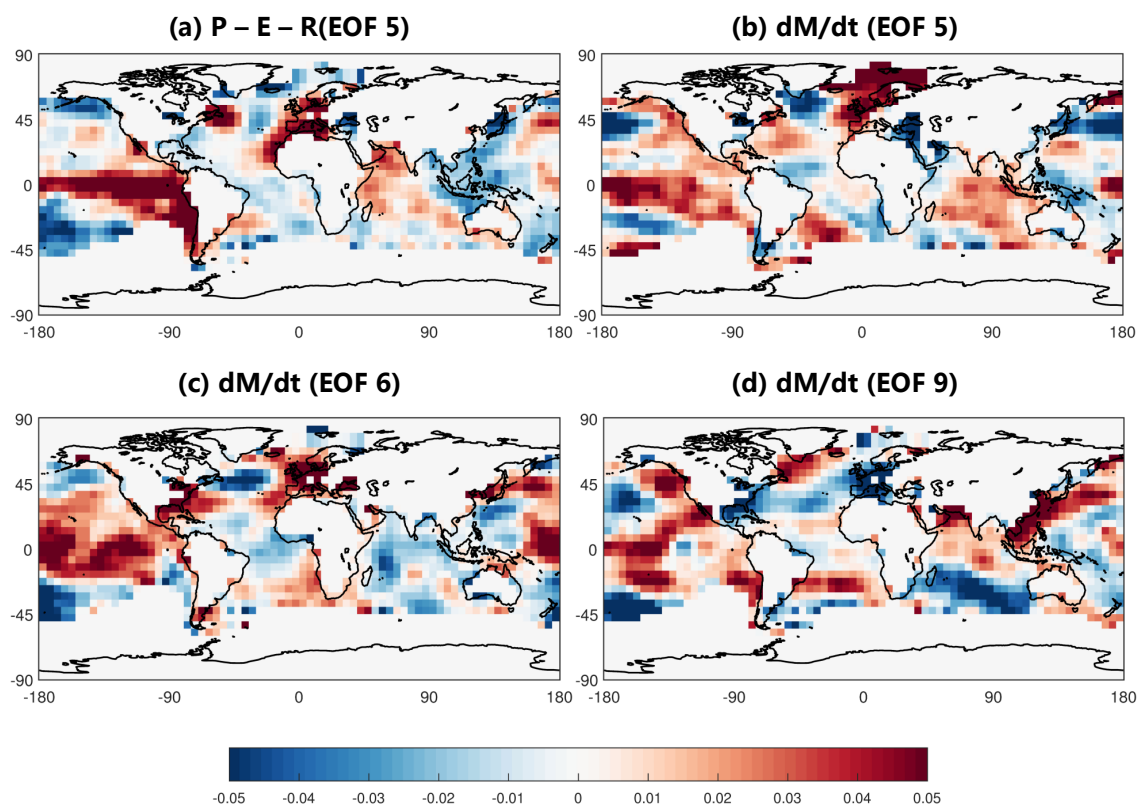


Figure 5.16: ENSO related spatial patterns of SST, associated with (a) water storage fluxes from water balance equation, and with water mass derivative from GRACE observations, represented in three different EOFs, i.e., (b) EOF 5, (c) EOF 6 and (d) EOF 9, respectively.

The differences in spatial patterns of precipitation, evaporation, runoff and temperature are now well interpreted using the results from water storage fluxes. For example, in Yenisei basin, ENSO has no impact on river runoff but caused a reduced precipitation and increased evaporation. Particularly, surface temperature decreases due to ENSO. We infer that the decrease of surface temperature over Yenisei after ENSO eventually leads to a deficit of water storage fluxes. As a result, the increase of evaporation does not contradict the decrease of temperature. In contrast, spatial patterns in Figure 5.14 (a), do not allow the interpretation that the water storage fluxes decrease.

Water storage fluxes are produced from GRACE as the time derivative of water mass change. Different from the results of water balance equation, three PCs show good correlation with

Nino 3.4 (PC 5: $\rho = 0.62$, PC 6 $\rho = 0.67$, PC 9: $\rho = 0.64$). The temporal component of modes 5, 6, 9 are thus selected in this study. Associated spatial EOFs are represented in Figure 5.15 (b), (c) and (d), respectively.

EOF 5 from GRACE water mass derivative does not show a clear connection to ENSO in the Ob, Yenisei and Lena basins. Figure 5.15 (b) illustrates that ENSO has a positive response in the Mackenzie river basin. EOF 6 of GRACE has a negative correlation in most parts of Ob, Yenisei and Lena, but no notable correlation in Mackenzie and Yukon. EOF 9 shows an alternating pattern over Siberia. Particularly, water storage fluxes in Lena and Ob have a positive correlation, while in part of Yenisei it has negative correlation with Nino 3.4. Compared with Figure 5.15 (a), we find that EOF 9 shows similar patterns in Ob, Lena and Yenisei. Although the difference still existed in some areas, like in Alaska, the consistent patterns in most areas demonstrate the connection between ENSO and the boreal water cycle. Even though EOF 6 has the largest correlation with Nino 3.4, both EOF 5 and EOF 9 still contain important information and are not negligible.

Water storage flux is notably sensitive to ENSO, unlike water storage. In Figure 5.14, water storage only reveals ENSO impact on the entire area of Lena and Yenisei. In Figure 5.15, the spatial response to ENSO is distinguished in different basins by water storage fluxes. Water storage flux reflects clearly the connection between ENSO and boreal hydrological cycle from associated spatial pattern.

Spatial patterns of SST related to Nino 3.4 are depicted as well in Figure 5.16. Compared with Fig 5.15, the difference of EOF 5, EOF 6 and EOF 9 are interpreted by the different spatial response in SST. It reflects different patterns on the central Pacific. The strong positive responses in SST move from central Pacific to the east and north, as shown in Figure 5.15 (b), (c), (d). We properly understand these three PCs as the dynamic response of ENSO.

Phase delay responding to ENSO To investigate the influence of ENSO on pan-Arctic region, phase difference is an important indicator. It reflects the consequence of ENSO events and the dynamic process in the terrestrial water cycle. Therefore, we used three different approaches here to estimate the phase and time difference between ENSO and each variables, as listed in Table 5.5.

Generally, we assume that ENSO leads to inter-annual variations in the terrestrial water cycle. Hence, the phase lags between hydrological observations and ENSO reflect important information. In this part, we estimate the phase lags between Nino 3.4 index and the identified temporal modes from each variable.

Using Hilbert transformation approach as described in 4.3, we obtain the phase difference $\Delta\phi$ and time shift Δt_1 between Nino 3.4 and each variable, and the results are given in Table 5.5. As a result, precipitation, runoff and evaporation have time lag to ENSO while total water storage shows a time lead to ENSO. Land surface temperature changes rapidly as ENSO nearly without any lags.

Also, we get the integer time lags Δt_2 from cross-correlation. Results in Table 5.5 reveal that precipitation, evaporation, runoff and temperature statistically respond to ENSO simultaneously with 1-month time lag, whereas there is no time delay between ENSO and total water

Table 5.5: Phase difference $\Delta\phi$ and time lag Δt_1 and Δt_2 between Nino 3.4 index and PCs from each variable. Positive values indicate the lead of ENSO, while negative values indicate the lag of ENSO to terrestrial observations. $\Delta\phi$ and Δt_1 are estimated from Hilbert transformation equation, and Δt_2 is calculated by cross-correlation.

Mode	$\Delta\phi$	Δt_1 [month]	Δt_2 [month]
M PC4	-0.12	-1.4	0
P PC3	0.12	1.4	1
R PC5	0.17	2.0	1
E PC6	0.18	2.2	1
T PC6	0.05	0.6	1

storage. Precipitation, runoff and evaporation represent the same time delay due to the limit of the temporal resolution.

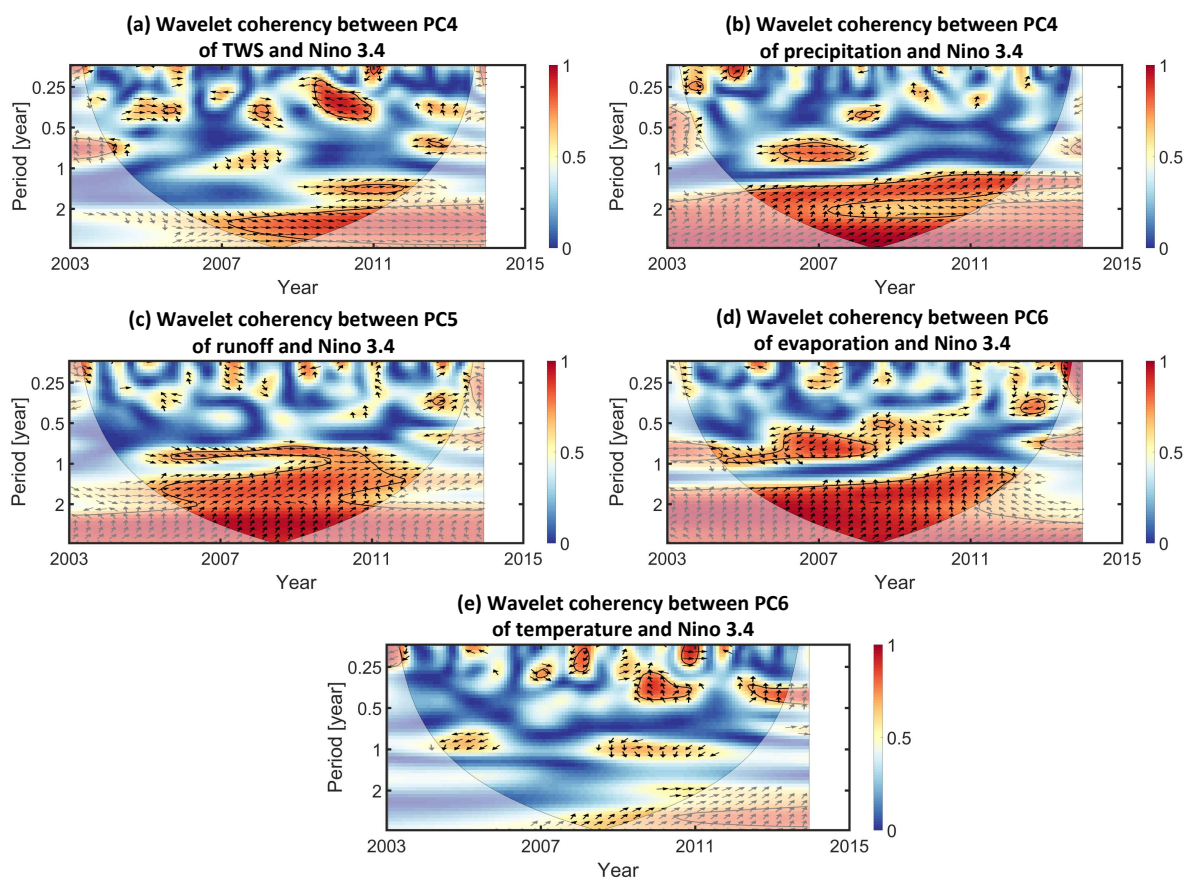


Figure 5.17: Wavelet coherency between Nino 3.4 index and (a) PC4 from total water storage, (b) PC3 from precipitation, (c) PC5 from runoff, (d) PC6 from evaporation and (e) PC6 from temperature, respectively. Same description as Figure 5.6.

Referring to wavelet coherency between ENSO and each associated mode, we gain the direction of phase differences. As shown in Figure 5.17, precipitation, runoff and evaporation show time lags to ENSO. Temperature also slightly time delay to ENSO, although the coherency is not so

significant. In Figure 5.17(a), water storage and ENSO are in phase for most of time, which indicates no lags between each other.

Comparing the results in Table 5.5 and in Figure 5.17 indicates that ENSO induces an inter-annual change in the water cycle. However, it is still difficult to explain the lead of inter-annual water storage to ENSO. Water storage change might not be sensitive to ENSO. To evaluate the influence of ENSO on terrestrial water cycle, we do further analysis on water storage fluxes.

In fact, the influence of ENSO on the water cycle is a dynamic process. Rising temperature causes increasing evaporation and ice melt, while increasing evaporation also leads to decrease of surface temperature. Wet and warm conditions likely reflect a increase of rainfall, while cold and dry conditions relate to a decrease of rainfall.

Table 5.6: Phase difference $\Delta\phi$ and time lag Δt_1 and Δt_2 between Nino 3.4 index and PCs from water storage fluxes by dM/dt and water balance $P - E - R$. Positive values indicate the lead of ENSO, while negative values indicate the lag of ENSO to water storage fluxes. $\Delta\phi$ and Δt_1 are estimated from Hilbert transformation equation, and Δt_2 is calculated by cross-correlation.

Mode	$\Delta\phi$	Δt_1 [month]	Δt_2 [month]
$P - E - R$ PC5	0.20	2.4	2
dM/dt PC5	0.13	1.5	2
dM/dt PC6	0.12	1.4	1
dM/dt PC9	-0.01	-0.1	0

Similar as above, we calculate the time lags between Nino 3.4 and identified modes of water storage fluxes from $P - E - R$ and dM/dt . In Table 5.6, except for PC 9 from water mass derivative, all the other associated modes show phase and time lags to ENSO. Δt_1 and Δt_2 have relatively consistent results. Water storage fluxes show consistent time lags to ENSO, comparing with precipitation, runoff and evaporation. Hence, we can infer that water storage fluxes is more sensitive to ENSO rather than water storage. This difference in Table 5.6 between $P - E - R$ and dM/dt is explained by the different sensitivities of spaceborne observations and model reanalysis data.

Referring to wavelet coherency in Figure 5.18, both $P - E - R$ and dM/dt perform relatively consistent. Water storage fluxes respond to ENSO with positive lag in phase. The water storage flux from water balance equation has more evident coherency with ENSO than those from mass derivative at both annual and biennial bands. It certifies the influence of ENSO on the terrestrial water cycle. In other words, it indicates that 1–2 month delay to ENSO evidently exists in pan-Arctic water cycle.

Additionally, the notable coherency in Figure 5.18 proves that each identified mode from dM/dt is associated with ENSO. Since PC 5, PC 6, PC 9 from water mass derivative are already proved to associated with ENSO, the different time lags explain a dynamic connection between ENSO and the boreal water cycle.

The teleconnection between ENSO and global TWS observed by GRACE is revealed in many studies. Phillips et al. (2012) found significant correlation between ENSO and TWS over the period 2003–2010 in many areas, especially Alaska and Siberia, using Hilbert transformation. They provided the connection patterns by correlation maps. However, they did not present temporal patterns to illustrate how TWS changed in relation with ENSO. Their time lags range

from 0 to 3 months. These time lags explain that inter-annual TWS changes as a consequence of ENSO events. Their patterns show strong connections in Siberia and Alaska, like our results. At high latitude, they did not provide time lags in details.

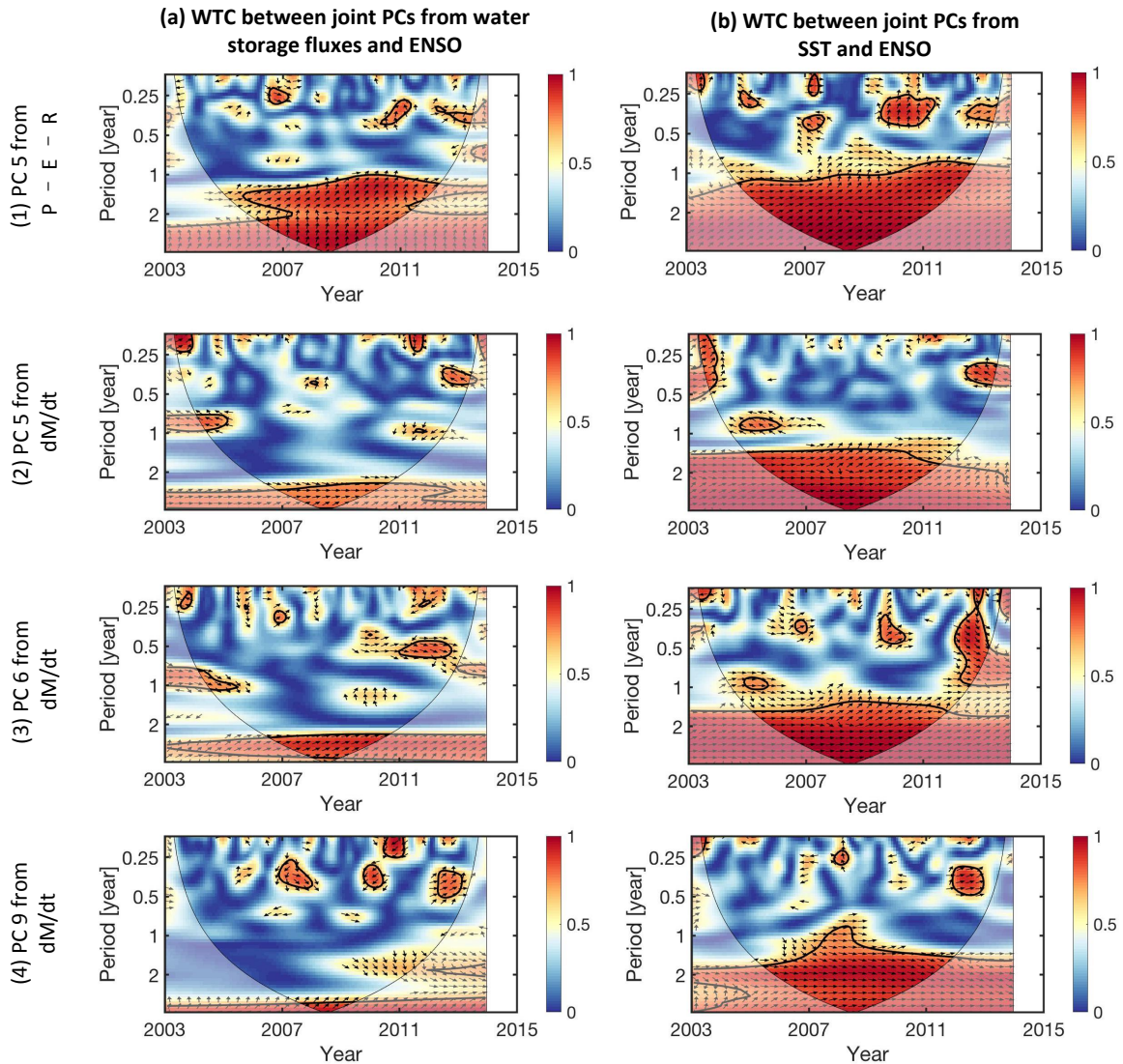


Figure 5.18: ENSO related spatial patterns of SST, associated with (a) water storage fluxes from water balance equation, and with water mass derivative from GRACE observations, represented in three different EOFs, i.e., (b) EOF 5, (c) EOF 6 and (d) EOF 9, respectively.

5.2.3 Signature of ENSO on individual boreal catchments

In order to recognize the signature of ENSO on specific catchments in pan-Arctic, a comprehensive analysis on catchments is required to interpret the influence of ENSO.

In this section, we select the three large Siberian catchments Ob, Yenisei and Lena as examples in the boreal region. Thus, we analyze more details by applying CCA again on the individual

catchments. The associated temporal modes of the three catchments are selected according to the correlation between SST modes and Nino 3.4 index, as represented in Figure 5.22. After identification of those modes from SST, associated temporal modes of each variable are consequently obtained. The identified temporal modes are not the same as the patterns shown in Figure 5.11. Instead, they represent temporal inter-annual changes in specific catchments, responding to ENSO events.

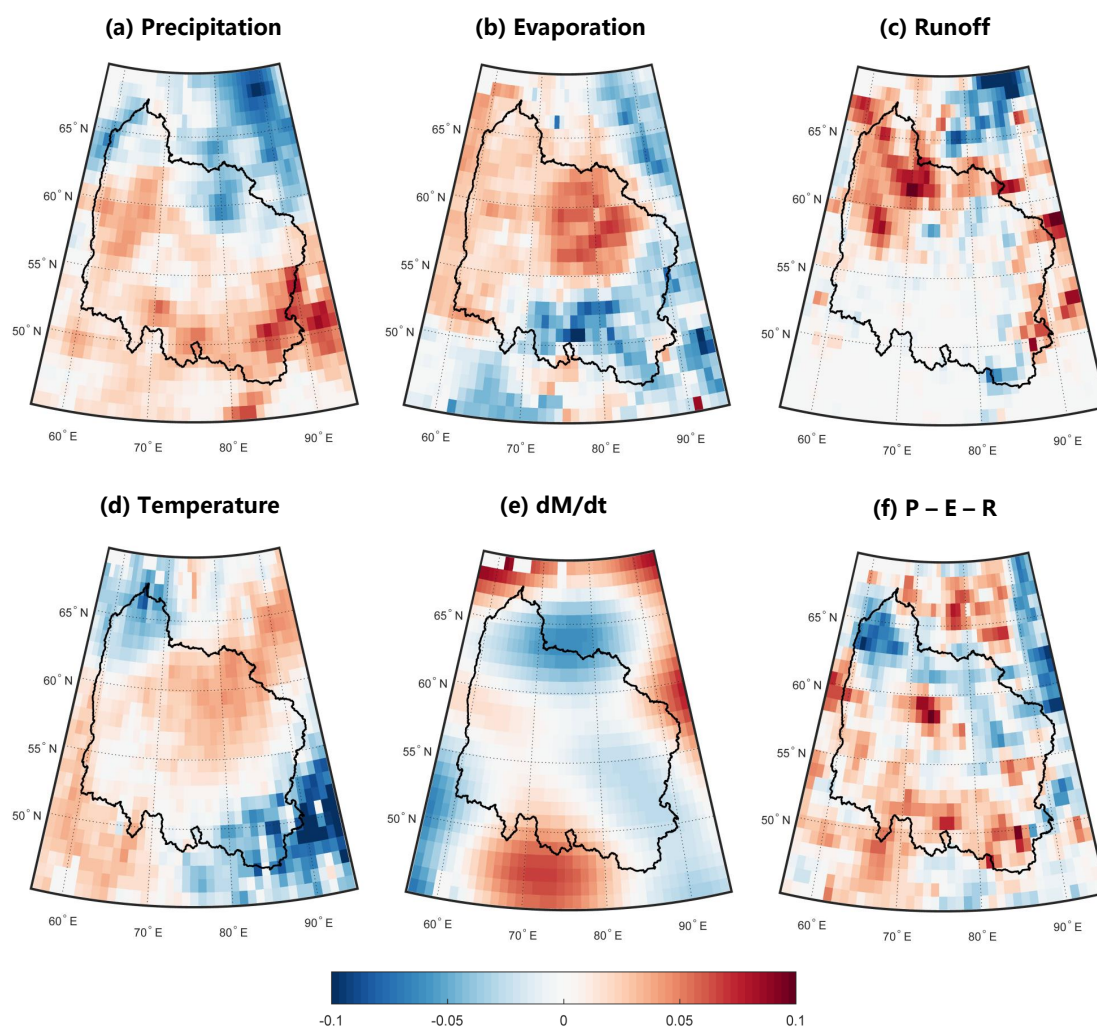


Figure 5.19: ENSO related spatial patterns in the Ob basin of (a) precipitation, (b) evaporation, (c) river runoff, (d) surface temperature, (e) water storage fluxes derived from GRACE observations and (f) from water balance equation.

Figure 5.19, 5.21, 5.20 illustrate ENSO related spatial patterns for Ob, Yenisei and Lena basin. Due to the incomparable performance of TWS, here in this section, we only analyze the teleconnection between ENSO and precipitation, evaporation, river runoff, surface temperature, and water storage fluxes.

Ob basin A rise of rainfall relates to ENSO in the Ob basin of Figure 5.19 (a). The increase of evaporation over Ob (Figure 5.19 (b)) is explained by temperature anomaly increment (Figure 5.19 (d)). As shown in Figure 5.19 (c), the northwestern part of Ob has larger runoff than under normal conditions. The patterns indicate that ENSO leads to more active behavior of precipitation, evaporation and runoff in Ob. The resulting water storage flux from the water balance equation becomes positive in the south and negative in the north of Ob (Figure 5.19 (f)). It can be seen that evaporation and runoff in Ob increase more strongly than precipitation, following an ENSO event. Comparing with the water mass derivative from GRACE, we find similar patterns in Figure 5.19 (e). A difference between Figure 5.19 (e) and (f) still exists, though, and is probably caused by model errors and inconsistent spatial resolutions.

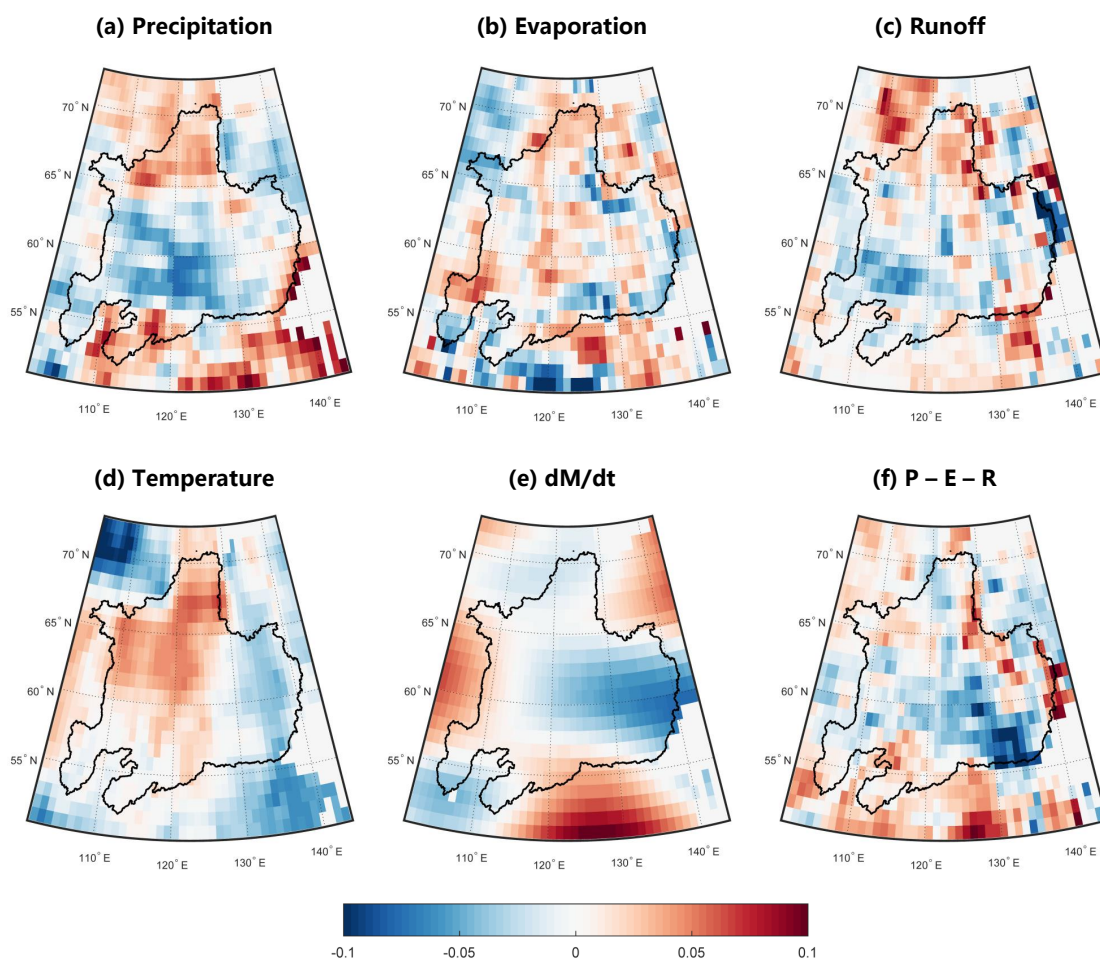


Figure 5.20: ENSO related spatial patterns in the Lena basin from (a) precipitation, (b) evaporation, (c) river runoff, (d) surface temperature, (e) water storage fluxes from water balance equation and (f) derived from GRACE observations.

Lena basin In Figure 5.20, we find that precipitation in the Lena basin reduces due to ENSO events. In contrast, neither evaporation nor runoff shows a clear positive or negative response

to ENSO in Figure 5.20 (b) and (c). Regardless of evaporation and runoff, the precipitation reduction probably induces the negative water storage fluxes in Lena.

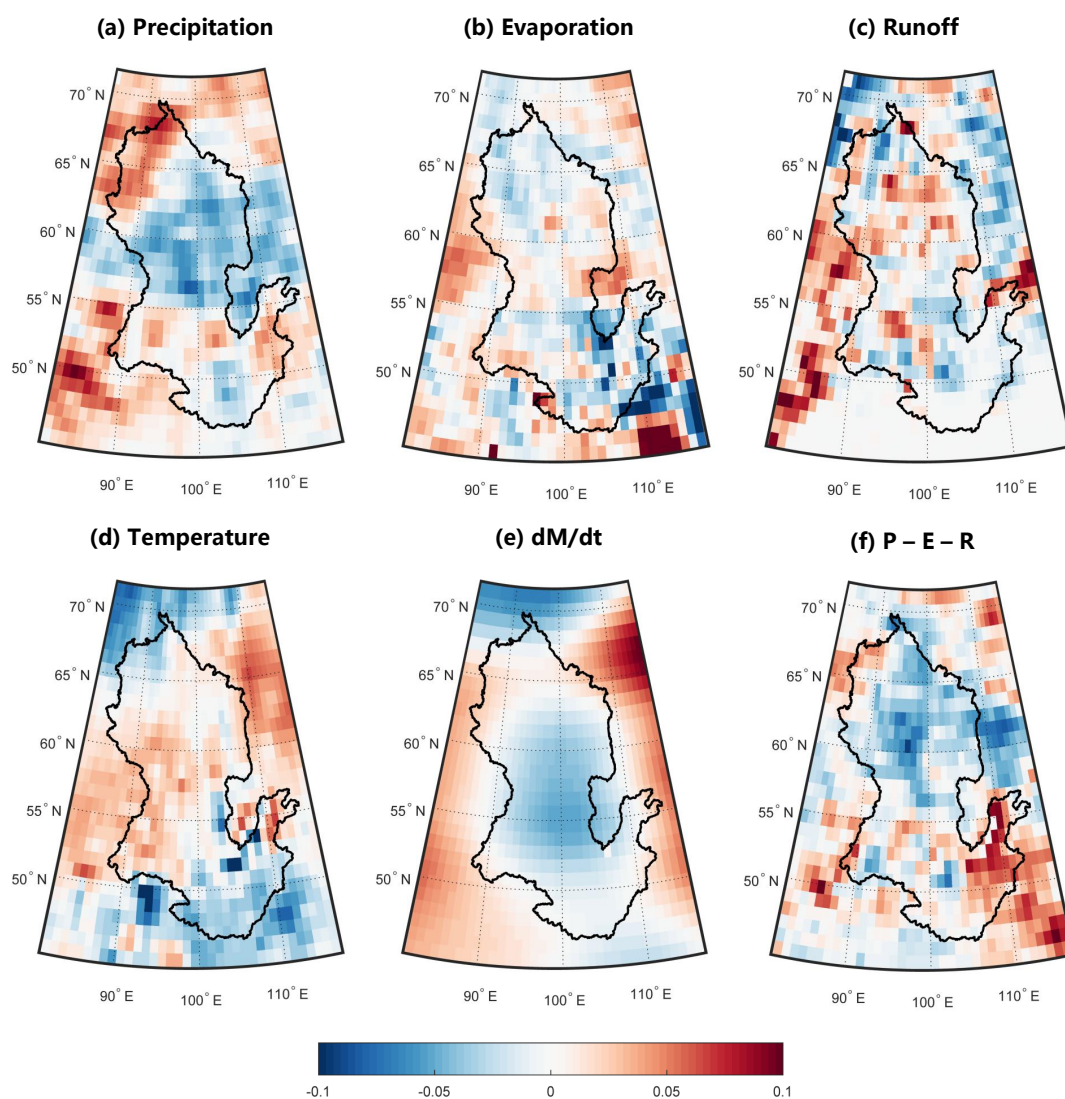


Figure 5.21: ENSO related spatial patterns in the Yenisei basin from (a) precipitation, (b) evaporation, (c) river runoff, (d) surface temperature, (e) water storage fluxes from water balance equation and (f) derived from GRACE observations.

As shown in Figure 5.20 (e) and (f), both of them represent strong negative patterns in the middle and southeast of Lena. Temperature anomalies relate positively to ENSO in the west part and negatively in the east (Figure 5.20 (d)). In comparison with Figure 5.20 (b) (c), the temperature increment in the west and in the middle does not cause a notable increase of evaporation and runoff, but reflects the reduction of precipitation in Lena.

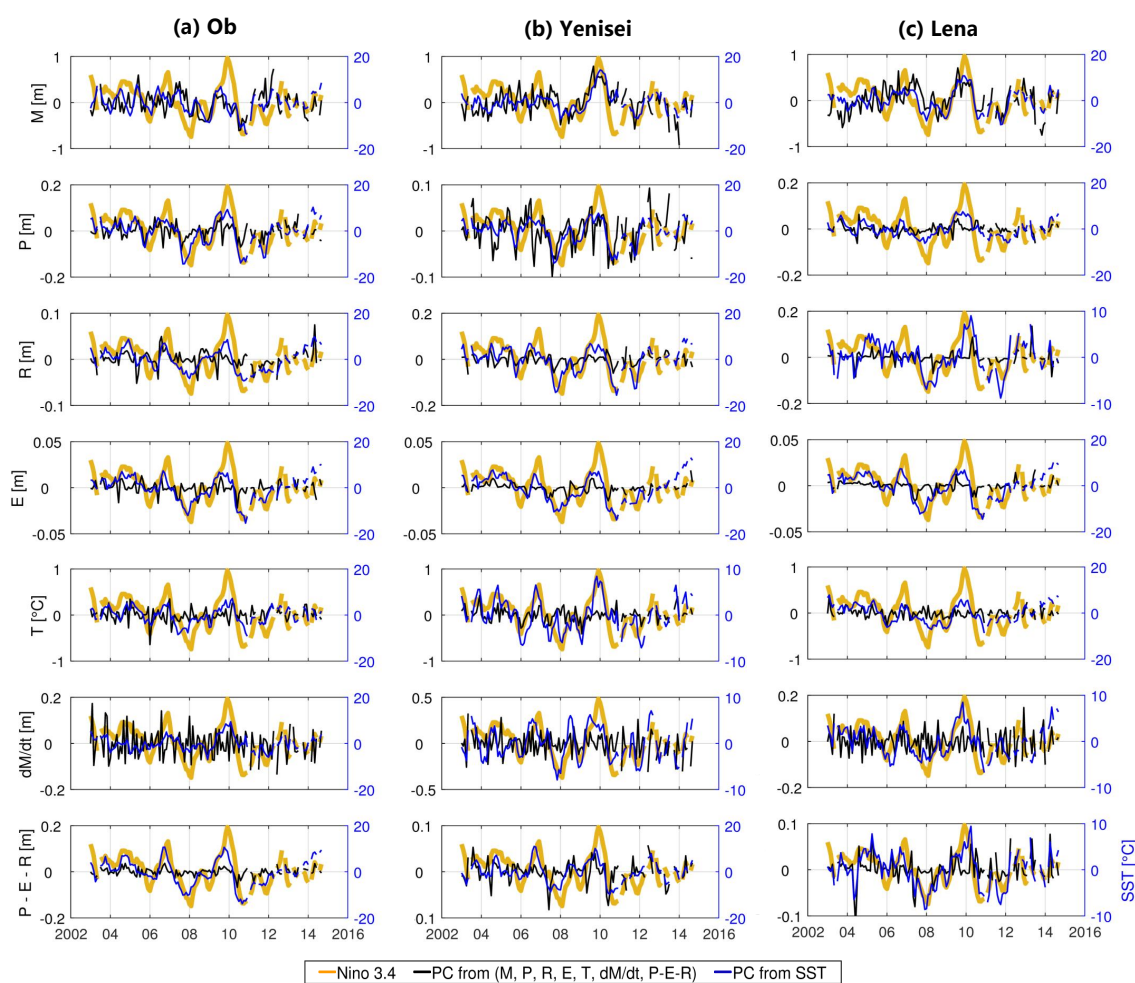


Figure 5.22: (a) Temporal modes of sea surface temperature anomalies compared with total water storage, precipitation, evaporation, runoff, surface temperatures, water mass derivative, water fluxes, respectively; (b) Temporal modes of sea surface temperature anomalies compared with Nino 3.4 index; (c) Temporal modes of each hydrologic variables compared with Nino 3.4.

Yenisei basin Different from the Ob basin, ENSO induces a strong negative precipitation over Yenisei, of Figure 5.21 (a). River runoff decreases notably in the north part of Yenisei (Figure 5.21 (c)). Both Figure 5.21 (e) and (f) reveal strong negative responses of water storage fluxes. However, a difference exists between GRACE observations and the water balance equation. Considering the water mass loss in Figure 5.21 (e) (f), evaporation is not affected by ENSO, as shown in Figure 5.21 (b). The spatial pattern of surface temperature in Figure 5.21 (d) supports this conclusion. The positive response of temperature in southeast outside of Yenisei convinces us that the result shown in Figure 5.19 (d) is reasonable.

Comparing Figure 5.14 and 5.15, we therefore understand that like in Yenisei, ENSO causes a notable reduction of precipitation and increase of evaporation, and consequently induces the negative output of water balance, which is revealed in Figure 5.21 as well. Normally, an increase of terrestrial evaporation causes a decrease of surface temperature. Sun et al. (2016)

indicated that evaporation and surface temperature maintain a positive relationship in cold and dry climate condition. The inconsistency between each variable in Figure 5.14 is therefore explained.

In summary, Yenisei evidently has a relevant connection to ENSO in precipitation and runoff. Abnormal large reduction of rainfall induces the negative water storage flux in most part of the catchment.

Phase delay responding to ENSO To detect the phase difference between terrestrial observations and ENSO, we refer to time delay estimated by Hilbert transformation in the linear regression model. As listed in Table 5.7, water storage, precipitation, evaporation and runoff in Ob show positive phase at about 1–2 month, which means 1–2 month lag to ENSO. Land surface temperature has nearly 0 phase difference, which indicates the temperature changes synchronously with ENSO. Different from Ob, water storage in Lena and Yenisei has more than 1-month lead to ENSO, while precipitation, evaporation and runoff has 1–2 month delay to ENSO. Water storage fluxes in Ob and Lena has phase shift around 0, which indicates the synchronous variation in water balance and ENSO. Temperature except for Ob has about 1-month lead to ENSO.

Table 5.7: Correlation ρ between Nino 3.4 index and identified PCs from SST, which is associated with each variable (i.e., M , P , R , E , T , dM/dt , $P - E - R$), with percentage of variance of identified PCs (σ) from each variable, and the time lags (Δt) of each variable to Nino 3.4, are listed for three boreal basins (Ob, Lena, Yenisei) in the table. In this case, positive Δ means time lag to ENSO, while negative stands for time lead to ENSO.

Variable	Ob			Lena			Yenisei		
	ρ	Δt [mo]	σ (%)	ρ	Δt [mo]	σ (%)	ρ	Δt [mo]	σ (%)
M	0.65	0.9	9	-0.75	-1.3	11	-0.62	-1.6	11
P	0.75	1.4	8	0.66	1.2	2	-0.69	1.8	8
R	-0.69	0.2	5	0.63	1.5	3	-0.71	1.3	5
E	0.74	1.7	2	0.71	1.8	1	-0.70	1.3	2
T	-0.70	-0.1	4	0.65	-1.0	3	0.70	-0.7	4
dM/dt	0.63	-0.4	2	0.65	0.2	2	0.60	0.2	3
$P - E - R$	-0.78	0.7	3	0.70	-0.3	2	0.68	1.2	3

The inconsistency still exists in the identified modes between dM/dt and $P - E - R$. Compared with other variables in the water cycle, the time lag to ENSO is more convinced by the results from $P - E - R$. Not only one mode from GRACE which is probably associated with ENSO might be the reason, as discussed in 5.2.2. In addition, according to the variance percentage of each variable in Table 5.7, ENSO has much larger influence on the water storage than other variables. In particular, the inter-annual change in evaporation is not significantly relevant to ENSO in these basins. The impact of ENSO on precipitation in Lena is not notable as in Ob and Yenisei.

Ni et al. (2017) calculated the cross-correlation between ENSO and interannual TWS change globally. Maximum correlation coefficients are found and represented in maps, which illustrate teleconnection patterns. They found no obvious and negative correlations in Lena basin by coherency spectrum. Our ENSO related spatial patterns (in Figure 5.14) reveals, however,

strong responses in part of Lena and Yenisei basin. Although the subpolar climate related hydrological cycle has no evident relationship with ENSO events, the signature of ENSO in the Lena basin is still revealed by our results. Clear correlation patterns over basins statistically indicate the impact of ENSO, even though the link between ENSO and terrestrial water cycle could hardly be modeled.

5.3 Discussion and summary

In this chapter, we aimed to investigate the teleconnection between ENSO and the terrestrial water cycle, and eventually to understand the role of terrestrial water mass change in the circulation of ocean, land and atmosphere.

PCA and ICA are successively applied to extract the associated patterns with ENSO from terrestrial water storage observations. PCA has compressed the signals into several dominant modes, one of which is relevant to ENSO. ICA has separated the observations into different independent components, and the ENSO-related variation are allocated in one or more independent components. In this chapter, we gain the spatial independent teleconnection patterns. Both PCA and ICA have proved to detect the signals associated with ENSO. A weakness still exists that those connection patterns are not automatically identified by either PCA or ICA.

CCA has the potential to isolate the inter-annual change from both SST and terrestrial observation time series simultaneously. Different from PCA and other decomposition method, CCA has an advantage on correlating linear relationship between two data sets, regardless of units. Based on its advantage of mutual relationship detection, CCA provides us another way to build up the link to ENSO. We consider sea surface temperature, which defines ENSO, as an intermedium between ENSO and terrestrial observations. In this case, we linked not only TWS from GRACE, but also other hydrological variables to ENSO, such as precipitation, evaporation, runoff as well as land surface temperature. The correlated inter-annual variations have been identified in associated canonical modes by CCA using SST as a bridge, compared with Nino 3.4 index. All the PCs from SST which have a correlation with the Nino 3.4 index larger than 0.6 are identified. The spatial pattern of terrestrial variables related to ENSO are obtained by projecting identified temporal modes in spatial domain.

As a result, we have identified the teleconnection patterns both temporally and spatially. The identified temporal modes of precipitation, runoff and evaporation show time lags to ENSO between 0 and 2 months. In addition, signatures of ENSO are also detected in specific boreal catchments, like Lena, Yenisei and Ob. ENSO influences TWS clearly in both the Ob and Yenisei basin, which ranges from -25 mm to 50 mm. ENSO results in a negative output of water over Yenisei and Lena, while no obvious negative response occurs over Ob. Precipitation behaves actively in the three basins due to ENSO. It is uncertain whether the temperature rise in the three basins relates to subsequent changes of evaporation or runoff, like in Yenisei and Lena.

The reaction of the boreal water cycle is a dynamic process, responding to ENSO in the central Pacific. Therefore, the phase differences and time lags are necessarily taken into consideration. We have introduced cross-correlation, the Hilbert transformation, as well as wavelet coherency to estimate the phase and time shift. In conclusion, water storage fluxes respond with about 1-month delay to ENSO, reflecting the impact of ENSO on terrestrial water cycle. Due to the

limited temporal resolution, we cannot explain physically the mechanism of ENSO impact on boreal catchments. Therefore, to interpret such a dynamic process, a more comprehensive analysis should consider to densify the temporal resolution by submonthly, weekly or even daily observations.

We investigate the teleconnection patterns only in a statistical way, without concerning the physical mechanism behind them. Our results illustrate notably the teleconnection between ENSO and boreal catchments. However, we still have to consider the interference of other oscillating climate patterns e.g., North Atlantic Oscillation (NAO), Arctic Oscillation (AO). AO effects on water mass change in the boreal region have been reported in (Peralta-Ferriz et al., 2014). The study of Déry and Wood (2004) reveals the important role of AO in the terrestrial hydrologic budget. Peterson et al. (2006) proved the impact of NAO on the Arctic and sub-arctic water cycle. ENSO happens in the Pacific, but influences globally. Despite AO/NAO significantly influences the water cycle in pan-Arctic, we find that the teleconnection between ENSO and pan-Arctic is also evident. A comparison of teleconnection patterns from ENSO and AO/NAO should be done in the future. Furthermore, based on the statistical associated patterns, it is still not known how much the abnormal inter-annual variations in boreal hydrological observations come from ENSO or AO/NAO. To investigate the contribution of ENSO to the inter-annual change in Arctic, an analysis considering those questions would need to be done in a comprehensive way.

A non-linear relationship exists between river runoff and terrestrial water storage change in the subpolar climate zone. This non-linear relationship is characterized by long and cold winters with cool and short summers, which is analyzed by Riegger and Tourian (2014). Extreme climate events like ENSO are difficult to characterize due to the nonlinear behavior. The linear inter-annual changes related to ENSO have been identified here. However, the existence of non-linear connection is not. Detection of non-linear relationship between two variables is a challenge for CCA. It might be overcome by developing a kernel-based CCA (Hsieh, 2001), which is beyond the scope of our study.

GRACE has proved its capability of sensing the inter-annual variation of the water cycle by the identified temporal and spatial patterns (Eicker et al., 2016). Nevertheless, an inconsistency still exists, when comparing the water mass derivative from GRACE with the results from the water balance equation. One cause of inconsistency are the model errors. Different spatial resolutions may also lead to such disagreement. Filtering applied on GRACE reduces the noise and simultaneously reduces the spatial resolution. GRACE observations cover the period only from 2002 to 2017, but it is still not sufficient for recognition of impact of climate change. The decadal change of terrestrial water cycle forced by climate variability can not be detected owing to the limitation of GRACE lifetime. Although the limitations of both spatial resolution and time scale are always big challenges for climate and water resource studies, the teleconnection revealed by GRACE still provides us confidence that GRACE has the capability to sense the signature of ENSO.

Chapter 6

Conclusion and Outlook

6.1 Conclusion

The water mass transports in the ocean-land-atmosphere circulation, particularly in the terrestrial water cycle. Monitoring the terrestrial water mass variation by means of geodetic, hydrological, and hydrometeorological observations motivates us to start our research. GRACE provides us the time-variable global gravity field, making it possible to monitor the large-scale water mass variation over the globe. Various hydrological models synthesize different data sources, providing highly-resolved model estimates of hydrological variables. Some other variables, e.g. SST, LST, allow us to link the continental water mass change with the dynamic processes in the ocean and atmosphere. Moreover, some climate indicators, e.g. ENSO indices, help us to understand the teleconnection between ocean and land. The main objective of this thesis is to assess the water mass change in the terrestrial water cycle and to interpret the water mass exchange in the ocean-land-atmosphere interaction. Given the observations from GRACE, the model estimates from hydrological models, the temperature of sea and land surface as well as the climate indices, therefore, the following tasks have been achieved in this study by employing appropriate statistical approaches:

1. Modelling the terrestrial water storage at catchment scale by using different hydrological variables.
2. Spatial downscaling of GRACE data by an assimilation of multiple hydrological variables with total water storage from a fine resolution model.
3. Identifying the signature of climate variability on the terrestrial water cycle using SST as an intermedium.
4. Investigating the temporal shifts in the dynamic water cycle and the causal relationships between the terrestrial water cycle and climate variability.

Understanding the terrestrial water cycle The linear relationships between water storage and other variables in the water cycle have been characterized in Chapter 3 and 4, which are the basis of our modelling of terrestrial water storage change. Based on these linear relationships, Chapter 3 has accomplished the modelling of terrestrial water storage at catchment scale by assimilating multiple hydrological variables. As a result, combining multiple hydrological variables always has better predictions of water storage than using any individual variable. Runoff outperforms other variables when regressing the water storage, which has evidently

illustrated the strong linear relationship between water storage and river runoff. Considering the dynamic temporal shifts in the water cycle, precipitation has shown us good performance in predicting water storage change by a moving average regression.

The modelling of terrestrial water storage in the catchments under different climatic conditions yields various performances. Good predictions have been achieved in the tropical basins since those basins demonstrate clear stationary seasonal behaviour. However, the terrestrial water storage is poorly predicted in the boreal catchments that have cold and dry climatic condition. It was shown that good agreement between prediction and observation is achieved in the tropical catchments with strong cyclo-stationarity, while the weak cyclo-stationarity in those boreal catchments leads to a low prediction accuracy. This might be explained by the non-linear relationships between water storage and other variables, and it remains a challenge for us to model the terrestrial water mass change in high-latitude regions.

Understanding the ocean-land teleconnection In Chapter 5, we have explored the teleconnection pattern between ENSO and the terrestrial water cycle in the boreal region for the time period 2003 to 2014 using monthly spaceborne observations and reanalysis data sets. The ENSO-correlated inter-annual variations have been extracted in one of the modes by PCA, separated in one or more independent components by ICA, and identified in the associated canonical modes by applying CCA on the joint datasets. Associating with Nino 3.4 index, we have eventually identified the temporal modes from each data source. The spatial pattern of terrestrial variables related to ENSO are obtained by projecting identified temporal modes in spatial domain. With the aid of CCA, the signature of ENSO on boreal water cycle has been successfully identified through SST. Using SST as intermedium helps us eventually link ENSO to terrestrial variables. SST seems like a bridge between ENSO and variables in the terrestrial water cycle.

The signature of ENSO in high latitude has been identified by both hydrological observations in that area and observations from GRACE. However, the disagreement of spatial patterns from the water storage fluxes still exists in some regions which might be due to the inconsistent spatial resolution. As a result of low spatial resolution, GRACE does not perform well in recognizing local details. Additionally, as discussed in 3.1.2, filtering on GRACE reduces the noise and simultaneously also reduces the spatial resolution.

Further, as the GRACE observations cover the period only from 2002 to 2017, the observing time period of GRACE is still not sufficient for recognizing the impact of climate change, which limits our study on detection of the decadal changes of terrestrial water cycle forced by climate variability. Although the limitations of both spatial resolution and time scale of GRACE are always big challenges for climatic and hydrological studies, the performance of GRACE still provides us confidence that it has the capability to sense the large-scale signature of ENSO.

Understanding the causal relationships As demonstrated in Chapter 4, the relationship between water storage and other variables in the terrestrial water cycle is statistically described as linear but behaves dynamically with temporal shifts. We have investigated the time lags in the terrestrial water cycle using the Hilbert transformation, and further have explored the causal relationships between ENSO and terrestrial variables by the Hilbert and wavelet transformation approaches.

After correcting the existing temporal shifts, the linear relationships in the water cycle have been characterized in the tropical and temperate basins. Meanwhile, this dynamic water cycle is statistically interpreted in terms of the estimated time leads or lags. As a consequence, estimating the phase/time differences by the Hilbert transformation has been proved reliable for stationary time series. Since resorting to the Hilbert transformation is not appropriate for non-stationary signals, it is still a challenge to characterize the relationships between water storage and other variables in the boreal catchments.

In Chapter 5, the time differences between different terrestrial variables (e.g., total water storage, precipitation, evaporation, runoff, land surface temperature, water fluxes) and ENSO have been estimated using cross-correlation coefficients, Hilbert transformation and wavelet coherency spectrum. Among these three approaches, the wavelet coherency spectrum has demonstrated its advantage on analyzing observations with non-stationary variability from both the frequency and the time aspects. The significant information of phase differences between ENSO and terrestrial variables at low frequency (e.g. biennial, inter-annual and decadal bands) are enhanced in the wavelet coherency maps.

Therefore, terrestrial variables responding to ENSO have been revealed in Chapter 4 and 5 by the quantified time lags. Time lags between ENSO and terrestrial variables range from 1 to 2 months in boreal region. The time lags between total water storage and ENSO is not distinguished, due to the limited temporal resolution. Although the cause and effect between ENSO and variables in the terrestrial water cycle is indirectly explained by the estimated phase/time differences, as a preliminary study, it supports us to explore the teleconnection between climate variability and terrestrial water mass change, helps us understanding the role of terrestrial water mass variation in the dynamic ocean-land-atmosphere circulation, and additionally inspires us to consider these temporal shifts in the regression models.

Adaptive moving average regression on prediction/assimilation As illustrated in Chapter 3 and 4, the time-invariant temporal shifts among the hydrological variables are significant in the dynamic water cycle. Considering these existing temporal shifts in the terrestrial water cycle, an adaptive moving average regression algorithm is consequently developed in this thesis for water mass change modelling.

Going back to Chapter 2 and 3, three different regression approaches, i.e. LSP/LSC, PCR and PLR, have been employed for water storage prediction. Although all the three approaches have been successfully implemented for water storage prediction such that the results generally meet our expectation, combining with a moving average process has highly improved the quality of our predictions in most catchments, particularly for the predictions from LSP. The prediction in boreal catchments still has a poor accuracy even with a moving average regression. Eventually, based on a moving average process, these three approaches perform at the same level of accuracy in predicting the water storage by multiple hydrological variables.

Moreover, such an adaptive moving average regression has also been used with PLR in an assimilation of hydrological models with GRACE to achieve a finer spatial resolution of total water storage in Chapter 3. The obtained downscaled total water storage has demonstrated the importance of an adaptive moving average in the regression/assimilation model.

Advantages of CCA on mutual feature detection The CCA method has been introduced in Chapter 2, together with PCA and ICA algorithms. Comparing with the performance of PCA and ICA, hence, CCA demonstrates its advantage on detecting the mutual properties from two different variables.

As analyzed in Chapter 5, CCA has represented its capability to isolate the inter-annual change from both SST and terrestrial observation time series simultaneously. Different from PCA and ICA, CCA has advantage on correlating linear relationship between two data sets, regardless of units. ENSO related inter-annual change has probably been identified in several different temporal modes. The results reveal clear teleconnections between ENSO and the terrestrial water cycle in boreal catchments, e.g. Ob, Lena and Yenisei.

Further, CCA has shown its potential in model regression and data assimilation. As described in Chapter 2, based on the mode separation of joint datasets, PLR inherits the main idea of CCA, using the selected canonical modes for regression. In Chapter 3, PLR has demonstrated its capability of modelling water storage by multiple variables. Different from PCR, PLR considers the relevancy of water storage to the other variables in the water cycle, providing a more stable performance than PCR. PLR makes use of associated information from predictors and predictands, and as a consequence, reduces the uncorrelated errors. Assimilation of multiple variables by PLR benefits from this property, and thus in this thesis, has been applied for spatial downscaling of GRACE. Avoiding any approximated model, which is a necessary step for the Kalman filter approach, PLR is a data-driven method, based on the empirical information. In the end, from the promising downscaled total water storage, we have confidence of PLR in the data assimilation, exhibiting its applicability for GRACE downscaling.

6.2 Outlook

Apart from the overall achievements of this thesis as summarized above, several challenges still remain and create opportunities for further investigations.

Challenges in characterization of non-linear relationships One of the remaining challenges is to model the non-linear relationships in the terrestrial water cycle. As discussed in Chapter 3 and 4, the terrestrial water storage is still poorly predicted in boreal catchments, although we have already used a moving average process in the regression model, considering the time-invariant temporal shifts. In fact, the solid/liquid water mass variation plays also an dominant role in the cold and dry regions, which results in a non-linear relationship. Hence, the inaccurate prediction of water storage change in boreal catchment probably refers to this non-linear relationship. However, from the given results, our current approaches adopted in this thesis can hardly figure out this issue.

Also, non-linear behaviours always exist in the ocean-land-atmosphere interaction. As discussed in Chapter 5, since extreme climate events (e.g. ENSO) are difficult to characterize due to the non-linear relationship with the other terrestrial variables, the non-linear association between ENSO and terrestrial variables is not identified by CCA yet in our study.

Therefore, to overcome the limitations motivates us in the future to improve the current methodologies (e.g. kernel-based CCA) or develop new algorithms (e.g. artificial neural network).

Perspectives on spatial downscaling and temporal densification Thanks to the global coverage and more than a decade of observing period, GRACE has been widely used for hydrological applications. However, the limited spatial and temporal resolution constrains its application for monthly monitoring. From the given results in Chapter 4, the temporal shifts between water storage and other hydrological variables are frequently decimal, not integer months. Also, as discussed in Chapter 5, we cannot distinguish the phase difference between ENSO and terrestrial water storage within one month, due to the monthly solutions from GRACE. Therefore, the acquirement of submonthly, weekly or even daily change of water storage is still a challenge for future works. As our approaches have demonstrated the potential in predicting the water storage by multiple variables in most catchments, as exhibited in Chapter 3, densifying the temporal sampling of GRACE could also be accomplished by dense sampled hydrological observations.

Additionally, the duration of GRACE is not sufficient for climate studies. Long-term large-scale variation (e.g. decadal change) of terrestrial water mass that affected by climate change cannot be investigated via GRACE observations. In order to fulfill this purpose, we could reconstruct the water storage by prediction in the past. It is worth to be done in future research, using statistical approaches (i.e. MA-LSP, MA-PCR, MA-PLR).

The insufficient spatial resolution of GRACE restricts its application only at large scales (e.g. large catchments). Fortunately, the given promising results of the downscaled total water storage in Amazon have demonstrated the successful spatial downscaling of GRACE. However, since Amazon is a typical tropical basin that has a strong cyclo-stationary seasonality, whether it is also applicable in other catchments under different climatic conditions (e.g. in boreal catchments) is still unknown. Consequently, this remaining work opens the door for further explorations in different type of catchments. Moreover, for lack of in-situ measurements, the reliability of our downscaled results still remains to be validated. As a consequence, a proper validation needs to be done in future works. For instance, it is worth to compare with other proposed downscaling approaches, e.g. Kalman filter, artificial neural network, etc.

In addition, as introduced at the beginning of this thesis, the downscaling of spatial resolution is valuable for flood and drought studies, providing more local details. The applications of downscaled total water storage for flood and drought analysis will be expected in the future for highly improvement.

Perspectives on teleconnection of various climate variabilities In this thesis, we explore the teleconnection between ENSO and terrestrial water cycle in the pan-Arctic regions in a statistical way, without concerning the physical mechanism. As we know, the anomalous water mass change in the pan-Arctic region is strongly influenced by other oscillations, e.g. North Atlantic Oscillation (NAO), Arctic Oscillation (AO). Therefore, to explain the physical mechanism behind the teleconnection, we also have to carefully consider the interference of NAO and AO. Similarly, the signature of AO/NAO on the terrestrial water cycle in pan-Arctic regions could be identified, resorting to CCA method. A comparison of teleconnection patterns from ENSO and AO/NAO remains to be done extensively in future studies.

Further, apart from SST, other indicators (e.g. sea bottom pressure) could also be used as an intermedium for teleconnection investigations. It might be beneficial of finding out the optimal intermedium variable to link the climate variability and the terrestrial water cycle.

Bibliography

- Adler, R. F., Huffman, G. J., Chang, A., Ferraro, R., Xie, P.-P., Janowiak, J., Rudolf, B., Schneider, U., Curtis, S., Bolvin, D., Gruber, A., Susskind, J., Arkin, P. and Nelkin, E. (2003), 'The version-2 global precipitation climatology project (GPCP) monthly precipitation analysis (1979-present)', *Journal of Hydrometeorology* **4**(6), 1147–1167. doi:10.1175/1525-7541(2003)004<1147:TVGPCP>2.0.CO;2.
- Aires, F., R. W. B. C. A. (2002), 'Rotation of EOFs by the independent component analysis: toward a solution of the mixing problem in the decomposition of geophysical time series.', *Journal of the Atmospheric Sciences* **59**, 111–123. doi:10.1175/1520-0469(2002)059<0111:ROEBTI>2.0.CO;2.
- Alexander, M. A., Bladé, I., Newman, M., Lanzante, J. R., Lau, N.-C. and Scott, J. D. (2002), 'The atmospheric bridge: The influence of ENSO teleconnections on air–sea interaction over the global oceans', *Journal of Climate* **15**(16), 2205–2231. doi:10.1175/1520-0442(2002)015<2205:TABTIO>2.0.CO;2.
- Alsdorf, D. E. and Lettenmaier, D. P. (2003), 'Tracking fresh water from space', *Science* **301**(5639), 1491–1494. doi:10.1126/science.1089802.
- Alsdorf, D. E., Rodríguez, E. and Lettenmaier, D. P. (2007), 'Measuring surface water from space', *Reviews of Geophysics* **45**(2). doi:10.1029/2006RG000197.
- Ashouri, H., Hsu, K.-L., Sorooshian, S., Braithwaite, D. K., Knapp, K. R., Cecil, L. D., Nelson, B. R. and Prat, O. P. (2015), 'PERSIANN-CDR: Daily precipitation climate data record from multisatellite observations for hydrological and climate studies', *Bulletin of the American Meteorological Society* **96**(1), 69–83. doi:10.1175/BAMS-D-13-00068.1.
- Awange, J., Forootan, E., Kuhn, M., Kusche, J. and Heck, B. (2014), 'Water storage changes and climate variability within the Nile Basin between 2002 and 2011', *Advances in Water Resources* **73**(Supplement C), 1 – 15. doi:10.1016/j.advwatres.2014.06.010.
- Barnston, A. G. and Livezey, R. E. (1987), 'Classification, seasonality and persistence of low-frequency atmospheric circulation patterns', *Monthly weather review* **115**(6), 1083–1126. doi:10.1175/1520-0493(1987)115<1083:CSAPOL>2.0.CO;2.
- Barros, V. R. and Silvestri, G. E. (2002), 'The relation between sea surface temperature at the subtropical South-Central Pacific and precipitation in Southeastern South America', *Journal of Climate* **15**(3), 251–267. doi:10.1175/1520-0442(2002)015<0251:TRBSST>2.0.CO;2.
- Baur, O., Kuhn, M. and Featherstone, W. (2009), 'GRACE-derived ice-mass variations over Greenland by accounting for leakage effects', *Journal of Geophysical Research: Solid Earth* **114**(B6). doi:/10.1029/2008JB006239.

- Berry, P., Garlick, J., Freeman, J. and Mathers, E. (2005), 'Global inland water monitoring from multi-mission altimetry', *Geophysical Research Letters* **32**(16). doi:10.1029/2005GL022814 .
- Bettadpur, S. (2007), 'Level-2 gravity field product user handbook', *The GRACE Project* .
- Boulanger, J.-P., Leloup, J., Penalba, O., Rusticucci, M., Lafon, F. and Vargas, W. (2005), 'Observed precipitation in the Paraná-plata hydrological basin: long-term trends, extreme conditions and ENSO teleconnections', *Climate Dynamics* **24**(4), 393–413. doi:10.1007/s00382-004-0514-x.
- Bracewell, Ronald, N. (1986), *The Fourier Transform and its applications*, McGraw-Hill Series in Electrical Engineering, Networks and Systems, New York: McGraw-Hill.
- Busuioc, A., Chen, D. and Hellström, C. (2001), 'Temporal and spatial variability of precipitation in Sweden and its link with the large-scale atmospheric circulation', *Tellus A* **53**(3), 348–367. doi:10.1034/j.1600-0870.2001.01152.x.
- Cai, W., van Rensch, P., Cowan, T. and Hendon, H. H. (2012), 'An asymmetry in the IOD and ENSO teleconnection pathway and its impact on Australian climate', *Journal of Climate* **25**(18), 6318–6329. doi:10.1175/JCLI-D-11-00501.1.
- Cardoso, J. (1999), 'High-order contrasts for independent component analysis', *Neural Computation* **11**, 157–192. doi:10.1162/089976699300016863.
- Cardoso, J.F., S. A. (1993), 'Blind beamforming for non-gaussian signals', *IEEE Proceedings* **140**, 362–370. doi:10.1049/ip-f-2.1993.0054.
- Chambers, D. P. (2006), 'Observing seasonal steric sea level variations with GRACE and satellite altimetry', *Journal of Geophysical Research: Oceans* **111**(C3). doi:10.1029/2005JC002914.
- Chambers, D. P. (2006b), 'Evaluation of new GRACE time-variable gravity data over the ocean', *Geophysical Research Letters* **33**(17).
- Chambers, D. P. and Willis, J. K. (2008), 'Analysis of large-scale ocean bottom pressure variability in the North Pacific', *Journal of Geophysical Research: Oceans* **113**(C11). doi:10.1029/2008JC004930.
- Chen, F., Mitchell, K., Schaake, J., Xue, Y., Pan, H.-L., Koren, V., Duan, Q. Y., Ek, M. and Betts, A. (1996), 'Modeling of land surface evaporation by four schemes and comparison with FIFE observations', *Journal of Geophysical Research: Atmospheres* **101**(D3), 7251–7268. doi:10.1029/95JD02165.
- Chen, J. L., Wilson, C. R. and Tapley, B. D. (2010), 'The 2009 exceptional Amazon flood and interannual terrestrial water storage change observed by GRACE', *Water Resources Research* **46**(12). W12526. doi:10.1029/2010WR009383.
- Chen, J., Tapley, B. and Wilson, C. (2006), 'Alaskan mountain glacial melting observed by satellite gravimetry', *Earth and Planetary Science Letters* **248**(1-2), 368–378. doi:10.1016/j.epsl.2006.05.039.
- Chen, J., Wilson, C., Blankenship, D. and Tapley, B. (2009), 'Accelerated Antarctic ice loss from satellite gravity measurements', *Nature Geoscience* **2**(12), 859.

- Chen, Q. (2015), 'Analyzing and modeling environmental loading induced displacements with GPS and GRACE', PhD thesis, Institute of Geodesy, University of Stuttgart.
- Cheng, M., Ries, J. C. and Tapley, B. D. (2011), 'Variations of the earth's figure axis from satellite laser ranging and grace', *Journal of Geophysical Research: Solid Earth* **116**(B1). doi:10.1029/2010JB000850.
- Chiew, F. H. S. and McMahon, T. A. (2002), 'Global ENSO-streamflow teleconnection, stream-flow forecasting and interannual variability', *Hydrological Sciences Journal* **47**(3), 505–522. doi:10.1080/02626660209492950.
- Dahle, C., Flechtner, F., Gruber, C., König, D., König, R., Michalak, G. and Neumayer, K. (2012), 'GFZ GRACE Level-2 Processing Standards Document for Level-2 Product Release 0005', *Scientific Technical Report-Data* **12**, –.
- Dai, A., Trenberth, K. E. and Qian, T. (2004), 'A global dataset of palmer drought severity index for 1870–2002: Relationship with soil moisture and effects of surface warming', *Journal of Hydrometeorology* **5**(6), 1117–1130. doi:10.1175/JHM-386.1.
- Dai, Y., Zeng, X., Dickinson, R. E., Baker, I., Bonan, G. B., Bosilovich, M. G., Denning, A. S., Dirmeyer, P. A., Houser, P. R., Niu, G., Oleson, K. W., Schlosser, C. A. and Yang, Z.-L. (2003), 'The common land model', *Bulletin of the American Meteorological Society* **84**(8), 1013–1024. doi:10.1175/BAMS-84-8-1013.
- Davis, J. and Elgered, G. (1998), 'The spatio-temporal structure of GPS water-vapor determinations', *Physics and Chemistry of the Earth* **23**(1), 91–96.
- Davis, J., Elósegui, P., Mitrovica, J. and Tamisiea, M. (2004), 'Climate-driven deformation of the solid earth from GRACE and GPS', *Geophysical Research Letters* **31**(24).
- de Linage, C., Famiglietti, J. and Randerson, J. (2014), 'Statistical prediction of terrestrial water storage changes in the Amazon basin using tropical Pacific and North Atlantic sea surface temperature anomalies', *Hydrology and Earth System Sciences* . doi:10.5194/hess-18-2089-2014.
- de Linage, C., Kim, H., Famiglietti, J. S. and Yu, J.-Y. (2013), 'Impact of Pacific and Atlantic sea surface temperatures on interannual and decadal variations of GRACE land water storage in tropical South America', *Journal of Geophysical Research: Atmospheres* **118**(19), 10,811–10,829. 2013JD020238. doi:10.1002/jgrd.50820.
- Dee, D. P., Uppala, S. M., Simmons, A. J., Berrisford, P., Poli, P., Kobayashi, S., Andrae, U., Balmaseda, M. A., Balsamo, G., Bauer, P., Bechtold, P., Beljaars, A. C. M., van de Berg, L., Bidlot, J., Bormann, N., Delsol, C., Dragani, R., Fuentes, M., Geer, A. J., Haimberger, L., Healy, S. B., Hersbach, H., Hólm, E. V., Isaksen, L., Kállberg, P., Köhler, M., Matricardi, M., McNally, A. P., Monge-Sanz, B. M., Morcrette, J.-J., Park, B.-K., Peubey, C., de Rosnay, P., Tavolato, C., Thépaut, J.-N. and Vitart, F. (2011), 'The ERA-interim reanalysis: configuration and performance of the data assimilation system', *Quarterly Journal of the Royal Meteorological Society* **137**(656), 553–597. doi:10.1002/qj.828.
- Déry, S. J. and Wood, E. F. (2004), 'Teleconnection between the Arctic Oscillation and Hudson Bay river discharge', *Geophysical Research Letters* **31**(18). L18205. doi:10.1029/2004GL020729.

- Devaraju, B. (2015), 'Understanding filtering on the sphere: Experiences from filtering GRACE data', PhD thesis, Institute of Geodesy, University of Stuttgart.
- Devaraju, B. and Sneeuw, N. (2016), 'on the spatial resolution of homogeneous isotropic filters on the sphere', in N. Sneeuw, P. Novák, M. Crespi and F. Sansò, eds, 'VIII Hotine-Marussi Symposium on Mathematical Geodesy', Springer International Publishing, Cham, pp. 67–73.
- Diaz, A. F., Studzinski, C. D. and Mechoso, C. R. (1998), 'Relationships between precipitation anomalies in Uruguay and Southern Brazil and sea surface temperature in the Pacific and Atlantic oceans', *Journal of Climate* **11**(2), 251–271. doi:10.1175/1520-0442(1998)011<0251:RBPAIU>2.0.CO;2.
- Diaz, H. F., Hoerling, M. P. and Eischeid, J. K. (2001), 'ENSO variability, teleconnections and climate change', *International Journal of Climatology* **21**(15), 1845–1862. doi:10.1002/joc.631.
- Döll, P., Fritsche, M., Eicker, A. and Müller Schmied, H. (2014a), 'Seasonal water storage variations as impacted by water abstractions: Comparing the output of a global hydrological model with GRACE and GPS observations', *Surveys in Geophysics* **35**(6), 1311–1331. doi:10.1007/s10712-014-9282-2.
- Döll, P., Kaspar, F. and Lehner, B. (2003), 'A global hydrological model for deriving water availability indicators: model tuning and validation', *Journal of Hydrology* **270**(1), 105 – 134. doi:10.1016/S0022-1694(02)00283-4.
- Döll, P., Müller Schmied, H., Schuh, C., Portmann, F. T. and Eicker, A. (2014b), 'Global-scale assessment of groundwater depletion and related groundwater abstractions: Combining hydrological modeling with information from well observations and GRACE satellites', *Water Resources Research* **50**(7), 5698–5720. doi:10.1002/2014WR015595.
- Drexler, J. Z., Snyder, R. L., Spano, D. and Paw U, K. T. (2004), 'A review of models and micrometeorological methods used to estimate wetland evapotranspiration', *Hydrological Processes* **18**(11), 2071–2101. doi:10.1002/hyp.1462.
- Eicker, A., Forootan, E., Springer, A., Longuevergne, L. and Kusche, J. (2016), 'Does GRACE see the terrestrial water cycle "intensifying"?', *Journal of Geophysical Research: Atmospheres* **121**(2), 733–745. 2015JD023808. doi:10.1002/2015JD023808.
- Eicker, A., Schumacher, M., Kusche, J., Döll, P. and Schmied, H. M. (2014), 'Calibration/data assimilation approach for integrating GRACE data into the WaterGAP Global Hydrology Model (WGHM) using an ensemble Kalman filter: First results', *Surveys in Geophysics* **35**(6), 1285–1309. doi:10.1007/s10712-014-9309-8.
- Elmi, O., Tourian, M. J. and Sneeuw, N. (2016), 'Dynamic river masks from multi-temporal satellite imagery: An automatic algorithm using graph cuts optimization', *Remote Sensing* **8**(12), 1005. doi:10.3390/rs8121005.
- Evans, A. G., Swift, E. R., Cunningham, J. P., Hill, R. W., Blewitt, G., Yunck, T. P., Lichten, S. M., Hatch, R., Malys, S. and Bossler, J. (2002), 'The global positioning system geodesy odyssey', *Navigation* **49**(1), 7–33. doi:10.1002/j.2161-4296.2002.tb00252.x.
- Fan, Y. and van den Dool, H. (2008), 'A global monthly land surface air temperature analysis for 1948-present', *Journal of Geophysical Research: Atmospheres* **113**(D1). D01103.

doi:10.1029/2007JD008470.

- Farge, M. (1992), 'Wavelet transforms and their applications to turbulence', *Annual Review of Fluid Mechanics* **24**(1), 395–458. doi:10.1146/annurev.fl.24.010192.002143.
- Farrell, W. E. (1972), 'Deformation of the Earth by surface loads', *Rev. Geophys.* **10**(3), 761–797.
- Forootan, E. and Kusche, J. (2012), 'Separation of global time-variable gravity signals into maximally independent components', *Journal of Geodesy* **86**(7), 477–497. doi:10.1007/s00190-011-0532-5.
- Forootan, E., Kusche, J., Loth, I., Schuh, W.-D., Eicker, A., Awange, J., Longuevergne, L., Diekkrüger, B., Schmidt, M. and Shum, C. K. (2014), 'Multivariate prediction of total water storage changes over west africa from multi-satellite data', *Surveys in Geophysics* **35**(4), 913–940. doi:10.1007/s10712-014-9292-0.
- Francis, J. A. and Vavrus, S. J. (2012), 'Evidence linking Arctic amplification to extreme weather in mid-latitudes', *Geophysical Research Letters* **39**(6). L06801. doi:10.1029/2012GL051000.
- Frappart, F., G. Ramillien, Leblanc, M., Tweed, S. O., Bonnet, M.-P. and Maisongrande, P. (2011b), 'An independent component analysis filtering approach for estimating continental hydrology in the GRACE gravity data', *Remote Sensing of Environment* **115**(1), 187 – 204. doi:10.1016/j.rse.2010.08.017.
- Frappart, F., Ramillien, G. and Famiglietti, J. S. (2011a), 'Water balance of the Arctic drainage system using GRACE gravimetry products', *International Journal of Remote Sensing* **32**(2), 431–453. doi:10.1080/01431160903474954.
- Gao, H., Birkett, C. and Lettenmaier, D. P. (2012), 'Global monitoring of large reservoir storage from satellite remote sensing', *Water Resources Research* **48**(9). doi:10.1029/2012WR012063.
- García-García, D., Ummenhofer, C. C. and Zlotnicki, V. (2011), 'Australian water mass variations from GRACE data linked to Indo-Pacific climate variability', *Remote Sensing of Environment* **115**(9), 2175 – 2183. doi:10.1016/j.rse.2011.04.007.
- Giannini, A., Kushnir, Y. and Cane, M. A. (2000), 'Interannual variability of Caribbean rainfall, ENSO, and the Atlantic Ocean', *Journal of Climate* **13**(2), 297–311. doi:10.1175/1520-0442(2000)013<0297:IVOCRE>2.0.CO;2.
- Glahn, H. R. (1968), 'Canonical correlation and its relationship to discriminant analysis and multiple regression', *Journal of the Atmospheric Sciences* **25**(1), 23–31. doi:10.1175/1520-0469(1968)025<0023:CCAIRT>2.0.CO;2.
- Glantz, M., Katz, R. and Nicholls, N. (1991), *Teleconnections linking worldwide climate anomalies.*, Cambridge University Press, Cambridge. doi:10.1002/joc.3370120308.
- Gochis, D. J., Brito-Castillo, L. and James Shuttleworth, W. (2007), 'Correlations between sea-surface temperatures and warm season streamflow in northwest Mexico', *International Journal of Climatology* **27**(7), 883–901. doi:10.1002/joc.1436.
- Golub, G. and Kahan, W. (1965), 'Calculating the singular values and pseudo-inverse of a matrix', *Journal of the Society for Industrial and Applied Mathematics Series B Numerical Analysis* **2**(2), 205–224. doi:10.1137/0702016.

- Grinsted, A., Moore, J. C. and Jevrejeva, S. (2004), 'Application of the cross wavelet transform and wavelet coherence to geophysical time series', *Nonlinear Processes in Geophysics* **11**(5/6), 561–566.
- Güntner, A. (2008), 'Improvement of global hydrological models using GRACE data', *Surveys in geophysics* **29**(4-5), 375–397. doi:10.1007/s10712-008-9038-y.
- Güntner, A., Stuck, J., Werth, S., Döll, P., Verzano, K. and Merz, B. (2007), 'A global analysis of temporal and spatial variations in continental water storage', *Water Resources Research* **43**(5). W05416. doi:10.1029/2006WR005247.
- Gupta, V. H., Sorooshian, S. and Yapo, O., P. (1999), 'Status of automatic calibration for hydrologic models: Comparison with multilevel expert calibration', *Journal of Hydrologic Engineering* **4**(2), 135–143. doi:10.1061/(asce)1084-0699(1999)4:2(135).
- Han, S.-C., Shum, C. K., Jekeli, C., Kuo, C.-Y., Wilson, C. and Seo, K.-W. (2005), 'Non-isotropic filtering of GRACE temporal gravity for geophysical signal enhancement', *Geophysical Journal International* **163**(1), 18–25. doi:10.1111/j.1365-246X.2005.02756.x.
- Harig, C. and Simons, F. J. (2012), 'Mapping Greenland's mass loss in space and time', *Proceedings of the National Academy of Sciences* **109**(49), 19934–19937. doi:10.1073/pnas.1206785109.
- Heiskanen, W. A. and Moritz, H. (1967), 'Physical geodesy', *Bulletin Géodésique (1946-1975)* **86**(1), 491–492. doi:10.1007/BF02525647.
- Honda, M., Inoue, J. and Yamane, S. (2009), 'Influence of low Arctic sea-ice minima on anomalously cold Eurasian winters', *Geophysical Research Letters* **36**(8). L08707. doi:10.1029/2008GL037079.
- Horel, J. D. and Wallace, J. M. (1981), 'Planetary-scale atmospheric phenomena associated with the Southern Oscillation', *Monthly Weather Review* **109**(4), 813–829.
- Höskuldsson, A. (1988), 'PLS regression methods', *Journal of Chemometrics* **2**(3), 211–228. doi:10.1002/cem.1180020306.
- Hotelling, H. (1936), 'Relations between two sets of variates', *Biometrika* **28**(3/4), 321–377.
- Hou, A. Y., Kakar, R. K., Neeck, S., Azarbarzin, A. A., Kummerow, C. D., Kojima, M., Oki, R., Nakamura, K. and Iguchi, T. (2014), 'The global precipitation measurement mission', *Bulletin of the American Meteorological Society* **95**(5), 701–722. doi:10.1175/BAMS-D-13-00164.1.
- Houborg, R., Rodell, M., Li, B., Reichle, R. and Zaitchik, B. F. (2012), 'Drought indicators based on model-assimilated gravity recovery and climate experiment (GRACE) terrestrial water storage observations', *Water Resources Research* **48**(7). doi:10.1029/2011WR011291.
- Hsieh, W. W. (2001), 'Nonlinear canonical correlation analysis of the tropical Pacific climate variability using a neural network approach', *Journal of Climate* **14**(12), 2528–2539. doi:10.1175/1520-0442(2001)014<2528:NCCAOT>2.0.CO;2.
- Huffman, G. J., Adler, R. F., Bolvin, D. T. and Nelkin, E. J. (2010), *The TRMM Multi-Satellite Precipitation Analysis (TMPA)*, Springer Netherlands, Dordrecht, chapter 1, pp. 3–22. doi:10.1007/978-90-481-2915-7_1.

- Huffman, G. J., Bolvin, D. T., Nelkin, E. J., Wolff, D. B., Adler, R. F., Gu, G., Hong, Y., Bowman, K. P. and Stocker, E. F. (2007), 'The TRMM multisatellite precipitation analysis (TMPA): Quasi-global, multiyear, combined-sensor precipitation estimates at fine scales', *Journal of Hydrometeorology* **8**(1), 38–55. doi:10.1175/JHM560.1.
- Humphrey, V., Gudmundsson, L. and Seneviratne, S. I. (2016), 'Assessing global water storage variability from GRACE: Trends, seasonal cycle, subseasonal anomalies and extremes', *Surveys in Geophysics* **37**(2), 357–395. doi:10.1007/s10712-016-9367-1.
- Hurrell, J. W. (1995), 'Decadal trends in the North Atlantic Oscillation: regional temperatures and precipitation', *Science* **269**(5224), 676–679. doi:10.1126/science.269.5224.676.
- Hyvärinen, A. (1999), 'Survey on independent component analysis', *Neural Computing Surveys* **2**, 94–128.
- Jekeli, C. (1981), 'Alternative methods to smooth the Earth's gravity field', *Tech. Rep. 327*. Dept. of Geodetic Science and Surveying.; Ohio State Univ.; Columbus, OH, United States.
- Jevrejeva, S., Moore, J. C. and Grinsted, A. (2003), 'Influence of the Arctic Oscillation and El Niño-Southern Oscillation (ENSO) on ice conditions in the Baltic Sea: The wavelet approach', *Journal of Geophysical Research: Atmospheres* **108**(D21). 4677. doi:10.1029/2003JD003417.
- Johnson, N. T., Martinez, C. J., Kiker, G. A. and Leitman, S. (2013), 'Pacific and Atlantic sea surface temperature influences on streamflow in the Apalachicola-Chattahoochee-Flint river basin', *Journal of Hydrology* **489**(Supplement C), 160–179. doi:10.1016/j.jhydrol.2013.03.005.
- Jolliffe, I. T. (1986), *Principal Component Analysis and Factor Analysis*, Springer New York, New York, NY, chapter 2-3, pp. 115–128.
- Kaplan, A., Cane, M. A., Kushnir, Y., Clement, A. C., Blumenthal, M. B. and Rajagopalan, B. (1998), 'Analyses of global sea surface temperature 1856-1991', *Journal of Geophysical Research: Oceans* **103**(C9), 18567–18589. doi:10.1029/97JC01736.
- Kendall, M. G. (1957), *A course in multivariate analysis*, Hafner Pub. Co., New York.
- Kim, J.-S., Kug, J.-S., Jeong, S.-J., Huntzinger, D. N., Michalak, A. M., Schwalm, C. R., Wei, Y. and Schaefer, K. (2017), 'Reduced North American terrestrial primary productivity linked to anomalous Arctic warming', *Nature Geoscience* **10**, 572.
- Kirchner, J. W. (2009), 'Catchments as simple dynamical systems: Catchment characterization, rainfall-runoff modeling, and doing hydrology backward', *Water Resources Research* **45**(2). doi:10.1029/2008WR006912.
- Klees, R., Revtova, E. A., Gunter, B. C., Ditmar, P., Oudman, E., Winsemius, H. C. and Savenije, H. H. G. (2008), 'The design of an optimal filter for monthly GRACE gravity models', *Geophysical Journal International* **175**(2), 417–432. doi:10.1111/j.1365-246X.2008.03922.x.
- Klees, R., Zapreeva, E. A., Winsemius, H. C. and Savenije, H. H. G. (2007), 'The bias in GRACE estimates of continental water storage variations', *Hydrology and Earth System Sciences* **11**(4), 1227–1241. doi:10.5194/hess-11-1227-2007.

- Koren, V., Schaake, J., Mitchell, K., Duan, Q.-Y., Chen, F. and Baker, J. M. (1999), 'A parameterization of snowpack and frozen ground intended for NCEP weather and climate models', *Journal of Geophysical Research: Atmospheres* **104**(D16), 19569–19585. doi:10.1029/1999JD900232.
- Koster, R. D. and Suarez, M. J. (1996), 'Energy and water balance calculations in the Mosaic LSM', *National Aeronautics and Space Administration, Goddard Space Flight Center*.
- Krarpup, T. (1969), *A Contribution to the Mathematical Foundation of Physical Geodesy*, Geodaetisk institut. Meddelelse, Geodætisk Institut.
- Kug, J.-S., Jeong, J.-H., Jang, Y.-S., Kim, B.-M., Folland, C. K., Min, S.-K. and Son, S.-W. (2015), 'Two distinct influences of Arctic warming on cold winters over North America and East Asia', *Nature Geoscience* **8**, 759. doi:10.1038/ngeo2517.
- Künzer, C., Klein, I., Ullmann, T., Georgiou, E. F., Baumhauer, R. and Dech, S. (2015), 'Remote sensing of river delta inundation: Exploiting the potential of coarse spatial resolution, temporally-dense MODIS time series', *Remote Sensing* **7**(7), 8516–8542. doi:10.3390/rs70708516.
- Kurtenbach, E., Eicker, A., Mayer-Gürr, T., Holschneider, M., Hayn, M., Fuhrmann, M. and Kusche, J. (2012), 'Improved daily GRACE gravity field solutions using a kalman smoother', *Journal of Geodynamics* **59**, 39–48. doi:10.1016/j.jog.2012.02.006.
- Kurtenbach, E., Mayer-Gürr, T. and Eicker, A. (2009), 'Deriving daily snapshots of the Earth's gravity field from GRACE L1B data using Kalman filtering', *Geophysical Research Letters* **36**(17). doi:10.1029/2009GL039564.
- Kusche, J. (2007), 'Approximate decorrelation and non-isotropic smoothing of time-variable GRACE-type gravity field models', *Journal of Geodesy* **81**(11), 733–749. doi:10.1007/s00190-007-0143-3.
- Kusche, J., Eicker, A., Forootan, E., Springer, A. and Longuevergne, L. (2016), 'Mapping probabilities of extreme continental water storage changes from space gravimetry', *Geophysical Research Letters* **43**(15), 8026–8034. 2016GL069538. doi:10.1002/2016GL069538.
- Kusche, J., Schmidt, R., Petrovic, S. and Rietbroek, R. (2009), 'Decorrelated GRACE time-variable gravity solutions by GFZ, and their validation using a hydrological model', *Journal of Geodesy* **83**(10), 903–913. doi:10.1007/s00190-009-0308-3.
- Landerer, F. W. and Swenson, S. C. (2012), 'Accuracy of scaled GRACE terrestrial water storage estimates', *Water Resources Research* **48**(4). doi:10.1029/2011WR011453.
- Larson, K. M., Gutmann, E. D., Zavorotny, V. U., Braun, J. J., Williams, M. W. and Nievinski, F. G. (2009), 'Can we measure snow depth with GPS receivers?', *Geophysical Research Letters* **36**(17). doi:10.1029/2009GL039430.
- Larson, K. M., Löfgren, J. S. and Haas, R. (2013), 'Coastal sea level measurements using a single geodetic GPS receiver', *Advances in Space Research* **51**(8), 1301–1310. doi:10.1016/j.asr.2012.04.017.
- Larson, K. M., Small, E. E., Gutmann, E. D., Bilich, A. L., Braun, J. J. and Zavorotny, V. U. (2008), 'Use of GPS receivers as a soil moisture network for water cycle studies', *Geophysical*

- Research Letters* **35**(24). doi:10.1029/2008GL036013.
- Liang, X., Wood, E. F. and Lettenmaier, D. P. (1996), 'Surface soil moisture parameterization of the VIC-2L model: Evaluation and modification', *Global and Planetary Change* **13**(1-4), 195–206. doi:10.1016/0921-8181(95)00046-1.
- Liu, P. C. (1994), Wavelet spectrum analysis and ocean wind waves, in E. Foufoula-Georgiou and P. Kumar, eds, 'Wavelets in Geophysics', Vol. 4 of *Wavelet Analysis and Its Applications*, Academic Press, pp. 151–166. doi:10.1016/B978-0-08-052087-2.50012-8.
- Lombard, A., Garcia, D., Ramillien, G., Cazenave, A., Biancale, R., Lemoine, J., Flechtner, F., Schmidt, R. and Ishii, M. (2007), 'Estimation of steric sea level variations from combined GRACE and Jason-1 data', *Earth and Planetary Science Letters* **254**(1-2), 194–202. doi:10.1016/j.epsl.2006.11.035.
- Long, D., Scanlon, B. R., Longuevergne, L., Sun, A. Y., Fernando, D. N. and Save, H. (2013), 'GRACE satellite monitoring of large depletion in water storage in response to the 2011 drought in Texas', *Geophysical Research Letters* **40**(13), 3395–3401. doi:10.1002/grl.50655 .
- Long, D., Shen, Y., Sun, A., Hong, Y., Longuevergne, L., Yang, Y., Li, B. and Chen, L. (2014), 'Drought and flood monitoring for a large karst plateau in Southwest China using extended GRACE data', *Remote Sensing of Environment* **155**, 145–160. doi:10.1016/j.rse.2014.08.006.
- Longuevergne, L., Scanlon, B. R. and Wilson, C. R. (2010), 'GRACE hydrological estimates for small basins: Evaluating processing approaches on the High Plains Aquifer, USA', *Water Resources Research* **46**(11). doi:10.1029/2009WR008564.
- Lorenz, C. (2009), Applying stochastic constraints on time-variable GRACE data, Master's thesis, Institute of Geodesy, University of Stuttgart.
- Lorenz, C., Tourian, M. J., Devaraju, B., Sneeuw, N. and Kunstmann, H. (2015), 'Basin-scale runoff prediction: An ensemble Kalman filter framework based on global hydrometeorological data sets', *Water Resources Research* **51**(10), 8450–8475. doi:10.1002/2014WR016794.
- Luo, Z., Yao, C., Li, Q. and Huang, Z. (2016), 'Terrestrial water storage changes over the Pearl river basin from GRACE and connections with Pacific climate variability', *Geodesy and Geodynamics* **7**(3), 171–179. doi:10.1016/j.geog.2016.04.008.
- Luthcke, S. B., Sabaka, T., Loomis, B., Arendt, A., McCarthy, J. and Camp, J. (2013), 'Antarctica, Greenland and Gulf of Alaska land-ice evolution from an iterated GRACE global mascon solution', *Journal of Glaciology* **59**(216), 613–631. doi:10.3189/2013JogG12J147.
- Mantua, N. J., Hare, S. R., Zhang, Y., Wallace, J. M. and Francis, R. C. (1997), 'A Pacific interdecadal climate oscillation with impacts on salmon production', *Bulletin of the American Meteorological Society* **78**(6), 1069–1080. doi:10.1175/1520-0477(1997)078<1069:APICOW>2.0.CO;2.
- Martens, B., Miralles, D. G., Lievens, H., van der Schalie, R., de Jeu, R. A. M., Fernández-Prieto, D., Beck, H. E., Dorigo, W. A. and Verhoest, N. E. C. (2017), 'GLEAM-v3: satellite-based land evaporation and root-zone soil moisture', *Geoscientific Model Development* **10**(5), 1903–1925. doi:10.5194/gmd-10-1903-2017.

- Massy, W. F. (1965), 'Principal components regression in exploratory statistical research', *Journal of the American Statistical Association* **60**(309), 234–256. doi:10.1080/01621459.1965.10480787.
- Matsuo, K. and Heki, K. (2010), 'Time-variable ice loss in Asian high mountains from satellite gravimetry', *Earth and Planetary Science Letters* **290**(1-2), 30–36. doi:10.1016/j.epsl.2009.11.053.
- Matsuo, K. and Heki, K. (2012), 'Anomalous precipitation signatures of the Arctic Oscillation in the time-variable gravity field by GRACE', *Geophysical Journal International* **190**(3), 1495–1506. doi:10.1111/j.1365-246x.2012.05588.x.
- Mayer-Gürr, T., Behzadpur, S., Ellmer, M., Kvas, A., Klinger, B., Strasser, S. and Zehentner, N. (2018), 'ITSG-Grace2018 - monthly, daily and static gravity field solutions from GRACE', *GFZ Data Services* . doi:10.5880/ICGEM.2018.003.
- McCabe, G. J., Palecki, M. A. and Betancourt, J. L. (2004), 'Pacific and Atlantic Ocean influences on multidecadal drought frequency in the United States', *Proceedings of the National Academy of Sciences* **101**(12), 4136–4141. doi:10.1073/pnas.0306738101.
- McCabe, G. J. and Wolock, D. M. (2014), 'Variability common to global sea surface temperatures and runoff in the conterminous United States', *Journal of Hydrometeorology* **15**(2), 714–725. doi:10.1175/JHM-D-13-097.1.
- Meyer-Christoffer, A., Becker, A., Finger, P., Rudolf, B., Schneider, U. and Ziese, M. (2015), 'GPCC climatology version 2015 (at 0.25°, 0.5°, 1.0°, 2.5°): Monthly land-surface precipitation climatology for every month and the total year from rain-gauges built on gts-based and historic data', *Global Precipitation Climatology Centre (GPCC, <http://gpcc.dwd.de/>) at Deutscher Wetterdienst* .
- Miralles, D. G., Holmes, T. R. H., De Jeu, R. A. M., Gash, J. H., Meesters, A. G. C. A. and Dolman, A. J. (2011), 'Global land-surface evaporation estimated from satellite-based observations', *Hydrology and Earth System Sciences* **15**(2), 453–469. doi:10.5194/hess-15-453-2011.
- Miro, M. E. and Famiglietti, J. S. (2018), 'Downscaling GRACE remote sensing datasets to high-resolution groundwater storage change maps of California's Central Valley', *Remote Sensing* **10**(1), 143. doi:10.3390/rs10010143.
- Moriasi, D. N., Arnold, G. J., Van Liew, W. M., Bingner, L. R., Harmel, D. R. and Veith, L. T. (2007), 'Model evaluation guidelines for systematic quantification of accuracy in watershed simulations', *Transactions of the ASABE* **50**(3), 885–900.
- Morison, J., Wahr, J., Kwok, R. and Peralta-Ferriz, C. (2007), 'Recent trends in Arctic Ocean mass distribution revealed by GRACE', *Geophysical Research Letters* **34**(7). L07602. doi:10.1029/2006GL029016.
- Moritz, H. (1980), *Advanced physical geodesy*, Wichmann.
- Nash, J. E. and Sutcliffe, J. V. (1970), 'River flow forecasting through conceptual models part I – A discussion of principles', *Journal of Hydrology* **10**(3), 282–290.

- Ni, S., Chen, J., Wilson, C. R., Li, J., Hu, X. and Fu, R. (2017), 'Global terrestrial water storage changes and connections to ENSO events', *Surveys in Geophysics*. doi:10.1007/s10712-017-9421-7.
- Nigam, S. (2003), 'Teleconnections', *Encyclopedia of Atmospheric Sciences* pp. 2243–2269.
- Ouarda, T. B., Girard, C., Cavadias, G. S. and Bobée, B. (2001), 'Regional flood frequency estimation with canonical correlation analysis', *Journal of Hydrology* **254**(1), 157 – 173. doi:10.1016/S0022-1694(01)00488-7.
- Pan, M. and Wood, E. F. (2006), 'Data assimilation for estimating the terrestrial water budget using a constrained ensemble Kalman filter', *Journal of Hydrometeorology* **7**(3), 534–547. doi:10.1175/JHM495.1.
- Papa, F., Durand, F., Rossow, W. B., Rahman, A. and Bala, S. K. (2010), 'Satellite altimeter-derived monthly discharge of the Ganga-Brahmaputra River and its seasonal to inter-annual variations from 1993 to 2008', *Journal of Geophysical Research: Oceans* **115**(C12). doi:10.1029/2009JC006075.
- Peralta-Ferriz, C., Morison, J. H., Wallace, J. M., Bonin, J. A. and Zhang, J. (2014), 'Arctic ocean circulation patterns revealed by GRACE', *Journal of Climate* **27**(4), 1445–1468. doi:10.1175/JCLI-D-13-00013.1.
- Peterson, B. J., McClelland, J., Curry, R., Holmes, R. M., Walsh, J. E. and Aagaard, K. (2006), 'Trajectory shifts in the Arctic and subarctic freshwater cycle', *Science* **313**(5790), 1061–1066. doi:10.1126/science.1122593.
- Phillips, T., Nerem, R. S., Fox-Kemper, B., Famiglietti, J. S. and Rajagopalan, B. (2012), 'The influence of ENSO on global terrestrial water storage using GRACE', *Geophysical Research Letters* **39**(16). L16705. doi:10.1029/2012GL052495.
- Preisendorfer, R. W. (1988), *Principal component analysis in meteorology and oceanography*, Elsevier Science.
- Rana, G. and Katerji, N. (2000), 'Measurement and estimation of actual evapotranspiration in the field under Mediterranean climate: a review', *European Journal of agronomy* **13**(2-3), 125–153. doi:10.1016/S1161-0301(00)00070-8.
- Rangelova, E., van der Wal, W., Braun, A., Sideris, M. G. and Wu, P. (2007), 'Analysis of Gravity Recovery and Climate Experiment time-variable mass redistribution signals over North America by means of principal component analysis', *Journal of Geophysical Research: Earth Surface* **112**(F3). F03002. doi:10.1029/2006JF000615.
- Rangelova, E., van der Wal, W., Sideris, M. G. and Wu, P. (2010), *Spatiotemporal Analysis of the GRACE-Derived Mass Variations in North America by Means of Multi-Channel Singular Spectrum Analysis*, Springer Berlin Heidelberg, Berlin, Heidelberg, pp. 539–546.
- Reager, J. and Famiglietti, J. S. (2013), 'Characteristic mega-basin water storage behavior using GRACE', *Water resources research* **49**(6), 3314–3329. doi:10.1002/wrcr.20264.
- Riegger, J. and Güntner, A. (2004), 'Time variation in hydrology and gravity', *Earth, Moon, and Planets* **94**(1-2), 41–55.

- Riegger, J. and Tourian, M. J. (2014), 'Characterization of runoff-storage relationships by satellite gravimetry and remote sensing', *Water Resources Research* **50**(4), 3444–3466. doi:10.1002/2013WR013847.
- Rodell, M. and Beaudoing, Hiroko Kato, N. (2015), 'GLDAS Noah land surface model L4 monthly 0.25 x 0.25 degree version 2.0', *Goddard Earth Sciences Data and Information Services Center (GES DISC)*.
- Rodell, M., Chen, J., Kato, H., Famiglietti, J. S., Nigro, J. and Wilson, C. R. (2007), 'Estimating groundwater storage changes in the Mississippi River basin (USA) using GRACE', *Hydrogeology Journal* **15**(1), 159–166.
- Rodell, M., Houser, P. R., Jambor, U., Gottschalck, J., Mitchell, K., Meng, C.-J., Arsenault, K., Cosgrove, B., Radakovich, J., Bosilovich, M., Entin, J. K., Walker, J. P., Lohmann, D. and Toll, D. (2004), 'The global land data assimilation system', *Bulletin of the American Meteorological Society* **85**(3), 381–394. doi:10.1175/BAMS-85-3-381.
- Rodell, M., Velicogna, I. and Famiglietti, J. S. (2009), 'Satellite-based estimates of groundwater depletion in India', *Nature* **460**(7258), 999–1002.
- Ronchail, J., Cochonneau, G., Molinier, M., Guyot, J.-L., De Miranda Chaves, A. G., Guimarães, V. and de Oliveira, E. (2002), 'Interannual rainfall variability in the Amazon basin and sea-surface temperatures in the equatorial Pacific and the tropical Atlantic Oceans', *International Journal of Climatology* **22**(13), 1663–1686. doi:10.1002/joc.815.
- Ropelewski, C. F. and Halpert, M. S. (1987), 'Global and regional scale precipitation patterns associated with the El Niño/Southern Oscillation', *Monthly Weather Review* **115**(8), 1606–1626. doi:10.1175/1520-0493(1987)115<1606:GARSPP>2.0.CO;2.
- Rouse, W. R., Douglas, M. S. V., Hecky, R. E., Hershey, A. E., Kling, G. W., Lesacke, L., Marsh, P., McDonald, M., Nicholson, B. J., Roulei, N. T. and Smol, J. P. (1997), 'Effects of climate change on the freshwaters of Arctic and subarctic North America', *Hydrological Processes* **11**(8), 873–902. doi:10.1002/(SICI)1099-1085(19970630)11:8<873::AID-HYP510>3.0.CO;2-6.
- Ruffhead, A. (1987), 'An introduction to least-squares collocation', *Survey Review* **29**(224), 85–94. doi:10.1179/sre.1987.29.224.85.
- Saff, E. B. and Snider, A. D. (1976), *Fundamentals of complex analysis for mathematics, science, and engineering*, New Jersey, Prentice-Hall, New Jersey.
- Sasgen, I., Martinec, Z. and Fleming, K. (2006), 'Wiener optimal filtering of GRACE data', *Studia Geophysica et Geodaetica* **50**(4), 499–508. doi:10.1007/s11200-006-0031-y.
- Save, H., Bettadpur, S. and Tapley, B. D. (2016), 'High-resolution CSR GRACE RL05 mascons', *Journal of Geophysical Research: Solid Earth* **121**(10), 7547–7569. doi:10.1002/2016JB013007.
- Schmidt, R., Petrovic, S., Güntner, A., Barthelmes, F., Wunsch, J. and Kusche, J. (2008), 'Periodic components of water storage changes from GRACE and global hydrology models', *Journal of Geophysical Research: Solid Earth* **113**(B8). B08419. doi:10.1029/2007JB005363.
- Schrama, E. J. O., Wouters, B. and Lavallée, D. A. (2007), 'Signal and noise in Gravity Recovery and Climate Experiment (GRACE) observed surface mass variations', *Journal of Geophys-*

- ical Research: Solid Earth* **112**(B8). doi:10.1029/2006JB004882.
- Seitz, F., Schmidt, M. and Shum, C. (2008), 'Signals of extreme weather conditions in Central Europe in GRACE 4-D hydrological mass variations', *Earth and Planetary Science Letters* **268**(1-2), 165–170. doi:10.1016/j.epsl.2008.01.001.
- Seyoum, W. M. and Milewski, A. M. (2017), 'Improved methods for estimating local terrestrial water dynamics from GRACE in the Northern High Plains', *Advances in Water Resources* **110**, 279 – 290. doi:10.1016/j.advwatres.2017.10.021.
- Sheffield, J., Ferguson, C. R., Troy, T. J., Wood, E. F. and McCabe, M. F. (2009), 'Closing the terrestrial water budget from satellite remote sensing', *Geophysical Research Letters* **36**(7). doi:10.1029/2009GL037338.
- Sivapalan, M., Jothityangkoon, C. and Menabde, M. (2002), 'Linearity and nonlinearity of basin response as a function of scale: Discussion of alternative definitions', *Water Resources Research* **38**(2), 4–1–4–5. doi:10.1029/2001WR000482.
- Sneeuw, N., Flury, J. and Rummel, R. (2005), Science requirements on future missions and simulated mission scenarios, in 'Future Satellite Gravimetry and Earth Dynamics', Springer, pp. 113–142.
- Sneeuw, N., Lorenz, C., Devaraju, B., Tourian, M. J., Riegger, J., Kunstmann, H. and Bárdossy, A. (2014), 'Estimating runoff using hydro-geodetic approaches', *Surveys in Geophysics* **35**(6), 1333–1359. doi:10.1007/s10712-014-9300-4.
- Stewart, G. (1993), 'On the early history of the singular value decomposition', *SIAM Review* **35**(4), 551–566. doi:10.1137/1035134.
- Strang, G. (1993), 'The fundamental theorem of linear algebra', *The American Mathematical Monthly* **100**(9), 848–855.
- Sun, A. Y. (2013), 'Predicting groundwater level changes using GRACE data', *Water Resources Research* **49**(9), 5900–5912. doi:10.1002/wrcr.20421.
- Sun, Z., Wang, Q., Batkhisig, O. and Ouyang, Z. (2016), 'Relationship between evapotranspiration and land surface temperature under energy- and water-limited conditions in dry and cold climates', *Advances in Meteorology* **2016**, 9. doi:10.1155/2016/1835487.
- Swenson, S., Chambers, D. and Wahr, J. (2008), 'Estimating geocenter variations from a combination of GRACE and ocean model output', *Journal of Geophysical Research: Solid Earth* **113**(B8). B08410. doi:10.1029/2007JB005338.
- Swenson, S. and Wahr, J. (2006), 'Post-processing removal of correlated errors in GRACE data', *Geophysical Research Letters* **33**(8). L08402. doi:10.1029/2005GL025285.
- Tapley, B. D., Bettadpur, S., Watkins, M. and Reigber, C. (2004), 'The gravity recovery and climate experiment: Mission overview and early results', *Geophysical Research Letters* **31**(9). L09607. doi:10.1029/2004GL019920.
- Teuling, A. J., Lehner, I., Kirchner, J. W. and Seneviratne, S. I. (2010), 'Catchments as simple dynamical systems: Experience from a Swiss prealpine catchment', *Water Resources Research* **46**(10). doi:10.1029/2009WR008777.

- Thomas, A. C., Reager, J. T., Famiglietti, J. S. and Rodell, M. (2014), 'A GRACE-based water storage deficit approach for hydrological drought characterization', *Geophysical Research Letters* **41**(5), 1537–1545. doi:10.1002/2014GL059323.
- Tootle, G. A. and Piechota, T. C. (2006), 'Relationships between Pacific and Atlantic ocean sea surface temperatures and U.S. streamflow variability', *Water Resources Research* **42**(7), W07411. doi:10.1029/2005WR004184.
- Torrence, C. and Gilbert, P. C. (1998), 'A practical guide to wavelet analysis', *Bulletin of the American Meteorological Society* **79**(1), 61–78. doi:10.1175/1520-0477(1998)079<0061:APGTWA>2.0.CO;2.
- Torrence, C. and Webster, P. J. (1999), 'Interdecadal changes in the ENSO-monsoon system', *Journal of Climate* **12**(8), 2679–2690. doi:10.1175/1520-0442(1999)012<2679:ICITEM>2.0.CO;2.
- Tourian, M., Elmi, O., Chen, Q., Devaraju, B., Roohi, S. and Sneeuw, N. (2015), 'A spaceborne multisensor approach to monitor the desiccation of Lake Urmia in Iran', *Remote Sensing of Environment* **156**, 349–360. doi:10.1016/j.rse.2014.10.006.
- Tourian, M. J., Sneeuw, N. and Bárdossy, A. (2013), 'A quantile function approach to discharge estimation from satellite altimetry (ENVISAT)', *Water Resources Research* **49**(7), 4174–4186. doi:10.1002/wrcr.20348.
- Tregoning, P., Watson, C., Ramillien, G., McQueen, H. and Zhang, J. (2009), 'Detecting hydrologic deformation using GRACE and GPS', *Geophysical Research Letters* **36**(15). doi:10.1029/2009GL038718.
- Trenberth, K. E. (1984), 'Signal versus noise in the Southern Oscillation', *Monthly Weather Review* **112**(2), 326–332. doi:10.1175/1520-0493(1984)112<0326:SVNITS>2.0.CO;2.
- Trenberth, K. E. (1997), 'The definition of El Niño', *Bulletin of the American Meteorological Society* **78**(12), 2771–2778. doi:10.1175/1520-0477(1997)078<2771:TDOENO>2.0.CO;2.
- Trenberth, K. E. and Caron, J. M. (2000), 'The Southern Oscillation revisited: Sea level pressures, surface temperatures, and precipitation', *Journal of Climate* **13**(24), 4358–4365. doi:10.1175/1520-0442(2000)013<4358:TSORSL>2.0.CO;2.
- Trenberth, K. E., Caron, J. M., Stepaniak, D. P. and Worley, S. (2002), 'Evolution of El Niño-Southern Oscillation and global atmospheric surface temperatures', *Journal of Geophysical Research: Atmospheres* **107**(D8), AAC 5–1–AAC 5–17. doi:10.1029/2000JD000298.
- Trenberth, K. E. and Hoar, T. J. (1996), 'The 1990–1995 El Niño-Southern Oscillation event: longest on record', *Geophysical research letters* **23**(1), 57–60. doi:10.1029/95GL03602.
- Trenberth, K. E. and Hurrell, J. W. (1994), 'Decadal atmosphere-ocean variations in the Pacific', *Climate Dynamics* **9**(6), 303–319. doi:10.1007/BF00204745.
- Trenberth, K. E., Smith, L., Qian, T., Dai, A. and Fasullo, J. (2007), 'Estimates of the global water budget and its annual cycle using observational and model data', *Journal of Hydrometeorology* **8**(4), 758–769. doi:10.1175/JHM600.1.
- Trenberth, K. E. and Stepaniak, D. P. (2001), 'Indices of El Niño Evolution', *Journal of Climate* **14**(8), 1697–1701. doi:10.1175/1520-0442(2001)014<1697:LIOENO>2.0.CO;2.

- van Dam, T., Wahr, J. and Lavallée, D. (2007), 'A comparison of annual vertical crustal displacements from GPS and Gravity Recovery and Climate Experiment (GRACE) over Europe', *Journal of Geophysical Research: Solid Earth* **112**(B3). doi:10.1029/2006JB004335.
- van Dam, T., Wahr, J., Milly, P., Shmakin, A., Blewitt, G., Lavallée, D. and Larson, K. (2001), 'Crustal displacements due to continental water loading', *Geophysical Research Letters* **28**(4), 651–654. doi:10.1029/2000GL012120.
- Van den Dool, H. M., Saha, S. and Johansson, Å. (2000), 'Empirical orthogonal teleconnections', *Journal of Climate* **13**(8), 1421–1435. doi:10.1175/1520-0442(2000)013<1421:EOT>2.0.CO;2.
- Velicogna, I. and Wahr, J. (2006), 'Measurements of time-variable gravity show mass loss in Antarctica', *Science* **311**(5768), 1754–1756. doi:10.1126/science.1123785.
- Vishwakarma, B. D., Devaraju, B. and Sneeuw, N. (2018), 'What is the spatial resolution of GRACE satellite products for hydrology?', *Remote Sensing* **10**(6). doi:10.3390/rs10060852.
- Volkov, D. L. and Landerer, F. W. (2013), 'Nonseasonal fluctuations of the Arctic Ocean mass observed by the GRACE satellites', *Journal of Geophysical Research: Oceans* **118**(12), 6451–6460. doi:10.1002/2013JC009341.
- Wahr, J., Molenaar, M. and Bryan, F. (1998), 'Time variability of the Earth's gravity field: Hydrological and oceanic effects and their possible detection using GRACE', *Journal of Geophysical Research: Solid Earth* **103**(B12), 30205–30229. doi:10.1029/98JB02844.
- Walker, G. T. (1924), 'Correlations in seasonal variations of weather. I. A further study of world weather', *Mem. Indian Meteorol. Dep.* **24**, 275–332.
- Wallace, J. M. and Gutzler, D. S. (1981), 'Teleconnections in the geopotential height field during the northern hemisphere winter', *Monthly Weather Review* **109**(4), 784–812. doi:10.1175/1520-0493(1981)109<0784:TITGHF>2.0.CO;2.
- Wallace, J. M., Smith, C. and Bretherton, C. S. (1992), 'Singular value decomposition of winter-time sea surface temperature and 500-mb height anomalies', *Journal of Climate* **5**(6), 561–576. doi:10.1175/1520-0442(1992)005<0561:SVDOWS>2.0.CO;2.
- Wanner, H., Brönnimann, S., Casty, C., Gyalistras, D., Luterbacher, J., Schmutz, C., Stephenson, D. B. and Xoplaki, E. (2001), 'North Atlantic Oscillation – concepts and studies', *Surveys in Geophysics* **22**(4), 321–381. doi:10.1023/A:1014217317898.
- Watkins, M. M., Wiese, D. N., Yuan, D.-N., Boening, C. and Landerer, F. W. (2015), 'Improved methods for observing Earth's time variable mass distribution with GRACE using spherical cap mascons', *Journal of Geophysical Research: Solid Earth* **120**(4), 2648–2671. doi:10.1002/2014JB011547.
- Willis, J. K., Chambers, D. P. and Nerem, R. S. (2008), 'Assessing the globally averaged sea level budget on seasonal to interannual timescales', *Journal of Geophysical Research: Oceans* **113**(C6). doi:10.1029/2007JC004517.
- Wold, S., Ruhe, A., Wold, H. and Dunn, III, W. (1984), 'The collinearity problem in linear regression. the partial least squares (pls) approach to generalized inverses', *SIAM Journal on Scientific and Statistical Computing* **5**(3), 735–743. doi:10.1137/0905052.

- Wolter, K. and Timlin, M. S. (1998), 'Measuring the strength of ENSO events: How does 1997/98 rank?', *Weather* **53**(9), 315–324. doi:10.1002/j.1477-8696.1998.tb06408.x.
- Zaitchik, B. F., Rodell, M. and Reichle, R. H. (2008), 'Assimilation of GRACE terrestrial water storage data into a land surface model: Results for the Mississippi river basin', *Journal of Hydrometeorology* **9**(3), 535–548. doi:10.1175/2007JHM951.1.
- Zhang, Y., Wallace, J. M. and Battisti, D. S. (1997), 'ENSO-like interdecadal variability: 1900–93', *Journal of climate* **10**(5), 1004–1020. doi:10.1175/1520-0442(1997)010<1004:ELIV>2.0.CO;2.

Acknowledgement

There are many people that have earned my gratitude for their contribution in my PhD career. Firstly, I would like to express my sincere gratitude to my advisor Prof. Nico Sneeuw for his continuous support of my PhD study and related researches, for his patience, motivation, and immense knowledge. His guidance helped me in all the time of research and writing of this thesis, making me thinking and developing in a scientific way during PhD study and also in the future. Without his invaluable suggestions and enormous supports, I could not reach here today. He is not only my advisor on scientific research but also my mentor in my life.

Secondly, I am quite appreciative of Prof. Annette Eicker for agreeing to be my dissertation committee member, for spending time on reading my thesis, for her kind invitation to give a presentation in Hamburg, and insightful suggestions on my researches.

Besides, I would like to give my thanks to Prof. Erik Grafarend, for sharing with me his tremendous experience in my research career and always giving me his encouragement in the past five years. On a personal level, his enthusiasm and attitude on research inspired me becoming the kind of researcher I am today. I would also like to thank Prof. Wolfgang Keller for answering me hard questions in science and giving me precious suggestions on my work.

Most specifically, I would like to express my gratitude to my colleague and collaborator, Dr. Mohammad J. Tourian, who gave me his crucial remarks that shaped my final outcomes and widened my research from various perspectives. I am also grateful to Dr. Qiang Chen for his scientific collaboration and personal help, Dr. Bramha Dutt Vishwakarma for the fruitful discussions, Dr. Markus Antoni for his supports on my final dissertation, and Dr. Zhi Yin for his support and suggestions on my dissertation in the last year of my PhD study. My sincere thanks also go to my GIS family, all my colleagues at and ever at the Institute of Geodesy. I am really appreciative of those excellent scientists whom I have collaborated for the past five years.

Many thanks also due to the agencies for providing me public data, including GFZ for GRACE data; GPCC, GPCP, TRMM, PERSIANN for precipitation data; ECMWF, GLEAM for evapotranspiration data; GLDAS, GRDC for runoff data; WGHM for water storage data; GHCN for temperature data; NCEP for SST data; CPC for climate indices. Otherwise, I would not have been able to develop my scientific researches. Dr. Aslak Grinsted is sincerely acknowledged for providing the wavelet toolbox for visualization.

I would like to acknowledge the Chinese Scholarship Council for their financial support during my PhD study in the past years.

I am immensely grateful to all of my friends in Stuttgart and in Germany. My PhD career in the past years was amazing because I was always surrounded by loving, supportive, and incredibly fun people. They leave me unforgettable experiences and a great memory in my life. Particularly, I would give my thanks to Walter, Sonja, Caroline and Margarete for our precious friendship, and Gabriele with her family for their kindly hosting during Christmas.

I would like to give my special thanks to Xinjie for her accompany, kindly understanding, encouragement and emotional support in these years.

Last but not least, I would like to express my deepest gratitude to my family, especially my parents. I am quite lucky to have such a family, who always unconditionally understands and supports me. This dissertation would not have been completed without their warm love, continued patience, and endless support.

Appendix A

Recipe for Computing Total Water Storage Changes from GRACE

To compute the total water storage (TWS) changes, the computational steps implemented in this thesis are summarized as follows:

- The GRACE level 2 data are based on the GSM RL05 solutions from GFZ, represented in fully normalized geopotential spherical harmonic coefficients with maximum degree of 90.
- The degree-2 coefficients $C_{2,0}$ are replaced with the solutions from Satellite Laser Ranging (Cheng et al., 2011).
- The degree-1 coefficients provided by Swenson et al. (2008) are filled in the data.
- The long-term mean which is calculated based on the period from 2004 to 2010 is removed from the data in spectral domain in order to acquire the spherical coefficients of time-variable field.
- An isotropic Gaussian filter with radius of 300 km is applied to the coefficients (Wahr et al., 1998).
- A destriping filter is also applied to the coefficients to minimize the effect of correlated errors (Swenson and Wahr, 2006).
- The monthly total water storage changes are eventually estimated by (3.6).

Appendix B

Joint Approximate Diagonalization of Eigenmatrices Algorithm

The JADE algorithm aims to find a rotation matrix R that optimally diagonalizes the cumulant tensor Q^X of X . It optimizes the Q^X by jointly diagonalize a set of matrices in Q^X , now described by the following steps (Cardoso, 1993):

Initialization The rotation matrix is initialized as an identity matrix, i.e. $R = I$. For a unitary rotation matrix

$$V = \begin{bmatrix} \cos\theta & -\sin\theta \\ \sin\theta & \cos\theta \end{bmatrix}, \quad (\text{B.1})$$

we initialize a rotation angle θ as 0.

Joint diagonalization According to (2.25) and (2.31), we calculate the cumulant tensor Q^X as a $n^2 \times n^2$ matrix for a given data matrix $X(n \times s)$. For each cumulant matrix,

$$Q_m = \begin{bmatrix} q_{ii} & q_{ij} \\ q_{ji} & q_{jj} \end{bmatrix}, \quad (\text{B.2})$$

where $i = 1, 2, \dots, n$, and $j = 1, 2, \dots, n$ denote the row and column index that one element of cumulant q at (i, j) . $m = 1, 2, \dots, n^2$, representing for one cumulant matrix index. Assume that after a symmetric rotation of Q_m by V_m , the squared sum of the off-diagonal elements of the rotated Q'_m are minimized (Cardoso, 1993),

$$Q'_m = V_m^T Q_m V_m = \begin{bmatrix} \cos\theta & \sin\theta \\ -\sin\theta & \cos\theta \end{bmatrix} \begin{bmatrix} q_{ii} & q_{ij} \\ q_{ji} & q_{jj} \end{bmatrix} \begin{bmatrix} \cos\theta & -\sin\theta \\ \sin\theta & \cos\theta \end{bmatrix} = \begin{bmatrix} q'_{ii} & q'_{ij} \\ q'_{ji} & q'_{jj} \end{bmatrix}. \quad (\text{B.3})$$

In fact, optimization of (B.3) is equivalent to finding a θ that maximizes the squared sum of the diagonal elements (Cardoso, 1993), writes

$$\max(q_{ii}'^2 + q_{jj}'^2). \quad (\text{B.4})$$

Notice that $2(q_{ii}'^2 + q_{jj}'^2) = (q_{ii}' - q_{jj}')^2 + (q_{ii}' + q_{jj}')^2$, and that the trace of $q_{ii}' + q_{jj}'$ is invariant in a unitary transformation, maximization of (B.4) is equivalent to

$$\max(q'_{ii} - q'_{jj})^2. \quad (\text{B.5})$$

According to (B.3), we derive

$$h_m = q'_{ii} - q'_{jj} = [q_{ii} - q_{jj} \quad q_{ij} + q_{ji}] \begin{bmatrix} \cos 2\theta \\ \sin 2\theta \end{bmatrix} = g_m \cdot u, \quad (\text{B.6})$$

where $g_m = [q_{ii} - q_{jj} \quad q_{ij} + q_{ji}]$ and $u = [\cos 2\theta \quad \sin 2\theta]$. Thus, we obtain $H = Gu$, if $H = [h_1, h_2, \dots, h_{n^2}]^T$ and $G = [g_1, g_2, \dots, g_{n^2}]^T$. To optimize (B.5), it becomes to jointly diagonalize the quadrant form $H^T H$ (Cardoso, 1993),

$$H^T H = u^T G^T G u. \quad (\text{B.7})$$

In (B.7), u can be considered as the dominant eigenvector of G and thus the rotation angle $\hat{\theta}$ is estimated. The joint diagonalization of all the cumulant matrices is iterated over different rows and columns. The unitary rotation matrix V_m is updated for each pair of cumulants based on the estimated angle $\hat{\theta}$ by

$$\hat{V}_m = \begin{bmatrix} \cos \hat{\theta} & -\sin \hat{\theta} \\ \sin \hat{\theta} & \cos \hat{\theta} \end{bmatrix}. \quad (\text{B.8})$$

Hence, each \hat{V}_m diagonalizes a cumulant matrix Q_m . The rotation matrix is subsequently estimated as a product of n^2 times rotation by \hat{V}_m , i.e. $\hat{R} = \prod_{m=1}^{n^2} \hat{V}_m$.

Update We update the rotation matrix $R = R \cdot \hat{R}$, after an entire loop for each row and column of Q^X . Also, the cumulant matrix Q_m is replaced by the rotated cumulant matrix Q'_m , so that each row and column of the Q^X is subsequently updated.

Determine to stop or not To decide whether to go to a new loop or stop the iteration, we use a threshold condition. The threshold $\xi = 1/100\sqrt{N}$ is selected by Cardoso (1999), where N is the length of the vector X_i . If $\hat{\theta} < \xi$ then the iteration is terminated, otherwise go back to the first step. It means that no further rotation can be applied to maximize $H^T H$. In other words, the cumulant tensor Q^X is iteratively diagonalized by \hat{R} .

As a consequence, we obtain the optimal estimated rotation matrix R . Finally, ICA is accomplished by implementing the last step in (2.30).